Universidade de Aveiro Departamento de Física
2016

Ana Teresa dos Santos Picado

Influência dos processos físicos na produção primária ao longo da costa noroeste da Península Ibérica

Influence of physical processes on the primary production along the Iberian Peninsula northwestern coast

Universidade de Aveiro Departamento de Física
2016

Universidade do Porto Faculdade de Ciências

Universidade do Minho Departamento de Física

Ana Teresa dos Santos Picado

Influência dos processos físicos na produção primária ao longo da costa noroeste da Península Ibérica

Influence of physical processes on the primary production along the Iberian Peninsula northwestern coast

Dissertação apresentada à Universidade de Aveiro para cumprimento dos requisitos necessários à obtenção do grau de Doutor em Física, realizada sob a orientação científica do Doutor João Miguel Sequeira Silva Dias, Professor Auxiliar com Agregação do Departamento de Física da Universidade de Aveiro e coorientação da Doutora Maria Ines Alvarez Fernandez, Professora Associada do Departamento de Física Aplicada da Faculdade de Ciências de Ourense da Universidade de Vigo e do Doutor Nuno Alexandre Firmino Vaz, estagiário de pós-doutoramento da Universidade de Aveiro.

A autora foi financiada pela Fundação para a Ciência e Tecnologia (FCT), através da bolsa de Doutoramento com a referência SFRH/BD/79920/2011, no âmbito do Quadro de Referência Estratégico Nacional (QREN) e do Programa Operacional de Potencial Humano (POPH), comparticipado pelo Fundo Europeu e por fundos nacionais do Ministério da Educação e Ciência (MEC).

o júri / the jury

presidente / president

Doutor António Manuel Rosa Pereira Caetano
Professor Catedrático do Departamento de Matemática da Universidade de Aveiro

vogais / examiners committee

Doutora María Teresa de Castro Rodríguez
Professora Titular do Departamento de Física Aplicada da Faculdade de Ciências de Ourense da Universidade de Vigo

Doutor Ramiro Joaquim de Jesus Neves
Professor Associado do Departamento de Engenharia Mecânica do Instituto Superior Técnico da Universidade de Lisboa

Doutor Fernando Manuel Raposo Morgado
Professor Associado com Agregação do Departamento de Biologia da Universidade de Aveiro

Doutor José Carlos Pinto Bastos Teixeira da Silva
Professor Associado do Departamento de Geociências, Ambiente e Ordenamento do Território da Faculdade de Ciências da Universidade do Porto

Doutor João Miguel Sequeira Silva Dias
Professor Auxiliar com Agregação do Departamento de Física da Universidade de Aveiro

Acknowledgements

Firstly, I would like to express my sincere gratitude to my supervisors Professor João Miguel Dias, Ines Alvarez and Nuno Vaz for the continuous support of my PhD study and related research, for their patience, motivation, and knowledge. Their guidance helped me during all the time of research and writing of this thesis.

I also like to thank Nieves Lorenzo for her help, Paulo Leitão and João Ribeiro for their precious support in the implementation of the circulation model and to Marcos Mateus for the tips in the biogeochemical model.

Thanks to all my colleagues at NMEC (Estuarine and Coastal Modelling Division) for their availability and help and all the fun we have had in the last years, specially to Magda and Carina for the support and encouragement.

A special thank to my friend Sandra Plecha not only for her scientific support but also for her friendship. I also thank to all my friends for the good moments we have shared, namely Anita, Marquito, Mariana, Zé Pedro, Cátia, Mariana Sardo, Canas, Michelle, Ana Sofia, Tiago, Marta, Sandra Costa.

I would like to thank my family, specially my parents, grand parents, aunt Celeste, sister, Pedro, for their encouragement, support and attention throughout writing this thesis.

A very special thank to my little niece Madalena and to Miguelito, Pedrocas and Adriana for the great moments.

Last but not the least, I am also grateful to Miguel for all the patience, love and support through this venture.

palavras-chave Península Ibérica, afloramento costeiro, fitoplâncton, clorofila, modelos de circulação e biogeoquímicos

resumo

A costa noroeste da Península Ibérica (PI) é caracterizada por intensa atividade hidrológica e biogeoquímica, resultante em importantes recursos de peixe e marisco. Neste contexto, o principal objetivo deste trabalho consiste no estudo da influência dos processos físicos na produção primária da região através de deteção remota e modelação numérica. Com este propósito, a linha de costa foi dividida em três domínios: segmentos costeiros oeste, intermédio e norte. Para cada um destes segmentos foi analisada a variabilidade do transporte de Ekman, do índice de afloramento (IA), da temperatura da superfície do mar (TSM) e da concentração de Clorofila-a (Clo-a) em termos de médias sazonais, anuais e mensais a partir de dados de deteção remota. A influência das condições meteorológicas, definidas através de padrões de circulação atmosférica (PCA), no IA e na concentração de Clo-a foi também avaliada e quantificada através de uma análise de probabilidade condicionada. Foi também implementado e validado um sistema de modelação de circulação e biogeoquímica para a área de estudo. A sua validação foi efetuada através da comparação das previsões numéricas com dados *in situ* e de satélite de várias variáveis físicas e biogeoquímicas. Esta implementação foi utilizada para investigar os padrões de fitoplâncton durante dois eventos de afloramento costeiro distintos, observados principalmente nos segmentos costeiros oeste e intermédio. Os resultados da análise aos dados de deteção remota sugerem que o transporte de Ekman, a TSM e a concentração da Clo-a têm diferentes ciclos anuais em cada segmento costeiro, apresentando elevada variabilidade. Em geral, as condições mais favoráveis à ocorrência de afloramento ocorrem nos segmentos costeiros oeste e intermédio durante os meses de primavera-verão e, consequentemente, é observada uma lente de água mais fria junto à costa do que ao largo, assim como níveis de Clo-a elevados. Pelo contrário, no segmento costeiro norte a TSM é elevada, devido ao aquecimento de verão na zona sudeste do Golfo da Biscaia, e a concentração de Clo-a é baixa. Durante o inverno são observados elevados níveis de Clo-a nos três segmentos costeiros, que estão relacionados com o efeito cumulativo de eventos de afloramento e de descargas fluviais, que favorecem a entrada de nutrientes na costa. Os resultados da análise de probabilidades efetuada evidenciam que ao longo do segmento oeste as relações mais fortes entre os PCA, o IA e a concentração de Clo-a foram obtidas na primavera-verão, quando padrões atmosféricos Norte, Nordeste e Noroeste ocorrem. Nos segmentos costeiros intermédio e norte verificam-se elevadas probabilidades de IA e de Clo-a quando os padrões atmosférico Este e Sul ocorrem, para as duas estações do ano referidas. O modelo numérico implementado demonstrou capacidade em reproduzir com precisão a dinâmica da região em estudo, quer à superfície, quer ao longo da coluna de água. A análise dos resultados de modelação revela a existência de duas células de afloramento nos dois eventos estudados, sendo os padrões de fitoplâncton diferentes para cada evento. De acordo com os resultados, quando ocorrem ventos fortes favoráveis ao afloramento o tempo de residência na zona costeira é muito baixo, não permitindo um crescimento significativo do fitoplâncton. As águas ricas em nutrientes e fitoplâncton são então advetadas para o largo, onde o tempo de residência é maior e existem condições favoráveis para a fotossíntese. Para eventos de afloramento fortes é observado um fluxo direcionado para o equador junto à costa ao longo da coluna de água, enquanto para eventos mais fracos este fluxo é em direção ao pólo, promovendo a retenção do fitoplâncton na zona costeira. Em suma, a análise efetuada aos dados de deteção remota e de modelação numérica contribuíram para melhorar o conhecimento dos principais processos que influenciam a produção primária ao longo da costa noroeste da PI, à escala sazonal e de eventos. Como trabalho futuro destaca-se a exploração com maior detalhe da dinâmica das células de afloramento detetadas e da resposta do ecossistema à sua presença, assim como o estudo da influência de descargas fluviais na produção primária da região, tirando partido da configuração numérica desenvolvida.

keywords Iberian Peninsula, coastal upwelling, phytoplankton, chlorophyll, circulation and biogeochemical models

abstract

The northwestern coast of Iberian Peninsula (IP) is a region of great hydrologic and biogeochemical activity, resulting in important fish and shellfish resources. In this context, the main aim of this work is to study the influence of physical processes on primary production of the region through remote sensing imagery and numerical modelling. For this propose, the coastline was divided in three domains: western, intermediate and northern coastal segments. For each coastal segment was analysed the variability of Ekman transport, upwelling index (UI), sea surface temperature (SST) and chlorophyll (Chl-a) concentration in terms of seasonal, annual and monthly averages of remote sensed data. The influence of meteorological conditions, defined by circulation weather types (CWTs), on UI and Chl-a concentration was also evaluated and quantified, through a conditional probability analysis. Afterwards, a coupled circulation and biogeochemical model was implemented and validated along the study area. Validation was performed through the comparison of numerical predictions with *in situ* and satellite data for several physical and biogeochemical variables. This implementation was then used to investigate phytoplankton patterns during two distinct upwelling events, mainly observed at western and intermediate coastal segments. Results from remote sensed data analysis suggest that Ekman transport, SST and Chl-a concentration had different annual cycles within each coastal segment and high seasonal variability. Generally, the most upwelling favourable conditions occur along the western and intermediate coastal segments during spring-summer months and consequently a lens of water colder than offshore is observed in the coastal region along with high Chl-a levels. Otherwise, at northern coastal segment high SST, related to the summer warming at the southeastern Bay of Biscay, and low Chl-a concentration are observed. During winter high Chl-a levels were also observed at the three coastal segments, that are related to the cumulative effect of upwelling events and river runoff, favouring the entrance of nutrients onto the coast. Results from the probability analysis show that along the western coastal segment the strongest relations between CWTs, UI an Chl-a concentration were obtained in spring-summer when weather types Northerly, Northeasterly and Northwesterly occur. At northern and intermediate segments results reveal high probabilities of UI and Chl-a when weather types Easterly and Southerly were observed, for both stations referred. The numerical model showed the capability to reproduce accurately the dynamics of the study region, either at surface or along the water column. The modelling results analysis reveals the existence of two upwelling cells for both events studied, being phytoplankton patterns different for each event. According to results, when upwelling favourable winds are strong, the residence time near coast is very short, not allowing significant phytoplankton growth. Nutrient and phytoplankton rich waters are then advected offshore, where the residence time is higher and favourable conditions for photosynthesis occur. For strong upwelling events an equatorward flow develops near coast along the water column, while for weaker events this flow is poleward, promoting the retention of phytoplankton in the coastal region. In summary, the analysis performed to remote sensed data and numerical modelling predictions, have contributed to improve the knowledge about the main processes that influence primary production along the northwestern coast of IP, at seasonal and event scales. For future, is highlighted the exploitation in detail of the upwelling cells dynamics and the ecosystem response to their presence, as well as the study of river runoff influence in the primary production of the region, taking advantage of the numerical application developed.

Contents

List of figures

List of tables

List of symbols

A	Surface
A_t	Coefficient for atmospheric transmission
$BIAS$	Bias
C_b	Bowen coefficient
C_d	Dimensionless drag coefficient
C_D	Bottom drag coefficient
C_n	Cloud cover
C_{10}	Drag coefficient function
$cov(x, y)$	Covariance
$c(t)$	Ramp coefficient function
D	Data
$e_{s,a}$	Saturated air pressure
$e_{s,w}$	Saturated water pressure
eX_X	Excretion rate
f	Coriolis parameter
FP	Source or sink term
g	Gravity
G_X	Grazing rate

h	Bottom depth
H_L	Latent heat
H_S	Sensible heat
I	Light intensity
I_0	Light intensity at surface
K	Turbulent mass diffusion coefficient
k_c	von Karman constant
k_L	Light extinction coefficient
K_S	Salinity turbulent diffusion
K_T	Temperature turbulent diffusion
M	Model predictions
m_X	Natural mortality rate (non-predatory)
n	Number of measures
n_i	Number of images
$\overrightarrow{n}$	Normal vector to surface
O_L	Oxygen fluxes
p	Pressure
P	Concentration
p_{atm}	Atmospheric pressure
Q	Solar radiation flux of short wavelength
Q_x, Q_y	Ekman transport
Q_0	Solar radiation flux
r_h	Relative humidity

$r_{x,y}$	Correlation coefficient
R_a	Net long-wave radiation
R_{br}	Infrared radiation
$RMSE$	Root mean square error
R_s	Albedo
r_X	Total respiration rate
S	Salinity
SS_S	Source and sink term of salinity
SS_T	Source and sink term of temperature
t	Time
T	Temperature
T_a	Air temperature
T_c	Ramping period
u_p	Particle velocity
u_F	Random fluctuation of particle velocity
u_M	Mean velocity
u, v, w	Velocity components
V	Volume
$\overrightarrow{v}$	Velocity vector
$\overrightarrow{v_T}$, $\overrightarrow{v_H}$, $\overrightarrow{v_V}$	Turbulent viscosity
W, W_x, W_y	Wind speed
$Wflux$	Vertical advective flux
x, y, z	Spatial coordinates

z_0^b	Bottom roughness length
α,β	Coefficients dependent on wind velocity
$\delta\lambda$	Eigenvalue error
ε	Water emissivity
η	Water elevation
θ	Latitude
λ	Eigenvalue
μ_X	Gross growth rate
ρ	Density
ρ_a	Air density
ρ_w	Seawater density
ρ_0	Reference density
σ_x, σ_y	Standard deviation
σ	Stefan-Boltzman constant
$\overrightarrow{\tau}$	Wind and bottom stresses
$\overrightarrow{\tau_w}$	Wind surface stress
ϕ_X	Biomass
Φ	Gravitational potential
$\overrightarrow{\Omega}$	Angular velocity vector
$\overrightarrow{\nabla}$	Gradient operator

List of acronyms

A	Anticyclonic
AC	Azores Current
ADI	Alternating Direction Implicit
AVHRR	Advanced Very High Resolution Radiometer
BUS	Benguela Upwelling System
C	Cyclonic
CanCS	Canary Current System
CCS	California Current System
CDOM	Colored Dissolved Organic Matter
CFSR	Climate Forecast System Reanalysis
CFUC	Cape Finisterre Upwelling Cell
Chl-a	Chlorophyll-a
C:N:P	Carbon:Nitrogen:Phosphorus ratio
CUE	Canary Upwelling System
CWTs	Circulation Weather Types
CZCS	Coastal Zone Color Scanner
DOM	Dissolved Organic Matter
E	Easterly

EBUS	Eastern Boundary Upwelling System
ENACW	Eastern North Atlantic Central Water
ENACWsp	Eastern North Atlantic Central Water of subpolar origin
ENACWst	Eastern North Atlantic Central Water of subtropical origin
EOF	Empirical Orthogonal Functions
FES	Finite Element Solution
FRS	Flow Relaxation Scheme
GEBCO	General Bathymetric Chart of the Oceans
GEV	Generalized Extreme Value
GODAS	Global Ocean Data Assimilation
GOTM	General Ocean Turbulence Model
IP	Iberian Peninsula
IPC	Iberian Poleward Current
IUS	Iberian Upwelling System
MLD	Mixed Layer Depth
MODIS	Moderate Resolution Imaging Spectroradiometer
MUC	Minho Upwelling Cell
N	Northerly
NAC	North Atlantic Current
NCDC	National Climatic Data Center
NCEP	National Centers for Environmental Prediction
NE	Northeasterly
NOMADS	National Model Archive and Distribution System

NW	Northwesterly
NPZD	Nitrogen-Phytoplankton-Zooplankton-Detritus
OBC	Open Boundary Conditions
PC	Portugal Current
PCC	Portugal Coastal Current
PCS	Portugal Current System
POM	Particulate Organic Matter
PUS	Peruvian Upwelling System
ROMS	Regional Ocean Modelling System
S	Southerly
SD	Standard Deviation
SE	Southeasterly
SeaWiFS	Sea-viewing Wide Field-of-View Sensor
SMHI	Swedish Meteorological and Hydrological Institute
SSE	Sea Surface Elevation
SST	Sea Surface Temperature
SVD	Singular Value Decomposition
SW	Southwesterly
TKE	Turbulent Kinetic Energy
TVD	Total Variation Diminishing
UI	Upwelling Index
UNESCO	United Nations Educational, Scientific and Cultural Organization

W	Westerly
WIBP	Western Iberian Buoyant Plume
WRF	Weather Research and Forecasting

Chapter 1

Introduction

1.1 Motivation

The knowledge of physical processes at global or regional scales in the ocean is essential to understand ocean biogeochemical processes, particularly those related to primary production. Phytoplankton is one of the marine ecosystem key components, representing the base of trophic web and therefore its variability affects the dynamics of the whole ecosystem. It is responsible for the conversion of carbon dioxide in organic carbon, through photosynthesis, *i.e.* primary production. The best measure of phytoplankton biomass would be to determine the amount of organic carbon in the phytoplankton cells. However, such a measure is almost impossible in a natural seawater sample due to the presence of other organisms, like detritus and dissolved organic matter. Consequently, photosynthetic pigments (usually chlorophyll-a (Chl-a), once it is a quantity monitored by satellite) are used as a proxy and its concentration can be used to estimate the phytoplankton biomass in water quality and ecological studies.

The most productive areas worldwide are the upwelling regions. The rising of cold water makes nutrients available for primary production in the euphotic zone, where mass and energy are transferred through trophic webs, which generates rich areas in terms of biological abundance. Therefore, the spatial and temporal analysis of Chl-a in coastal upwelling regions is really important considering its high economic value. Upwelling is usually linked to an increase in primary production in most coastal areas, creating an extraordinary commercial interest for fisheries. In fact, more than

20% of global fish catches occur in upwelling areas, although they occupy less than 1% of the world's ocean surface (McGregor et al., 2007). The relationship between Chl-a and fishery depends upon the number of linkages between phytoplankton and the higher trophic level. For some species, such as anchovies and sardines, which eat phytoplankton at some phase in their life cycle, the linkage is direct (Ware and Thomson, 2005), whereas for other species there are many trophic levels in between. In the open ocean 2% of primary production is needed to support the fishery catch, but in coastal regions the requirements ranges from 24-35%, suggesting that these systems are at or beyond their carrying capacity (Pauly and Christensen, 1995). Freshwater and sediment inputs from rivers also play a major role in sustaining coastal ecosystems, carrying nutrients that promote biological productivity. Therefore, the study of marine biogeochemistry in coastal waters and its dependence on physical, chemical and biological factors is imperative. The demand for this kind of information arises from a range of fields and applications, such as scientific research on marine ecosystems, monitoring of seawater quality and decision-making support for marine and coastal management.

Moreover, ocean primary production and Chl-a levels can be highly sensitive to changes in sea surface temperature (SST) and wind patterns. The ocean temperatures worldwide have shown a global warming trend (Levitus et al., 2000), which may have a negative impact on marine ecosystems generating latitudinal displacements of the population of phytoplankton and zooplankton toward cooler regions (Richardson, 2008; Richardson and Schoeman, 2004). Global warming could intensify alongshore winds and accelerate coastal upwelling circulation (Bakun, 1990; McGregor et al., 2007; Relvas et al., 2009; Bakun et al., 2010) leading to an increase in primary production.

Remote sensing data constitutes an efficient way to improve the knowledge on environmental conditions of an ecosystem, being extensively used for monitoring different variables over the oceans, such as Chl-a concentration, SST and wind patterns. The exploitation of these data gives the opportunity to analyse spatial maps containing more information than isolated points. Therefore, satellite data provide valuable information about spatial and temporal distribution of these variables, which can be used to research the possible implications of their variations on coastal ecosystems, and therefore to characterize the primary production over vast areas. However, due to cloud cover, mainly in winter, the satellite information is often missing.

The demand for numerical models able to reproduce physical and biogeochemical interactions along the oceans arise to overcome the lack of continuous and long term observations of physical and biological variables and to provide forecasts of coastal ocean state, allowing the comprehension and quantification of the different processes that occur in coastal waters. Water temperature, salinity, current velocity, chlorophyll and primary production rank among the top products demanded by research scientists and coastal managers (Marta-Almeida et al., 2012).

The northwestern coast of Iberian Peninsula (IP) (Figure 1.1) is the northern boundary of the Canary Upwelling Ecosystem (CUE), which is one of the four major Eastern Boundary Upwelling Systems (EBUS) of the world (Pelegri et al., 2005). It is a region of great hydrologic and biogeochemical activity, as a result of coastal upwelling induced by seasonal wind that is the main recognized source of phytoplankton (Fraga, 1981; Tenore et al., 1995; Peliz et al., 2002; Relvas et al., 2007). Coastal upwelling in this area shows a well defined seasonality (Wooster et al., 1976; Fraga, 1981; Fiúza, 1983), with active and persistent conditions prevailing from June to September (Wooster et al., 1976), promoting high levels of Chl-a. It is remarkable that due to the different coastline direction, northerly winds produce upwelling off the western coastal segment

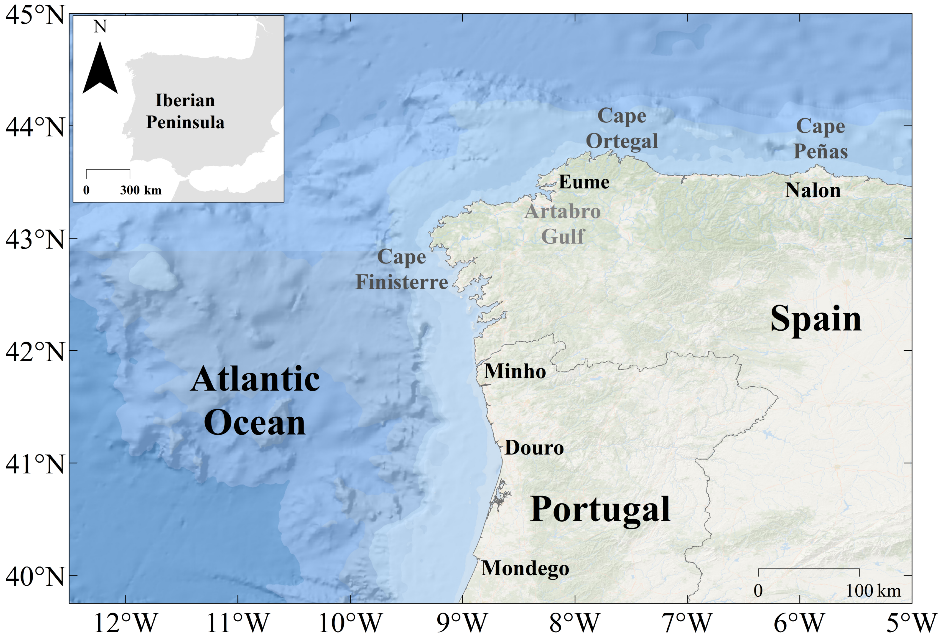

Figure 1.1: Study area, with the location of the main freshwater sources (Mondego, Douro, Minho, Eume and Nalon Rivers) and capes (Cape Finisterre, Ortegal and Peñas).

(from 40 °N to 43 °N), northerly and easterly winds at intermediate coastal segment (between Cape Finisterre and Cape Ortegal) (McClain et al., 1986; Torres et al., 2003), whereas easterly winds do it off the northern coastal segment (between 8 °W and 5 °W). In wintertime, the wind regime favours coastal convergence (Peliz and Fiúza, 1999), however upwelling events may also occur and an increase in its frequency and intensity in the last decades was reported (Alvarez et al., 2003; Borges et al., 2003; deCastro et al., 2006; Prego et al., 2007; Santos et al., 2004). In addition, the spring and autumn Chl-a maxima occur within the transitional periods of onset and cessation of upwelling season, respectively, determining the fate of the accumulated Chl-a: off-shelf export *versus in situ* mineralization (Alvarez-Salgado et al., 2003).

The northwestern IP is also strongly influenced by freshwater input from rivers, being the most important Mondego, Douro and Minho at western, Eume at intermediate and Nalon at northern coastal segments (Figure 1.1). Generally, river plumes are turbid and rich in nutrients, remaining near surface due to their buoyancy and breaking up into lenses of less saline water, stimulating phytoplankton growth (Lunven et al., 2005).

1.2 Aims

The main goal of this work is to study the influence of physical processes on the spatial and temporal patterns of Chl-a concentration along the northwestern coast of IP, through remote sensing imagery and numerical modelling. Due to the coastaline direction (Figure 1.1), three coastal segments were considered for analysis: the western coastal segment from 40 °N to Cape Finisterre; the intermediate coastal segment from Cape Finisterre to Cape Ortegal; and the northern coastal segment from Cape Ortegal to 5 °W. In particular, this work aims to:

- characterize the Chl-a concentration, SST and wind patterns;
- perform a comparative review between the processes along the three coastal segments;
- investigate the atmosphere-ocean-land conditions that drive phytoplankton blooms development and highlight localized changes;

- understand and evaluate the influence of the meteorological conditions, through Circulation Weather Types (CWTs) on upwelling and Chl-a concentration variability;
- develop a 3D biogeochemical model application coupled to a circulation numerical model to reproduce the main hydrodynamic and biogeochemical features of the study region, as well as spatio-temporal patterns of water temperature, salinity, phytoplankton and oxygen;
- evaluate circulation and phytoplankton patterns during two distinct upwelling events through numerical modelling.

1.3 Literature review

1.3.1 Primary production: Chl-a concentration

As previously referred, coastal upwelling systems generally exhibit high productivity rates and biological diversity and therefore they have significant economic importance. Accordingly, Patti et al. (2008) aimed to identify the responsible factors for the differences in Chl-a concentration observed between the different EBUS that supports large commercial fisheries: California, Canary, Humboldt and Benguela (Pauly and Christensen, 1995). Authors found that nutrient concentration levels, which are mainly governed by local upwelling intensity, explain the differences between relatively low (Canary and California) and high (Benguela and Humboldt) production areas. Also, the extent of the continental shelf width is the key factor explaining the higher primary production observed in Benguela region compared to Humboldt region. Patti et al. (2008) work was performed using Chl-a remote sensed data (1998–2004), revealing its importance to analyse the surface ocean over a larger spatial and temporal context.

The first studies regarding the temporal and spatial variability of regional remote sensing Chl-a concentration have used the Coastal Zone Color Scanner (CZCS) product: Scarla and Frank (1994), Arrigo et al. (1998), Yoder et al. (2001) and Yoder et al. (2002). With the success of CZCS, a number of missions were approved by various space agencies, some of which were meant for technology development and others for research. Among these missions are Sea-viewing Wide Field-of-view Sensor (SeaWiFS)(1997-

2009) and Moderate Resolution Imaging Spectroradiometer (MODIS) (2002 to present) sensors, which were designed for quantitative global research purposes and have been used in a significant number of studies, being their quality similar (Franz et al., 2007).

The first studies with SeaWiFS appeared to evaluate trends in primary production, through comparison with CZCS (Gregg and Conkright, 2002; Gregg et al., 2003; Antoine et al., 2005). The results obtained underscore the importance of the international science community converging on processing algorithms and collaborating on product validation. A few global comparisons between *in situ* data and SeaWiFS products were then performed, such as Gregg and Casey (2004) and Bailey and Werdell (2006) and satisfactory results were achieved.

More recently, a number of studies were carried out in order to investigate Chl-a concentration distribution all over the world, using SeaWiFS product. For instance, Brickley and Thomas (2004) used this ocean-color satellite data to present a synoptic quantification of Chl-a variability on seasonal and interannual time scales over the Northeast Pacific and Coastal Gulf of Alaska, Navarro and Ruiz (2006) applied the Empirical Orthogonal Functions (EOF) technique to the weakly Chl-a composite images in Gulf of Cádiz, Krezel et al. (2005) investigated the influence of coastal upwelling on primary production in the Polish coast of the Baltic Sea and Gao et al. (2013) studied the temporal and spatial distribution of Chl-a and its responses to changes in SST and wind patterns along the western South China Sea. Most of these studies also used remote sensed SST from the Advanced Very High Resolution Radiometer (AVHRR) to infer about the Chl-a dependence on SST. Many other works have been conducted in the last decade using SeaWiFS data to improve global and regional knowledge about Chl-a variability (Gregg et al., 2005; Ho et al., 2004; Venegas et al., 2008; Demarcq, 2009).

MODIS products have also been used to study the Chl-a and SST variability along several coastal regions worldwide. Examples can be found in the South China Sea (Liu et al., 2014), in the Gulf of Finland (Uiboupin et al., 2012), in the Gulf of Alaska (Waite and Mueter, 2013), in South Atlantic Bight (Miles and He, 2010) and in the Gulf of Maine (Li and He, 2014).

Several studies have also investigated the influence of river discharges on primary production and Chl-a concentration distribution, in different regions over the world, like the Pacific northwest Coast (Hickey and Banas, 2003), the northeastern Gulf of Mexico (Nababan et al., 2011), the coast off northern Japan (Lihan et al., 2011), the La Plata continental shelf region (Garcia and Garcia, 2008) and the adjacent sea area of Yangtze River Estuary (Wang et al., 2015). These studies were based on remote sensed Chl-a data and *in situ* measurements and concluded that rivers runoff promote phytoplankton blooms. However, near coastal waters, global algorithms usually show an overestimation in Chl-a retrievals due to optical interference of both dissolved and particulate material from continental influence (Gordon and Morel, 1983; Hu et al., 2001; Darecki and Stramski, 2004).

Therefore, the advances of the last decades in satellite remote sensing have significantly improved the understanding and clarified many aspects of ocean biogeochemestry and ecosystem dynamics (Longhurst, 1998; Moore et al., 2002).

Comparing with *in situ* and remote sensing data, physical-biological coupled models provide a much more complete description of ocean biogeochemistry, depending on the complexity of the model. Indeed, oceanographic modelling has helped to further understand the different EBUS that share high biological productivity as consequence of the nutrients supply from upwelling.

The first physical-biological coupled model was developed by Fasham et al. (1990), where plankton populations are aggregated into seven compartments (phytoplankton, zooplankton, bacteria, nitrate, ammonium, dissolved organic nitrogen and detritus). Fasham et al. (1993) applied this model to North Atlantic and, despite its simplicity, results were encouraging. Since then, a huge effort has been performed to develop more complete and robust biological models.

The California Current System (CCS) constitutes an important case study that motivated the development of a large number of physical-biological coupled model studies (Edwards et al., 2000; Powell et al., 2006; Gruber et al., 2006; DiLorenzo et al., 2008). Powell et al. (2006) coupled a high resolution three-dimensional circulation model of the CCS with a relatively simple (one component in each category) lower trophic level ecosystem model for Nutrient-Phytoplankton-Zooplankton-Detritus (NPZD). Authors compared the model temporal patterns with satellite observations and found significant skill of the model. Recently, Siedlecki et al. (2015) studied the oxygen seasonal and interannual variability on the Washington and Oregon continental shelves, that experiences seasonal decline over the summer upwelling season, using a regional model. Authors found that model captures the observed seasonal decline as well as spatial trends in bottom oxygen.

Echevin et al. (2008) coupled a biogeochemical and a physical model for the Peruvian Upwelling System (PUS, part of the Humboldt system). Authors compared the model outputs with satellite and *in situ* data, finding a good agreement. Therefore the model was then used to investigate the mechanisms controlling Chl-a distribution as a proxy of the productivity in the area. Lachkar and Gruber (2011) compared California and Canary current systems using a physical-biological coupled model and concluded that, although nutrient concentrations were higher in California, production was almost half than in the Canary Current System (CanCS). At northern Gulf of Mexico, Fennel et al. (2011) implemented a physical-biological coupled model to analyse phytoplankton variability. After demonstrating that model realistically reproduces many observed features of nitrate and phytoplankton dynamics, authors analysed phytoplankton source and sink terms along the ecological gradient from high-nutrient plume waters to low-nutrient waters far from the direct influence of the Mississippi River. More recently, Montes et al. (2014) investigated the connection between the equatorial mean circulation and the oxygen minimum zone in Eastern Tropical Pacific with a high resolution coupled physical-biological model. Hernández-Carrasco et al. (2014) analysed the impact of horizontal stirring on phytoplankton dynamics in the Benguela Upwelling System (BUS) within an idealized two dimensional modelling framework. Authors found that mesoscales eddies and filaments transport a significant fraction of the recently upwelled waters towards the open ocean before being efficiently used by the pelagic food web.

1.3.2 Northwestern coast of Iberian Peninsula

The northwestern coast of IP is characterized by high biological activity due to phytoplankton blooms associated with the enrichment of surface waters with nutrients from below. The upwelling events that occur in the Iberian Upwelling System (IUS) have been characterized, either in terms of their physical processes (Fiúza et al., 1982; Alvarez-Salgado et al., 1993; Peliz et al., 2002), either of its associated biological processes (Santos et al., 2001; Queiroga et al., 2007; Arístegui et al., 2009). Indeed, the region is one of the main spawning and recruitment areas for sardine (Ré et al., 1990; Carrera and Porteiro, 2003; Marques et al., 2005), horse mackerel (Murta et al., 2008) and several marine invertebrates (dos Santos et al., 2008) and therefore has attracted large interest in the scientific community.

In the last decades, several studies regarding Chl-a concentration variability along the IP coast have been carried out, mainly during spring and summer. Bode et al. (1994) have summarized data from several cruises along the Galician shelf, showing differences in primary production and biomass between the rich areas south of Cape Finisterre and the northern shelf. Additional information on Chl-a and phytoplankton concentration along the region was described in oceanographic surveys (Tenore et al., 1995; Casas et al., 1997; Castro et al., 2000; Bode et al., 2002; Varela et al., 2005). In most of these studies, the coastal upwelling and continental runoff appeared as the main driving forces of pelagic primary productivity and phytoplankton composition. However, they were focused on data measured at stations located in different regions of the coast and therefore provide localized knowledge of Chl-a patterns in space. The development of remote sensing technology allows making high resolution measurements of ocean color over the world's oceans. Accordingly, several studies using remote sensed Chl-a concentration were published in the region. For instance, McClain et al. (1986) have studied an upwelling event along the Galician coast during April 1982, through SST data (AVHRR), Chl-a concentration (CZCS), *in situ* measurements and numerical simulations. Moreover, Peliz and Fiúza (1999) presented a complete study on the spatio-temporal variability of surface phytoplankton pigment concentrations derived from CZCS off western IP coast. Ribeiro et al. (2005) studied the response of Chl-a to a winter upwelling event off western Iberia, while Alvarez et al. (2012) have investigated the seasonal variability of Chl-a concentration along the Galician coast and its response to upwelling and river discharges. Focused on the southern part of IP, Navarro and Ruiz (2006) studied the temporal and spatial variability of phytoplankton in the Gulf of Cádiz and Cravo et al. (2010) analysed an upwelling filament off southwest Iberia.

Changes in coastal upwelling frequency and intensity are one of the most studied processes influencing phytoplankton and fish distribution all over the world (Narayan et al., 2010; Barton et al., 2013; Patti et al., 2010; Aravena et al., 2014; Garcia-Reys and Largier, 2010; Seo et al., 2012). One of the most important works regarding this matter was published by Bakun (1990), where the four EBUS were analysed, based on observations for the period 1946-1988. This author showed an alongshore wind stress intensification trend during summer in all systems, which implicate an upwelling intensification. Several studies focused on different upwelling regions have investigated the Bakun hypothesis worldwide. Along the IP coast, Lemos and Pires (2004) found a weakening trend in the last 60 years of the 20th century, through the analysis of both meriodional wind component and SST datasets. Also, Alvarez et al. (2008b) confirmed this negative trend for the period 1967-2006 for March, April and July-December, however for the remaining months, no clear seasonal trend in upwelling intensity was found. In a more recent study Alvarez et al. (2011) noticed that the number of upwelling favourable days off western Galician coast decreased in the period of 1967-2008. Otherwise, Santos et al. (2005) reported an intensification of the coastal upwelling off western Iberian coast from 1992 onwards. This result is in accordance with Relvas et al. (2009) that, through satellite SST data, reported an intensification of coastal upwelling in the Portuguese southwest region since 1985. Moreover, Miranda et al. (2012) have published a study that also supports the Bakun (1990) hypothesis, that upwelling intensity is likely to increase with global warming. Those authors found the increase in upwelling intensity more prominent in the northern limit of the region, near Cape Finisterre. This study was performed using ocean modelling, that allow to perform long simulations (30 years) and to design future scenarios.

In the last decades, numerical modelling was broadly used to simulate the hydrodynamic and circulation features of the Atlantic Iberian margin (northern part of the CanCS) (Coelho et al., 2002; Peliz et al., 2003; Marta-Almeida and Dubert, 2006; Nolasco et al., 2013; Peliz et al., 2013), however only in the last years a strong effort has been performed to simulate its biogeochemistry, from which resulted several studies. For instance, Marta-Almeida et al. (2012) presented an operational biogeochemical forecast system for the Portuguese and Galician regions, using the Regional Ocean Modeling System (ROMS), integrating the atmospheric, hydrodynamic and biogeochemical variables. An extreme upwelling event along the Galician coast was also studied through numerical modelling by Rocha et al. (2013). Those authors coupled the NPZD biogeochemical model to an oceanic circulation model (ROMS) and studied the behaviour and evolution of a phytoplankton bloom generated by a large upwelling core. Authors highlighted the importance of ocean circulation in Chl-a distribution and found an inverse relation between SST and Chl-a concentration. Reboreda et al. (2014, 2015) also used ROMS to study the seasonal and interannual variability (2001-2010) of Chl-a and oxygen along the Iberian margin. Focused in the southern part of IP coast, Macias et al. (2014) coupled a newly biogeochemical model to the circulation model developed by Peliz et al. (2013), specially designed to represent the Gulf of Cadiz and Alboran region pelagic ecosystem. Model performance was assessed against data and results revealed its accuracy to represent seasonal and climatological distribution of primary and secondary producers, with some mismatches that are mainly attributed to the missing of tidal forcing.

Using a different model (MOHID), Mateus et al. (2012b) developed a regional scale operational modelling tool for the west Iberian coast, discussing its potential for products and services for both scientific and coastal management activities. Recently, Vaz et al. (2015) analysed the SST and Chl-a patterns in a coupled estuary-coastal system off Portugal using the MOHID numerical model. The model was evaluated during a very dynamic and biologic productive period of the year and under the influence of strong freshwater inflow. Authors concluded that the general trends of surface Chl-a and water temperature are satisfactorily reproduced by the model, however some differences were found between model predictions and measurements of the vertical profiles of Chl-a concentration.

Despite these works provided many insights in the study of circulation and biogeochemistry of the region, in this work a step forward is intended in order to further understand the main physical processes that influence the primary production along the northwestern coast of IP, through remote sensing imagery analysis and numerical modelling. Most of the studies described are focused at local stations or particular coastal regions and usually for a specific period, only contributing to localized and limited knowledge. Therefore, in the present thesis the relationship between SST, Chl-a, wind patterns, freshwater input and meteorological conditions is assessed and quantified during a ten year period along the northwestern coast of IP.

Furthermore, most of the physical-biological coupled models applied in the region are based on climatological initial and open boundary conditions, which can be a limitation, once they represent an average of the ocean state. Moreover, tidal forcing is usually missing and therefore model predictions may be unrealistic. Otherwise, the model developed in this study relies in MyOcean global solution of physical and biological variables that includes tidal forcing, which lead to more accurate results.

1.4 Structure of the work

This dissertation is divided in 7 chapters. Chapter 1 presents the Introduction, where motivation, main objectives, literature review, thesis structure and publications in the context of the thesis are described. In Chapter 2 a general description of the study area (IP coast) is performed in terms of its main physical characteristics, circulation patterns and water masses. Next, a seasonal analysis of Chl-a concentration, SST, upwelling conditions, rivers discharge and nutrients is carried out. In Chapter 3 the influence of atmosphere-ocean-land conditions that drive phytoplankton growth and generation are evaluated, and in Chapter 4 the influence of changes in meteorological conditions on upwelling and Chl-a concentration are researched along the northwestern coast of IP. Chapter 5 presents a general overview of the MOHID model along with details about its implementation in the study area. The model validation is also presented in this chapter, being the hydrodynamic and biogeochemical model predictions extensively compared with observations. In Chapter 6 the numerical tools developed are used to explore the phytoplankton patterns during two upwelling events: a strong that occurred during July 2014 and a weak during August 2013. Finally, in Chapter 7, the final conclusions of the dissertation and future work are drawn.

1.5 Publications and communications in the context of this dissertation

Several publications in peer reviewed journals and presentations at international and national conferences resulted from the research developed in this thesis. The publications were used as basis for several chapters of this thesis (marked in bold in the list below).

1.5.1 Papers in international journals indexed in Web of Science:

- Picado, A., Alvarez, I., Vaz, N., Dias, J.M., 2013. Chlorophyll concentration along the northwestern coast of the Iberian Peninsula vs. atmosphere-ocean-land conditions. *Journal of Coastal Reseach*, SI65, 2047-2052. (**Chapter 3**)

- Picado, A., Alvarez, I., Vaz, N., Gomez-Gesteira, M. and Dias, J.M., 2014. Assessment of chlorophyll variability along the northwestern coast of Iberian Peninsula. *Journal of Sea Research* 93, 2-11. (**Chapter 2, 3**)

- Picado, A., Lorenzo, N., Alvarez, I., deCastro, M., Vaz, N. and Dias, J.M., *in press*. Upwelling and Chl-a spatio-temporal variability along the Galician coast: dependence on circulation weather types. *International Journal of Climatology.* (**Chapter 2, 4**)

1.5.2 Other publications:

- Picado A., Sousa M.C., Alvarez I., Vaz N., Dias J.M., 2012. Influence of Upwelling Events on the Chlorophyll Concentration Variability along the Northwestern Coast of Iberian Peninsula, In: Freitas, M.C., Cascalho, J., Taborda, R., Ribeiro, M., Drago, T., Andrade, C., Fatela, F., Cruces, A. (Eds), Actas do VII Simpósio sobre a Margem Ibérica Atlântica, Universidade de Lisboa, 220 pp., ISBN: 978-989-20-3448-5, 83-87.

- Picado, A., Alvarez, I., Vaz, N. and Dias, J.M., 2013. Variabilidade espacial e temporal da Chl-a na costa noroeste da Península Ibérica. *Revista Avances en Ciencias de la Tierra (ACT)* 4, 62-73.

- Picado, A., Alvarez, I., Vaz, N. and Dias, J.M., 2013. Deteção remota da produção primária na costa noroeste da Península Ibérica: variabilidade espacial e temporal. *8º Simpósio de Meteorologia e Geofísica da APMG*, 165-170.

1.5.3 Conference abstracts, proceedings and communications:

- Picado A., Alvarez I., Vaz N., Dias J.M., 2012. Caracterização da concentração de Clorofila na costa noroeste da Península Ibérica. *Encontro de Oceanografia Física*, 15-16 June, Quiaios, Portugal.

- Alvarez I., Dias J.M., Gomez-Gesteira M., deCastro M., Picado A. Influence of upwelling events along the coast of Iberian Peninsula (2012). *Research Day*, Aveiro, Portugal, 13 June 2012.
- Picado A., Sousa M.C., Alvarez I., Vaz N., Dias J.M., 2012. Influence of Upwelling Events on the Chlorophyll Concentration Variability along the Northwestern Coast of Iberian Peninsula. VII Simpósio sobre a Margem Ibérica Atlântica, 16-20 December, Universidade de Lisboa, Lisboa, Portugal.
- Picado, A., Alvarez, I., Vaz, N. and Dias, J.M., 2013. Deteção remota da produção primária na costa noroeste da Península Ibérica: variabilidade espacial e temporal. *8º Simpósio de Meteorologia e Geofísica da APMG*, 18-20 March, Ericeira, Portugal.
- Picado, A., Alvarez, I., Vaz, N., Dias, J.M., 2013. Chlorophyll concentration along the northwestern coast of the Iberian Peninsula vs. atmosphere-ocean-land conditions. *12th International Coastal Symposium* (ICS 2013). 8-12 April, Plymouth University, UK.
- Picado, A., Alvarez, I., Vaz, N. and Dias, J.M., 2014. Variabilidade da clorofila na costa da Península Ibérica: análise comparativa entre as costas noroeste Atlântica e da Cantábria. *Encontro de Oceanografia* 21-22 March, Nazaré, Portugal.

Chapter 2

Characterization of the northwestern Iberian margin

2.1 Introduction

The northwestern Iberian shelf is the habitat of important fish and shellfish resources with commercial interest, like octopus (Otero et al., 2009), pelagic fish species, such as sardine and horse mackerel (Santos et al., 2001, 2004), anchovy (Allain et al., 2001), or albacore (Lavín et al., 2007).

The area under study (Figure 2.1) includes the western (from 40 °N and 44 °30'N) and the northern (from 11 °W to 5 °W) shelves of IP, being characterized by an abrupt change of coastline geometry (Cape Finisterre and Cape Ortegal). Several recent works (Alvarez et al., 2008b; Torres et al., 2003) have shown that the wind field is not homogeneous along northwestern IP, which influences upwelling and biological productivity. Consequently, in this work, three coastal segments are considered taking into account the coastline direction: western (from 40 °N to 43 °N, north-south direction), intermediate (from Cape Finisterre to Cape Ortegal, northeast-southwest direction) and northern (from Cape Ortegal to 5 °W, west-east direction) coastal segments (Figure 2.1).

At western coastal segment are located the most important freshwater sources of the northwestern coast of IP: Minho, Douro and Mondego Rivers (Figure 2.1), which during winter are responsible for the formation of low salinity plumes, still traceable in summer. These buoyant plumes respond rapidly to wind changes and have strong

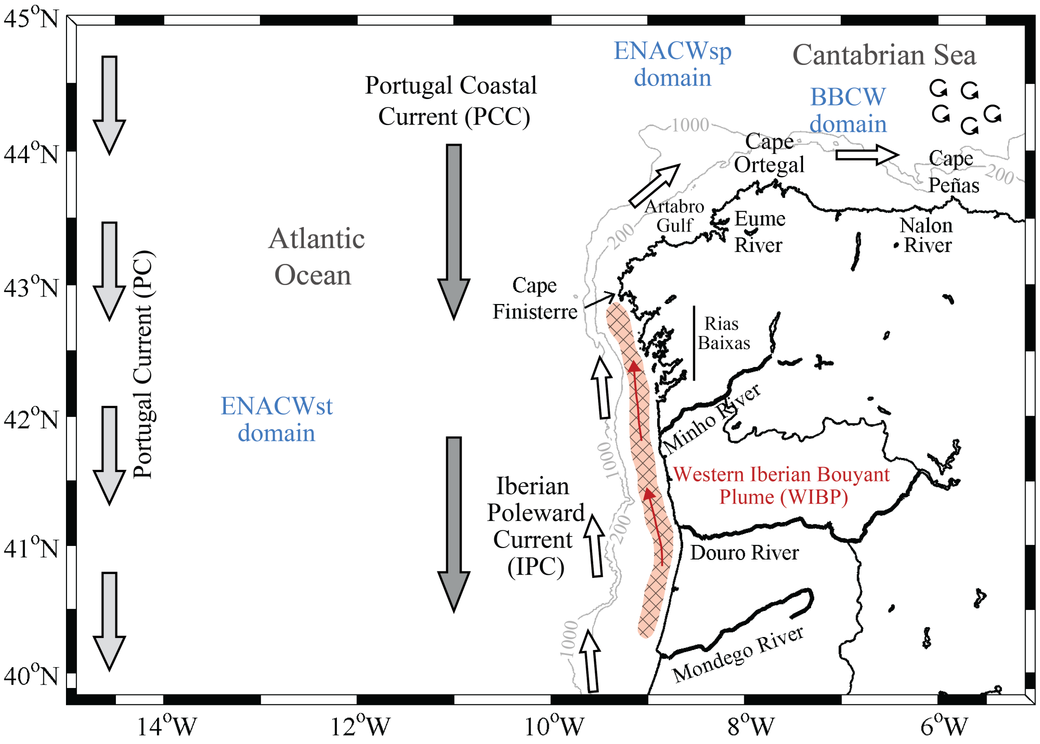

Figure 2.1: Circulation features of the northwestern IP and 200 and 1000 m isobaths.

impact on the inner-shelf dynamics, due to the increased density gradients, and on biological fields due to their efficiency in providing a mean for organic matter retention (Santos et al., 2004; Ribeiro et al., 2005; Otero et al., 2008) and therefore survival of early life stages of several marine species (Arístegui et al., 2009).

North of Minho River are located several estuaries locally named as Rias Baixas (Figure 2.1), which are similar from a morphological point of view and share several common features (Alvarez et al., 2005). Freshwater contribution into Rias Baixas comes from four small rivers, enhancing water dynamics and biogeochemistry of the coastal adjacent region (Alvarez-Salgado et al., 1996). The freshwater discharge from these four rivers are not considered in this work once they have low fluxes when compared to Mondego, Douro and Minho Rivers. Moreover, Rias Baixas are V shaped, presenting strong mixing, being the river flow diluted with oceanic waters and therefore hard to identify. Additionally, these small freshwater inputs may be masked by Minho and Douro plumes, which reach Rias Baixas during specific atmospheric and circulation conditions (Mendes et al., 2016).

Upwelling has important biological implications at western coastal segment due to high input of nutrients that trigger a great primary productivity, supporting an intense mussel raft culture at Rias Baixas (Blanton et al., 1987; Figueiras et al., 2002). Otherwise, upwelling can have negative impact on the survival of pelagic fish first developmental stages through increased offshore transport to unfavourable areas (oligotrophic oceanic waters). Indeed, sardine spawn occur off IP, predominantly in winter (Ré et al., 1990; Marques et al., 2005) and therefore upwelling winter events may generate fluctuations in its productivity leading to problems of sustainability and of fishery management and policies.

At intermediate coastal segment, immediately north of Cape Finisterre is located the Artabro Gulf that receives small inputs of freshwater from Eume River (Figure 2.1). This region supports a significant number of mussel rafts and local fisheries, although with a total yield lower than from Rias Baixas. At intermediate coastal region phytoplankton dynamics show a seasonal cycle, determined by alternating periods of mixing and stratification in water column (Bode et al., 2002). These typical patterns are largely modified by spring-summer upwelling, which fertilize surface waters resulting in an increase in primary production, supporting important fisheries. Nevertheless, these phytoplankton productive events are less important than those observed south of Cape Finisterre (Varela et al., 2005). Cape Finisterre and Cape Ortegal are frequently a place of upwelling maximum and recurrent upwelling filaments are observed (Haynes et al., 1993; Torres et al., 2003). These filaments are associated with topographic features and wind stress caused by orographic effects, however they may result from the coastal jet when upwelling occurs along the northern coast (Narimousa and Maxworthy, 1989).

The northern coastal segment is characterized by a narrow continental shelf ($7-20$ km wide) (deCastro et al., 2009) and presents a complex topography and a wide range of substrates that results in many different types of habitats (Sánchez et al., 2005). Near Cape Peñas is located the Nalon River (Figure 2.1) that is the most important source of nutrients to the sea in this region (Prego and Vergara, 1998). Here upwelling is also present enhancing primary production, although is not a common event and is generally restricted to a narrow band near the coast (Dickson and Hughes, 1981; Botas et al., 1990). The production of the area is also influenced by hydrographic mesoscale structures along the shelf break, which is a consequence of winter fluxes from the warm poleward current that determines the coastal distribution of plankton, fish eggs, and larvae in Cantabrian Sea (González-Quirós et al., 2003; Villamor et al., 2004). These produce a regular pattern of hydrographic conditions throughout the year characterized by winter mixing and summer stratification, with phytoplankton blooms occurring during the transition periods.

In this chapter it is intended to perform a characterization of the main features of the study region, in terms of the main circulation patterns and water masses, Chl-a concentration, SST, Ekman transport, river discharges and nutrients variability along the three coastal segments of the IP, for the period of 1998-2007.

2.2 Circulation patterns and water masses

Oceanic circulation patterns are crucial for the definition of nutrients and heat distribution, and therefore are important for primary production processes. The adjacent region of IP is under the direct influence of two large scale currents that are originated from the Gulf Stream and splits into two branches, the northern branch becoming the North Atlantic Current (NAC) and the southern branch the Azores Current (AC).

The surface circulation off IP (Figure 2.1) is dominated by the Portugal Current System (PCS) that includes the Portugal Current (PC) and the Portugal Coastal Current (PCC) (Ambar and Fiúza, 1994). Off western and intermediate coastal segments, in the open ocean, the PC dominates, flowing equatorward during all the year from 10 to 20 °W, at the interface between the NAC and AC (Krauss, 1986). The PC is somewhat weak (1.6 cm s^{-1}) (Pollard and Pu, 1985) with maximum speed reaching up to 5.7 cm s^{-1} (Martins et al., 2002).

The circulation pattern is more complex at the ocean margin and is defined by the wind regime at the western (Huthnance et al., 2002), intermediate and northern (van Aken, 2002) coastal segments.

Approximately parallel to PC, but closer to the shelf break, develops the seasonally reversing PCC (Ambar and Fiúza, 1994; Fiúza, 1983, 1984). During summer, the PCC is $30 - 40$ km wide and $50 - 100$ m deep and flows southward (with maximum velocity of about 40 cm s^{-1} (Peliz et al., 2002)) in the vicinity of western segment shelf break, being driven by northerly winds. It then transports the Eastern North Atlantic Central Water (ENACW) that is the main responsible for the fertility of the coast during upwelling processes. Two subtypes of this water mass were identified according to their origin, temperature and salinity (Fraga et al., 1982): a warmer and saltier of subtropical origin (ENACWst, $12.2 - 18.5\,^{\circ}\mathrm{C}$ and $35.66 - 36.75$) and a colder and less saline of subpolar origin (ENACWsp, $4 - 12\,^{\circ}\mathrm{C}$ and $34.96 - 35.66$) (Fiúza, 1984; Rios et al., 1992; Fiúza et al., 1998). These two subtypes are separated in summer by a subsurface front at $42\,^{\circ}\mathrm{N}$ near Cape Finisterre (Fraga et al., 1982) and therefore PCC transports cold and nutrient rich upwelled ENACWsp water in intermediate and northern segments, and warmer and nutrient poor ENACWst formed along the Azores Front in western segment, while during September to April the PCC piratically vanishes (Alvarez-Salgado et al., 2003).

A northward salty surface current (about 200 m deep), called Iberian Poleward Current (IPC) (Peliz et al., 2002, 2003; Frouin et al., 1990), is geographically trapped by the bathymetric discontinuity at the shelf break upper slope zone. The IPC is a narrow ($25 - 40$ km) slope-trapped tongue and is present almost yearlong, including in summer months, when it is close to the shelf-break (deCastro et al., 2011; Arístegui et al., 2006). Moderately strong upwelling and downwelling favourable winds, can modify the poleward flow but do not significantly change the density-driven current structure at the slope. The alongshore transport within the slope region is reduced by 0.2-0.3 Sv (from 1.2 Sv), under influence of either downwelling or upwelling winds (Peliz et al., 2003). After September, the IPC intensifies, flowing over the upper slope and outer shelf of the Western Iberian margin and extending all along to the intermediate and northern segments of IP (Frouin et al., 1990; Garcia-Soto et al., 2002). Due to the inability of the poleward flow to follow the abrupt changes of topography, such as Cape Ortegal, the IPC exhibits a turbulent nature, producing unstable structures and eddies in the Cantabrian Sea (Pingree and Cann, 1990; Garcia-Soto et al., 2002) (Figure 2.1). This current have been extensively described in several studies (Frouin et al., 1990; Pingree and Cann, 1990; Martins et al., 2002; Peliz et al., 2005; Torres and Barton, 2006).

At western coastal segment the ocean circulation is also influenced by freshwater plumes resulting from rivers discharge. Their estuarine outflow originates a low salinity water lens that extends along the coast. The freshwater input is more intense during the winter, but low salinity values persist during all year as a buoyant plume, called Western Iberian Buoyant Plume (WIBP) (Peliz et al., 2002). During typical non-upwelling winter conditions, the plume is confined to the inner-shelf from the Mondego river mouth with a preferential propagation northward and salinity values less than 35.7–35.8 (Peliz et al., 2002), while during upwelling favourable winds stretches offshore (Peliz et al., 2002; Mendes et al., 2016).

2.3 Data and methods

Chl-a concentration, SST and Ekman transport seasonal distributions were analysed over the northwestern coast of IP from 1998 to 2007, considering four seasons: winter (JFM), spring (AMJ), summer (JAS) and autumn (OND). The time evolution of the spatially averaged Chl-a concentration, SST and wind derived upwelling index (UI) and their monthly average were also determined at 40, 18 and 20 points in case of Chl-a and SST and at 10, 8 and 9 triangles in case of UI, located at western, intermediate and northern coastal segments, respectively (Figure 2.2). Points are approximately 16.5 km offshore and triangles at 60 km (Figure 2.2). Maxima levels of Chl-a concentration and the timing of these maxima were also analysed for the period 1998-2007, for the entire study region.

Chl-a data were obtained for the period 1998-2007, from SeaWiFS through NASA's Goddard Space Flight Center (http://oceancolor.gsfc.nasa.gov/SeaWiFS/) with a spatial resolution of 9 km and a temporal resolution of 7 days. Chl-a data from SeaWIFS have been extensively used over the last decade in the world's oceans to analyse its spatial and temporal variability (Brickley and Thomas, 2004; Navarro and Ruiz, 2006; Patti et al., 2010; Gao et al., 2013). A global comparison between SeaWiFS and *in situ* Chl-a data from NASA and NOAA was performed by Gregg and Casey (2004) using 4168 coincident data points. From the analysis carried out along the eastern North Atlantic, they found a root mean square error ($RMSE$) of 19.7% and a correlation of 0.65 between both data sets. Moreover, Ribeiro et al. (2005) have analysed the response of Chl-a to a winter upwelling event using SeaWIFS and *in situ* data along the western coast of the IP and found relative errors lower than 35%.

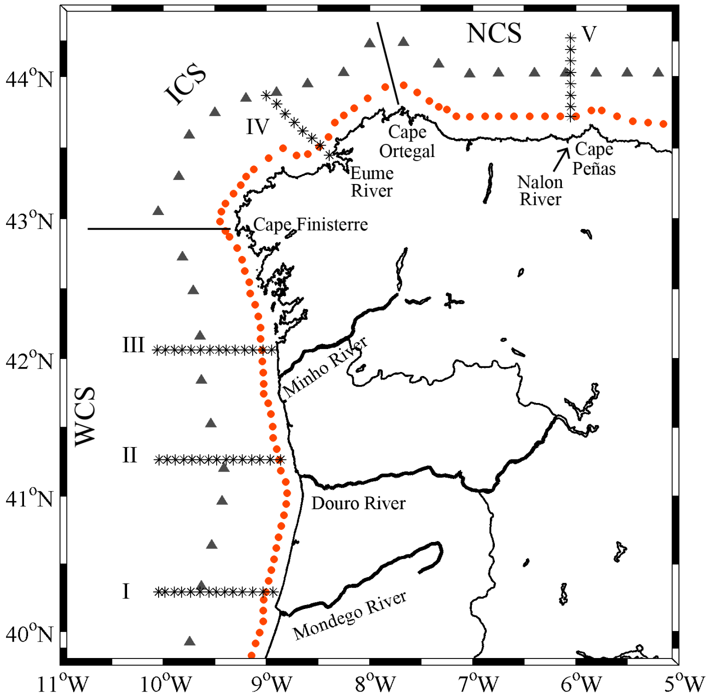

Figure 2.2: Map of the northwestern IP coast. Near coast dots and asterisks represent the locations where Chl-a and SST were retrieved and offshore triangles where upwelling index was computed. Three coastal segments are delimited: WCS, western coastal segment; ICS, intermediate coastal segment and NCS, northern coastal segment.

Therefore, SeaWiFS products can be considered reliable for the study of Chl-a along the northwestern coast of IP.

SST data measured by the AVHRR on board NOAA series satellites (http://poet.jpl.nasa.gov) were also analysed. Data are available since 1985 with a high spatial resolution of 4 km. A temporal average of 8 days from 1998 to 2007 was considered. Data from this sensor is the most used in the estimation of SST for scientific and operational applications in oceanography and fisheries (Torres et al., 2003; Williams et al., 2010) and therefore is considered a valuable tool for the study of SST patterns along the study area.

The Ekman transport was computed through surface wind fields obtained from the National Centers for Environmental Prediction (NCEP) Climate Forecast System Reanalysis (CFSR) (http://rda.ucar.edu/pub/cfsr.html). Data were retrieved from NOAA National Operational Model Archive and Distribution System (NOMADS) which is maintained by the NOAA National Climatic Data Center (NCDC). Detailed information about CFSR database can be obtained from Saha et al. (2010). This database presents a high spatial resolution (0.3°), which is adequate to accurately resolve conditions at the scale of coastal upwelling in intense and localized upwelling zones. It has a temporal resolution of 6 hours from January 1982 to December 2010 and the reference height of wind data is 10 m. This database allows the analysis of wind behaviour at small scales, which is essential when considering coastal mesoscale effects as upwelling. Recent studies have compared wind from this database and from other sources with wind measured by several buoys along the IP coast (Alvarez et al., 2014; Carvalho et al., 2014a,b), showing that datasets with finer spatial resolution, such as CFSR, give better results, especially near the coast. Thus, CFSR data are considered reliable and used to study Ekman transport variability over the study area.

Ekman transport was computed in terms of CFSR wind speed at the 10 m level, W, the seawater density, $\rho_w = 1025$ kg m^{-3}, a dimensionless drag coefficient $C_d = 1.4 \times 10^{-3}$ and the air density, $\rho_a = 1.22$ kg m^{-3}, through

$$Q_x = \frac{\rho_a C_d}{\rho_w f}(W_x^2 + W_y^2)^{1/2} W_y \tag{2.1}$$

$$Q_y = -\frac{\rho_a C_d}{\rho_w f}(W_x^2 + W_y^2)^{1/2} W_x \tag{2.2}$$

where f is the Coriolis parameter, defined as twice the vertical component of the Earth's angular velocity, Ω, about the local vertical given by $f = 2\Omega sin(\theta)$ at latitude θ. The subcript x corresponds to the zonal component and the y to the meridional one.

As previously referred the time evolution of the spatially averaged wind derived UI was also computed. UI can be considered as the Ekman Transport component in the direction perpendicular to the shoreline by means of UI $= -Q_x\ sin(\theta - \frac{\pi}{2}) + Q_y cos(\theta - \frac{\pi}{2})$, where θ is the angle defined by an unitary vector normal to the shoreline pointing seaward (Gomez-Gesteira et al., 2006). The shoreline angle is different along each coastal segment, presenting 180 ° relative to the equator for western coastal segment, 135 ° for intermediate coastal segment and 90 ° (parallel to the equator) for northern coastal segment. Positive (negative) UI values mean upwelling favourable (unfavourable) conditions.

Monthly mean freshwater inflows of the main rivers discharging at each coastal segment were computed and analysed for the period 1998-2007. At western coastal segment the freshwater input from Rias Baixas was not considered due to its minor importance when compared with Minho, Douro and Mondego Rivers discharge. The Minho discharge data were provided by the Confederación Hidrográfica del Miño-Sil (http://www.chminosil.es/) and the Douro and Mondego discharges by the Instituto Nacional da Água (http://www.snirh.pt/). Both datasets have a daily temporal resolution. At intermediate and northern coastal segments Eume and Nalon Rivers were considered for analysis. Given the absence of *in situ* data for Nalon and Eume Rivers during this period, discharges were obtained from estimations presented in Otero et al. (2010) for Nalon River and provided by the Swedish Meteorological and Hydrological Institute (SMHI - http://www.smhi.se/en) for Eume River.

Nutrients (phosphate and nitrate) monthly mean concentration and loads were also computed for the period 1999-2009 for Mondego, Douro, Minho, Eume and Nalon Rivers. Nutrient load is the mass of nutrient transported by flow over time, and is estimated as the product of nutrient concentration and flow. Nutrients concentration data were provided by SMHI that used the E-Hype model to compute hydrological variables (e.g. runoff, discharge, snow depth, groundwater level) and nutrient variables (e.g. concentrations and loads) for over 35000 sub-basins across all of Europe (Donnelly et al., 2013).

2.4 Results and discussion

2.4.1 Chl-a concentration variability

2.4.1.1 Seasonal analysis

In this section is discussed the seasonal evolution and the spatio-temporal variability of Chl-a concentration along the northwestern coast of IP, from 1998 to 2007.

From Figure 2.3 is found that Chl-a concentration presents a cross-shelf gradient, with higher values near coastal areas (between 2 and 6 mg m^{-3}).

High Chl-a concentrations are detected at western coastal segment, off Rias Baixas and at the southern region off the Portuguese coast (between Mondego and Minho Rivers). These maxima are more noticeable during summer months (JAS) with values

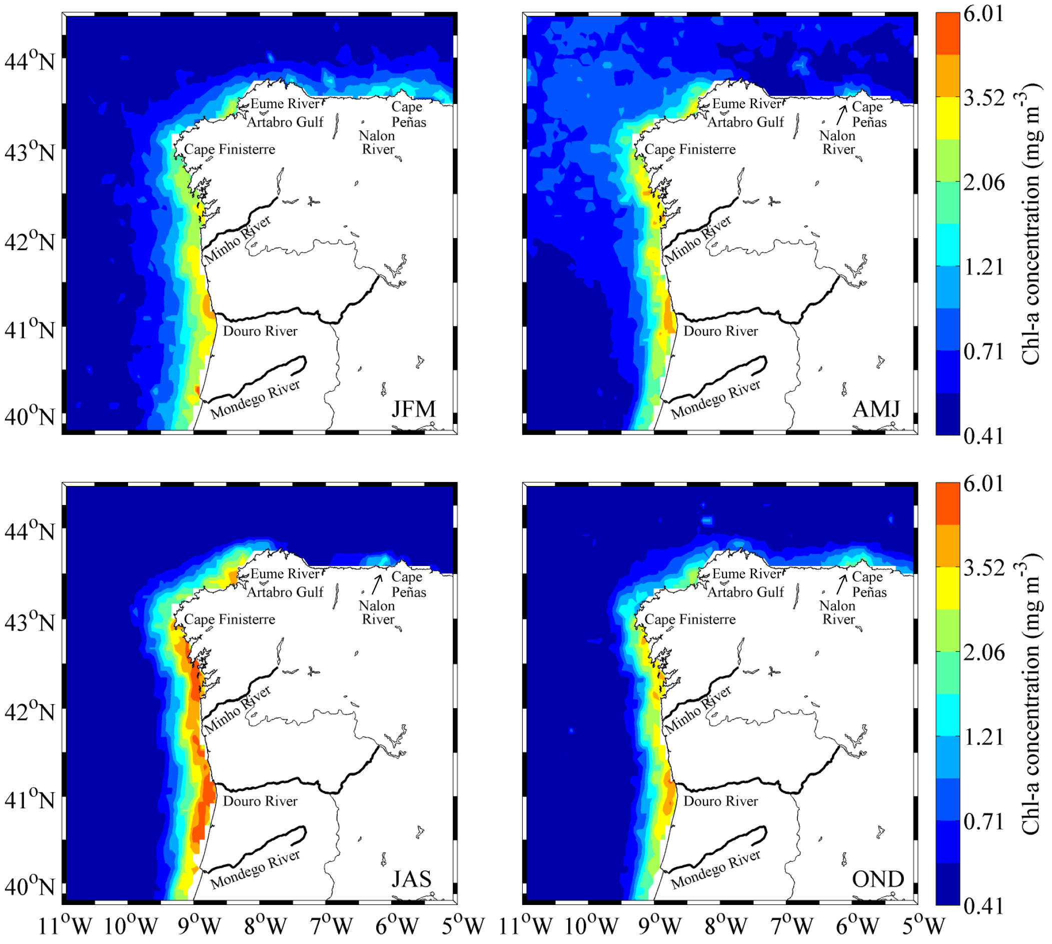

Figure 2.3: Seasonal (JFM, AMJ, JAS and OND) distributions of Chl-a concentration (mg m^{-3}) along the northwestern coast of IP.

exceeding 6 mg m^{-3}. This pattern may be related to the frequent upwelling events occurring south of Cape Finisterre during this period (Alvarez et al., 2008b; Gomez-Gesteira et al., 2006; Relvas et al., 2007), which bring nutrient-rich water to surface layers. Nutrients are used by phytoplankton together with dissolved CO_2 and solar energy to produce organic compounds through photosynthesis, generating high primary production which supports the large biological diversity in this region (Huthnance et al., 2002; Santos et al., 2004; Tenore et al., 1995; Torres and Barton, 2006).

For the remaining seasons (JFM, AMJ and OND), Chl-a concentration is lower than in summer, however values are still considered significant, between 2 and 4 mg m^{-3}. These conditions may be related not only to the occurrence of winter upwelling events (Alvarez et al., 2003; Borges et al., 2003; deCastro et al., 2006; Prego et al., 2007; Santos et al., 2004), but also to the effect of the river discharge, which promotes the input of nutrients onto the coastal waters. One additional point that should be considered is that high concentrations of coloured dissolved organic matter (CDOM), associated with river runoff, are present in the ocean surface in winter, leading to an erroneous strong signal of the satellite (Carder et al., 1999).

Near Douro River (approximately at 41 °N), which has the strongest outflow of IP western coastal segment, a strong signal of Chl-a (between 3.5 and 4.5 mg m^{-3}) was observed during autumn (OND) and winter (JFM). Also, off Mondego and Minho Rivers regions of influence were found higher concentrations than at the surroundings (between 2 and 3 mg m^{-3}), revealing the importance of these rivers for the local ecosystems.

At intermediate coastal segment the highest productivity is observed in the vicinity of Artabro Gulf during summer season (between 2.5 and 4 mg m^{-3}) therefore related with upwelling events. Here upwelling is discontinuous and distant from the coast, being near to the edge of the continental shelf (Prego and Bao, 1997; Prego and Varela, 1998), and strong Chl-a levels are observed. Winter Chl-a concentrations higher than 2 mg m^{-3} are detected here and can be associated with Eume River influence, which discharges nutrients into the Artabro Gulf. During AMJ, phytoplankton blooms are detected near the coast and offshore, with values between 2 and 3.5 mg m^{-3}. Indeed, during spring, the rising of surface water temperatures associated with longer daylight hours stimulate phytoplankton activity levels, after slow or dormant periods during winter.

The northern coastal segment of IP is the least productive, being the Chl-a concentrations more significant during JFM and OND, with values ranging from 1 to 2 mg m^{-3} near Cape Peñas (Figure 2.3). The JFM peaks are a situation characteristic of the planktonic cycle along the Cantabrian coast: winter mixing followed by summer stratification, favouring phytoplankton blooms (Varela et al., 2008, 2010; Alvarez et al., 2011). Moreover, high Chl-a concentrations during OND may be associated with the input of nutrients by Nalon River, which is the most important freshwater source in this region (Prego and Vergara, 1998).

The time evolution of the spatially averaged Chl-a concentration was also analysed for the period 1998-2007, considering the red dots represented in Figure 2.2 for each coastal segment. A 1-year running average (*i.e.* the value of a month is the average of this month with the same month of the previous year) was applied to smooth out the short terms fluctuations (Figure 2.4).

As previously observed, western coastal segment is characterized by higher Chl-a levels than intermediate and northern segments. Strong Chl-a concentrations between June and October were observed at western coastal segment, being the years of 2006 and 2007 the most productive, with values higher than 5 mg m^{-3}. High Chl-a levels were also observed in winter, mainly during JFM of 1998, 1999 and 2001. During the year of 2007, high Chl-a concentration (more than 3 mg m^{-3}) was also detected from November to December. The summer season of the years 2004 and 2005 was the least productive along the western coastal segment (Figure 2.4a).

The annual cycle of Chl-a concentration (Figure 2.4b) shows that, on average, the highest values occurred in August and September (more than 3 mg m^{-3}) and the lowest values in December and January (2 mg m^{-3}).

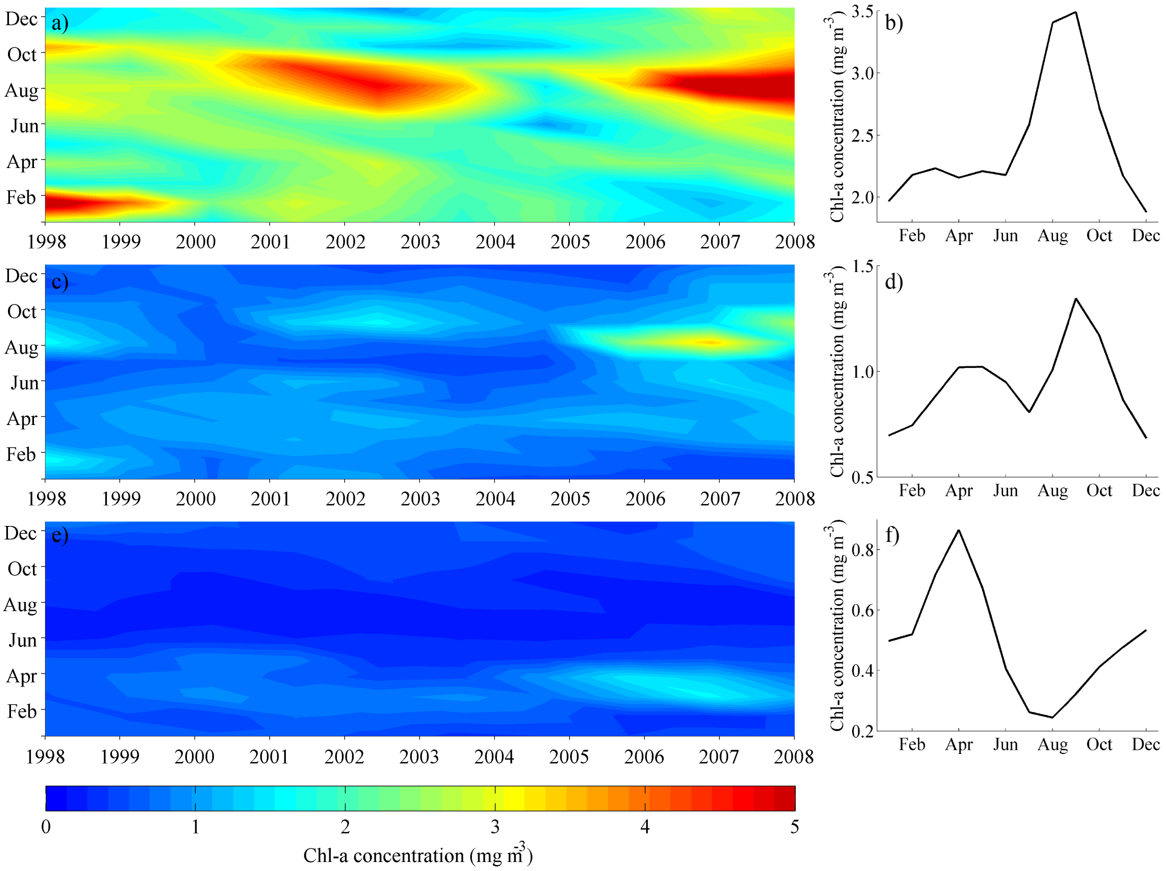

Figure 2.4: Time evolution of the spatially averaged Chl-a concentration (mg m^{-3}) (left column) and monthly average (right column) from 1998-2007, for western (a and b), intermediate (c and d) and northern (e and f) coastal segments of IP.

At intermediate coastal segment should be highlighted the strong Chl-a concentration observed during 2005 and 2007 for June and July, with values higher than 3 mg m^{-3}. Also in August and September high Chl-a concentrations are observed, however with lower values (2 mg m^{-3}). For monthly average of Chl-a concentration was not found a clear seasonal cycle, like at western segment. In fact, April, May and September are the most productive months, with values ranging from 1 to 1.5 mg m^{-3} (Figure 2.4d).

Regarding the northern coastal segment, primary production is weak during summer season, with Chl-a concentrations close to 0 mg m^{-3}. During February and March, Chl-a levels were generally higher than for summer months, being the highest Chl-a concentrations found for the end of the period under analysis (between 2005 and 2007, with values of approximately 2 mg m^{-3}). Here, the monthly average shows a clear seasonal cycle, with low values (approximately 0.2 mg m^{-3}) in summer (for July and August) and high values during winter and spring (0.5 and 0.8 mg m^{-3}, respectively) (Figure 2.4f).

2.4.1.2 Maxima levels

Maxima Chl-a concentrations, the period of occurrence of these maxima and its percentage of occurrence were also computed over the ten year period under analysis for every pixel (Figure 2.5).

From Figure 2.5 is found that approximately 85% of the study region total area has maxima values of Chl-a concentration ranging from 1 to 4 mg m^{-3}. This area corresponds mainly to the open ocean waters and peaks occur essentially during March and April (Figure 2.5c), with percentages of 18 and 50%, respectively (Figure 2.5d).

The highest concentrations occur south of Cape Finisterre, with maxima values higher than 7 mg m^{-3}, representing 4.4% of the study region area. These peaks are essentially visible in August (see Figure 2.5c), and are thus associated with upwelling events that are mainly a spring-summer process (Alvarez et al., 2008a).

Regarding the coastal region, at western coastal segment, summer (August) Chl-a peaks overlap autumn (October) peaks (Figure 2.5c), with exception south of Douro River mouth, where maxima Chl-a concentrations occur in October (higher than 10 mg m^{-3}).

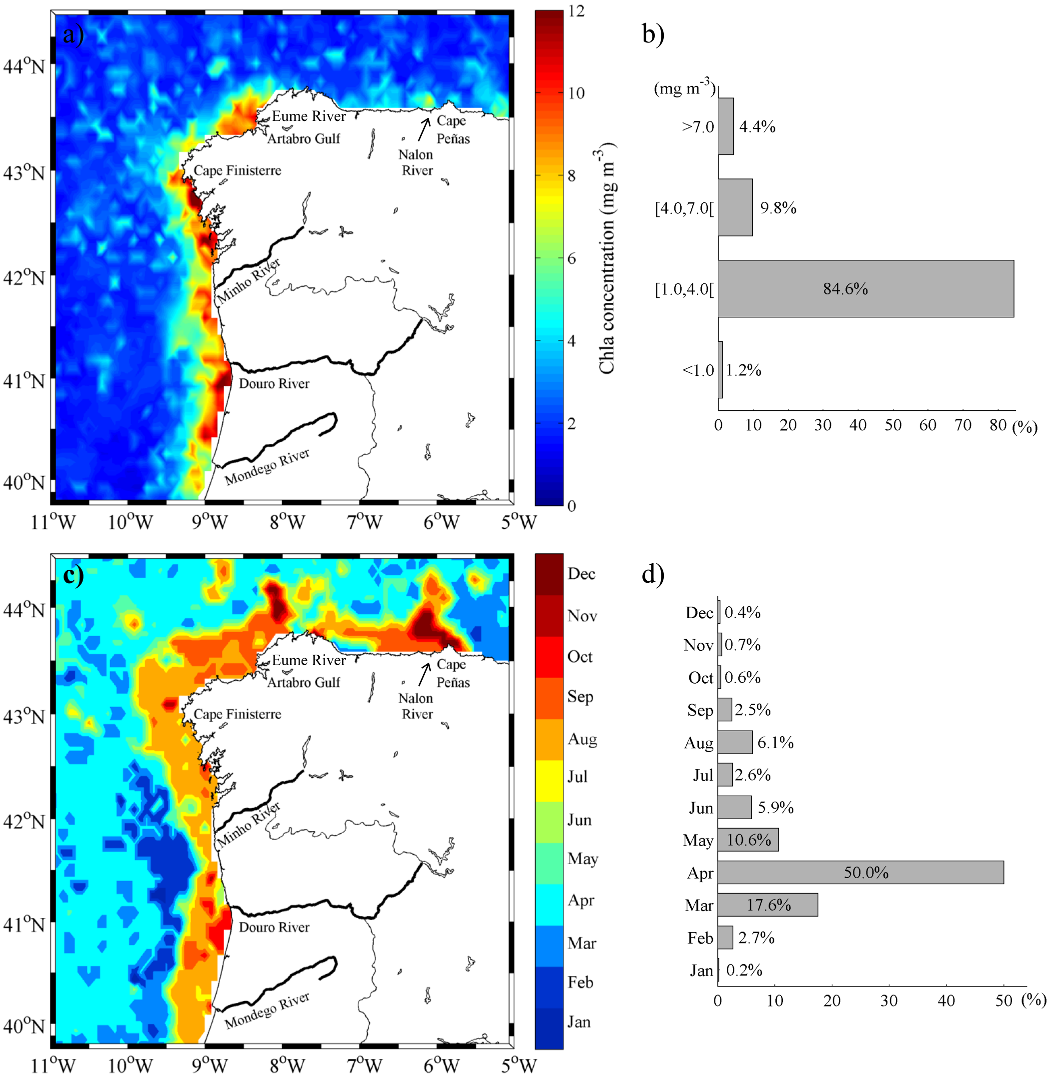

Figure 2.5: a) Maximum Chl-a concentration (mg m^{-3}) and c) correspondent period of occurrence during 1998-2007. b) and d) represent the percentage of occurrence of a) and c), respectively.

At intermediate coastal segment maxima Chl-a concentrations, which are mainly observed in Artabro Gulf, with values between 7 and 9 mg m^{-3}, occur during August and September (Figure 2.5c). Immediately north of Cape Finisterre maxima values are lower than 7 mg m^{-3}, and occur mainly during August.

Finally, at northern coastal segment, maxima Chl-a concentrations occur in September and December near Cape Peñas (less than 4 mg m^{-3}), and may be associated with the input of nutrients through Nalon River. Moreover, eastward to Cape Peñas, maxima Chl-a concentrations were observed (4.5 mg m^{-3}, Figure 2.5a), occurring mainly during March (Figure 2.5c), revealing that in this region the phytoplankton blooms generated during the transition phases (in this case mixing to stratification) overlap those originated by periodic episodes of coastal upwelling.

In summary, according to the statistics of Figure 2.5, at western coastal segment Chl-a maxima occur mainly during August, at intermediate during August and September and at northern during September and December, while in open ocean it occurs in April and reveals high temporal variability.

2.4.2 SST variability

Seasonal averages of SST are also analysed along the northwestern coast of IP, and are presented in Figure 2.6, showing that SST is highly variable throughout the year. Indeed, from January to March (JFM, Figure 2.6) maximum SST observed in the study area is 14.5 °C in the southern part of western coastal segment. Moreover, JFM surface temperatures evidence a filament of water warmer than at surrounding coastal and oceanic waters, turning east of Cape Finisterre. This warm water is associated with the IPC jet that usually arrives to the north coastal segment at the beginning of each winter (Garcia-Soto et al., 2002; Peliz et al., 2005; deCastro et al., 2011). This surface temperature signature is usually sharper during January, being masked herein due to the JFM average performed. The band of colder water (13 °C) observed between the warm water filament and nearshore region may be related to the net heat loss from surface during the preceding months (Alvarez et al., 2012; Fiúza, 1983).

From April to June (AMJ), temperatures higher than for JFM are observed along the study area. A band of coastal cold water is also observed along the western coastal segment, which is explained by the upwelling favourable conditions observed during this period (Figure 2.6). Also, a band of warm water, originated in southern latitudes, was detected along the western coastal segment. Along the intermediate coastal segment a SST minimum (14 °C) is evident from the nearshore to open-ocean latitudes and at northern, surface temperature increases, ranging from 15 to 15.5 °C.

For JAS at western and intermediate coastal segments, a nearshore band of water colder than offshore is evident and wider than for AMJ, generating a longitudinal temperature gradient. This pattern is related to upwelling events that occur mainly in summer months, which is corroborated by the Ekman Transport patterns represented in Figure 2.8 during JAS. Otherwise, the highest surface temperatures were observed at

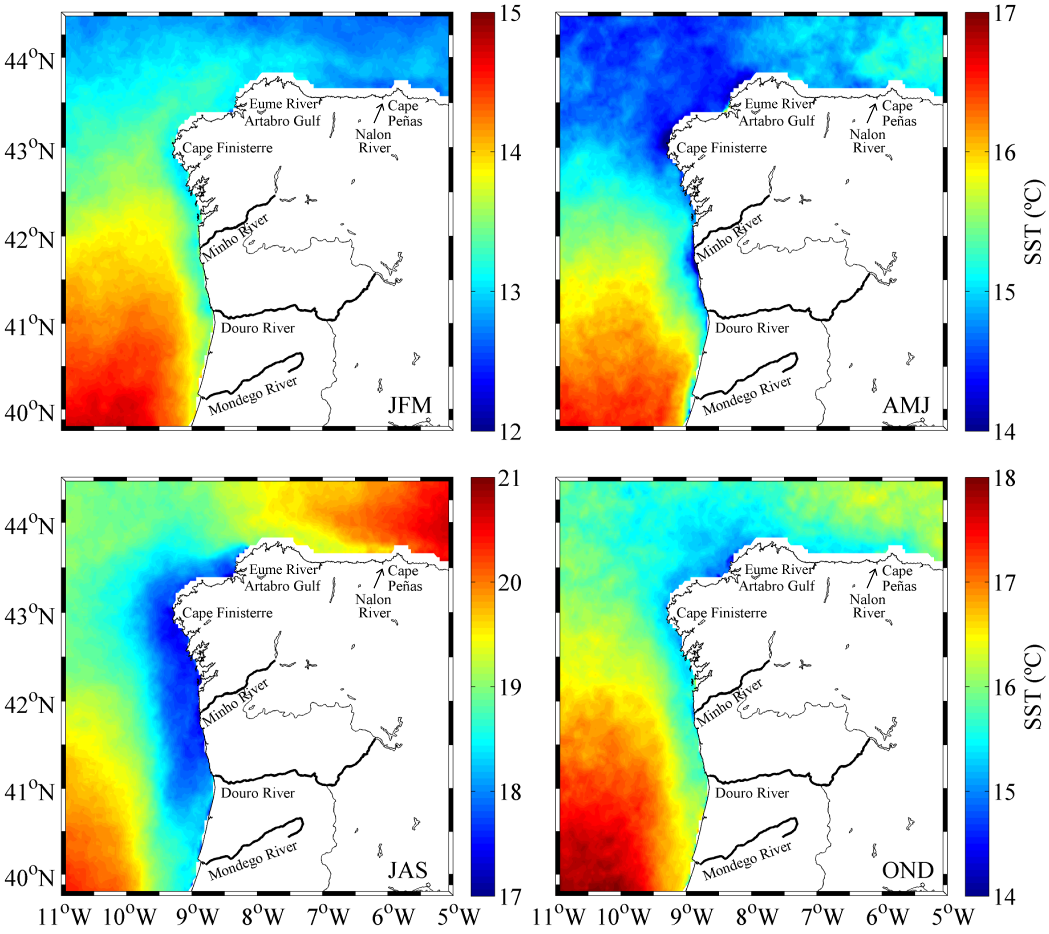

Figure 2.6: Seasonal (JFM, AMJ, JAS and OND) distributions of SST (°C) along the northwestern coast of IP.

northern coastal segment, increasing eastward (between 19.5 and 21 °C). In fact, this pattern is an effect of the warming observed during the summer at the southeastern corner of the Bay of Biscay (Pingree and Cann, 1989; Koutsikopoulos and Cann, 1996; Gomez-Gesteira et al., 2008).

The time SST evolution computed at the red dots represented in Figure 2.2 for each coastal segment is presented in Figure 2.7. In this case a 1-year running average was also considered. In general, the results show a clear seasonal cycle for all the coastal segments, with higher temperatures during summer (between June and September) and at northern coastal segment.

Different modulations in SST are observed. In particular, at western coastal segment the width of the summer band ($16 < \mathrm{SST} < 19\,°\mathrm{C}$) is thinner during the year of 2002 and thicker in 2007. The same characteristics are observed at intermediate and

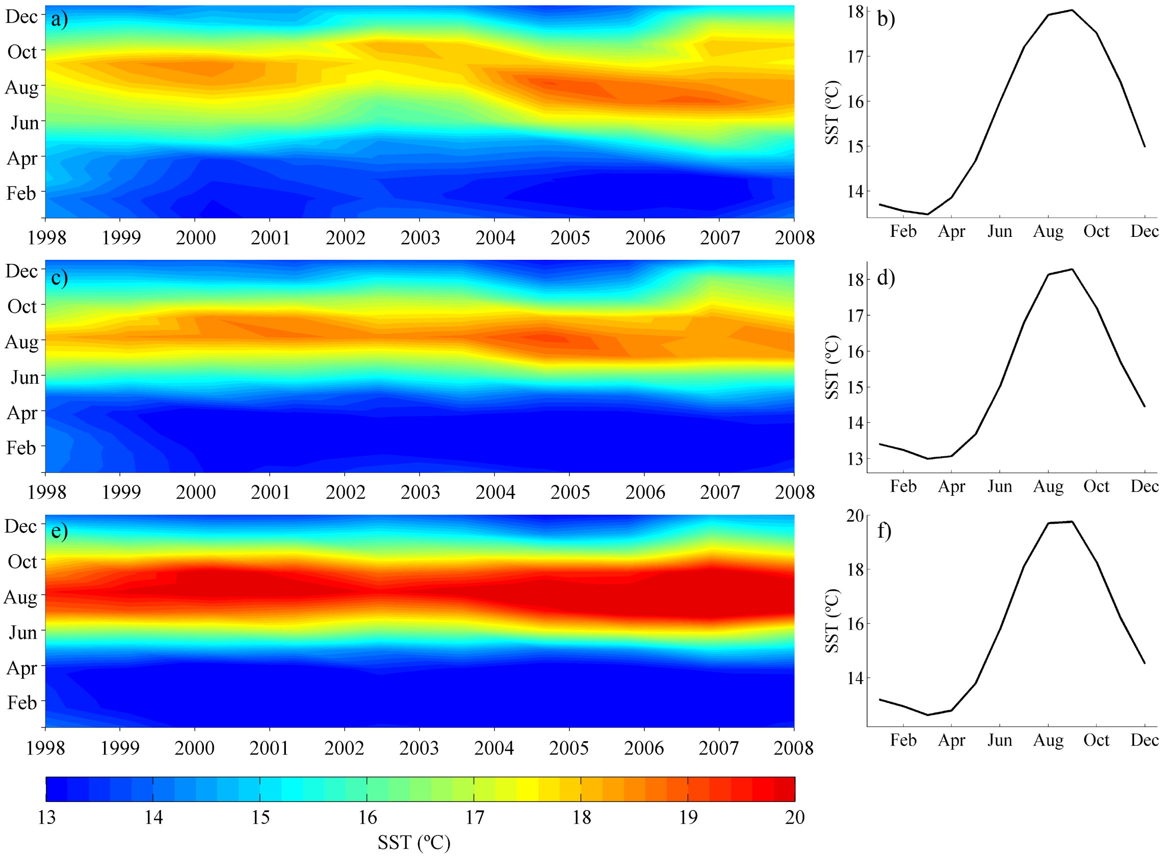

Figure 2.7: Time evolution of the spatially averaged SST (°C) (left column) and monthly average (right column) from 1998-2007, for western (a and b), intermediate (c and d) and northern (e and f) coastal segments of IP.

northern coastal segments, although less pronounced.

At western and intermediate coastal segments the thermal amplitude is approximately 5 °C (Figure 2.7a, b, c and d), with a minimum of 13.5 °C in February and a maximum of 18.5 °C in August, while for northern coastal segment the thermal amplitude is much higher, 7 °C (Figure 2.7e and f). Similar results were obtained by Gómez-Gesteira et al. (2011), where SST patterns for more than 150 years were evaluated in the study region.

2.4.3 Ekman transport and UI variability

In order to characterize the spatio-temporal variability of upwelling events along the northerwestern coast of IP, the Ekman transport was computed through the Equations 2.1 and 2.2 and is represented in Figure 2.8, considering the seasons previously referred.

Generally, the seasons JFM and OND show identical patterns of Ekman transport, as well as AMJ and JAS. Indeed, from April to September (AMJ and JAS), the strongest Ekman transport occurred along the western coastal segment, while from October to March (OND and JFM) maxima values were observed at intermediate and northern coastal segments (Figure 2.8).

During AMJ and JAS, Ekman transport is directed south-westward at western coastal segment (upwelling favourable), with values between 400 and 600 m^3 s^{-1} km^{-1}, being the near shore transport weaker than the offshore (between 100 and 200 m^3 s^{-1} km^{-1}). Otherwise, at intermediate and northern coastal segments a weak south-westward (upwelling unfavourable) transport is observed (100 m^3 s^{-1} km^{-1}) during AMJ, while between July and September (JAS), Ekman transport is directed north-westward (upwelling favourable). The magnitude of the transport ranges from 100 to 200 m^3 s^{-1} km^{-1} at intermediate coastal segment and is less than 100 m^3 s^{-1} km^{-1} at northern, during JAS. Therefore, on average, during JAS transport is upwelling favourable at

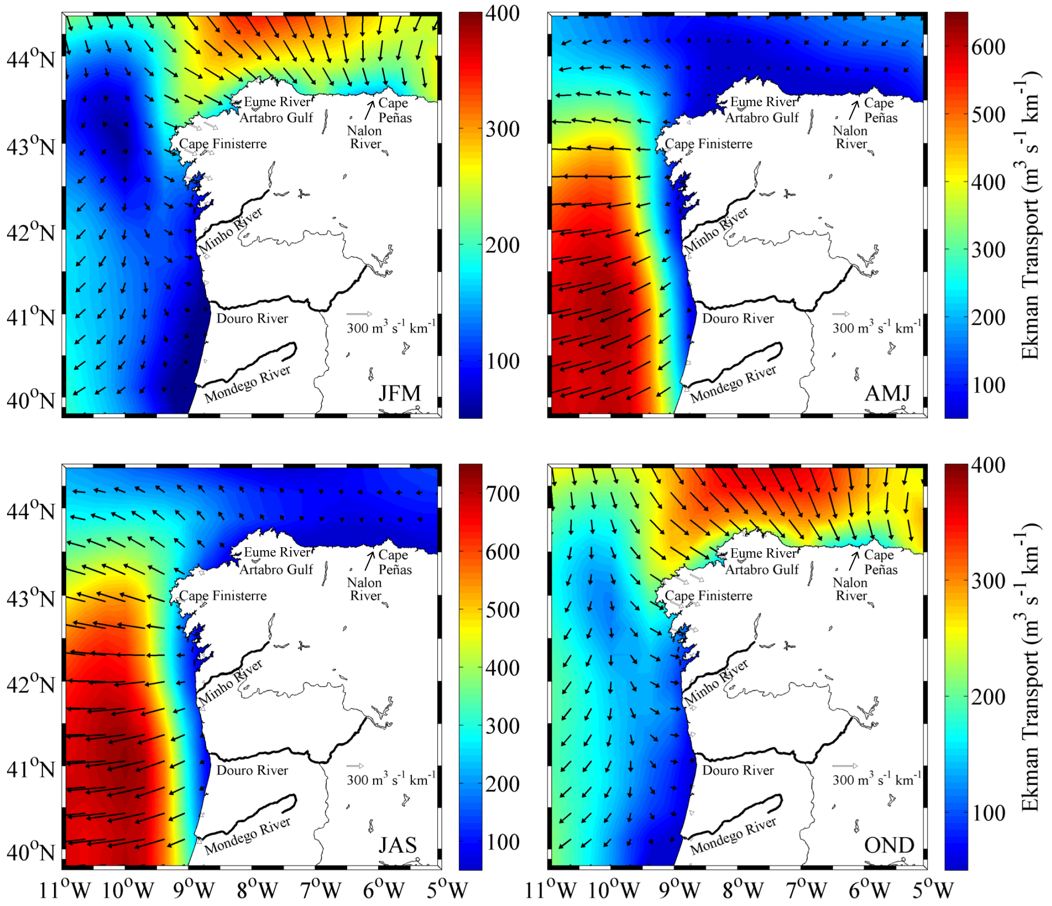

Figure 2.8: Seasonal (JFM, AMJ, JAS and OND) distributions of Ekman Transport (m^3 s^{-1} km^{-1}) along the northwestern coast of IP.

the three coastal segments, while during AMJ is only favourable at the western coastal segment.

For JFM and OND are found differences in the transport pattern, which shows an important southward component, unfavourable to the occurrence of coastal upwelling events. The strongest values were observed at intermediate (350 $m^3 s^{-1} km^{-1}$ on average) and at northern (250 to 350 $m^3 s^{-1} km^{-1}$) coastal segments, while at western the transport was weak (150 $m^3 s^{-1} km^{-1}$).

In order to better identify the upwelling favourable months along each coastal segment, the time evolution of the spatially averaged UI (computed at triangles represented in Figure 2.2) was also analysed from 1998–2007 (Figure 2.9). A 3-year running average was considered to smooth out the short term fluctuations.

Highest upwelling favourable conditions at western and intermediate coastal segments were found from February to October, while at northern segment occurred between May and September, presenting differences among years.

Regarding the western coastal segment (Figure 2.9a), the highest UI values (between 800 and 900 $m^3 s^{-1} km^{-1}$) correspond to the begin of the period under analysis from June to September. At this time Chl-a concentration is high and therefore related to upwelling events. During March, from 2001 until the end of 2007, UI is upwelling unfavourable with values approximately -200 $m^3 s^{-1} km^{-1}$. The same pattern was observed in November from 2002 until the end of the period under analysis. It is noteworthy that Chl-a concentration is high for these two periods, suggesting that primary production is not related with upwelling events, for this period. During February positive values of UI (upwelling favourable) were observed for the whole period, except in the late 2003 and in 2004. Moreover, during the years of 2006 and 2007, positive values were observed during winter (December-January), indicating the possibility of winter upwelling events. The monthly average of UI (Figure 2.9b) shows a clear seasonal cycle, with the most favourable conditions observed in summer (maximum of 700 $m^3 s^{-1} km^{-1}$ in July) and the least in winter (minimum of -200 $m^3 s^{-1} km^{-1}$ in December). However, in February and November are also observed favourable conditions to upwelling, with UI values reaching 200 $m^3 s^{-1} km^{-1}$ (Figure 2.9b).

Along the intermediate coastal segment (Figure 2.9c) UI patterns are similar to those observed at western, however with lower values. The most intense upwelling

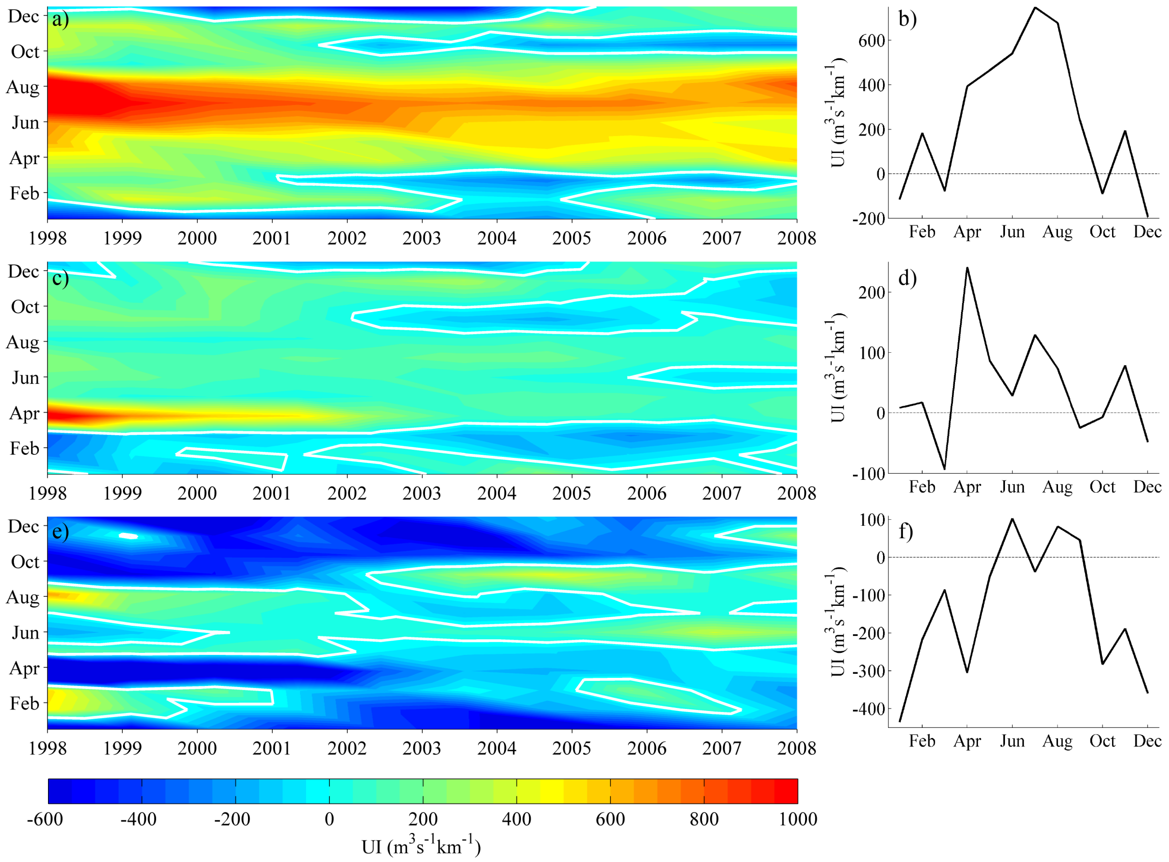

Figure 2.9: Time evolution of the spatially averaged UI (m^3 s^{-1} km^{-1}) (left column) and monthly average (right column) from 1998-2007, for western (a and b), intermediate (c and d) and northern (e and f) coastal segments of IP.

events occurred in April during the period between 1998 (1000 m^3 s^{-1} km^{-1}) and 2001 (500 m^3 s^{-1} km^{-1}). From 2001 to 2007, UI is still upwelling favourable, however with less pronounced values (400 m^3 s^{-1} km^{-1}). Here, as showed through the Chl-a monthly distribution, the seasonal pattern is not so pronounced as in western coastal segment. The most favourable condition occurred in April (250 m^3 s^{-1} km^{-1}) and consequently high Chl-a values are observed (more than 1.5 mg m^{-3}). Otherwise, unfavourable upwelling conditions occurred in March (-100 m^3 s^{-1} km^{-1}) (Figure 2.9d).

At northern coastal segment, the strongest upwelling favourable conditions were observed at the end of nineties, during February and August and during September 2004 and 2005, however Ekman transport never exceed 500 m^3 s^{-1} km^{-1}. On average, favourable conditions to the occurrence of upwelling are observed during three months: June, August and September, with values of 100 m^3 s^{-1} km^{-1} (Figure 2.9f).

In summary, both Ekman transport and UI suggest that the most favourable upwelling conditions occur at western coastal segment of IP between April and September, generating high primary production. These results are in agreement with several previous studies (Wooster et al., 1976; Fraga, 1981; Blanton et al., 1987; Torres et al., 2003; Gomez-Gesteira et al., 2006; Alvarez et al., 2008b, 2011).

2.4.4 River runoff and nutrients variability

Monthly mean discharges, nutrients concentration and loads of the main freshwater sources flowing into western (Mondego, Douro and Minho Rivers), intermediate (Eume River) and northern (Nalon River) coastal segments of the IP are represented in Figures 2.10 and 2.11, respectively. Generally, results show a typical pattern, with high values during winter and low values during summer, being the Douro River the most important freshwater source into the ocean. Western coastal segment main rivers generate an alongshore low salinity water lens (< 35.8) (Relvas et al., 2007), the WIBP (Peliz et al., 2002). Plume waters in the vicinity of rivers are identified in winter through SST imagery from its low temperature signature compared to the shelf waters. On the other hand, during summer, plume waters are warmer than those from surrounding (Torres and Barton, 2006).

Douro river basin is the largest hydrographic basin in the northwestern coast of IP, with an area of 97682 km^2 (Mendes et al., 2014). The mean freshwater discharge ranges from 100 m^3 s^{-1} in August to 1100 m^3 s^{-1} in January, with an annual average discharge of 530 m^3 s^{-1} for the period 1998-2007 (Figure 2.10). The Douro estuarine turbid plume has a particular relevance in the modulation of the biogeochemical features of the

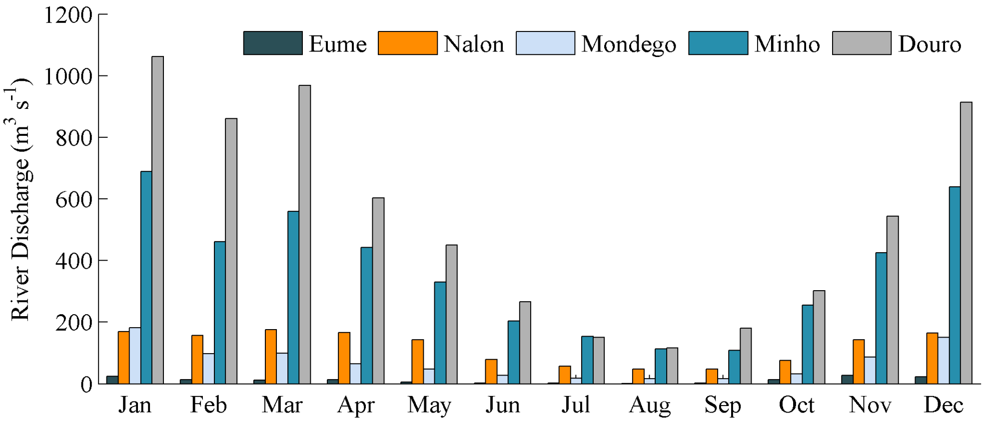

Figure 2.10: Monthly mean discharges (m^3 s^{-1}) from 1998 to 2007.

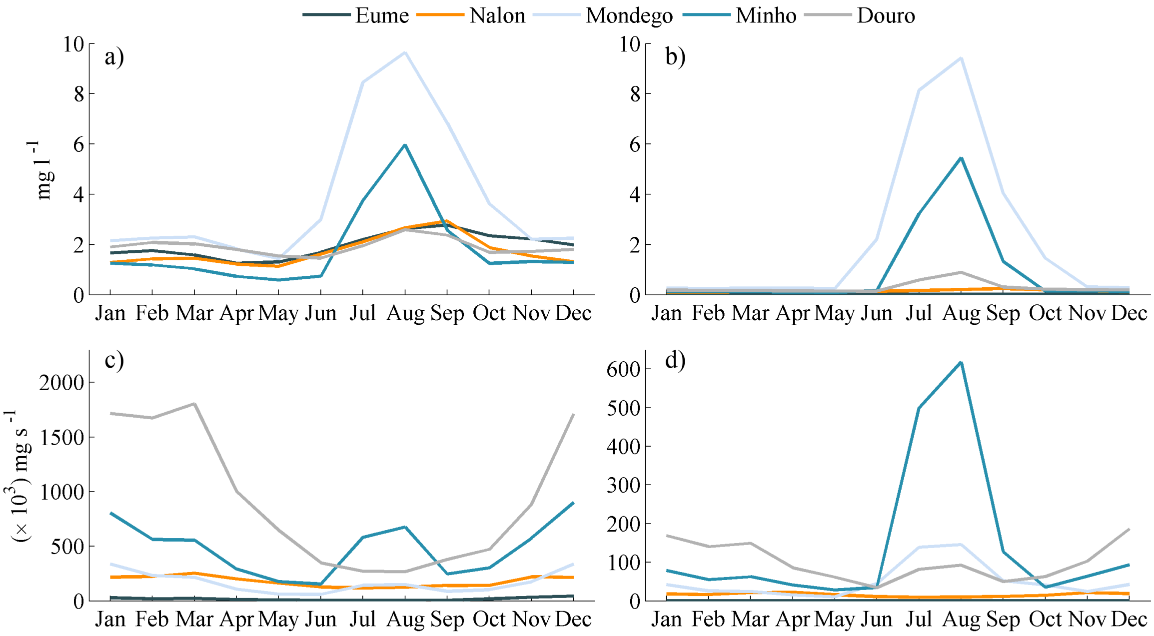

Figure 2.11: a) Nitrate and b) phosphate monthly mean concentration (mg l^{-1}) and c) nitrate and d) phosphate loads (mg s^{-1}) from 1999 to 2009.

northwestern Iberian coast (Ribeiro et al., 2005) due to the large amount of terrestrial nutrients present in the plume. Indeed, according to Figure 2.11, during winter nitrate (phosphate) concentration is approximately 2 (0.2) mg l^{-1} and an average of 1800 (160) mg s^{-1} is transported to the coast.

Minho River is approximately 300 km long, having a south-east direction alignment in the boundary between Portugal and Spain (see Figure 2.2). The river has a catchment area of 17080 km^2 (Sousa et al., 2014b) and an annual average discharge of 360 m^3 s^{-1} computed for the period 1998-2007. Its monthly average discharge oscillates between 600 m^3 s^{-1} in January and 100 m^3 s^{-1} in August (Figure 2.10). Nutrients concentrations are higher during summer months, reaching the maximum value during August (6 mg l^{-1} for the 1999-2009 average), however due to the low flow (110 m^3 s^{-1}), only 600 mg s^{-1} are loaded into the coast.

Mondego River has a catchment area of 6700 km^2 and it runs along 234 km. Comparatively to Minho and Douro rivers, Mondego has a low flow, with discharges ranging from 15 m^3 s^{-1} in August to 180 m^3 s^{-1} in January, and an annual average of 70 m^3 s^{-1} for the 1998-2007 period. Mondego is an important source of nutrients, reaching concentrations of 10 mg l^{-1} of nitrate and phosphate in August and 2.2 of nitrate and 0.3 mg l^{-1} of phosphate in November. Indeed, Mondego estuary is under severe environmental stress, namely an ongoing euthrophication process, induced by human activities: industries, aquaculture farms and nutrients from agricultural lands of low Mondego River valley (Duarte et al., 2002). Regarding the nutrient load, during summer Mondego transports approximately 150 mg s^{-1} of nitrate and phosphate, while during winter transports 350 and 50 mg s^{-1} of nitrate and phosphate, respectively.

According to Saraiva et al. (2007), Mondego, Douro and Minho are estuaries with short residence times and therefore phytoplankton and nutrients are flushed out of the system, and the uptake of nutrients occurs in coastal zone.

Eume River, located at intermediate coastal segment has a catchment area of 470 km^2. The ten years mean discharges range from 1.5 m^3 s^{-1} in June to 26 m^3 s^{-1} in November, with an annual average discharge of approximately 12 m^3 s^{-1} (Figure 2.10). Nutrients concentration from Eume River are highly influenced by an upstream dam that controls fluvial inflow nutrients and retains in sediments as organic matter (Prego et al., 2015). The annual average concentration and loads of nitrate are 2 mg l^{-1} and 21 mg s^{-1} for the period of 1999-2009, respectively. Phosphate concentration and loads are negligible (Figure 2.11).

Finally, at northern coastal segment is located the Nalon River with 153 km long and a basin area of 4866 km^2 (Prego and Vergara, 1998). It is an important source of nutrients in the region, with the highest concentration of nitrate found in September (3 mg l^{-1}) and the highest load in March (250 mg s^{-1}). Its monthly mean discharge oscillates between 50 m^3 s^{-1} in August and 170 m^3 s^{-1} in January (Figure 2.10) and the annual average discharge is approximately 120 m^3 s^{-1}.

The interannual evolution of freshwater runoff from the five rivers was also computed (Figure 2.12), revealing peculiar differences among years. For instance, it is noteworthy that the strongest discharges are observed during winter of 2001 for all the rivers analysed. Maximum discharge for Douro, Minho, Mondego, Nalon and Eume Rivers were 4500, 2000, 700, 400 and 70 m^3 s^{-1}, respectively. Indeed, during 2001 winter high rainfall events were observed along the northwestern coast of IP (Alvarez et al., 2005). The second highest discharge occurred in winter 2003, with values of 2500, 1500, 500, 300 and 50 m^3 s^{-1} for Douro, Minho, Mondego, Nalon and Eume Rivers, respectively. For Nalon River similar values occurred in 1998 and from 2004 to 2007, mainly during March.

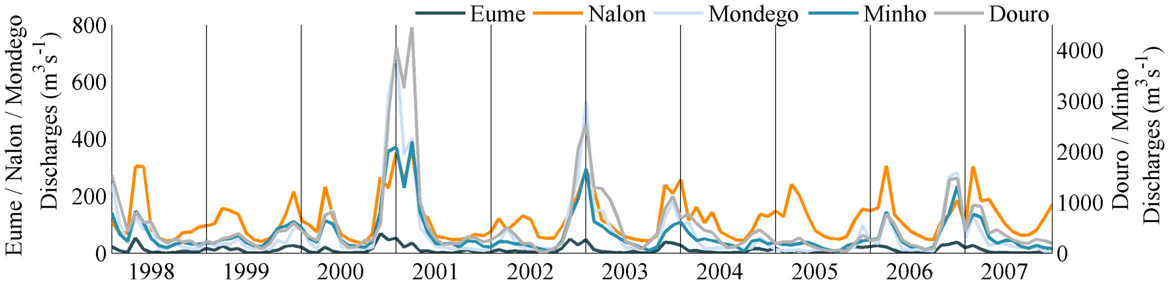

Figure 2.12: Interannual evolution of discharges (m^3 s^{-1}) for 1998-2007, for the Douro, Minho, Mondego, Eume and Nalon Rivers.

For western coastal segment rivers, strong discharges were also detected in January 1998. Besides the already mentioned periods, also for the late 2006 and early 2007 high discharges were observed, with values of 1400 m^3 s^{-1} for Douro and Minho Rivers and 300 m^3 s^{-1} for Mondego River.

Most of the strong discharges highlighted are concurrent with the strong signal of Chl-a concentration (Figure 2.4), suggesting that they may be related.

2.5 Conclusions

The variability of Ekman Transport, UI, SST, Chl-a concentration, river discharges and nutrients over the northwestern coast of IP were characterized through *in situ* and remote sensing data, from 1998 to 2007. The analysis was carried out in terms of annual and monthly averages, showing the following:

- Ekman transport, SST and Chl-a concentration had different annual cycles within each coastal segment, with high seasonal variability;
- At western and intermediate coastal segments, maxima Chl-a levels (10 mg m^{-3}) occur in August and September, suggesting that upwelling is the main responsible for phytoplankton growth. At northern coastal segment it occurs in September and December (4 mg m^{-3}) and in the open ocean phytoplankton blooms occur in April (2 mg m^{-3});
- The seasonality of Chl-a concentration is mainly related to the upwelling events, which are more frequent along the western and intermediate coastal segments;
- During AMJ and JAS the strongest Ekman transport occurs along the western

coastal segment directed westward, inducing the displacement of deep and nutrient-rich water to surface. Consequently, during this period a band of cold water and high levels of Chl-a are observed near the coast. At intermediate coastal segment, upwelling favourable conditions also occur during summer, however with lower intensity than at western segment. A band of cold water and high Chl-a concentration is also observed near coast. At northern coastal segment the Ekman transport is weak, and high temperatures related to the summer warming at the southeastern corner of the Bay of Biscay are observed. Furthermore, Chl-a concentrations are low;

- During OND and JFM unfavourable upwelling conditions were observed for all the study region. At western and intermediate coastal segments high levels of Chl-a are also observed, however lower than during summer months. This may be associated with the input of nutrients from rivers, which can induce phytoplankton growth in the coast and consequently primary production increases. At northern coastal segment Chl-a levels are higher than in summer and stronger near Nalon River;
- High discharges were found during winter and therefore high nutrient loads, being Douro river the most important freshwater source into the ocean.

Chapter 3

Chl-a concentration dependence on upwelling and rivers runoff

3.1 Introduction

Along the northwestern coast of IP, coastal upwelling is usually considered the main responsible for the high primary production that characterizes this region (Huthnance et al., 2002; Tenore et al., 1995) supporting a high biological diversity. The upwelling phenomenon occurs due to a combination of three factors: the existence of a persistent wind, the presence of a solid boundary, and the apparent deviation of a moving object from its straight path in a rotating reference system (Coriolis effect). In the northern hemisphere, when the winds blow toward the Equator, leaving the coast on the left, surface waters moves offshore due to the effect of Ekman transport and are replaced by deep colder nutrient-rich waters. The influence of coastal upwelling on primary production and Chl-a concentration was studied along the northwestern coast of the IP, mainly during summer (Casas et al., 1997; Castro et al., 2000; Bode et al., 2002; Cravo et al., 2010; Cardeira et al., 2013; Oliveira et al., 2009; Ribeiro et al., 2005). However, most of these studies focused on data at isolated locations along the coast and during short periods of time, providing a localized knowledge.

Otherwise, freshwater input from rivers has also an important implication on phytoplankton growth, once river plumes are generally rich in nutrients and remains near surface and thereby supports high primary production. Along the northwestern coast of IP, Alvarez et al. (2012) referred the importance of Minho River plume in phytoplankton generation during winter, however were not found studies examining the influence of other freshwater sources discharging in region.

Although some results regarding the Chl-a concentration variability along the northwestern coast of IP have been presented in Chapter 2, it is important to further investigate the effect of external factors to phytoplankton blooms development and highlight localized changes, once phytoplankton is the base of trophic web and therefore its variability affects the dynamics of the whole ecosystem. Therefore, the main objective of this chapter is to investigate the Chl-a concentration dependence on coastal upwelling and rivers runoff along the northwestern coast of IP. In this context, the Empirical Orthogonal Functions (EOF) technique was used to examine the temporal and spatial variability of Chl-a concentration and infer about the main physical forcings that influence its generation and growth. Additionally, SST imagery complemented by wind information and river discharges will be used to analyse atmosphere-ocean-land conditions that drive phytoplankton generation. Correlations between these variables were also computed in order to quantify the relation between them.

3.2 Data and Methods

3.2.1 SST, Ekman transport and Chl-a analysis

Upwelling along the northwestern coast of IP is a seasonal phenomenon, mainly occurring during spring-summer months. Otherwise, freshwater input is more intense during winter. Moreover, in temperate areas seasonality accounts for most of the temporal phytoplankton biomass variability. Consequently, the monthly evolution of Chl-a, SST and Ekman transport was analysed between 1998 and 2007 to further investigate the Chl-a variability and its response to external forcing, along the three coastal segments: western, intermediate and northern. Chl-a concentration and SST annual cycles were calculated at the points and UI at the triangles located at each coastal segment represented in Figure 2.2 (Chapter 2). SST and Chl-a concentration data were obtained from AVHRR and SeaWiFS, respectively, as described in detail in Chapter 2. The monthly evolution of Chl-a concentration and SST were also computed in five sections (Figure 2.2) to assess its zonal (I, II and III) and meridional (IV and V) variability near the most important freshwater sources discharging in the study area.

To better characterize the influence of upwelling events and river discharges on Chl-a variability along the three coastal segments, the interannual evolution of Chl-a concentration, SST, UI and discharges of the main rivers at each coastal segment were analysed for summer and winter between 1998 and 2007. SST and Chl-a concentration interannual evolution was computed considering meridional and zonal interpolation of these variables at the points located at each coastal segment (Figure 2.2), while the mean UI interannual evolution was computed considering the triangles of Figure 2.2. Positive (negative) UI values means upwelling favourable (unfavourable) conditions.

3.2.2 Fluvial and mixed layer depth data

River discharges (Mondego, Douro, Minho, Nalon and Eume) were also analysed in order to understand its implications in the Chl-a blooms for the period 1998-2007. The Minho data were provided by the Confederación Hidrográfica del Miño-Sil (http://www.chminosil.es/), Douro and Mondego discharges by the Instituto Nacional da Água (http://www.snirh.pt/), Nalon discharges were obtained from estimations presented in Otero et al. (2010) and Eume from SMHI, as described in Chapter 2.

Mixed layer depth (MLD) data was also analysed, and was obtained from operational data sets produced routinely by the Global Ocean Data Assimilation System (GODAS) developed at NCEP. MLD data has a monthly temporal resolution and a spatial resolution of 0.3° in latitude and 1° in longitude.

3.2.3 EOF analysis

EOF analysis was used to examine the spatio-temporal Chl-a variability in the study region using SeaWiFS weekly images of Chl-a concentration. There are several studies using EOF analysis of Chl-a images concerning ocean-colour data (Brickley and Thomas, 2004; Ho et al., 2004; Navarro and Ruiz, 2006).

There are two different ways of computing EOF, which depends on the technique to build data matrix (Parada and Canton, 1998). One technique subtracts the temporal mean (the mean of each pixel in all images) of each data pixel and the other subtracts the spatial mean (each image mean) of each pixel.

In this work the first method was chosen to study the spatio-temporal variability of 450 images of SeaWiFS Chl-a concentration, once, according to Parada and

Canton (1998), it is the most appropriate to analyse structures associated with the seasonal temperature variability in a specific area. Therefore, Chl-a temporal mean was subtracted from each pixel data. Afterwards, the covariance matrix was computed and its eigenvectors and singular values were found through the singular value decomposition (SVD) method. This method requires complete matrices and cannot skip over any missing data. Consequently, pixels without Chl-a data were replaced by the average of the surrounding pixels (Navarro and Ruiz, 2006; Gao et al., 2013; Xu et al., 2011). Land has been masked in all images to ensure that the EOF results obtained correspond only to sea. This methodology was followed by several authors to analyse ocean colour images (Navarro and Ruiz, 2006; Yoder et al., 2002).

Regarding EOF analysis the sampling errors of the eigenvalues were estimated using the following approximation (North et al., 1982):

$$\delta\lambda \approx \lambda \left(\frac{2}{n_i}\right)^{1/2} \tag{3.1}$$

where λ is the eigenvalue and n_i is the number of images used in the EOF analysis. If no overlap is found between the confidence intervals (*i.e.* $\lambda \pm \delta\lambda$) of successive eigenvalues, then the EOF modes are not degenerated (Anderson, 1963). A diagram of the first five eigenvalues is presented in Figure 3.1. Degeneracy is found from the third mode and therefore only the first two modes will be interpreted.

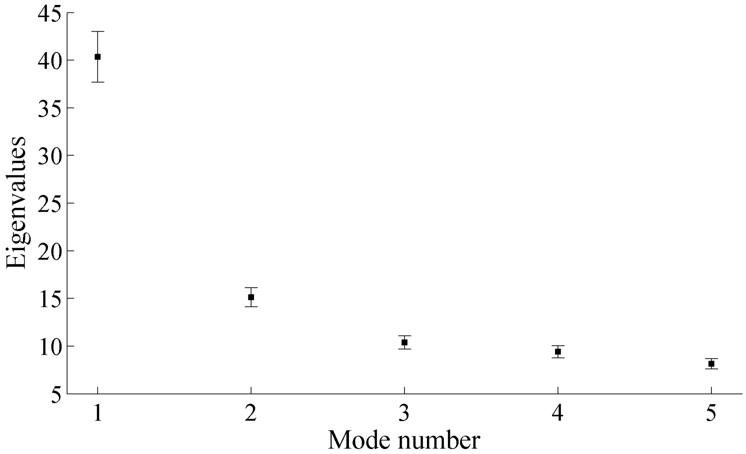

Figure 3.1: Eigenvalues of the first five EOF modes with error bars.

3.2.4 Correlation analysis

To better quantify the dependence of Chl-a formation along the northwestern coast of IP with upwelling phenomena, SST and river discharges, correlations between these variables were computed. Chl-a and SST time series considered to compute correlations correspond to time series average of the nearest four points of each river mouth, while for UI corresponds to the time series of the nearest triangle of each river mouth. Based on results, and considering that Chl-a concentration has different annual cycles at each coastal segment, correlation analysis was only considered for winter (JFM for Mondego, Douro and Minho and FMA for Nalon and Eume Rivers) and summer (JAS). The correlation coefficients were computed through the equation:

$$r_{x,y} = \frac{cov(x,y)}{\sigma_x \sigma_y} \tag{3.2}$$

where $cov(x,y)$ is the covariance between data and σ the standard deviation. The significance level ($p < 0.05$) was also computed through a matrix of p-values. P-value is the probability of getting a correlation as large as the observed value random chance, assuming that the null hypothesis is true. If p-value is small (less than 0.05) then the correlation will be significant.

3.3 Results and discussion

3.3.1 Chl-a EOF analysis

As previously referred, EOF analysis was computed to study the temporal and spatial variability of Chl-a concentration along the northwestern coast of IP. According to the results of the eigenvalues errors (Figure 3.1), only the first two modes were considered significant and studied herein.

The first two modes of the EOF analysis explained 29.5% of the total Chl-a variance (Figure 3.2), containing the first mode 21.5% of the data total variance. These results were similar to those obtained by Navarro and Ruiz (2006) for the Gulf of Cadiz and by Brickley and Thomas (2004) for the Coastal Gulf of Alaska, nevertheless higher percentages were obtained along the south coast of Madagascar (Ho et al., 2004).

The EOF spatial coefficients of the two first modes represent the spatial extension

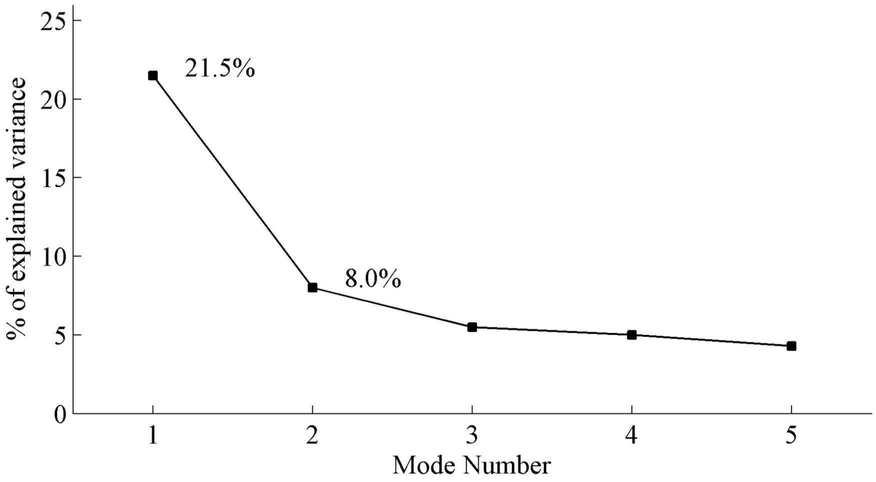

Figure 3.2: Percentage of explained Chl-a variance of the first five EOF modes.

and the dynamic importance of the processes in the study region, while the temporal EOF mode indicates the importance of the phenomenon (Navarro and Ruiz, 2006). All spatial coefficients corresponding to the first mode were positive (Figure 3.3) with maxima found nearshore and decreasing offshore. Two main areas were identified: one near coast with positive coefficients and comprising the IP upwelling area, and other offshore with values close to zero. At northern coastal segment the spatial coefficients near coast were very low, close to zero, while at western and intermediate coastal segments they are higher than 0.10. These results showed that the dynamics of the first mode was only related to the dynamics of the nearshore region, mainly at western

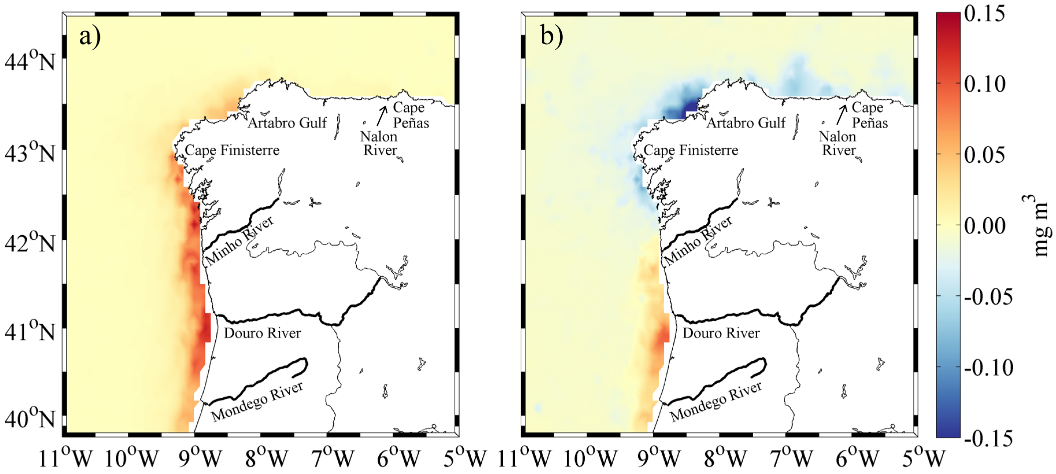

Figure 3.3: Spatial coefficients maps of the first two EOF modes for Chl-a: a) Mode 1 and b) Mode 2.

and intermediate coastal regions.

The spatial coefficients of the first mode were maxima in a coastal fringe that spatially coincides with maxima values of Chl-a concentration (Figure 2.3). Therefore, the first spatial mode suggest that high Chl-a concentration always exist along western and intermediate coastal segments of IP, extending essentially to 60 km off the coast (Figure 3.3), with values ranging from 0.05 to 0.15 mg m^{-3}.

When the spatial patterns and its associated time amplitude have the same sign this means a positive deviation at that time, in relation to climatology. Conversely, when signs are opposite it means negative deviation from the mean. Thus, according to the EOF analysis, the Chl-a concentration has a positive deviation relatively to the climatology in summer season (JAS) for all years, occurring the highest concentration (more than 6 mg m^{-3}) in August 2006 (Figure 3.3a and 3.4a). However, some negative deviations were also found for this season. For instance, for 2003 and 2004 the temporal coefficients were mostly negative with mean amplitudes of 1 mg m^{-3}.

Temporal amplitudes (Figure 3.4a) also indicate that the occurrence of these high Chl-a concentrations (with positive deviation from the climatology) during summer were modulated by the general seasonal cycle. Seasonal analysis of Chl-a concentration for the whole area (Figure 2.3) confirms the previous results, showing the same pattern. The interannual variability is highlighted as differences in both amplitude and time

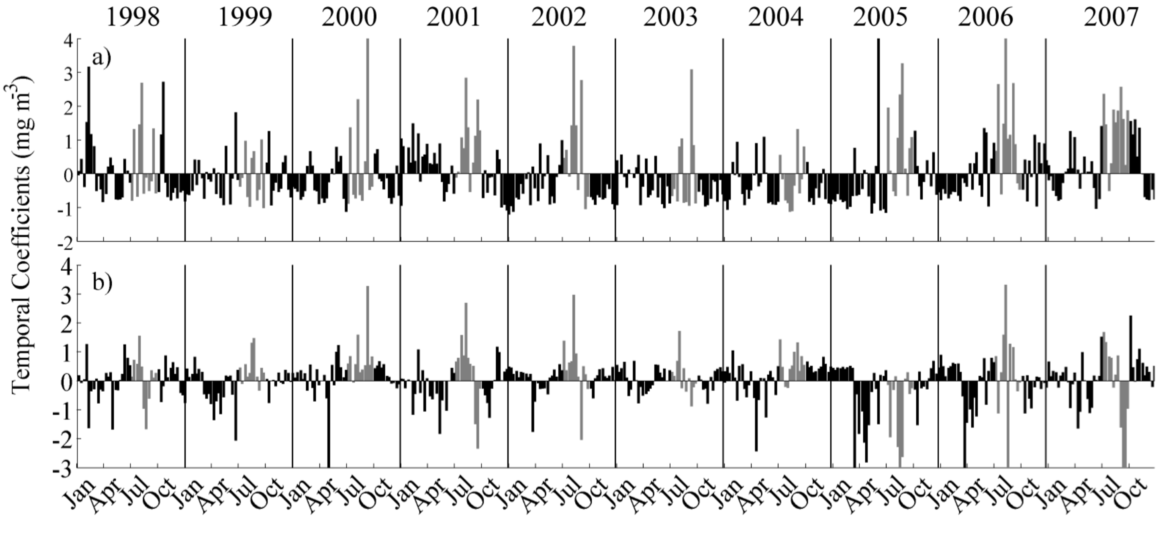

Figure 3.4: Temporal amplitudes of the first two EOF modes for Chl-a: a) Mode 1 and b) Mode 2. Gray bars indicate summer months (July, August and September).

occurrence of maximum values (peaks) (Figure 3.4a). For instance, in 1998 and 2001, temporal coefficients were positive during the first months of the year (with mean values of 2 mg m^{-3}), while for the remaining years, they were negative (with mean values of -1 mg m^{-3}). Moreover, between April and June and between October and December negative temporal amplitudes were detected for all years, except for 2006 and 2007.

The second EOF mode explains 8% of the total Chl-a variance (Figure 3.2) and its spatial variability allows the identification of different zones. Spatial distributions (Figure 3.3b) were low over the open ocean and more intense near the coast, as in the first mode. Two opposite patterns were observed near the coast (Figure 3.3b), showing that main forcing mechanisms of Chl-a concentration in these two regions were different. Spatial coefficients were high and negative above Minho River (42 °N) and in the surroundings of Artabro Gulf, with values between -0.10 and -0.15 mg m^{-3}, and lower along the northern coastal segment, with values of -0.05 mg m^{-3}. Otherwise, in Portuguese coast the spatial coefficients are positive (between 0.05 and 0.15 mg m^{-3}, Figure 3.3b) and highest southward of Douro River. This result indicates a dynamical response of different phases south Minho River compared to the northern area. Indeed, by analysing both spatial and temporal coefficients of the second EOF mode, it is recognized that positive (negative) temporal amplitude indicates high (low) chlorophyll concentration south of Minho River and low (high) chlorophyll concentration north of it.

Generally, the highest Chl-a concentration occurred between July and September, the most favourable upwelling season. Moreover, on average, between December and February of each year the temporal amplitudes of the second mode were positive, followed by a period of negative amplitudes (between March and June/July). This means that Chl-a concentrations were stronger below 42 °N than above this latitude, for winter months. Otherwise, during spring months primary production is enhanced above 42 °N and attenuated southward. This variability can be associated with the winter vertical mixing cycle, which is strong in February (Figure 3.5), and tends to decrease the Chl-a concentration north of 42 °N by dilution/light limitation effects (also known as phyto-convection mechanism) (Perez et al., 2005). Actually, in late winter (February), the MLD was deeper north of 42 °N (Figure 3.5), being the ten year (1998-2007) average depth equal to 350 m, while south of this latitude the average

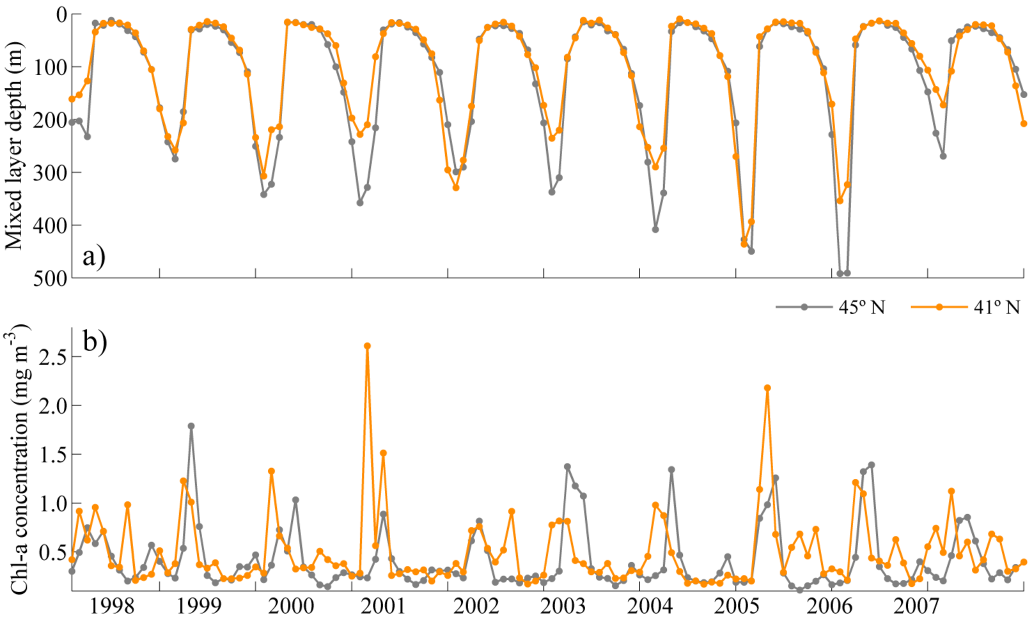

Figure 3.5: a) Mixed Layer Depth (MLD) from GODAS (m) and b) monthly mean distribution of Chl-a concentration (mg m^{-3}) at two distinct latitudes: 41 °N and 45 °N.

MLD is about 250 m.

South of 42 °N the deepening of the mixed layer to shallow depths during February seemed to favour Chl-a concentration increase, by providing new nutrients to the surface after the summer depletion. At the same time, north of 42 °N the MLD is deepest and Chl-a concentration low, occurring maxima concentrations one month after (Figure 3.5), and thus corroborating the second mode of EOF spatial coefficient.

3.3.2 Monthly distribution of Chl-a, SST and UI

The monthly distribution of Chl-a, SST and Ekman transport are presented in Figure 3.6, for the three coastal segments. Generally, these parameters showed seasonal and spatial variability along the northwestern coast of the IP.

The highest Chl-a concentrations were noticed along the western coastal segment during summer months, reaching maximum values (4 – 5 mg m^{-3}) between 40 and 41 °N, around 41.5 °N and in front of Rias Baixas (42.5 °N). These maxima values are related with the upwelling events occurring at this season (Alvarez et al., 2008a; Gomez-Gesteira et al., 2006; Relvas et al., 2007) that bring nutrient rich water to surface. Indeed, from Figure 3.6g, during summer UI is stronger than for the rest of the year and upwelling favourable, with values reaching 800 m^{3} s^{-1} km^{-1}. In addition,

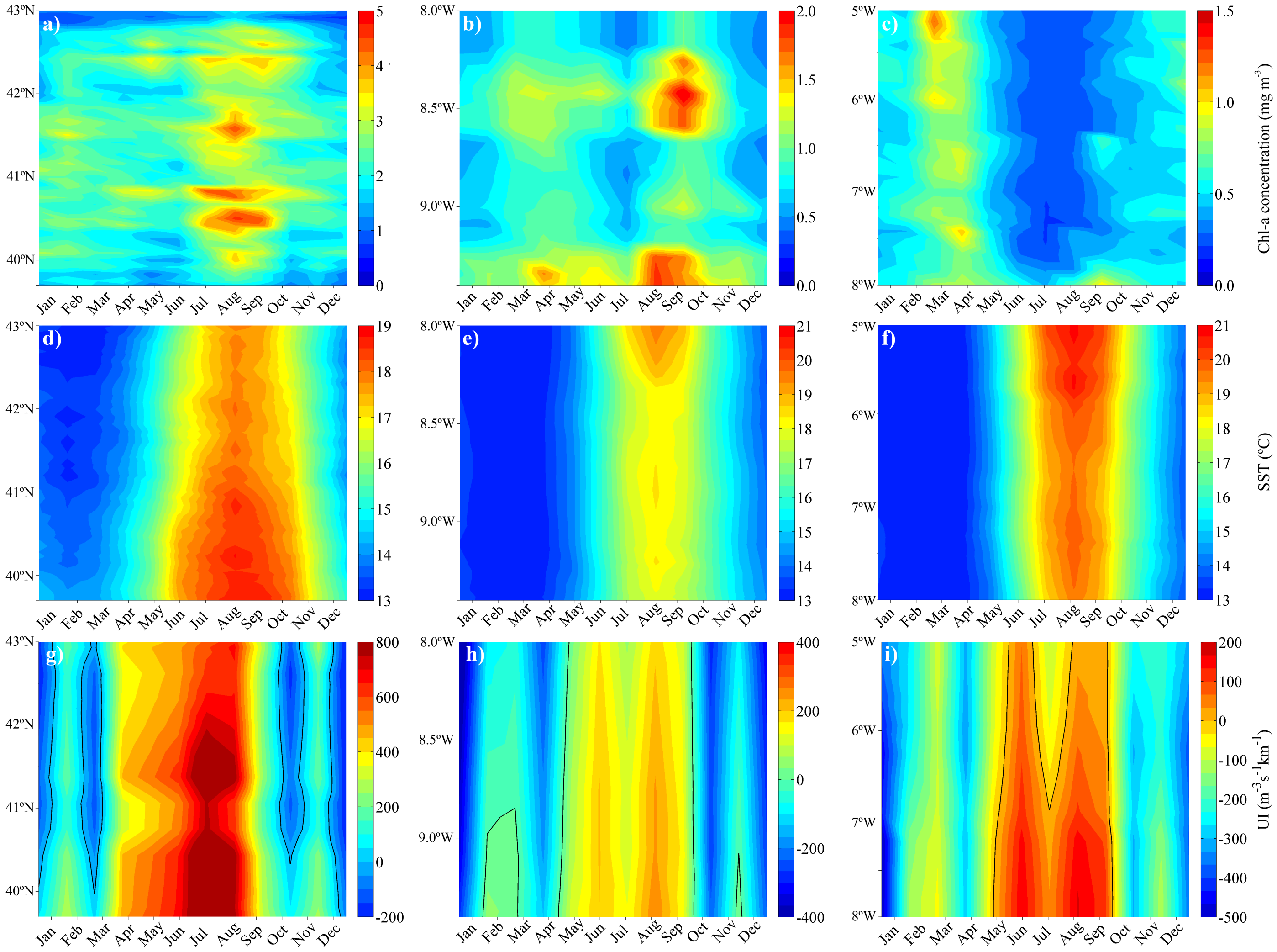

Figure 3.6: Monthly evolution of Chl-a concentration (mg m^{-3}), SST (° C) and Ekman transport (m^3 s^{-1} km^{-1}), for west (a, d and g), intermediate (b, e and h) and north (c, f and i) coastal segments. The black lines in g, h and i correspond to the zero isoline.

the upwelling intensity was observed to increase southward.

Also in winter and spring, high values of Chl-a concentration were observed in IP western coastal segment, although lower than in summer (between 2 and 3.5 mg m^{-3}). Actually, in winter phytoplankton development is light limited due to the short day light periods. These winter maxima Chl-a concentrations were observed during February (between 3 and 3.5 mg m^{-3}) and may be related to nutrients input from land through river discharge or to strong winter vertical mixing. However, the SeaWiFS algorithm can lead to an erroneous overestimation of Chl-a concentration in turbid coastal areas, mainly during winter and in the vicinity of the river mouths, due to the input of large quantities of organic matter, suspended sediments and pollutants.

Nevertheless, from Figure 3.6g and according to previous studies (Alvarez et al., 2003; Borges et al., 2003; Santos et al., 2004; deCastro et al., 2006; Prego et al., 2007), upwelling favourable conditions occur during winter, with an average Ekman transport of 250 m^3 s^{-1} km^{-1} for February and November. These winter upwelling events contribute to enhance primary production in coastal region, but in lower extent when compared to those generated by summer upwelling events (Alvarez et al., 2003; Santos et al., 2004; Prego et al., 2007). Indeed, during winter, the IPC transports ENACW of subtropical origin that has lower concentration of nutrients when compared to subpolar ENACW that only reach surface during strong summer upwelling events.

During spring, maxima values were observed mainly around Rias Baixas (between 42 and 42.5 °N,) and between Mondego and Douro Rivers (41 °N), with the highest values in May. This high productivity is related with the known spring blooms that usually overlap with upwelling blooms from May to October. The annual cycle of Chl-a described coincides with the results obtained by Bode et al. (2009) in a station located in front of the Rias Baixas using data series collected from 1989 to 2006. Those authors concluded that summer blooms have increased over the years.

Chl-a concentration shows a similar pattern along the intermediate coastal segment, however with lower intensity than at western. Spring blooms were also present during April and May (mainly near Cape Finisterre), as well as upwelling favourable conditions, with UI values between 100 and 200 m^3 s^{-1} km^{-1}. In summer, essentially in August, Chl-a concentration reaches values higher than 2 mg m^{-3} northward Cape Finisterre and near Artabro Gulf, which are associated with upwelling favourable conditions, corroborated by UI represented in Figure 3.6h (approximately 400 m^3 s^{-1} km^{-1}). In February and November positive UI values were detected in both western and intermediate coastal segments, reflecting the existence of upwelling favourable conditions in winter that can turn the water more productive, although to a lower extent than during summer events (Prego et al., 2007).

Northern coastal segment is the least productive, with Chl-a concentration more significant between February and April with values around 1.2 mg m^{-3}. During this period unfavourable upwelling conditions are observed in this region, with UI values between -100 in February and -300 m^3 s^{-1} km^{-1} in April (Figure 3.6i). Between May and September upwelling favourable conditions were observed at northern coastal segment, with the highest UI values found at the westerly region (approximately 200 m^3 s^{-1} km^{-1}). However, during this period Chl-a concentration values are weak or null. In December, Chl-a concentration reach values of 0.8 mg m^{-3}, around 6 °W (Cape Peñas), which are probably attributed to the input of nutrients through Nalon River, which is the most important freshwater source in the region (Alvarez et al., 2012; Prego and Vergara, 1998).

The annual cycle of SST showed a clear seasonal pattern for three coastal segments (Figure 3.6d, e and f). At western coastal segment minima values were found from January to April and maxima from July to October. The thermal amplitude was on the order of 6 °C, with the minimum in February (13 °C) and the maximum in August (19 °C). A thermal gradient associated with latitude was also identified. The amplitude of seasonal variability was approximately 2 °C, and higher summer and winter temperatures are reached at south (18.5 and 14 °C, respectively) and lower summer and winter at north (16 and 13 °C, respectively).

At intermediate coastal segment, summer season also presents higher SST, that increase eastward, from 18 °C near Cape Finisterre to more than 19 °C at 8 °W. During winter, between December and April, SST is homogeneous and about 13 °C.

Finally, at northern coastal segment maxima values occurred between July and September. A thermal gradient in longitude was detected in summer, with higher temperatures reached at east (approximately 21 °C) and lower at west (approximately 19 °C). During winter, SST was zonally uniform with values of approximately 13 °C.

In order to study the cross-shelf variability of SST and Chl-a concentration along the three coastal segments near the main rivers mouth, their monthly evolution along sections I, II, III, IV and V (Figure 2.2) were computed and results are depicted in Figure 3.7.

Regarding the sections located at western coastal segment (I, II and III, Figure 3.7), it is observed that spring-summer Chl-a maxima were confined near coastal region (approximately 6 km), while winter maxima spread offshore. Indeed, spring-summer high Chl-a concentrations were related to upwelling events, that were evident through SST pattern (colder coastal waters than offshore) (Figure 3.7 bottom panel).

Otherwise, during winter, primary production was related to WIPB (Peliz et al., 2002) that have lower temperatures than surrounding offshore waters and may even be colder than waters beneath (Santos et al., 2004). Actually, for sections II and III that correspond to the mouth of the rivers with more significant discharges, a lens of cold water (approximately 13 °C) is noticeable at least to 10 °W of longitude. This fast cooling is due to plume high buoyancy, which allow heat exchange between surface and atmosphere in a different way from the surrounding waters as the thermally driven convection is limited to a thinner layer (Santos et al., 2004).

At intermediate coastal segment (section IV, Figure 3.7), results show a pattern similar to that found at western segment, either for Chl-a and SST. Between August and October, Chl-a concentrations higher than 4 mg m^{-3} are observed near the coast, as well as SST values between 17 and 18 °C. In winter Chl-a maxima concentrations were lower than in summer, with values between 1 and 1.5 mg m^{-3}, spreading further offshore. SST reaches its minimum during the months of February and March (12 °C).

Concerning to section V (Figure 3.7), located at northern coastal segment, SST pattern is similar to that observed for other sections, however Chl-a concentration pattern is opposite. Between February and April, high primary production (higher than 1 mg m^{-3}) occurs over 60 km and a lens of cold water (approximately 12 °C) was detected, while during summer, Chl-a levels were low and water temperatures rise reaching more than 20 °C.

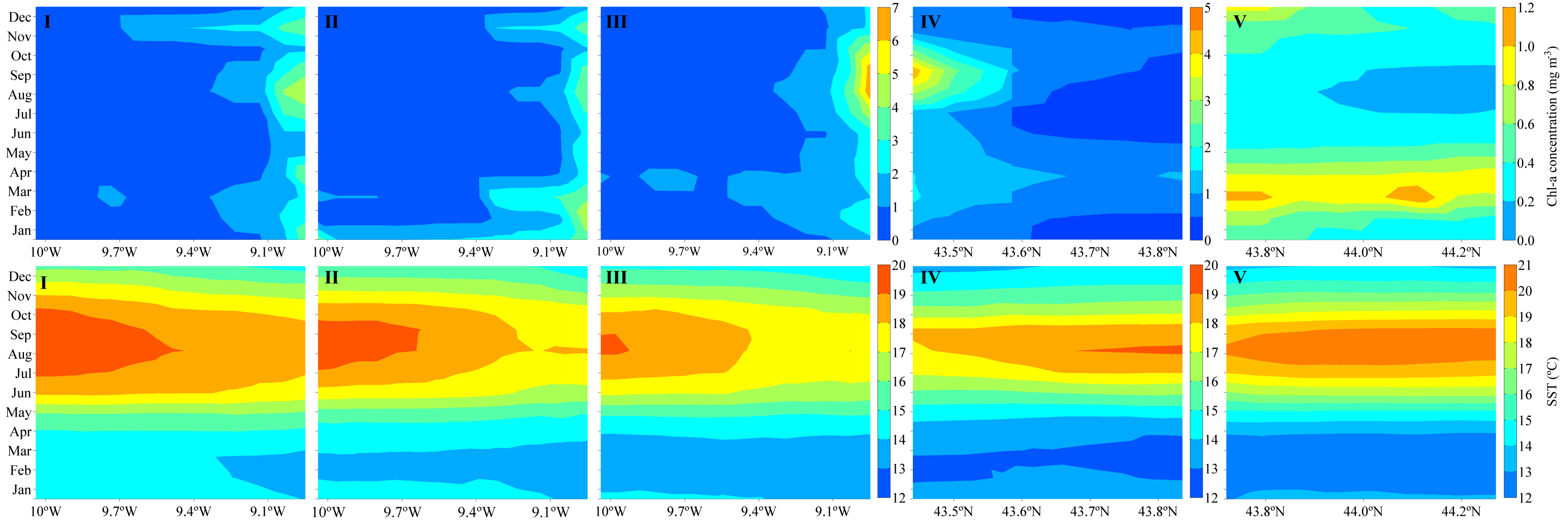

Figure 3.7: Monthly evolution (1998-2007) of Chl-a concentration (mg m^{-3}) (top panel) and SST (°C) (bottom panel) for sections I (Mondego), II (Douro), III (Minho), IV (Eume) and V (Nalon).

3.3.3 Interannual variability of Chl-a and its response to SST, Ekman transport and rivers runoff

According to previous results, phytoplankton blooms occurred mainly during summer and winter along the northwestern coast of IP. Consequently, in this section the interannual variability of Chl-a concentration, SST, UI and river discharges are analysed during these two seasons. Therefore, for western coastal segment JFM and JAS were considered to represent winter and summer, respectively, while for intermediate and northern coastal segments were considered FMA and JAS. Winter and summer months were chosen taking into account the period of high primary production at each coastal segment.

The interannual variability for Chl-a concentration is significant showing important differences among years and coastal segment. At western coastal segment, 1998, 2001, 2003 and 2007 were the most productive years during winter (Figure 3.8). It is noteworthy that, particularly for 1998, the Chl-a concentration peaks were found slightly upstream the main rivers mouth, with the most significant values (7 mg m^{-3}) occurring at 41.5 °N (Figure 3.8a). Nearby latitudes where Chl-a maxima occur, SST was lower than for surrounding waters (Figure 3.8b), and upwelling unfavourable conditions (Figure 3.8c) were detected. Therefore, high productivity observed during winter 1998 was related to rivers runoff that exhibited high discharges: 1500, 800 and 240 m^{3} s^{-1} for Douro, Minho and Mondego Rivers, respectively, for January. A similar pattern is observed for 2001, 2003 and 2007. Chl-a concentration during these years showed high values (from 2.5 to 6 mg m^{-3}) under upwelling unfavourable conditions, and temperature minima are found approximately at the same latitudes as Chl-a maxima. The winter of 2001 was characterized by intense southerly winds which favour downwelling conditions over the shelf (Alvarez-Salgado et al., 2003), originating adverse weather conditions with high rainfall events (Alvarez et al., 2005) and consequently high river discharges. Indeed, strong negative values of UI are observed for this year (Figure 3.8c), as well as the highest discharges (Douro discharge reached values of 4000 m^{3} s^{-1}). Although these high discharges may influence the estimation of Chl-a by SeaWiFS, generating a very strong signal in the satellite product due to high concentrations of CDOM, it seems that river discharges has a direct relation with Chl-a concentration.

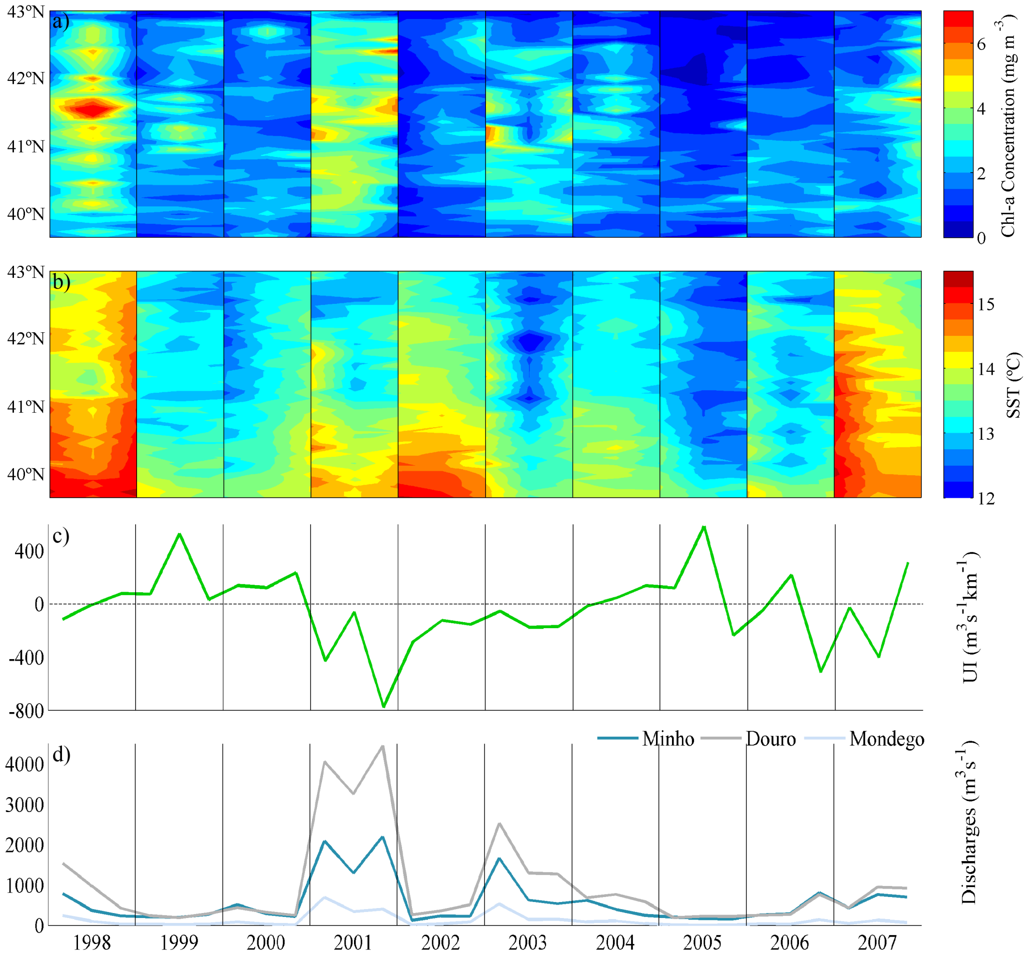

Figure 3.8: JFM interannual distributions for western coastal segment of: a) Chl-a concentration (mg m^{-3}), b) SST (°C), c) UI (m^3 s^{-1} km^{-1}) and d) rivers discharge (m^3 s^{-1}).

The 2005 winter was the least productive, although upwelling favourable conditions were observed. In fact, when strong winter winds occur (upwelling favourable or not) the water column stability decreases and may inhibit phytoplankton blooms.

Relatively to the summer season (Figure 3.9), the years of 2005, 2006 and 2007 revealed some evidences of being the most productive along the western coastal segment. Maxima values were mainly evident for 2006 summer, with concentrations higher than 9 mg m^{-3} between the latitudes 41 and 42 °N, while for 2007, the maximum Chl-a concentration was 8 mg m^{-3}, around 40.5 °N (Figure 3.9a). Moreover, between July and September minima values of SST were registered approximately at the same latitude as the Chl-a maxima (Figure 3.9b). Therefore, results suggest that these high Chl-a concentrations are explained by upwelling processes that occur in this zone during the summer period (Alvarez et al., 2008b; Gomez-Gesteira et al., 2006; Relvas et al.,

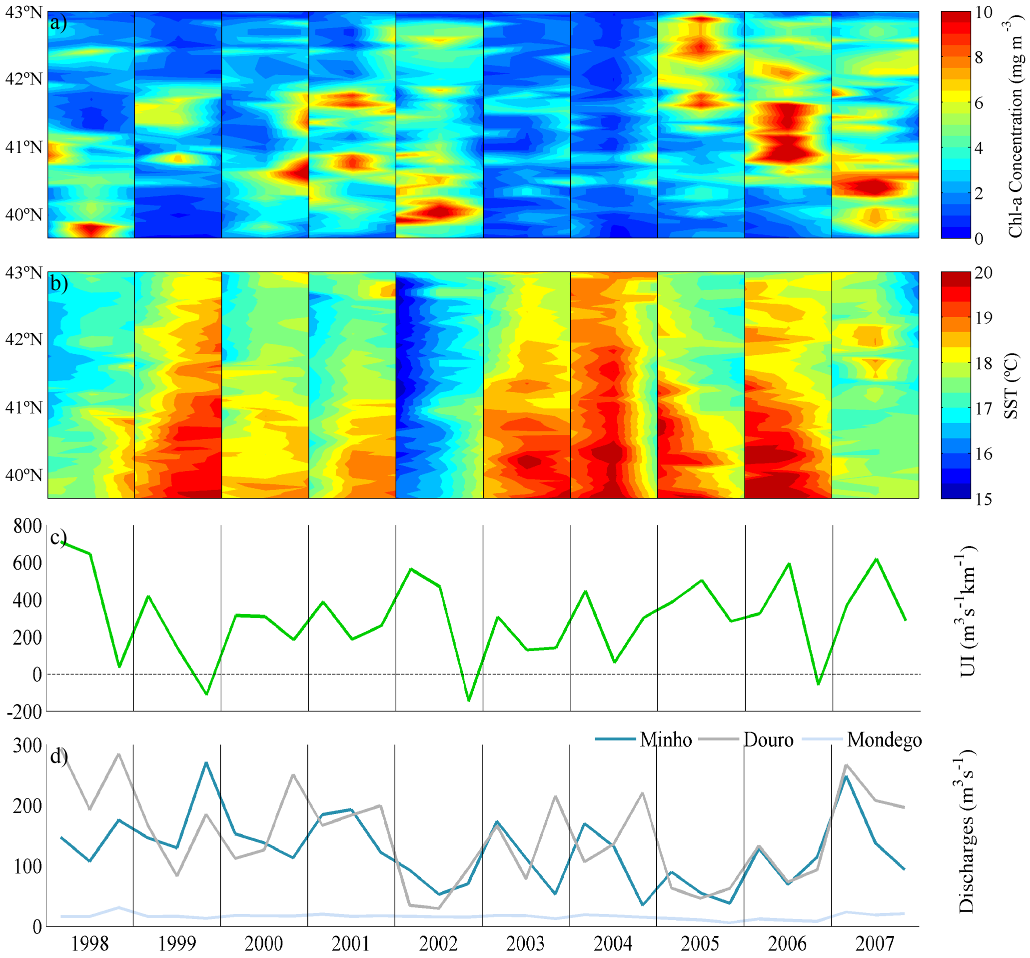

Figure 3.9: JAS interannual distributions for western coastal segment of: a) Chl-a concentration (mg m^{-3}), b) SST (°C), c) UI (m^3 s^{-1} km^{-1}) and d) rivers discharge (m^3 s^{-1}).

2007). Indeed, upwelling favourable conditions were observed (Figure 3.9c), *i.e.* the transport was directed westward, with average values of 500 m^3 s^{-1} km^{-1}. The westward transport during upwelling season generates water depletion in the upper layers and colder nutrient rich water from below (ENACW) is upwelled in order to re-establish the equilibrium near the coast. For 2005, the highest primary production was found off Rias Baixas, with values of approximately 8 mg m^{-3}.

Similar patterns have occurred during 1999, 2000 and 2001, however less significant and affecting a smaller area. The relation between upwelling processes (decrease of water temperature) and increased Chl-a concentration was evident for most of the years indicating that the variability of Chl-a mainly depends on these phenomena during the summer season. Figure 3.9a also indicates that 2003 and 2004 were the least productive years during summer, with the lowest values of Chl-a concentration

(2 – 4 mg m^{-3}) along the coast. For these years, UI also showed upwelling favourable conditions (200 m^3 s^{-1} km^{-1}), although with less intensity than for the period 2005-2007. Moreover, the SST decrease near the more productive regions was low (Figure 3.9c). Additionally, from Figure 3.9d was found that river discharges during summer are low, with mean values of 120 and 150 m^3 s^{-1} for Minho and Douro rivers and 16 m^3 s^{-1} for Mondego, revealing that primary production peaks were mainly originated by the fertilization of surface waters through upwelling events.

The interannual analysis was also performed along the intermediate and northern coastal segments during FMA and JAS. At intermediate coastal segment, for FMA high Chl-a levels are observed, mainly in the surroundings of Artabro Gulf, where Eume River discharges (Figure 3.10a). Particularly, for the years of 2004 and 2007 Chl-a concentration reach values of more than 2 mg m^{-3}. These high concentrations

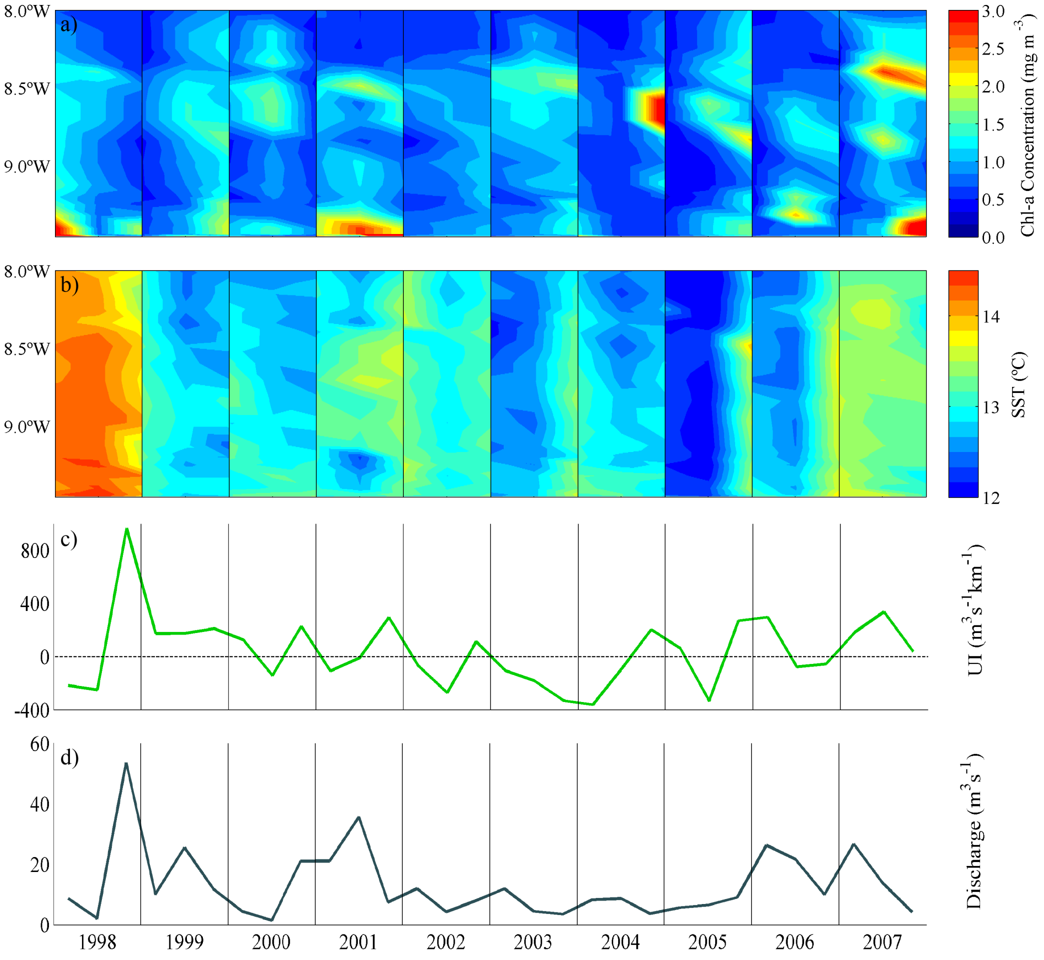

Figure 3.10: FMA interannual distributions for intermediate coastal segment of: a) Chl-a concentration (mg m^{-3}), b) SST (°C), c) UI (m^3 s^{-1} km^{-1}) and d) river discharge (m^3 s^{-1}).

may be related with weak upwelling events, which were identified through the low SST observed in this region (Figure 3.10b) and through the positive low UI (between 100 in February and 400 m^3 s^{-1} km^{-1} in March 2007) (Figure 3.10c). Otherwise, spring blooms produced by a transient stratification in the winter mixed surface layer may also generate high primary production, as predicted by the Sverdrup model (Sverdrup, 1953). In this case, discharges are weak (between 20 in February and 5 m^3 s^{-1} in April 2007) and probably not responsible for the high Chl-a levels detected. Also in 2001, mainly northward Cape Finisterre and Artabro Gulf, high levels of Chl-a concentration were observed in March, which may be associated with the highest discharges of Eume River found for period analysed (40 m^3 s^{-1}).

During JAS (Figure 3.11), the most productive years were 1998, 2001 and from 2005 to 2007, reaching values higher than 3 mg m^{-3}. The least productive were 1999 and 2004. The strong levels of Chl-a were probably related with upwelling events, that, despite weak (on average UI is 200 m^3 s^{-1} km^{-1}), contribute to the upwell cold and nutrient rich water to surface. These assumption is corroborated by SST patterns observed for this specific years. Moreover, during JAS, Eume discharge is negligible (less than 4 m^3 s^{-1}) and therefore may not promote primary production in the region (Figure 3.11d).

Northern coastal segment results suggest that, generally, it is the least productive, presenting an average Chl-a concentration of approximately 1 mg m^{-3} for winter (Figure 3.12). Nonetheless, high phytoplankton biomass is found for most of the years during March, being 2005 and 2006 the most productive years. Indeed, values of 3.0 mg m^{-3} are found near Cape Peñas (5.5°W) in March 2006 (Figure 3.12a), while during 2005 high Chl-a levels (1.5 – 2.5 mg m^{-3}) occur in March and April between 5.5 and 6°W. Moreover, the winter of 2005 and 2006 were characterized by an extreme mixed layer deepening (Figure 3.5), resulting in a nutrient content increase in the upper layer (Somavilla et al., 2009). This extreme mixed layer deepening is caused by an anomalous atmospheric pattern characterized by a strong anticyclonic anomaly located west of British Isles during all the 2004-2005 winter (Somavilla et al., 2009; Cabrillo et al., 2011). Indeed, surface mixing resulting from air-sea exchanges provides one of the main mechanisms of nutrient supply from the rich deep water to the euphotic layer, and consequently high levels of Chl-a were observed (Figure 3.12a). Favourable

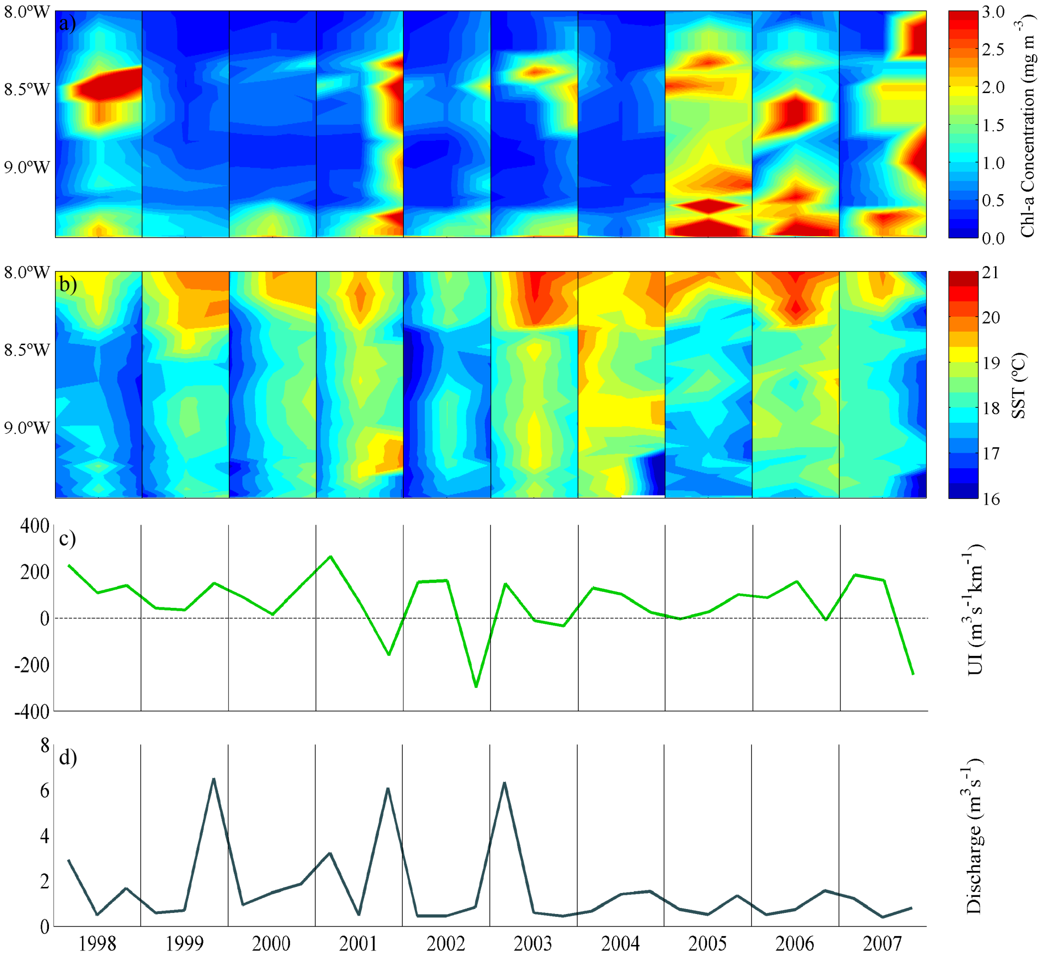

Figure 3.11: JAS interannual distributions for intermediate coastal segment of: a) Chl-a concentration (mg m^{-3}), b) SST (°C), c) UI (m^3 s^{-1} km^{-1}) and d) river discharge (m^3 s^{-1}).

upwelling conditions were detected in March 2005 and April 2006, with UI values of 250 m^3 s^{-1} km^{-1} and 400 m^3 s^{-1} km^{-1}, respectively. The Sverdrup effect (Sverdrup, 1953) explains the seasonal cycles and interanual variability of primary production (Varela et al., 2008, 2010; Alvarez et al., 2011).

Also, for these two years, Nalon discharges are significant (250 and 300 m^{-3} s^{-1} for 2005 and 2006, respectively) in March and may have contributed to the transport of cold water (12 °C, Figure 3.12c) and nutrients, that consequently enhance primary production near coast (Figure 3.12d).

Despite the high Nalon discharges observed during the winter of 1998 and 2001, these were the least productive years at northern coastal segment, with values of Chl-a concentration lower than 0.5 mg m^{-3} (Figure 3.12). These two years were also characterized by the highest SST, between 13 and 14 °C.

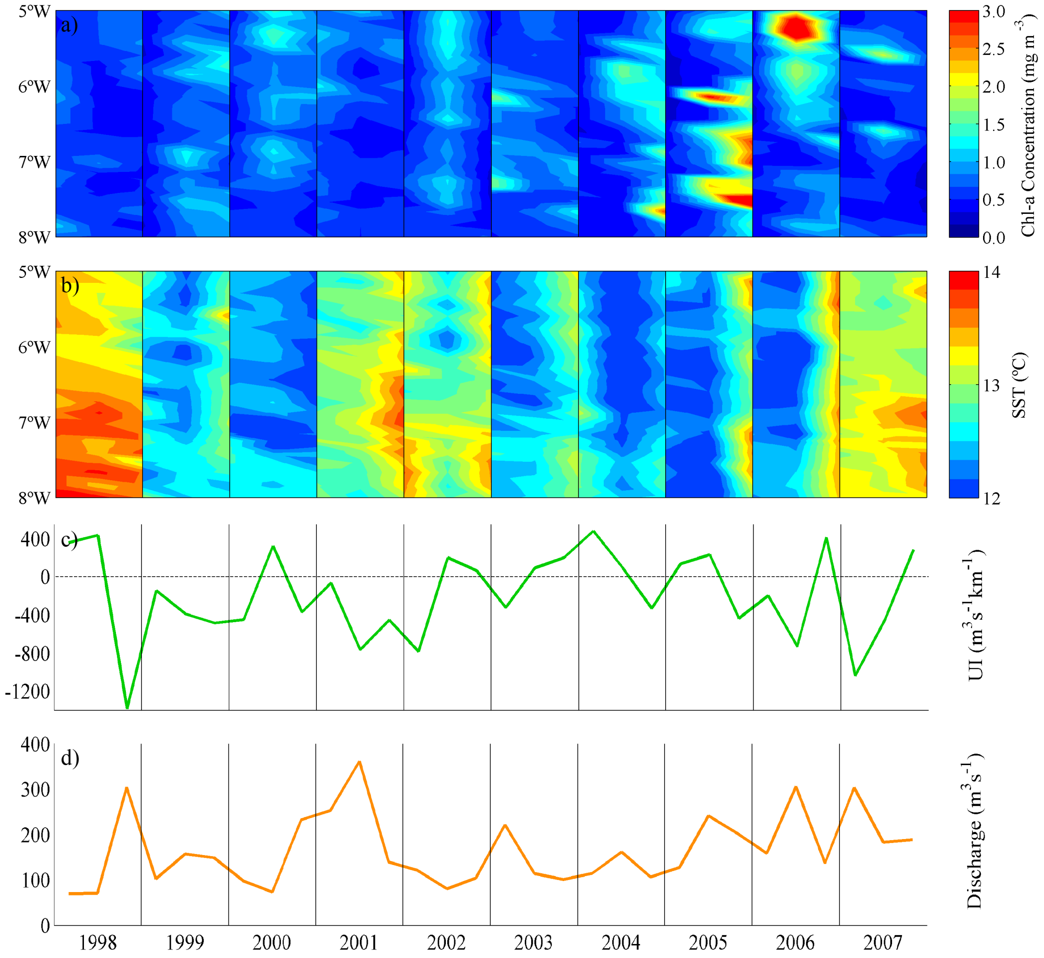

Figure 3.12: FMA interannual distributions for northern coastal segment of: a) Chl-a concentration (mg m^{-3}), b) SST (°C), c) UI (m^3 s^{-1} km^{-1}) and d) Nalon discharge (m^3 s^{-1}).

Between July and September (Figure 3.13), primary production along the northern coastal segment was generally low, with mean Chl-a concentrations of approximately 0.5 mg m^{-3}. September 2007 was the most productive month, showing the strongest upwelling favourable conditions (800 m^{-3} s^{-1} km^{-1}) and therefore lower temperatures (16 – 17 °C) than surrounding waters. Otherwise, the preceding months showed low levels of Chl-a concentrations and unfavourable upwelling conditions. Also, for July 2007 the highest flow from Nalon (75 m^3 s^{-1}) during summer season was detected, however was not enough to promote high primary production. During JAS 2003, high levels of Chl-a concentration are detected in the surroundings of Cape Ortegal, reaching values of 2 mg m^{-3}. This happens under weak upwelling favourable conditions (between 100 and 200 m^{-3} s^{-1} km^{-1}).

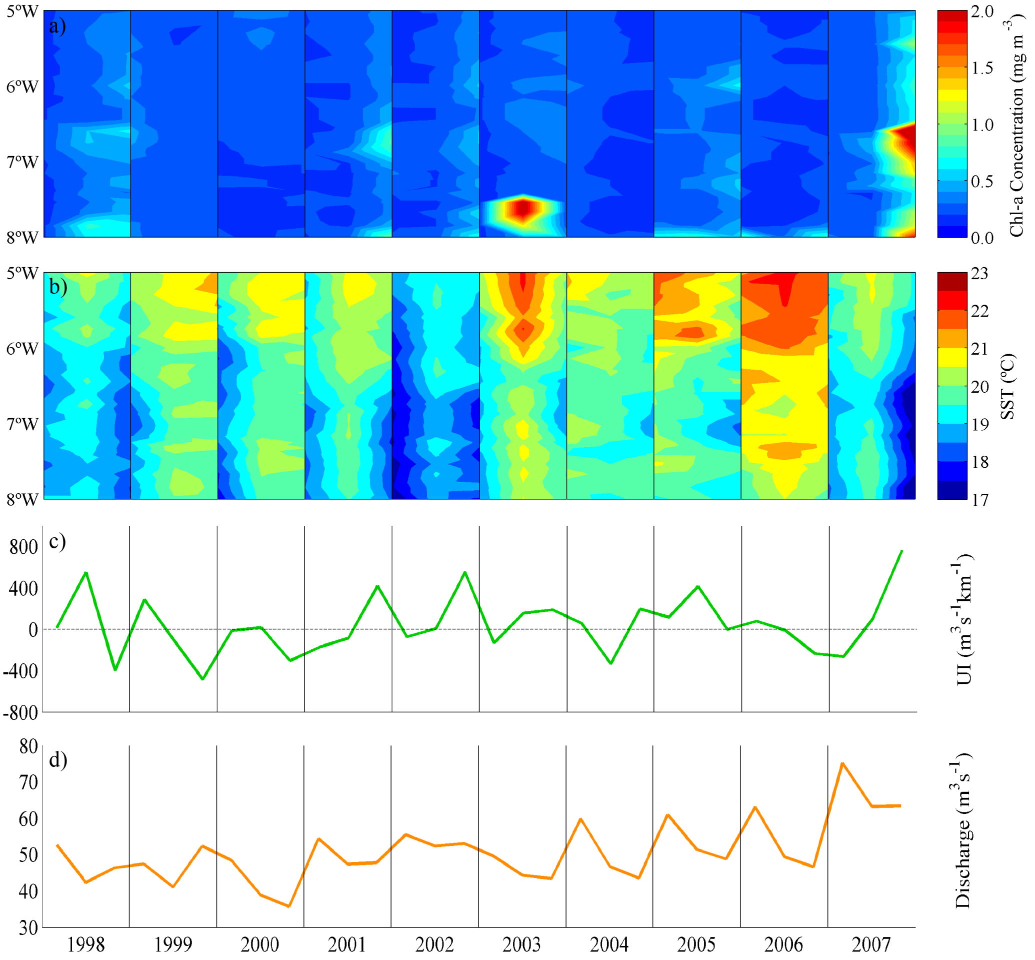

Figure 3.13: JAS interannual distributions for northern coastal segment of: a) Chl-a concentration (mg m^{-3}), b) SST (°C), c) UI (m^3 s^{-1} km^{-1}) and d) Nalon discharge (m^3 s^{-1}).

3.3.4 Correlation analysis

Pearson's correlations between Chl-a concentration, UI, river discharge and SST were computed (Table 3.1) for the points near each river mouth, considering two seasons: winter (JFM for the western and FMA for the intermediate and northern coastal segments) and summer (JAS).

During the JFM (FMA), positive correlations were found between Chl-a concentration and rivers discharge, with Minho and Douro showing the highest values (0.51 and 0.43, respectively), with the exception of Eume discharge, which is negatively correlated with Chl-a concentration (-0.11). Indeed, Eume River flow is very low compared to the other rivers and probably the influence of its plume is restricted to the near coast region. No significant correlations were found between UI and Chl-a

Table 3.1: Correlation coefficients between Chl-a and river discharges, UI and SST. All the correlations have a significance level higher than 97% (*p-value* < 0.03) except the value marked with an asterisk (*) that have a significance level of 70%.

	Chl-a *vs.* Discharges	Chl-a *vs.* UI	Chl-a *vs.* SST
	JFM (FMA)	JAS	JAS
Mondego	0.29	0.40	−0.52
Minho	0.51	0.35	−0.26
Douro	0.43	0.33	−0.36
Eume	−0.11*	0.43	−0.30
Nalon	0.25	0.22	−0.28

concentration for this season and therefore high Chl-a levels at intermediate coastal segment may be explained by spring blooms produced by the transition of mixing to stratification and at western and northern coastal segments mainly by the river discharges.

Moreover, Chl-a concentration and UI showed significant positive correlations during summer (JAS) at the points located at the three coastal segments, with the highest correlation found at intermediate coastal segment (0.43). Also no significant correlations were found for this period between Chl-a and discharges. These results suggest that for summer Chl-a was mostly generated by upwelling favourable conditions. This assumption is corroborated by the correlations between Chl-a and SST, which are negative for all points analysed (between -0.28 and -0.52). Indeed, when upwelling conditions were observed, cold water rises to surface carrying nutrients and therefore generating high primary production.

3.4 Conclusions

The influence of coastal upwelling and rivers runoff on Chl-a concentration over the northwestern coast of IP was analysed through remote sensing data and *in situ* observations of the main rivers discharging into the study area, from 1998-2007. This study has shown the following:

- The EOF analysis revealed that the dynamics of the first mode is only related with the dynamics of the nearshore region of western and intermediate coastal segments, once positive spatial coefficients were found here, while at northern coastal segment coefficients are close to zero. Therefore, through the associated time amplitude of Mode 1, it was found that Chl-a concentration had a positive deviation relatively to the climatology in summer season (JAS) for all the years along the western and intermediate coastal segment. From the second mode coefficients, two patterns near coastal region were identified: positive values along south of Minho River mouth and negative north of it, showing that the main forcing mechanisms of Chl-a concentration in these two regions were different. The analyses of both spatial and temporal coefficients of the second EOF mode reveals that positive (negative) temporal amplitude indicates high (low) chlorophyll concentration south of Minho River mouth and low (high) chlorophyll concentration north of this region;

- The annual cycle of SST and UI shows that spring-summer months are the most favourable season to the occurrence of upwelling events, which generate water depletion in the upper layers and upwelling of colder nutrient rich water from below. Therefore, high productivity occurs and high Chl-a concentration was detected at the surface in the western and intermediate coastal segments. At northern segment, despite the upwelling favourable conditions observed during these season, Chl-a levels were low. Here the highest Chl-a levels were observed between February and May, when unfavourable upwelling conditions were generally observed;

- The interannual variability of UI, river discharges, SST and Chl-a concentration was also analysed during the summer and winter seasons, for the three coastal segments. At western and intermediate coastal segments 2005, 2006 and 2007 seemed to be the most productive years for the JAS with high Chl-a values along most of the coast occurring under strong upwelling favourable conditions. In winter, Chl-a concentration seemed to be mainly affected by the input of nutrients in the zone through rivers discharge at western coastal segment. The most productive year was 1998 with the most significant Chl-a levels around 41.5 °N, SST colder than the surrounding waters, upwelling unfavourable conditions and high discharges. At intermediate coastal segment, the most productive years in winter were 2004 and 2007, which may be related with the weak upwelling favourable conditions or with the spring blooms, once Eume River discharge is too weak to promote high primary production. At northern coastal segment high phytoplankton biomass was found mainly during March, being 2005 and 2006 the most productive years, which is related with the winter vertical mixing cycle and high discharges from Nalon River;

- From the correlation analysis it was found that the phytoplankton biomass is mainly associated with upwelling during JAS for the three coastal segments and with river runoff in JFM (FMA).

Due to the importance of coastal upwelling in the maintenance of marine ecosystems, its intensity and frequency have been researched in several works, with contradictory results. Accordingly, along IP coast, several studies argue an increase of upwelling intensity over time, while other works report a decrease. In both cases, changes in phytoplankton biomass are expected mainly in upwelling regions, which have high levels of biological activity. However, the ecosystem response to upwelling changes in these regions will depend on a complex balance of several physical factors, such as water temperature, water column stratification and light availability. Consequently, the study of forcing mechanisms of phytoplankton development in such productive areas is of extreme importance, as well as their dependence on meteorological conditions. Therefore, in next chapter the influence of meteorological conditions in Chl-a levels and upwelling occurrence will be assessed.

Chapter 4

Upwelling and Chl-a: dependence on weather types

4.1 Introduction

Owing to its ecological and economic importance, changes in coastal upwelling are one of the most studied processes influencing fish production and distribution all over the world. Over the last decades, changes in upwelling have been mainly studied in terms of the variability of atmospheric conditions focusing on wind patterns (Garcia-Reys and Largier, 2010; Narayan et al., 2010; Patti et al., 2010; Seo et al., 2012; Barton et al., 2013; Aravena et al., 2014). The alongshore winds could be intensified in future due to global warming and consequently accelerate coastal upwelling circulation (Bakun, 1990; McGregor et al., 2007; Relvas et al., 2009; Bakun et al., 2010) leading to an increase in primary production. Moreover, changes in upwelling off western Iberia have recently been connected to the occurrence of different CWTs (Ramos et al., 2013), which describe different meteorological conditios in terms of atmospheric variables. These authors found that upwelling activity was mostly driven by wind flow from the northern quadrant (northerly or northeasterly).

In recent years, several natural processes were investigated pertaining to the impact of changes in the frequency of occurrence of CWTs around Iberia: i) changes in climate variables (Trigo and DaCamara, 2000; Paredes et al., 2006; Lorenzo et al., 2008; Ramos et al., 2010; Lorenzo et al., 2011; Cortesi et al., 2014); ii) avalanches (Esteban et al., 2005); iii) related health issues (McGregor et al., 1999; dePablo et al., 2009) and iv) lightning activity (Ramos et al., 2011). However, no studies examining the relationship between the variability of CWTs and primary production have been carried out.

The main objective of this chapter is to evaluate and quantify the influence of meteorological conditions on upwelling variability and Chl-a concentration along the northwestern coast of IP, through a probability analysis. Once meteorological conditions (CWTs) can be accurately predicted (Ramos et al., 2013; Lorenzo et al., 2011), upwelling and primary production changes can be also anticipated. These provide the conditions for the identification of the most nutrient rich regions and therefore to improve fisheries and aquaculture productivity along the northerwestern coast of IP.

4.2 Data and methods

CWTs were computed using the procedure specified by Lamb (1972) and Jones et al. (1993). They were computed using daily mean sea level pressure (SLP) data from NCEP/NCAR reanalysis (2.5° × 2.5°) between 1998 and 2007 at 16 points (Figure 4.1) located between 35 °N – 55 °N and 25 °W – 5 °E. In total, 26 weather types were computed, however in this work only ten are considered to define the meteorological conditions, eight directional indices: NE (northeasterly), E (easterly), SE (southeasterly), S (southerly), SW (southwesterly), W (westerly), NW (northwesterly), N(northerly) and two vorticity indices: C (cyclonic) and A (anticyclonic). A description of the meteorological conditions under each weather type is performed for the period 1998-2007. The monthly mean frequency of each weather type considered was also computed for this period, in order to characterized its variability.

Weekly Chl-a concentration from SeaWiFS was used at the points represented in Figure 2.2, described in Chapter 2, covering the period of 1998-2007. Wind data were acquired from NCEP CFSR database, for the same period, and was used to compute the UI at the triangles of Figure 2.2. A detailed description of these datasets is presented in Chapter 2.

Three coastal segments were considered for analysis: western, intermediate and northern, as defined in previous chapters.

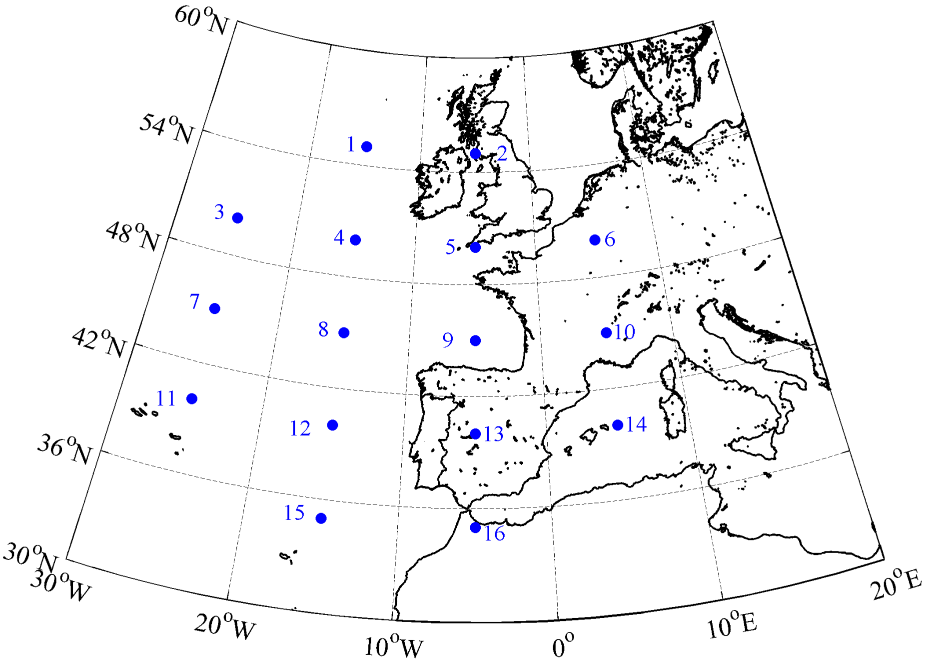

Figure 4.1: Location of the 16 grid points used to compute the geostrophic (vorticity and directional flow) indices.

A conditional probability was computed to further infer about the dependence of upwelling occurrence and Chl-a concentration on meteorological conditions. In this case, the conditional probability is interpreted as the probability that UI or Chl-a exceeds a certain value given the occurrence of a specified weather type. In the case of UI, the threshold value considered was the 75th percentile of the maximum annual mean, computed for the period 1998-2007 and for each coastal segment (western: 464 m^3 s^{-1} km^{-1}, intermediate: 267 m^3 s^{-1} km^{-1} and northern: 107 m^3 s^{-1} km^{-1}). For Chl-a, the threshold value was considered as the mean value plus the standard deviation calculated for the same period and also along each coastal segment. Consequently, the threshold values considered are 3.5, 1.6 and 0.8 mg m^{-3}, for western, intermediate and northern coastal segments, respectively.

Results are discussed for the three coastal segments separately and considering two seasons: the spring-summer season corresponding to April-September and autumn-winter season corresponding to October-March.

4.3 Results and discussion

4.3.1 Circulation weather types

The weather circulation affecting Western Iberia was characterized through the use of a set of indices associated with the direction and vorticity of geostrophic flow for the period 1998 to 2007. As previously referred, the directional indices used herein are: NE, E, SE, S, SW, W, NW, N and the vorticity indices are: C and A. In general, the conditions of wind direction correspond to the respective weather type, *i.e.*, for instance, NW weather type corresponds to the number of days with northwesterly winds. However, as the CWTs are directly related with geostrophic flow, the real flow is slightly oriented a few degrees towards lower pressure systems (counter clockwise in Northern Hemisphere) due to the effect of surface friction (Wallace and Hobbs, 2006), therefore a NW CWT pattern originates WNW winds.

The use of CWTs allows to distinguish different meteorological conditions by describing them in terms of circulation parameters or local weather elements. A brief description of the meteorological conditions associated with each weather type, between 1998 and 2007, around IP coast is given here (Figure 4.2):

- North-Easterly (NE) days are characterized by an extended Azores high-pressure towards the British Islands and by low-pressure values over the Mediterranean region;
- Easterly (E) days are characterized by an anticyclone centered over the British Isles;
- South-Easterly (SE) and Southerly (S) days showed a similar pattern. They are characterized, on average, by a high-pressure system located over British Isles and a low pressure in the Atlantic. Therefore, both weather types promote south-easterly winds over the study region;
- South-westerly (SW) days are characterized by a weakening of the Azores high-pressure and by a strong low pressure located between Iceland and the Azores Islands;
- Westerly (W) represented situations characterized by the establishment of the

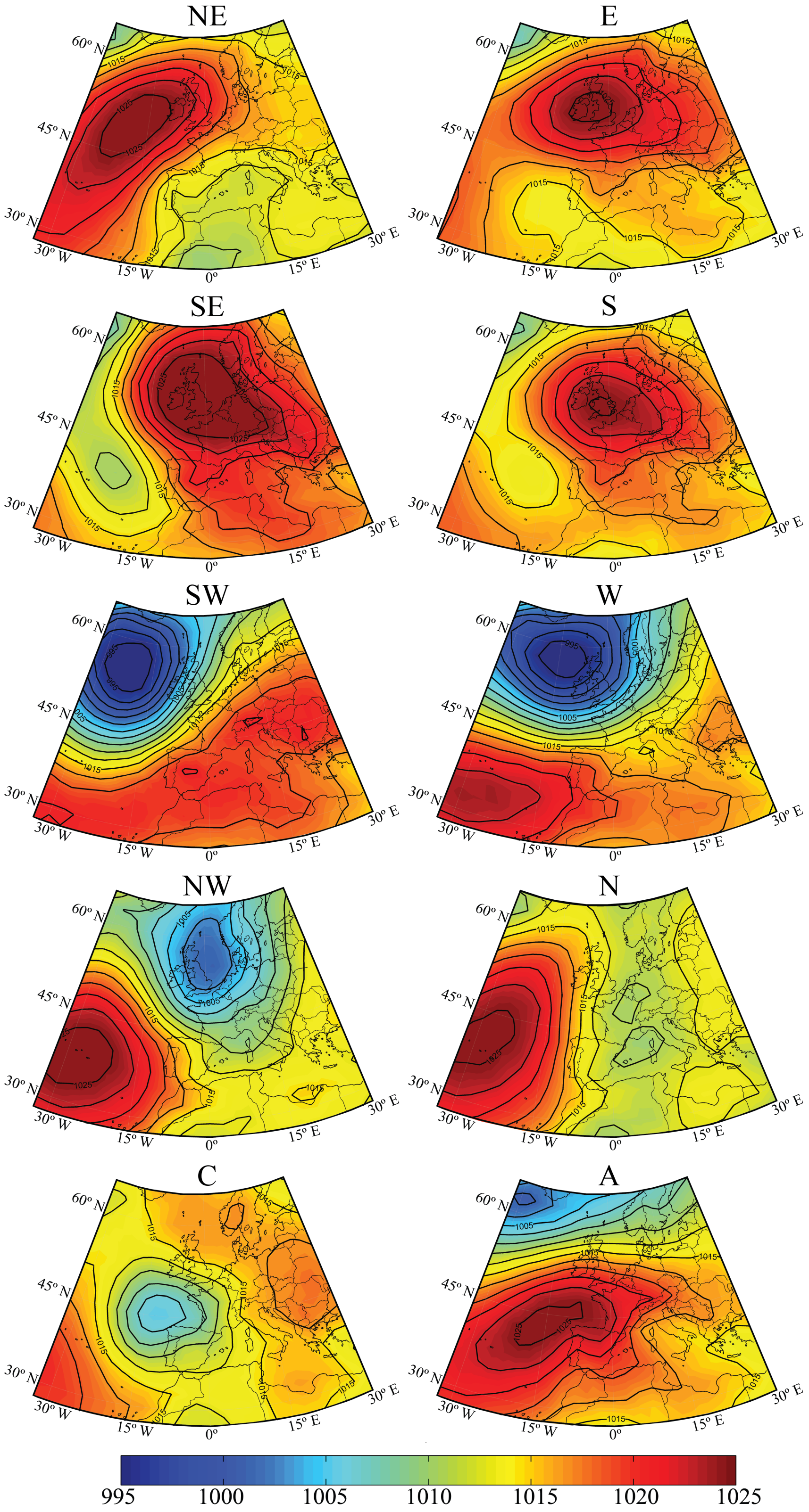

Figure 4.2: Composite maps of SLP fields for 8 directional weather types (NE, E, SE, S, SW, W, NW and N) and 2 vorticity weather types (C and A), for 1998-2007.

Azores high-pressure around 30 °N and by the presence of deep low-pressure centered south of Iceland;

- North-Westerly (NW) days were characterized by the presence of the Azores high-pressure centered over the Azores Islands and a low-pressure centered off northern France;
- Northerly (N) represents a situation characterized by the Azores high-pressure centered north of the Azores Islands;
- Cyclonic (C) days correspond to relatively strong low-pressure systems located close or over the northwestern Portuguese coast. The wind direction depends on the position of the low-pressure, but on the overall, westerly winds tend to dominate towards southern Portugal. These days are often characterized by strong winds;
- Anticyclonic (A) days are characterized by an extended high-pressure center between the IP and the Azores Islands. Conditions along the IP coast are generally characterized by south-westerly winds in western Iberia, while easterlies winds can be found in the northern IP coast. Nevertheless, this type is generally characterized by lighter winds, resulting from small pressure gradients associated with the close position of the high pressure system.

In order to understand the monthly variability of the CWTs, the monthly mean relative frequency of each synoptic weather type was computed for the period 1998-2007 (Figure 4.3). Results show that weather types NE and N have maxima frequencies in spring and summer, with values above the annual average (0.34 and 0.25%). During autumn and winter frequencies are below the annual average. NW weather type tends to appear with a similar frequency in all months (close to the annual average 0.46%), except for January, February and March, that have frequencies of 0.25%. E, SE and S types occur with a low frequency throughout the year, being the annual averages 0.21, 0.13 and 0.24%, respectively. Maxima frequencies occur in May, December and May/September for the E, SE and S types, respectively. SW and W weather types present maxima frequencies for winter, showing a seasonal behaviour opposite to NE type. Finally, A weather type is the most frequent for all months, with maxima

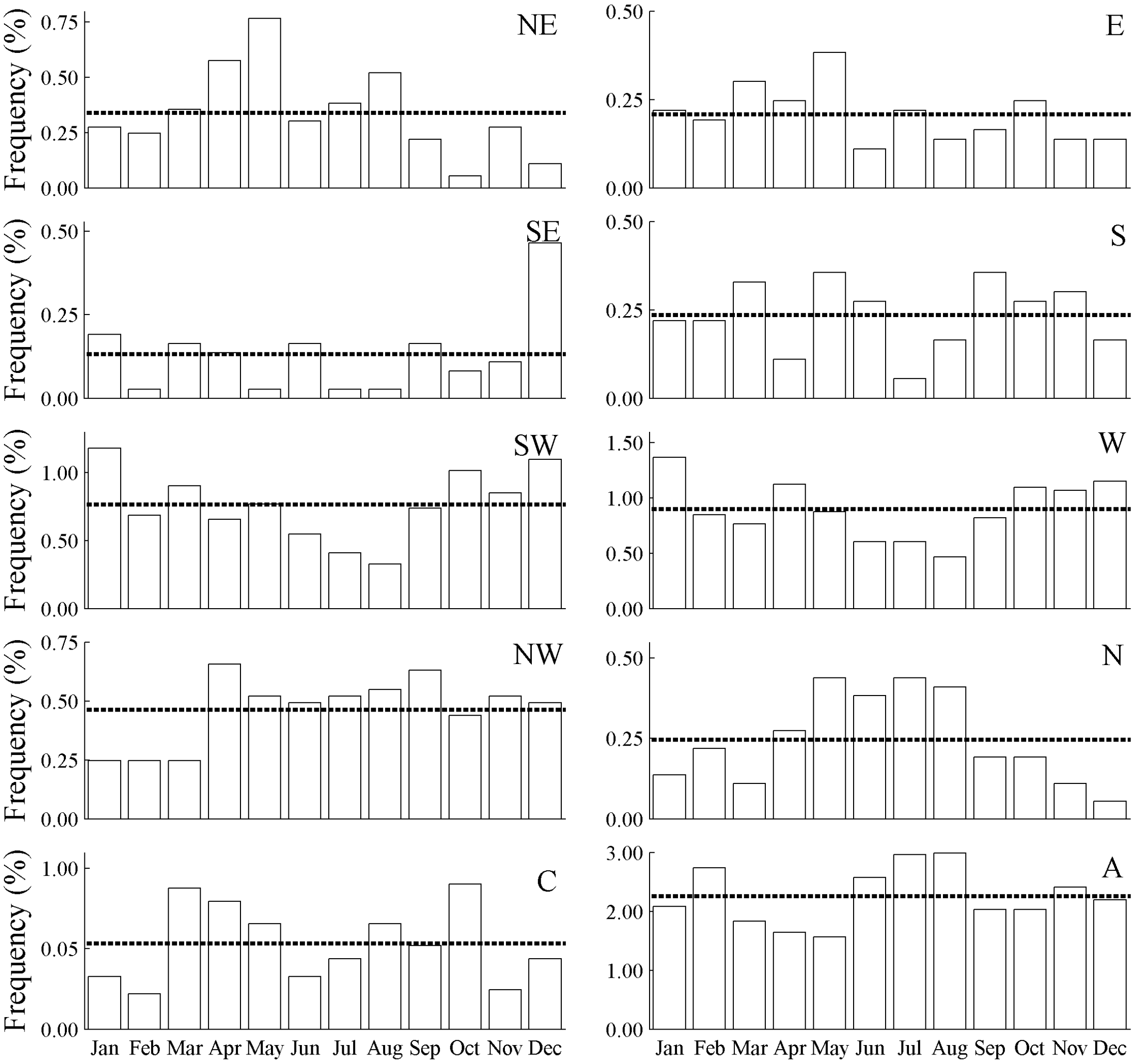

Figure 4.3: Monthly mean frequency (%) of the synoptic weather types for the period 1998-2007. The dashed line represents the annual average.

occurring in summer months (June, July and August) and February, with values above the annual average (2.3%). Otherwise, C type reaches its maximum in March, April, May and October, meaning that this weather type tends to appear in spring and autumn. These results are in accordance with Lorenzo et al. (2008).

Once the probability analysis will be performed considering two seasons (April-September and October-March), CWTs frequency (%) is also computed for these two seasons, with results showed in Figure 4.4.

Vorticity weather types (C and A) were the most frequent for both seasons analysed, showing frequency values of approximately 27% for anticyclonic type and 6-7% for cyclonic type. dePablo et al. (2009) obtained a higher frequency (34%) for A type

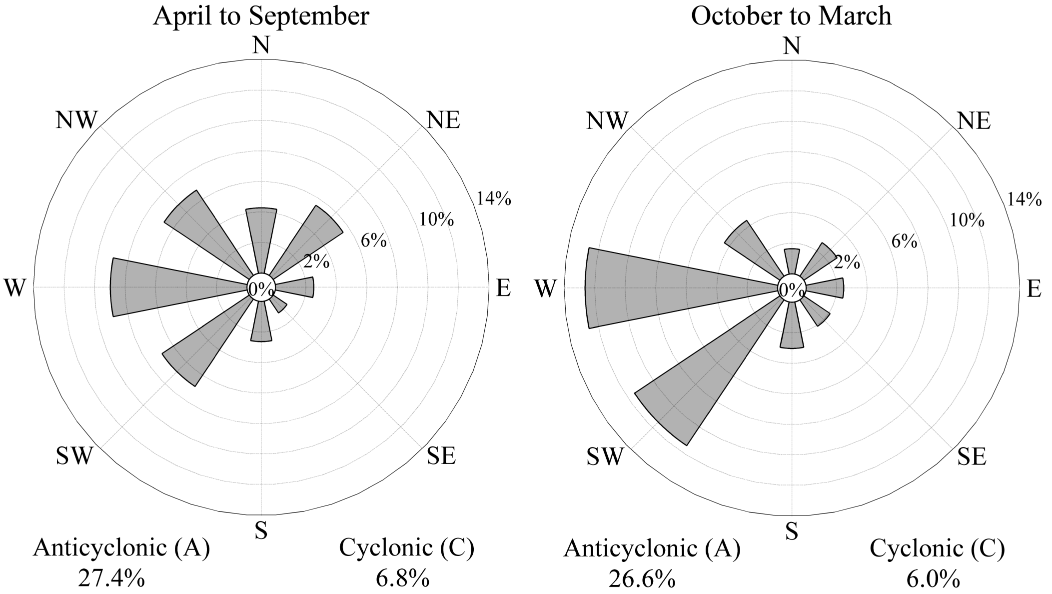

Figure 4.4: Circulation weather types frequency (%) during the April-September (left) and October to March (right) months for the period 1998-2007.

during winter season for the period 1995-2005 over the whole IP. Differences are due to the fact that those authors considered only two months as representative of winter (November and December), while in this study a period of six months (October to March) was considered. Regarding the directional CWTs, the most frequent is W for both seasons, with a percentage of occurrence of approximately 9% for April-September season and higher than 12% for October-March. Lorenzo et al. (2008) also found that W type is significant in autumn and winter, considering a different period. The least frequent weather types are SE (1.1%) along with E (2.5%) for summer and N (1.6%) and SE (2.1%) for winter season. Relative to CWTs with a north component, the most frequent is NW with a percentage of approximately 6.7% and higher than 4.0% for April-September and October-March, respectively. NE and N weather types also present high frequency of occurrence during summer (5.5% and 4.3%, respectively). Finally, for weather types with a south component it is observed that the SW is the most frequent occurring 6.8% of the days analysed between April and September and 11.5% between October and March. These results are similar to those obtained by Lorenzo et al. (2008) and Ramos et al. (2013).

4.3.2 UI and Chl-a concentration

Figure 4.5 illustrates the monthly mean evolution of UI and Chl-a concentration spatial average for each coastal segment for the period 1998-2007. The UI and Chl-a values tended to be higher along the western coastal segment (black line) than along the intermediate (grey line) and northern (black dashed line) segments throughout the whole period. Maximum UI values were observed in spring-summer and minimum in autumn-winter along the three regions, however remarkable differences were found among years (Figure 4.5a). Particularly, 2001 and 2003 were characterized by the lowest UI values during winter along the three coastal segments, with values lower than -1000 m^3 s^{-1} km^{-1}, which are related with the meteorological conditions (intense southerly winds). In response to these adverse weather conditions and high rainfall during the winter of these two years, Chl-a concentration is high at the three coastal segments, with maxima values at western (between 3 and 4 mg m^{-3}). Conversely, for the majority of the period analysed high values of UI were found during summer, occurring the highest (1200 m^3 s^{-1} km^{-1}) at western coastal segment in 1998. These high UI values are associated with high Chl-a concentrations (Figure 4.5b), with values of approximately 4 mg m^{-3}, at the western coastal segment. Differences were also observed on the UI signal amplitude. Thus, 2004 and 2005 represented the lowest amplitudes

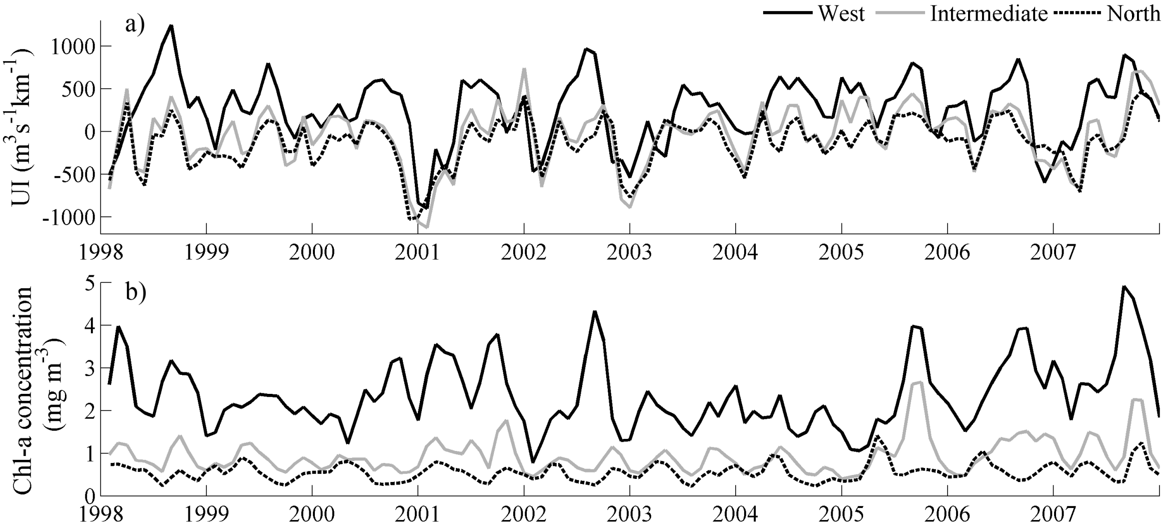

Figure 4.5: Mean evolution of the spatial average of a) UI (m^3 s^{-1} km^{-1}) and b) Chl-a concentration (mg m^{-3}) from 1998 to 2007, at western, intermediate and northern coastal segments.

(approximately 600 m^3 s^{-1} km^{-1}) with positive values for most of the years at western and intermediate coastal segments. At northern coastal segment, the amplitude is also low for these two years (approximately 400 m^3 s^{-1} km^{-1}), showing small variations between winter and summer months (Figure 4.5a).

4.3.3 Weather types implications on upwelling and ecosystem productivity

Table 4.1 shows the probability of UI and Chl-a concentration to exceed the threshold value, defined in Section 4.2, given a specific weather type, for the period 1998-2007 measured at each coastal segment.

When no values appear in Table 4.1 that means UI or Chl-a never exceed the threshold value when the considered weather type occurred.

The conditional probability of UI to exceed the threshold value given the occurrence of A type was important at the three coastal segments and for both seasons. Values between 30-60% for spring-summer season and 30-50% for autumn-winter season were identified. The probability of Chl-a concentration to exceed its mean value was lower than 20% at the three coastal segments and both seasons. The CWT A was generally characterized by an extended high pressure centred between the IP and Azores islands, promoting light northeasterly winds at western coastal segment and easterly winds at intermediate and northern coastal segments (Figure 4.2), and therefore generating weak upwelling events.

Concerning C type, upwelling favourable conditions were only observed at northern coastal segment, although with low probabilities (approximately 5% for summer). In contrast, the probability of Chl-a concentration to exceed its mean value was 15 and 21% for summer and winter, respectively. Indeed, according to Figure 4.2, C type was characterized by a relatively strong low pressure system located close or over the western IP coast. The wind direction depends on the position of the low pressure, but generally strong westerly winds (which are upwelling unfavourable) tended to dominate at western and southwesterly at intermediate and northern coastal segments. Therefore, phytoplankton presence at northern coastal segment may be due to the rivers discharging in this area, once Lorenzo et al. (2008) associated the C weather type with intense precipitation events along the Galician coast.

Between April and September, NE weather type presented high probability

Table 4.1: Probability (%) of UI and Chl-a concentration to exceed the threshold value given the occurrence of a specified weather type, between April-September and October-March seasons, from 1998 to 2007, and for the three coastal segments: WCS - western coastal segment, ICS - intermediate coastal segment and NCS - northern coastal segment.

	April-September	**NE**	**E**	**SE**	**S**	**SW**	**W**	**NW**	**N**	**C**	**A**
UI	WCS	81						28	75		57
	ICS	100	100		100				75		48
	NCS	90	100		100					5	32
	October-March	**NE**	**E**	**SE**	**S**	**SW**	**W**	**NW**	**N**	**C**	**A**
	WCS	100	50					43	100		33
	ICS	67	100	55	100						51
	NCS	33	100	90	100						50
Chl-a	**April-September**	**NE**	**E**	**SE**	**S**	**SW**	**W**	**NW**	**N**	**C**	**A**
	WCS	28	26		17	13		14	44	13	20
	ICS	20	50		33	4	3	7	24	9	11
	NCS	8	13		50	21	4		8	15	6
	October-March	**NE**	**E**	**SE**	**S**	**SW**	**W**	**NW**	**N**	**C**	**A**
	WCS				20	19	8	34		10	18
	ICS		26	26	40	19	12			18	15
	NCS		25	25	40	9	10			21	12

of UI (Chl-a) to exceed the threshold value: 81%, 100% and 90% (28%, 20% and 8%) for western, intermediate and northern coastal segments, respectively. Upwelling probability at intermediate coastal segment was the highest because of its orientation, leading to an offshore Ekman transport almost perpendicular to the coast which favours the upwelling. From October to March upwelling favourable conditions under the NE type were also observed at the three coastal segments with the highest conditional probability values (100 %) for western coastal segment; nonetheless this weather type presented a lower frequency during winter (about 3%) than during spring-summer. In a study that aimed the use of CWTs to predict upwelling activity, it was found that NE type presents the highest correlations with upwelling along the western coast of IP (0.7 near Rias Baixas) (Ramos et al., 2013).

Under NW weather type, upwelling favourable conditions only occurred at western coastal segment, with probabilities of 28% and 43% for spring-summer and autumn-winter, respectively. Actually, due to the coast alignment, this weather type promotes a displacement of surface waters south-westward, which is upwelling unfavourable along the intermediate and northern coastal segments. Along the western coastal segment the south-westward transport may generate upwelling events. The probability of Chl-a concentration to exceed its mean value at western coastal segment was 14% and 34%, for spring-summer and autumn-winter, respectively. Also, between April and September a probability of 7% was found for Chl-a at intermediate coastal segment.

The probability of UI to exceed the threshold value given the occurrence of N weather type, ranges from 75 to 100% (Table 4.1) at western and intermediate coastal segments, being the highest probability between October and March and along the western coastal segment. Ramos et al. (2013) concluded that the second CWT most related to UI was the N type, with correlations frequently above 0.5 along the western coastal segment. At the northern coastal segment UI never exceeded the threshold value during the occurrence of N weather type. Moreover, Chl-a concentration only exceeded its mean value for spring-summer season and along the western and intermediate coastal segments, with high probabilities, 44 and 24%, respectively. This weather type induced northerly winds all over the region (Figure 4.2), which due to coastal orientation, is upwelling favourable along the western and intermediate coastal segments and therefore increase primary production, and it is unfavourable along the northern.

During winter, besides the observed upwelling favourable conditions along the western coastal segment when N and NE types occurred (Table 4.1), Chl-a concentration never exceeded its mean value. This may happen because when strong winter winds occur (upwelling favourable or not) the water column stability decreases and may dilute phytoplankton blooms. Furthermore, in winter light availability also limits the phytoplankton growth and consequently the Chl-a concentration at the surface. It is also necessary to take into account that the frequency of occurrence for N and NE types during autumn-winter is lower than for spring-summer.

The probability of UI to exceed the threshold value under E weather type is 100%, at intermediate and northern coastal segments and for both seasons considered (Table 4.1). Also, Chl-a probability to exceed the mean value is 50% at intermediate coastal segment and 13% at northern, during summer season, indicating that upwelling events are the main responsible for high Chl-a levels. At western coastal segment UI never exceeds its threshold value between April and September, however between October and March, for 50% of the occurrences, UI exceeds the threshold value. Indeed, although E type is related to offshore flow and upwelling occurrence at western coastal segment, Ramos et al. (2013) also found low correlations between them in summer season. Actually, this type of synoptic conditions generally does not originate intense winds.

S and SE types could generate upwelling favourable conditions at intermediate and northern coastal segments. According to Figure 4.2, S weather type was characterized, on average, by a high pressure system located over central Europe and a low pressure in the Atlantic, showing a similar pattern to the SE type. Therefore, both weather types promote southeasterly winds over the region. Between April and September, when the SE type occurs (that was only 1% of the analysed period) neither UI nor Chl-a exceed the threshold value. On the other hand, high probabilities of upwelling favourable conditions under this weather type were observed at intermediate (55%) and northern (90%) coastal segments from October to March. Also, for this period it was observed that Chl-a concentration exceeded its mean value at both coastal segments, with a probability of approximately 25%. Owing to the orientation of the northern coastal segment (parallel to the equator), southeasterly winds are favourable to upwelling conditions along this region producing an offshore movement of surface waters. Along the intermediate coastal segment, SE type was related to a displacement of surface water along this coast, generating upwelling conditions at some places due to the jagged coastline. Taking into account that wind conditions under S type were similar to SE (Figure 4.2), upwelling favourable conditions should also occur along the intermediate and northern coastal segments under S type. In fact, the conditional probability of UI to exceed the threshold value during the occurrence of S type was high for both seasons and coastal segments with maximum values (100%) at northern region.

Finally, for SW and W weather types, UI never exceed the threshold value, however, probabilities of Chl-a between 10 and 20% were found for October to March, for the whole region. Chl-a detected during this period was related to river outflow that transports nutrient rich water from land, increasing phytoplankton biomass. Intense southerly and westerly winds originate adverse weather conditions with high rainfall events increasing the rivers discharge into the coast (Alvarez et al., 2005). In fact, Lorenzo et al. (2008) concluded that SW and W regimes are responsible for the vast majority of very intense precipitation events.

4.3.4 Adverse weather conditions influence on Chl-a concentration patterns

Several Chl-a images were analysed during periods in which the meteorological conditions are similar to that observed when SW and W CWTS occur (strong precipitation and therefore high rivers discharge), to further understand the influence of adverse weather conditions on Chl-a concentration patterns at the river's mouth adjacent areas. Five rivers were considered for analysis: Mondego, Douro, Minho, Eume and Nalon.

Therefore, for Minho and Nalon rivers, an image from late October 2002 was chosen as representative of strong discharge (Figure 4.6). The days before to the image were characterized by a strong low pressure located over the British Isles and a weak high pressure system located over the IP. This results in southwesterly winds at western

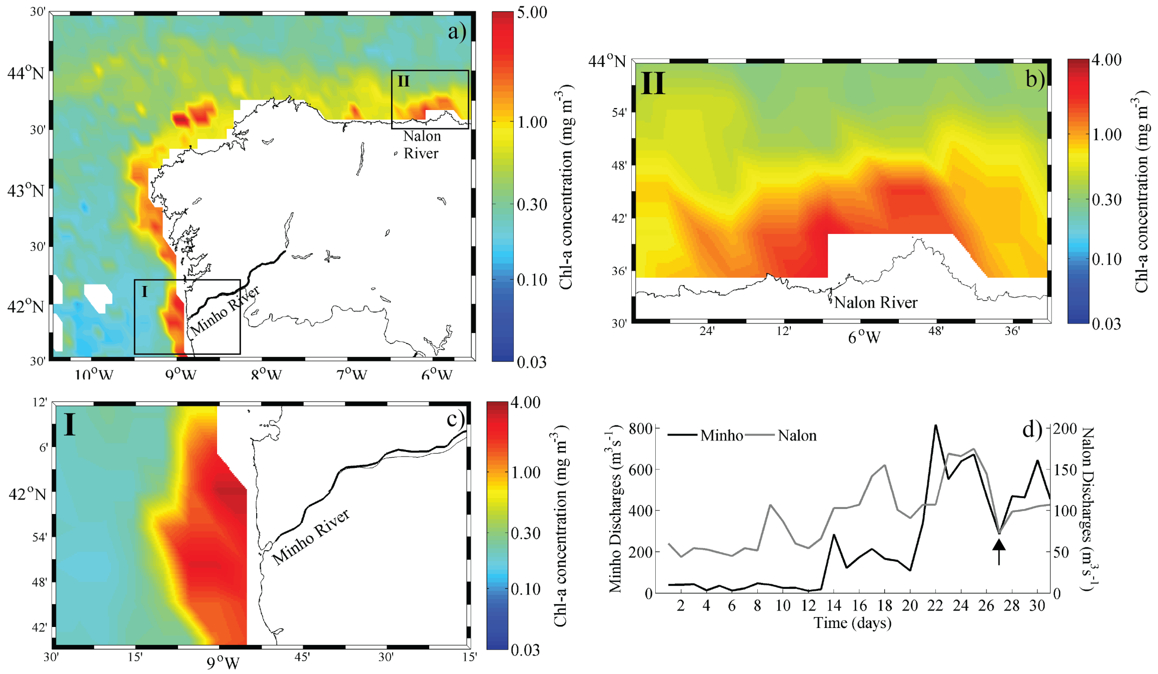

Figure 4.6: a) Chl-a concentration (mg m^{-3}) along Galician coast after a period of high discharge (late October 2002). b) and c) Zoom of the regions II and I and d) discharges (m^3 s^{-1}) for Minho and Nalon rivers. The arrow indicates the timing of Chl-a concentration images.

coastal segment of IP and westerlies at northern. Therefore, meteorological conditions for this period may be, on average, characterized by SW or W weather types that were associated with high precipitation by Lorenzo et al. (2008). The image corresponds to a date after high river discharge for both Nalon (176 m^3 s^{-1}) and Minho (816 m^3 s^{-1}) rivers (Figure 4.6).

Results reveal that Chl-a concentration was locally related with river discharges, which affect Chl-a signal in areas under the influence of riverine plumes. For Nalon, the highest Chl-a concentrations ($>$ 2 mg m^{-3}) were observed near its mouth, being diluted with distance. Its influence was detected within a radius of approximately 35 km along the coast. The signal of Minho discharge was observed within a radius of approximately 30 km along the coast, being the maximum Chl-a concentration detected near its mouth, with values higher than 3 mg m^{-3}. Indeed, according to a recent study the Minho estuarine plume reaches Rias Baixas when wind blows eastward and favours the accumulation of freshwater outside its mouth (Sousa et al., 2014a).

For Eume, Mondego and Douro rivers another period was chosen (February 2001) because there are missing values in their adjacent area for October 2002. The weather conditions for February 2001 are similar to those observed at October 2002, with a strong low pressure located south of Iceland and high pressure over the IP, resulting in southwesterly winds at both northern and western coastal segments of IP. 2001 winter was characterized by intense southerly winds which favour downwelling over the shelf (Alvarez-Salgado et al., 2003), originating adverse weather conditions with high rainfall events (Alvarez et al., 2005). For February 2001, Eume discharges reached a maximum of 45 m^3 s^{-1}, Douro of 8600 m^3 s^{-1} and Mondego of 600 m^{3}s^{-1}, being the Chl-a images analysed after these high discharges (Figure 4.7). As a result of these strong discharges, values from 7 mg m^{-3} near coast to 1 mg m^{-3} at 10 °W are observed in the region (Figure 4.7a).

Regarding Eume River adjacent zone, Chl-a concentrations of 4 mg m^{-3} were found near its mouth, decreasing to values lower than 2 mg m^{-3} with distance. The influence of its plume is detected only within a radius of approximately 12 km. Indeed, Eume River has a very low discharge (Figure 4.7b). Chl-a concentrations between 4 and 6 mg m^{-3} were observed in the adjacent area of Mondego river, with the maximum Chl-a located upstream its mouth. Its influence could be detected up to 50 km northward. Chl-a

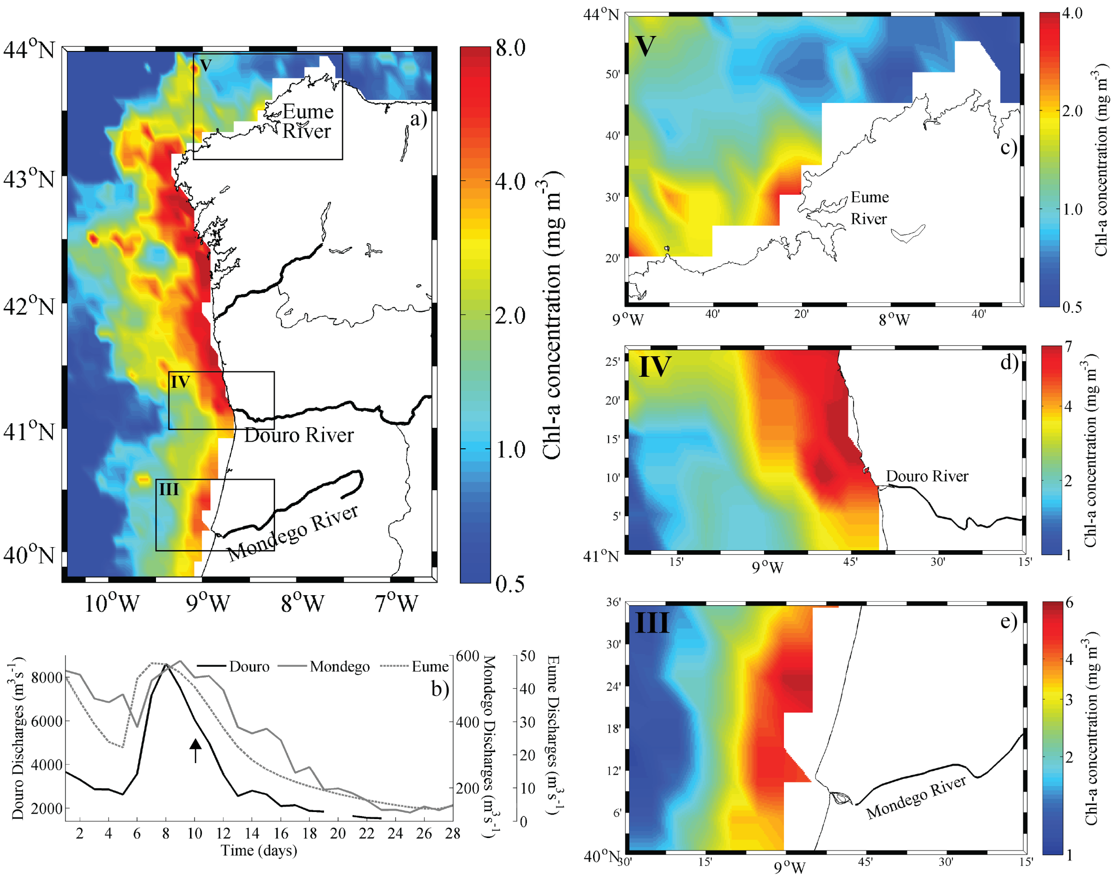

Figure 4.7: a) Chl-a concentration (mg m^{-3}) along the western and intermediate coastal segments of IP after a period of high discharge (middle February 2001). b) Discharges (m^3 s^{-1}) for Douro and Mondego and Eume rivers. The arrow indicates the timing of Chl-a concentration images. c), d) and e) Zoom of the regions V, IV and III.

concentration in the adjacent area of Douro River ranges from 7 mg m^{-3} upstream its mouth and less than 4 mg m^{-3} westward. The highest Chl-a concentrations are confined to coast, expanding in the alongshore directions and interacting with Minho plume, which is in agreement with the results reported by Mendes et al. (2014).

4.4 Conclusions

The main aim of this study was to evaluate and quantify the influence of meteorological conditions (through atmospheric conditions identified, CWTs) on upwelling variability and Chl-a concentration along the IP coast.

The study began by identifying the main CWT along the IP and its monthly frequency of occurrence during the period of 1998-2007. Afterwards, the frequencies for spring and summer seasons were computed and the link between the atmospheric conditions identified (CWTs) and upwelling and Chl-a conditions were established for the period 1998-2007. Results has shown the following:

- The weather types most favourable to the occurrence of upwelling and primary production were different for each coastal segment under analysis, depending on the coastline orientation. For western coastal segment north component circulation weather types (N, NE and NW) induced most of the times upwelling and phytoplankton generation. It is noteworthy that during winter, when SW and W weather types occur (recurrent, considering a frequency higher than 10%), upwelling was never observed; however Chl-a concentrations higher than it mean value occurs with probabilities between 5 and 17%. Therefore, in this case, the existing Chl-a in ocean surface is related with the rivers outflow that transports CDOM;
- At intermediate coastal segment, upwelling occurred essentially under NE, E, S and N circulation weather types during spring and summer. A probability of 75% for N and 100% for the other three CWTs was found as well as an offshore surface transport almost perpendicular to coast, favouring upwelling and generating high rates of phytoplankton at the surface;
- Finally, at northern coastal segment and for both seasons, south circulation weather type (S) induced significant upwelling generation (probability of 100%). Indeed, due to the coastline orientation (parallel to the equator) S type can generate upwelling favourable conditions transporting nutrient-rich water from lower depths to the surface and thus generating high primary production. The probabilities of upwelling occurrence under NE and E circulation weather types were also high (90-100%) for summer season, being the probability of Chl-a to exceed its mean value under these conditions between 13% and 20%.

These novel results are of major relevance for this region considering that changes in future CWTs frequency along the northwestern coast of IP for the end of the 21st century were predicted by Lorenzo et al. (2011). Results showed an increase in NE and a decrease in C, W and SW circulation types in spring and summer months. Moreover, as changes in future circulation weather types are being accurately predicted (Lorenzo et al., 2011), and taking into account the probabilities obtained in this work, changes in the probability of upwelling and primary production occurrence can be inferred from them. Therefore, the new results obtained in this study provide valuable information about the local relationship among CWTs, upwelling occurrence and Chl-a over the last decades, which may facilitate the prediction of future changes on primary production along the northwestern coast of IP.

Chapter 5

Numerical model

5.1 Introduction

To study the biogeochemical processes along the northwestern coast of IP, a coupled circulation and biogeochemical model was implemented. This model constitutes a valuable tool, allowing to complement observational gaps and provide continuously estimates and forecasts of coastal ocean state. However, modelling ocean/coastal biogeochemistry is a challenging task, due to the frequent lack of all the necessary data, high spatial and temporal variability of properties and the enormous number of processes that are involved. Moreover, biogeochemical properties are strongly dependent from hydrodynamics, and therefore an ocean circulation model able to accurately reproduce the variability of currents, salinity and water temperature is also required.

The numerical model used in this work is MOHID (www.mohid.com) (Martins et al., 2001). This model has been applied to several different coastal and estuarine areas, showing ability to simulate flows in shallow systems as well as to study the western Iberian coastal circulation. Recently, Sousa et al. (2014a,b) implemented MOHID to simulate the Minho River plume intrusion as well as its influence on Rias Baixas. Along the Portuguese coast, MOHID has been applied to coastal lagoons: Ria de Aveiro (Vaz et al., 2005; Picado et al., 2013) and Ria Formosa (Martins et al., 2004) and estuaries: Tagus (Vaz and Dias, 2014) and Sado (Martins et al., 2001). Regarding the biogeochemical processes, a few works have been carried out with MOHID. For instance, Vaz et al. (2015) used MOHID to simulate SST and chlorophyll patterns in an estuary-coastal system adjacent to Tagus estuary, and Mateus et al. (2012b) studied the influence of physical, chemical and environmental parameters on the biogeochemistry of the Tagus estuary. Moreover, Mateus et al. (2012a) developed an operational model for the west Iberian coast (MOHID-PCOMS), where physical and biogeochemical properties are available, and may be used as model forcing or boundary conditions.

Here, the main objective is the implementation and validation of a coupled circulation and biogeochemical configuration with MOHID along the northwestern coast of IP, using a downscalling methodology with two nested domains. The first domain is a 2D (two dimensional) barotropic tidal model, while the second domain is 3D (three dimensional) baroclinic and simulates hydrodynamic, water properties and biogeochemical variables along the region under study. The main differences between this configuration and that presented by Mateus et al. (2012a) are the resolution of the baroclinic domain, which is higher herein, and the boundary conditions source, which in Mateus et al. (2012a) is from Mercator-Océan and here is from MyOcean solution. In addition, in the present work biogeochemical properties are imposed as initial and open boundary conditions. Thus, in this chapter a general overview of the model, regarding the hydrodynamic, lagrangian and biogeochemical models is performed, presenting their main formulations. The nesting modelling methodology developed to reproduce the biogeochemical dynamics of the study area is also described, as well as the validation of the hydrodynamic and biogeochemical models.

5.2 Hydrodynamic model

MOHID is a free-surface, baroclinic model, which adopts the hydrostatic and Boussinesq approximations. It solves horizontal momentum (ρu and ρv) and the advection-diffusion of water temperature (T) and salinity (S), expressed in the following equations:

$$\frac{\partial}{\partial t}\int_V \vec{v}\,dV + \oint_A (\vec{n}\cdot\vec{v})\vec{v}\,dS + \int_V 2\vec{\Omega}\times\vec{v}\,dV = \oint_A \Big((\vec{n}\cdot\overrightarrow{v_T\nabla})\vec{v} \\ -g(\eta - z)\vec{n} - c(t)\int_z^{\eta}\frac{\rho-\rho_0}{\rho_0}dz\,\vec{n} - \frac{p_{atm}}{\rho_0}\vec{n} + \Phi\vec{n}\Big)dS \qquad (5.1)$$

$$\frac{\partial}{\partial t}\int_V TdV + \oint_A (\overrightarrow{n}\cdot\overrightarrow{v})TdT = \oint_A (\overrightarrow{n}\cdot\overrightarrow{K_T\nabla})TdT + SS_T \tag{5.2}$$

$$\frac{\partial}{\partial t}\int_V SdV + \oint_A (\overrightarrow{n}\cdot\overrightarrow{v})SdS = \oint_A (\overrightarrow{n}\cdot\overrightarrow{K_S\nabla})SdS \tag{5.3}$$

where V is an orientable control volume fixed relative to the reference frame origin, A is its surface and $\overrightarrow{n}$ is its outwards normal vector. SS_T is the source and sink terms of water temperature. K_T and K_S are the water temperature and salinity turbulent diffusion vectors. p_{atm} is the atmospheric pressure, Φ is the gravitational potential, which is the sum of the Earth gravitational potential with the astronomical tide potential. g is the vertical component of the gravitational pull near the Earth's surface, where it is considered constant. $\frac{\partial}{\partial t}$ is the explicit time derivative, z is the vertical coordinate and $\overrightarrow{\nabla}$ is the gradient operator. $\overrightarrow{v_T\nabla} \equiv \left(v_H\frac{\partial}{\partial x}, v_H\frac{\partial}{\partial y}, v_V\frac{\partial}{\partial z}\right)$ is a vector expressing the combination of the turbulent viscosity vector $\overrightarrow{v_T} = (v_H, v_H, v_V)$ with the gradient operator.

It also solves the equation of continuity, $\partial_x u + \partial_y v + \partial_z w = 0$, to determine the vertical velocity W and the water elevation η. The vertical velocity is obtained by integrating the equation of continuity between the bottom $(-h)$ and the depth z:

$$w(z) - w(-h) = -\Big(\partial_x\int_{-h}^{z} udz + \partial_y\int_{-h}^{z} vdz\Big) \tag{5.4}$$

assuming that $w(-h) = 0$.

The water elevation is obtained by integrating the equation of continuity over the water column (between free surface elevation $\eta(x, y)$ and the bottom (–h)):

$$\partial_t\eta = -\Big(\partial_x\int_{-h}^{\eta} udz + \partial_y\int_{-h}^{\eta} vdz\Big) \tag{5.5}$$

The density (ρ) is solved as function of T, S and pressure (p) through the United Nations Educational, Scientific and Cultural Organization (UNESCO) state equation (Fofonoff and Millard, 1983).

The equations for the vertical turbulent kinetic energy and the eddy dissipation rate due to viscosity are solved using the General Ocean Turbulence Model (GOTM) solver (Burchard, 2002), embedded in the MOHID code (Ruiz-Villareal et al., 2005).

5.3 Lagrangian model

The Lagrangian model is a subset of the MOHID modelling system, that derives from the hydrodynamic information determined by the system and updates the calculations without having the need to solve all the variables at the same time. It uses the concept of passive tracers, characterized by their spatial coordinates (x, y, z). The major factor responsible for particle movement (u_p) is generally the mean velocity (u_M) provided by the model and a small scale random fluctuation (u_F) so that $u_p = u_M + u_F$. The spatial coordinates are given by the definition of velocity:

$$\frac{dx_i}{dt} = u_p(x_i, t) \tag{5.6}$$

where x stands for particle position. This equation is solved using an explicit method:

$$x_i^{t+\Delta t} = x_i^t + \Delta t u_p^t \tag{5.7}$$

The random movement is calculated following the procedure of Allen (1982) and is calculated using the mixing length and the standard deviation of the turbulent velocity component, as given by the turbulence closure of the hydrodynamic model. Particles retain velocity during the necessary time to perform the random movement, which is dependent on the local turbulent mixing length.

5.4 Biogeochemical model

The biogeochemical model uses parameterizations adapted from EPA (1985), including the nitrogen, oxygen, phosphorus and silica cycles.

Nitrogen and phosphorus biogeochemical cycles are simulated explicitly, and constant Carbon:Nitrogen:Phosphorous (C:N:P) ratios were assumed for organic matter and plankton. Model includes as state variables nutrients (nitrate, ammonia, and phosphate), phytoplankton, zooplankton, dissolved and particulate organic matter.

The evolution over time of each state variable can be described by the general advection–diffusion equation:

$$\frac{\partial P}{\partial t} + u_j \frac{\partial P}{\partial x_j} = \frac{\partial}{\partial x_j}\Big(K \frac{\partial P}{\partial x_j}\Big) + FP \tag{5.8}$$

where, P is the concentration, j the index for the correspondent Cartesian axis (x, y, z), K the turbulent mass diffusion coefficient (horizontal/vertical) and FP is the source or sink term.

The growth and decay of phytoplankton is developed with the following considerations (Figure 5.1):

- Phytoplankton consumes inorganic nutrients (ammonia and nitrate from the nitrogen cycle and inorganic phosphorus from the phosphorus cycle) depending on their availability.
- Light availability (as a source of energy for photosynthesis) influences the growth of phytoplankton.
- Dissolved oxygen is produced during photosynthesis.
- Respiration process consumes oxygen and produces ammonia.
- Excretion of phytoplankton produces dissolved organic material (DOM: Refractory Dissolved Organic Nitrogen, Non-Refractory Dissolved Organic Nitrogen, Refractory Dissolved Organic Phosphorus and Non-Refractory Dissolved Organic Phosphorus).
- By mortality, phytoplankton increases DOM and particulate organic material (POM: Particulate Organic Nitrogen and Particulate Organic Phosphorus).
- Through mineralization, DOM and POM are converted into inorganic nutrients that are available again for primary production.
- Phytoplankton concentration decreases by the grazing of phytoplankton by zooplankton.

Primary production of phytoplankton follows an exponential growth model, where temporal variation of biomass depends on available biomass, nutrients and light

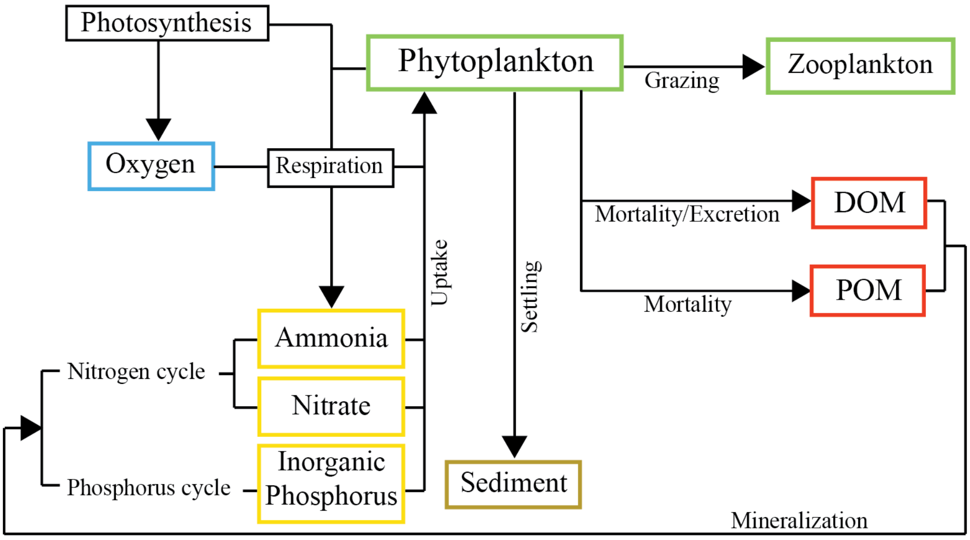

Figure 5.1: Phytoplankton cycle.

(Gotelli, 1995). This process is governed by equation:

$$\frac{\partial \phi_X}{\partial t} = (\mu_X - r_X - eX_X - m_X - G_X)\phi_X \tag{5.9}$$

where t is the time (day), ϕ_X is the biomass (gC m^{-3} for phytoplankton) and other terms can be seen as net production rate, composed by: μ_X gross growth rate (day^{-1}); r_X total respiration rate (day^{-1}); eX_X excretion rate (day^{-1}); m_X natural mortality rate (non-predatory) (day^{-1}); and G_X grazing rate (day^{-1}). Respiration, excretion and mortality formulations can be found in EPA (1985). Growth rates are determined by external concentration of available nutrients, and they are linearly dependent on nutrient uptake rates. Thus, the redfield ratio is assumed for C:N:P ratio (106:16:1, average in marine environment) for phytoplankton, zooplankton and organic matter. Model uses a fixed stoichiometry approach, where elemental composition of algal cells remains constant.

Photosynthetic organisms only exists where light is available and able to reach their cells. Therefore, phytoplankton is limited to the upper layers of the water column (photic zone). The model assumes that the light extinction in depth follows the decay given by Lambert-Beer's Law:

$$I(z) = I_0 e^{-k_L z} \tag{5.10}$$

where I (W m^{-2}) is the light intensity at a given depth z (m), I_0 the light intensity at the surface and k_L the light extinction coefficient (m^{-1}).

5.5 Discretization

5.5.1 Spatial discretization

MOHID uses a finite volume approach (Chippada et al., 1998; Martins et al., 2001) to discretize the equations in a structured grid, allowing the application of the model in areas with diverse geometries and horizontal spatial resolutions, and the easy expansion to eventually more adequate coordinate systems (Martins et al., 2001; Mateus et al., 2012a; Vaz, 2007). The geometries supported by MOHID include the sigma, cartesian, lagrangian and fixed depth. All types of vertical coordinates have a wet/dry cell scheme. In the horizontal, the model uses a staggered Arakawa C grid (Arakwa and Lamb, 1977), *i.e.* the horizontal velocities are located in the center of the cell faces and elevation, turbulent magnitudes and any tracer are placed in the element center. In the vertical, a staggered grid is also used, with the vertical velocity, tracers and turbulent magnitudes placed in the top and bottom faces and horizontal velocities and elevation in the center.

5.5.2 Temporal discretization

The model solves a semi-implicit ADI (Alternating Direction Implicit) algorithm to compute the sea level evolution with two time levels per iteration, following the method proposed by Leendertse (1967). The two components of the horizontal velocity are globally centred in time, $t + dt/2$, leading to a second order time accuracy (Martins et al., 2001). Advection and diffusion of tracer properties such as water temperature and salinity are computed explicitly in the horizontal and implicitly in the vertical, using a Total Variation Diminishing (TVD) Superbee method (Roe, 1985).

For baroclinic force, MOHID uses a z-level approach for any type of vertical coordinate. This methodology integrates the horizontal density gradient always in the cartesian space.

5.6 Initial conditions

In the present study a downscaling methodology with two nested domains was developed, being the first domain 2D and the second 3D. At first domain an initial elevation equal to the mean water level of the study region was used as well as a null velocity. At second domain 3D fields of salinity, water temperature and concentration of biogeochemical variables are provided as initial conditions, which were interpolated from an external 3D solution (in this case from MyOcean). A null velocity field is assumed as well as a sea surface height field with null gradient.

5.7 Boundary conditions

MOHID uses five types of boundaries: surface, bottom, lateral closed, lateral opened and moving boundaries.

5.7.1 Surface boundary

At free surface boundary, all advective fluxes across the surface are assumed to be null. This condition is imposed by assuming a null vertical flux ($Wflux$) at the surface:

$$Wflux|_{surface} = 0 \tag{5.11}$$

Diffusive flux of momentum is imposed explicitly by means of wind surface stress, $\overrightarrow{\tau_W}$:

$$\nu \frac{\partial \overrightarrow{v_H}}{\partial z}|_{surface} = \overrightarrow{\tau_W} \tag{5.12}$$

where ν is the vertical eddy viscosity. Wind stress is calculated following a quadratic friction law:

$$\overrightarrow{\tau_W} = C_{10} \rho_a \overrightarrow{W} |\overrightarrow{W}| \tag{5.13}$$

where C_{10} is a drag coefficient function of wind speed (W) measured at a height of 10 m over the sea surface and ρ_a is the air density. C_{10} is computed through the following equations (Large and Pond, 1981):

$$\begin{aligned} C_{10} &= 1.14e^{-3} && \text{W}< 10 \text{ m s}^{-1} \\ C_{10} &= 4.4e^{-4} + 6.5e^{-5}\overrightarrow{W}|\overrightarrow{W}| && 10 < \text{W} < 26 \text{ m s}^{-1} \end{aligned} \tag{5.14}$$

Solar radiation flux of short wavelength is given by Brock (1981) formulation:

$$Q = Q_0 A_t (1 - 0.65 C_n^2)(1 - R_s) \tag{5.15}$$

where Q_0 is the solar radiation flux at the top of atmosphere, A_t is the coefficient for atmospheric transmission, C_n the cloud cover percentage and R_s stands for albedo (0.055).

The net long-wave radiation R_a is calculated using (Swinbank, 1963):

$$R_a = 0.937 \times 10^{-5} \sigma (273.15 + T_a)^6 (1 + 0.17 C_n^2)(1 - R_s) \tag{5.16}$$

where σ is the Stefan-Boltzman constant (5.6697×10^{-8} W m^{-2} K^{-4}) and T_a the air temperature.

The infrared radiation R_{br} is calculated applying the Stefan-Boltzman law:

$$R_{br} = \varepsilon \sigma (273.15 + T)^4 \tag{5.17}$$

where ε is the water emissivity ($\sim$0.97).

The latent H_L and sensible H_S heat fluxes are calculated using the Dalton and Bowen laws:

$$H_L = (19 + 0.95 W^2)(e_{s,w} - r_h e_{s,a}) \tag{5.18}$$

$$H_S = C_b (19 + 0.95 W^2)(T - T_a) \tag{5.19}$$

where $e_{s,w}$ is the saturated water pressure, r_h is the relative humidity, $e_{s,a}$ is the air saturation pressure, C_b is the Bowen coefficient (0.47 mmHg K^{-1}).

The velocity of oxygen transfer is given by:

$$O_L = \alpha W^{\beta} \tag{5.20}$$

where O_L represents the oxygen transfer velocity, α and β are coefficients dependent on the wind velocity:

$$\begin{aligned} &\alpha = 0.2 \qquad \text{and} \qquad \beta = 1 \qquad \text{W} < 3.5 \text{ m s}^{-1} \\ &\alpha = 0.057 \qquad \text{and} \qquad \beta = 2 \qquad \text{W} > 3.5 \text{ m s}^{-1} \end{aligned} \tag{5.21}$$

Surface boundary conditions are computed by the model from meteorological data/conditions provided by the user, such as wind intensity and direction, air temperature, atmospheric pressure, relative humidity and solar radiation.

5.7.2 Bottom boundary

At bottom, advective fluxes are imposed as null, while diffusive flux of momentum is estimated by means of bottom stress calculated by a non-slip method with a quadratic law that depends on the near-bottom velocity. The diffusive term at bottom is written as:

$$\nu \frac{\partial \overrightarrow{v_H}}{\partial z}|_{bottom} = C_D \overrightarrow{v_H} |\overrightarrow{v_H}| \tag{5.22}$$

where C_D is the bottom drag coefficient which is computed through:

$$C_D = \left(\frac{k_c}{log\left(\frac{z+z_0^b}{z_0^b}\right)} \right)^2 \tag{5.23}$$

where k_c is von Karman constant and z_0^b is the bottom roughness length. In the present implementation a constant bottom roughness length is used and was set to 0.0025 m. For numerical stability reasons, the bottom stress is calculated semi-implicitly. No fluxes of salinity and water temperature are considered at the bottom.

5.7.3 Lateral closed boundaries

Closed boundaries of the domain correspond to land. In this case, an impermeable free slip condition was adopted:

$$\frac{\partial \overrightarrow{v_H}}{\partial \eta} = 0 \tag{5.24}$$

$$\overrightarrow{v} \cdot \overrightarrow{n} = 0 \tag{5.25}$$

Using the finite volume approach, these conditions are implemented specifying zero water fluxes and zero momentum diffusive fluxes for the cell faces in contact with land.

5.7.4 Lateral open boundaries

Two types of lateral open boundaries are considered: ocean and landward boundaries. At the first domain, amplitude and phase of fourteen tidal constituents, from a global solution (Finite Element Solution (FES2004)) are imposed in the oceanic open boundary to simulate the barotropic tidal motion.

The hydrodynamic variables (water levels and velocities) are imposed in the second domain combining the solution from the first domain with an external solution (MyOcean). Specifically, a mathematical sum of both solutions is applied to the second domain using a Flather (1976) radiation scheme. This methodology is adopted due to the low temporal resolution of MyOcean variables. Water temperature, salinity and concentration of phytoplankton, nitrate, inorganic phosphorus and oxygen, provided by an external solution (MyOcean), are also imposed in the second domain. A Flow Relaxation Scheme (FRS) (Martinsen and Engedahl, 1987) is applied to the hydrodynamic composite and to water properties at second domain. The FRS adds small corrections to model predictions by diminishing deviations from the reference solution.

As landward boundary condition, rivers discharge, water temperature, salinity and concentrations of biogeochemical variables are imposed at the second domain for each local estuarine/riverine input.

5.7.5 Moving boundaries

Moving boundaries are closed boundaries whose position changes with time. This type of situation arises in domains with inter-tidal areas, where some points can be alternatively covered or uncovered depending on tidal elevation. Based on the study region characteristics moving boundaries are not used in this study.

5.8 Model setup

5.8.1 Circulation model

As previously referred a coupled circulation and biogeochemical model was implemented in northwestern coast of IP, using a downscalling methodology with two nested domains (Figure 5.2). The first domain (D1) (Figure 5.2a) includes the whole IP, from 33 to 50 °N and 0 to 13 °W, and has a horizontal resolution of 0.06 °. In this domain is used a 2D barotropic tidal model forced by FES2004 global solution (Lyard et al., 2006) using a time step of 120 s and a horizontal eddy viscosity of 60 m^2 s^{-1}. This domain is necessary due to the low temporal resolution (daily) of water levels and velocities available from the adopted external solution (MyOcean), which is insufficient to accurately propagate tide along the study area. Moreover, the first domain is large enough to correct eventual instabilities of the tidal signal in its boundaries.

The second domain (D2) (Figure 5.2b) is a 3D baroclinic model, with a horizontal resolution of 0.03 °, which includes the northwestern coast of IP, from 39.5 to 44.5 °N and 5 to 11 °W. Bathymetry was constructed based on General Bathymetric Chart of the Oceans (GEBCO), with some corrections at the continental shelf. A z-level

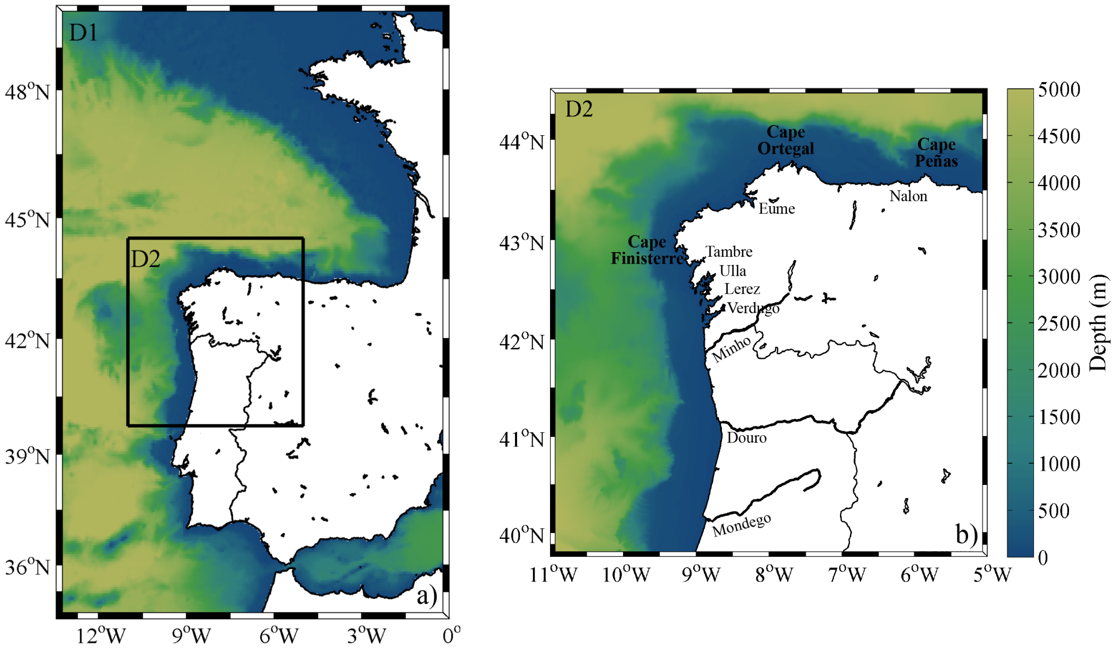

Figure 5.2: MOHID downscalling system with the location of the freshwater sources considered in the model.

vertical discretization was adopted, with 45 vertical layers, being the first seven sigma coordinate layers (near surface) and the remaining 38 cartesian coordinate layers. The time step is set to 30 s and the turbulent horizontal eddy viscosity inside the domain is set to 30 m^2 s^{-1}.

At lateral open boundary D2 is forced using tidal levels computed by D1 along with hydrodynamic and water properties provided by MyOcean Global circulation model (http://marine.copernicus.eu/). MyOcean solution has a horizontal resolution of 0.08 ° and 50 vertical layers, including daily mean fields of water temperature, salinity and currents from the top to the bottom and sea level at surface over the Global Ocean. MyOcean 3D fields were interpolated for D2 grid, using triangulation interpolation in space and linear in the vertical and in time.

The surface boundary condition is imposed using results from Weather Research and Forecasting model (WRF) (http://www.wrf-model.org), provided by the Regional Forecast Agency Meteogalicia (www.meteogalicia.es). WRF solution used herein has a spatial resolution of 0.12 °, and hourly fields of air temperature, atmospheric pressure, wind, solar radiation, relative humidity and mean sea level pressure were interpolated for D2 grid using a triangulation interpolation in space and linear in time.

As landward boundary condition, freshwater input from Mondego, Douro, Minho, Verdugo, Lerez, Ulla, Tambre, Eume and Nalon Rivers was considered (Figure 5.2b). Discharge, water temperature and salinity data for Minho River were provided by Confederacion Hidrográfica del Miño-Sil and for Douro and Mondego by Instituto Nacional da Água. Both datasets have a daily temporal resolution. Given the absence of *in situ* discharges for the remaining rivers during the simulation period (2013 and 2014), predicted data provided by SMHI (E-Hype model) for the period 1980-2009 was monthly averaged and imposed in coastal model (D2).

5.8.2 Biogeochemical model

To simulate the trophic levels and biogeochemical components of the system, the biogeochemical model was implemented coupled to the hydrodynamic. Parametrization of sink and source terms used in the model are listed in Table 5.1.

Table 5.1: Values of the parameters used in the biogeochemical model.

	Parameter	**Units**	**Value**	**Reference**
	Light extinction water coefficient	None	0.08	(EPA, 1985)
Phytoplankton	Maximum gross growth rate at 20 °C	day^{-1}	1.0	Calibrated
	Optimum light intensity for photosynthesis	W m^{-2}	100	(EPA, 1985)
	Endogenous respiration constant	day^{-1}	0.0175	(Portela, 1996)
	Excretion rate	None	0.07	(Portela, 1996)
	Maximum mortality rate at 20°C	day^{-1}	0.02	(Portela, 1996)
	Growth limitation by P half-saturation coefficient	mg P l^{-1}	0.001	(Valiela, 1995)
	Growth limitation by N half-saturation coefficient	mg N l^{-1}	0.014	(Valiela, 1995)
	Carbon to chlorophyll ratio	None	30	Calibrated
Zooplankton	Grazing rate on phytoplankton	day^{-1}	0.3	Calibrated
	Half saturation constant for zooplankton grazing	mg C l^{-1}	0.85	(Pina, 2001)
	Minimum prey concentration for zooplankton grazing	mg C l^{-1}	0.045	Calibrated
	Assimilation efficiency coefficient	None	0.80	(Pina, 2001)
	Mortality rate	day^{-1}	0.09	(EPA, 1985)
Oxygen	Oxygen/Carbon ratio in CO$_2$	None	1.28	(Pina, 2001)
	Oxygen/nitrogen ratio in nitrate	None	3.43	(Pina, 2001)
	Oxygen/nitrogen ratio in phosphate	None	2.06	(Pina, 2001)
	Organic matter nitrogen/carbon ratio (redfield)	None	0.18	(Pina, 2001)
	Organic matter phosphorus/carbon ratio (redfield)	None	0.024	(Pina, 2001)
	Photosynthesis oxygen/carbon ratio	None	2.67	(Valiela, 1995)
Nitrogen	Nitritication rate at 20 °C	day^{-1}	0.06	(Portela, 1996)
	Nitrification rate temperature coefficient	None	1.08	(EPA, 1985)
	Denitrification rate at 20 °C	day^{-1}	0.125	(EPA, 1985)
	Denitrification rate temperature coefficient	None	1.045	(EPA, 1985)
	Half saturation constant for nitrification oxygen limitation	mg O$_2$ l^{-1}	2.0	(EPA, 1985)
	Half saturation constant for denitrification oxygen limitation	mg O$_2$ l^{-1}	0.1	Calibrated
Phosphorus	Mineralization rate of dissolved organic phosphorus at 20 °C	day^{-1}	0.1	Calibrated
	Temperature coefficient for mineralization rate of dissolved organic phosphorus	None	1.06	(Valiela, 1995)

Initial and boundary conditions for the ecological model were supplied by MyOcean solution: weekly 3D fields (50 vertical layers) of nitrate, inorganic phosphorus, oxygen and phytoplankton with a horizontal resolution of 0.5 ° are used in the coastal model (D2).

For landward boundary, nitrate and phosphate concentrations were provided by SMHI for the period 1999-2009 for all rivers considered. Once simulation period (2013 and 2014) is not included in the data provided, a statistical analysis was performed for Mondego, Minho and Douro Rivers, using the information of discharges for the simulation period as well as nutrients concentration and discharges for 1999-2009. For Eume, Ulla, Tambre, Verdugo, Lerez and Nalon Rivers no discharges are available for the simulation period (2013 and 2014), and therefore this statistical analysis was not performed. Instead, monthly mean nitrate and inorganic phosphorus concentrations computed for 1999-2009 were imposed in the model.

For Mondego, Minho and Douro Rivers, nutrients and discharges for the period between 1999 and 2009 were adjusted to probability distributions. The empirical cumulative distribution function was computed according to Kaplan and Meier (1958), while the theoretical distributions were determined by calculating the location, scale and shape parameters of each annual mean series. Distributions considered were: Generalized Extreme Value (GEV), Gamma, Log-normal, Exponential and Weibull. The best distribution was then selected by testing the quality of the fit using two statistical tests (Chi-squared and the Kolmogorov-Smirnov tests) at 95% confidence level and by computing errors between discharges (nutrients) empirical cumulative distribution and each probability cumulative distributions. The best distribution was then selected for each nutrient and discharge for the period 1999-2009. Therefore, monthly mean discharges for the simulation period (2013 or 2014) were computed and, the probability (P) of the 1999-2009 discharge being equal to the 2013/2014 monthly mean was found. Finally, the nutrients concentration imposed in the model corresponds to the concentration with a probability of occurrence P.

5.9 Model validation

5.9.1 Methodology

The vertical structure and thereby the vertical fluxes of organic matter and primary production within estuaries and coastal regions are largely controlled by the vertical mixing and therefore the vertical distribution of turbulence in the water column (Denman and Gargett, 1995). Consequently, before model validation process it is important to test turbulence schemes in the region under study. Thus, in order to choose the best turbulent kinetic energy (TKE) method, the length scale equation and the stability function to be used by the model four simulations were performed (Table 5.2). For these simulations the biogeochemical model is off, *i.e.* only the hydrodynamic, heat and salt transport were considered. Results were then compared with *in situ* data from Argo floats, described later, being an example represented in Figure 5.3.

According to the profiles represented in Figure 5.3 it is observed that both Runs #1 and #3 describe better the thermohaline and pycnocline features than Runs #2 and #4. However, the mean values of water temperature and salinity of Run #1 are closest to the measured values. Therefore, Run #1 parameters gives better agreement with *in situ* (Argo) water temperature and salinity data than other runs. Thus, according to these results and with results from other implementations for the study region (Mateus et al., 2012a; Sousa et al., 2014a,b; Vaz et al., 2015), the parameters of Run #1 will be used hereafter.

Once the best set of parameters was chosen, a fifth simulation was performed covering the years of 2013 and 2014 and considering the biogeochemical model. Therefore, a quantitative validation was performed comparing time series of sea surface elevation (SSE), synthesized from local tidal constituents, for Vigo (V), Leixões (L)

Table 5.2: Simulations characteristics.

	TKE method	**Length Scale Equation**	**Stability function**
Run #1	$k - \epsilon$	Dynamic dissipation rate	Canuto et al. (2001) A
Run #2	Mellor and Yamada (1982)	KL equation	Canuto et al. (2001) A
Run #3	$k - \epsilon$	Dynamic dissipation rate	Canuto et al. (2001) B
Run #4	Mellor and Yamada (1982)	KL equation	Canuto et al. (2001) B

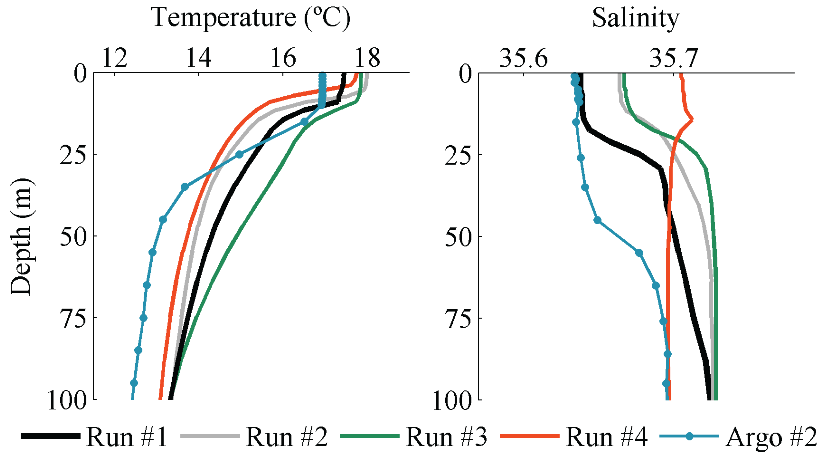

Figure 5.3: Profiles of predicted and *in situ* (Argo # 2) water temperature (°C) and salinity for the runs presented in Table 5.2.

and Aveiro (A) (triangles in Figure 5.4) with model results. Harmonic analysis for the model predictions was also performed and predicted and observed harmonic constants were compared.

Water temperature, salinity and currents from oceanographic moored buoys settled near the Galician shelf (P, B, VS and S - Figure 5.4) and provided by

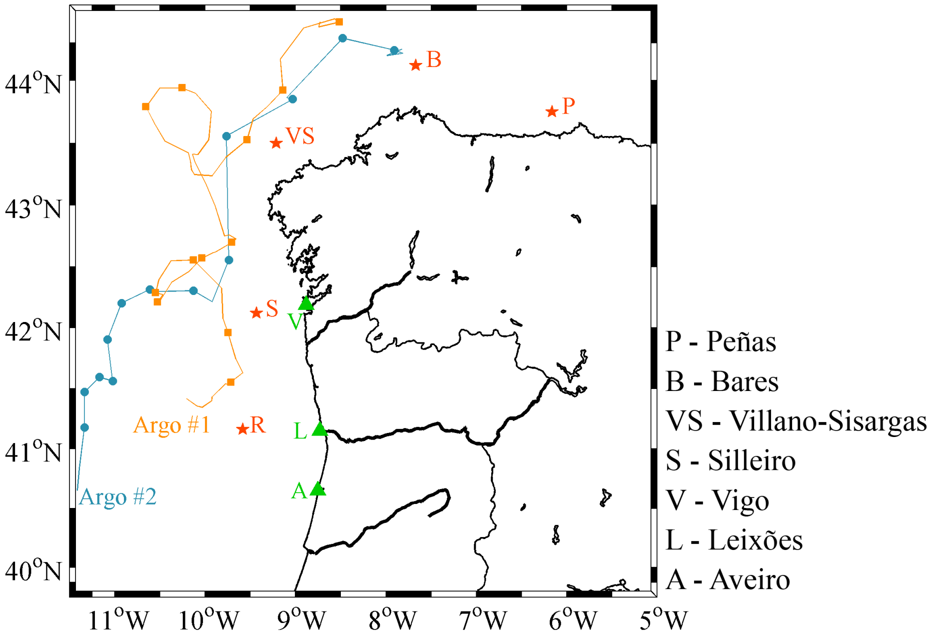

Figure 5.4: Location of the stations used in model validation. Green triangles correspond to buoys with time series of SSE data, red stars to time series of surface water temperature, salinity and currents, orange squares and blue circles to Argo buoys profiles of water temperature, salinity and oxygen.

the Spanish Agency Puertos del Estado (http://www.puertos.es/) were also used to validate the model. Data are available every hour and measured at 3 m depth. Predicted water temperature, currents and Chl-a concentration were also compared with *in situ* data from a buoy located at the surface near Douro River (R) (Figure 5.4). These data was collected and provided in the scope of RAIA project (http://www.observatorioraia.org/mg-web-raia/index.action) and are of free access.

Afterwards, profiles from Argo floats of water temperature, salinity and occasionally oxygen were compared with model predictions. Argo data is freely available in real time downloading (http://www.ifremer.fr/co-argoFloats/).

Argo floats can alter its buoyancy by inflating or deflating a bladder from an oil reservoir, allowing it to submerge to $1-2$ km beneath the surface (phase 1 to 2 in Figure 5.5). It remains at that depth during several days, depending on the buoy characteristics and then descends again a few meters (phase 2 to 4, Figure 5.5). Then, it rises rapidly to the surface (phase 4 to 5, Figure 5.5), measuring physical/biogeochemical properties during its ascent that are stored on board the float. Once it arrives to the surface these data are transmitted to a land station via satellite (phase 5, Figure 5.5). Argo floats can repeat this cycle for many years without human intervention.

During 2013 two floats travelled throughout the study area being their trajectories

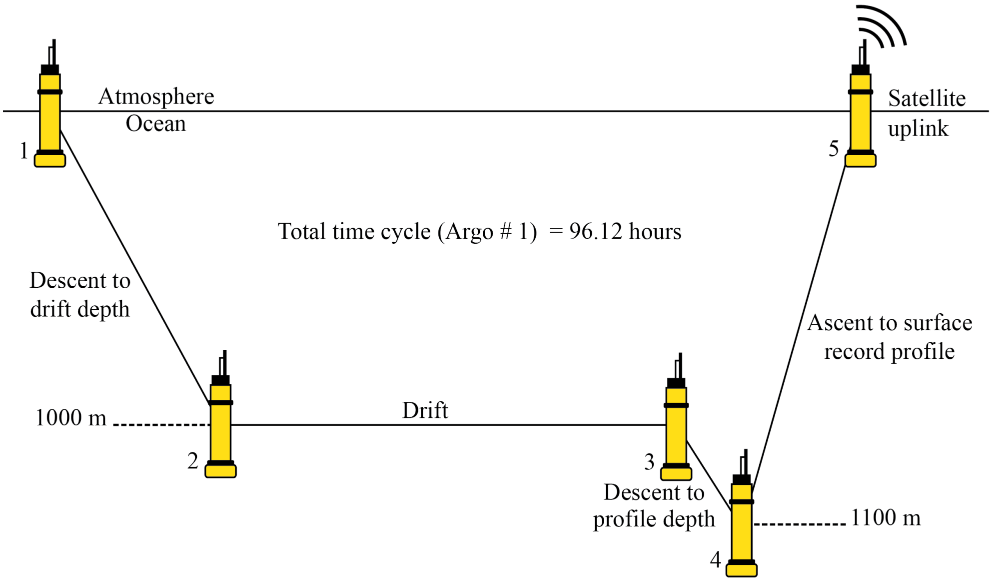

Figure 5.5: Scheme of the Argo float cycle.

represented in Figure 5.4 (Argo # 1 and Argo # 2). Fifty eight profiles for Argo # 1 and twenty one for Argo # 2 were compared with model results, being only twelve profiles for each float analysed here (dots and squares in Figure 5.4).

In order to validate the current velocity at 1000 m depth, an attempt to reproduce the trajectory of Argo # 1 during its drift (Figure 5.5) was performed. The only available information is the position of float at the surface, total time of Argo float cycle (descent + drifting + ascent + surface), which for Argo # 1 is 96.12 hours (for Argo # 2 is 240 hours) and the depth of subsurface drift (1000 m for both floats). With this information, 6 hours for float descent (phase 1 to 2) and 71 hours for the drift (phase 2 to 3) was estimated. Therefore, using Lagrangian model, 100 particles were released at 1000 m at the known position and simulations of 71 hours were performed. The trajectories were averaged and then compared with Argo floats positions.

Finally, SST and Chl-a satellite imagery are also used to validate model (D2). Maps of SST and Chl-a concentrations for winter and summer were compared for the year 2013 and 2014. Differences between predictions and observations were computed along with linear regression parameters, $RMSE$, $BIAS$ and Pearson correlation for all study area, reshaping the matrices of predicted and observed data in two vectors. 8-days composite of SST and Chl-a concentration from the MODIS-AQUA satellite with spatial resolution of 1 km were obtained from the NASA Ocean Colour web site (http://oceancolor.gsfc.nasa.gov). MODIS is a key instrument comprising the Terra (EOS AM) and Aqua (EOS PM) satellites. The orbit is sun-synchronous, meaning that satellite always passes over a particular part of the Earth at about the same local time each day. MODIS Aqua always crosses the equator from south to north at about 1:30 PM local time. One of the instruments on Aqua, measures 36 spectral frequencies of light reflected off the Earth in a 2300 km wide swath along this orbit. Measurements can only be taken in ocean regions that are cloud free.

For a quantitative comparison $BIAS$ and $RMSE$ reliability indices between data and model predictions were computed. $BIAS$ gives an indication of whether the model predictions are systematically overestimating or underestimating observations, being model predictions as better as $BIAS$ is closest to zero. It gives a measure of the model's accuracy and is expressed as:

$$BIAS = \frac{1}{n}\sum_{i=1}^{n}(M_i - D_i) \tag{5.26}$$

The $RMSE$ contributes to evaluate the model precision and is given by:

$$RMSE = \left(\frac{1}{n}\sum_{i=1}^{n}(M_i - D_i)^2\right)^{\frac{1}{2}} \tag{5.27}$$

A $RMSE$ close to zero means a good fit between model predictions and observations. M corresponds to the model predictions, D to data and n is the total number of model-data matches.

5.9.2 Results and discussion

5.9.3 Near coast validation

Once the main objective of this implementation is to evaluate the biogeochemical features related with wind induced coastal upwelling phenomenon along the IP coast, the model predictions were compared with *in situ* data located near coast.

First, times series of SSE at Vigo (V), Leixões (L) and Aveiro (A) stations were compared with model predictions and represented in Figure 5.6.

In general, a good agreement between predicted and synthesized SSE for the three stations is achieved, revealing the model's ability to reproduce data. $RMSE$ between predicted and synthesized SSE is 0.07, 0.09 and 0.13 m, for Vigo, Leixões and Aveiro, respectively. $BIAS$ are close to zero for all stations and therefore model reproduces tide accurately along this coast.

Harmonic analysis was also applied to predict SSE, in order to compare with *in situ* harmonics. Results for the main tidal constituents in the region (M_2, S_2, O_1 and K_1 (Marta-Almeida and Dubert, 2006; Herrera et al., 2008)) are presented in the Table 5.3.

Results reveal that both predicted amplitude and phase for all the constituents are in agreement with observations. For M_2 tidal constituent the major differences were found for Aveiro station, being the amplitude difference of 0.12 m and the phase difference of 4°, which means a delay of 8 minutes between observed and predicted tide. These

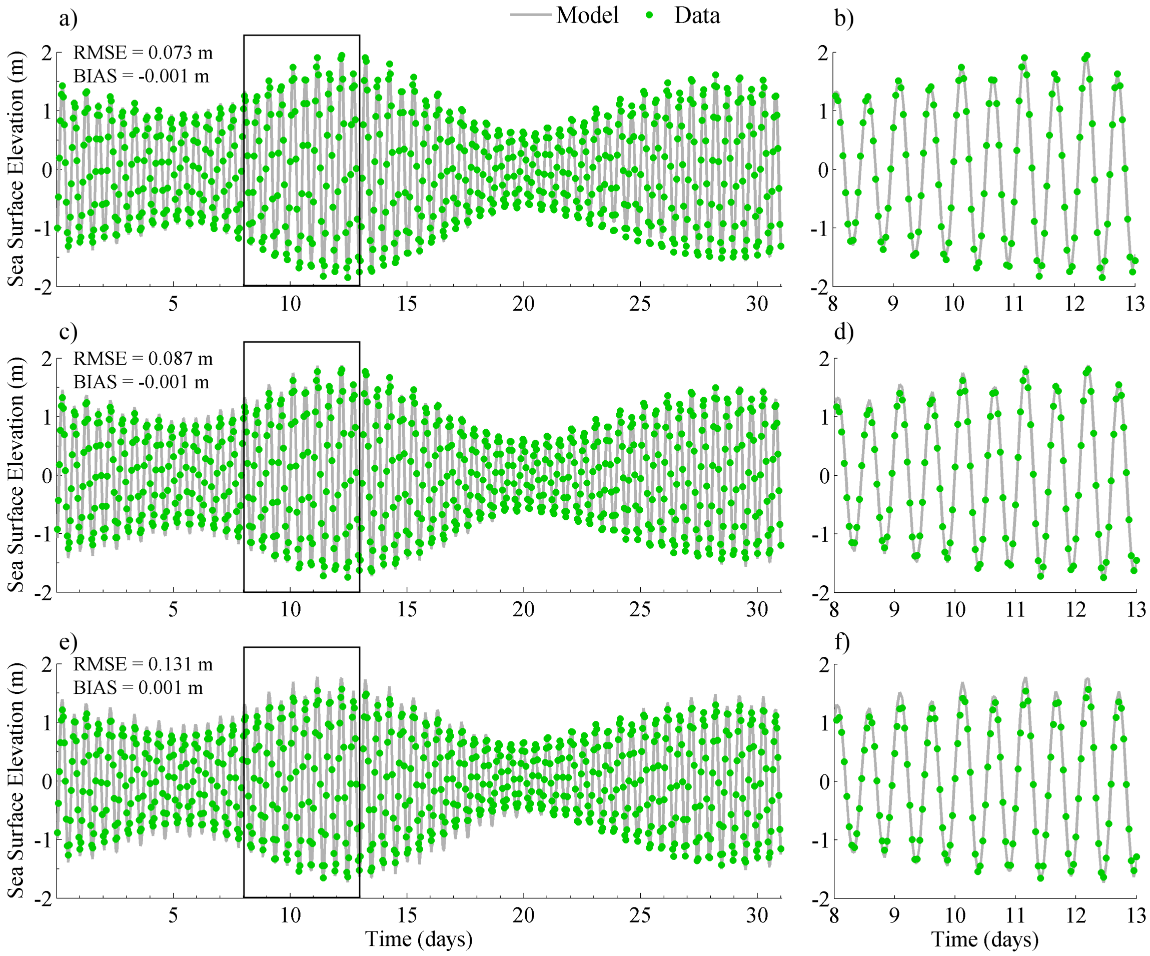

Figure 5.6: Observed and predicted SSE time series at a) Vigo (V), c) Leixões (L) and e) Aveiro (A) stations. Right panel (b, d and f) represents a zoom of the selected area of the respective station.

discrepancies may be due to the fact that station Aveiro is located in Ria de Aveiro inlet and lagoon is not represented by the model grid. Therefore, the nearest model cell, which is at 3 km distance, is chosen to represent Aveiro tide gauge. Moreover, in a study dedicated to assess floods in Ria de Aveiro (Lopes et al., 2013), a $RMSE$ of 0.07 m was obtained and therefore results obtained in this work are considered good. Otherwise, for S_2 constituent major differences between model and data occur at Vigo station, where a delay of 28 minutes and an amplitude difference of 0.02 m is observed. For diurnal constituents, the highest phase difference was observed in Leixões station with a delay of 40 minutes for O_1 and 75 minutes for K_1 tidal constituent, while the amplitude difference between predictions and data is low.

Therefore, results of SSE time series and respective harmonic analysis reveal that

Table 5.3: Harmonic analysis of observed and predicted SSE for Vigo, Leixões and Aveiro stations.

	Station	**Amplitude (m)**			**Phase (°C)**		
		Data	Model	Difference	Data	Model	Difference
M_2	Vigo	1.12	1.13	-0.01	76.74	77.77	-1.03
	Leixões	1.05	1.09	-0.04	76.47	74.60	1.87
	Aveiro	0.96	1.08	-0.12	77.54	73.50	4.04
S_2	Vigo	0.39	0.37	0.02	106.22	119.17	-12.95
	Leixões	0.36	0.36	0.00	104.80	115.66	-10.86
	Aveiro	0.35	0.36	-0.01	108.40	114.38	-5.98
O_1	Vigo	0.07	0.06	0.01	318.66	321.99	-3.33
	Leixões	0.06	0.06	0.00	318.51	309.08	9.43
	Aveiro	0.05	0.05	0.00	318.76	311.50	7.26
K_1	Vigo	0.07	0.09	-0.02	60.03	74.73	-14.70
	Leixões	0.07	0.09	-0.02	60.59	79.39	-18.80
	Aveiro	0.06	0.09	-0.03	62.98	74.30	-11.32

model is able to accurately reproduce tidal propagation in coastal area under research in this study.

Predicted time series of water temperature, salinity and current velocity were also compared with data from oceanographic buoys that are located in the coastal region (stars in Figure 5.4). Results are presented for the whole year of 2013 in order to analyse not only the diurnal, but also the seasonal variations. Results for only two stations are shown for the entire year: Cape Peñas (P) and Villano-Sisargas (VS) (Figures 5.7 and 5.8, respectively), because data for the other three stations have too many gaps, and therefore only a specific period is shown (Figures 5.9 and 5.10).

Generally, results suggest that model reproduces satisfactorily the seasonal evolution of water temperature for both stations (Figures 5.7a and 5.8a), showing the characteristic succession of winter minima and summer maxima. $RMSE$ for the whole year is 0.564 and 0.608 °C for Cape Peñas and Villano-Sisargas stations, respectively, being the highest differences registered in summer. Indeed, for the first quarter of the year (January to March), $RMSE$ is 0.112 (0.144) °C, while for the third quarter (July

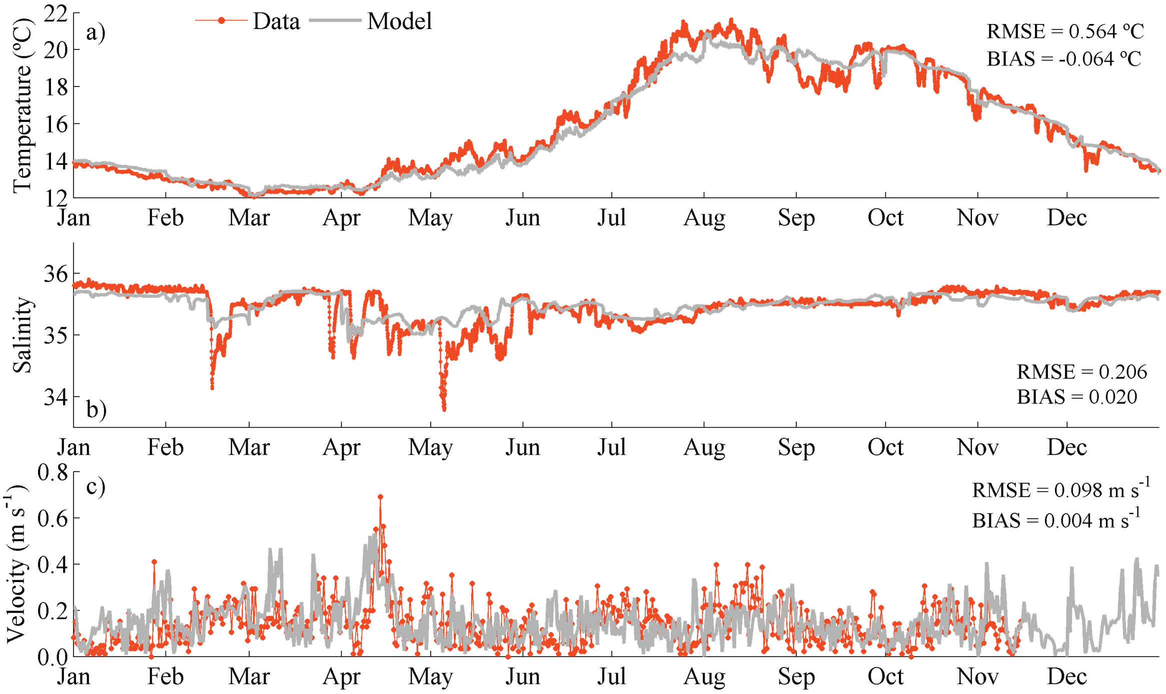

Figure 5.7: Observed and predicted water temperature (°C), salinity and velocity (m s^{-1}) for the Cape Peñas station (P) represented in Figure 5.4 for 2013. Statistical results are also presented.

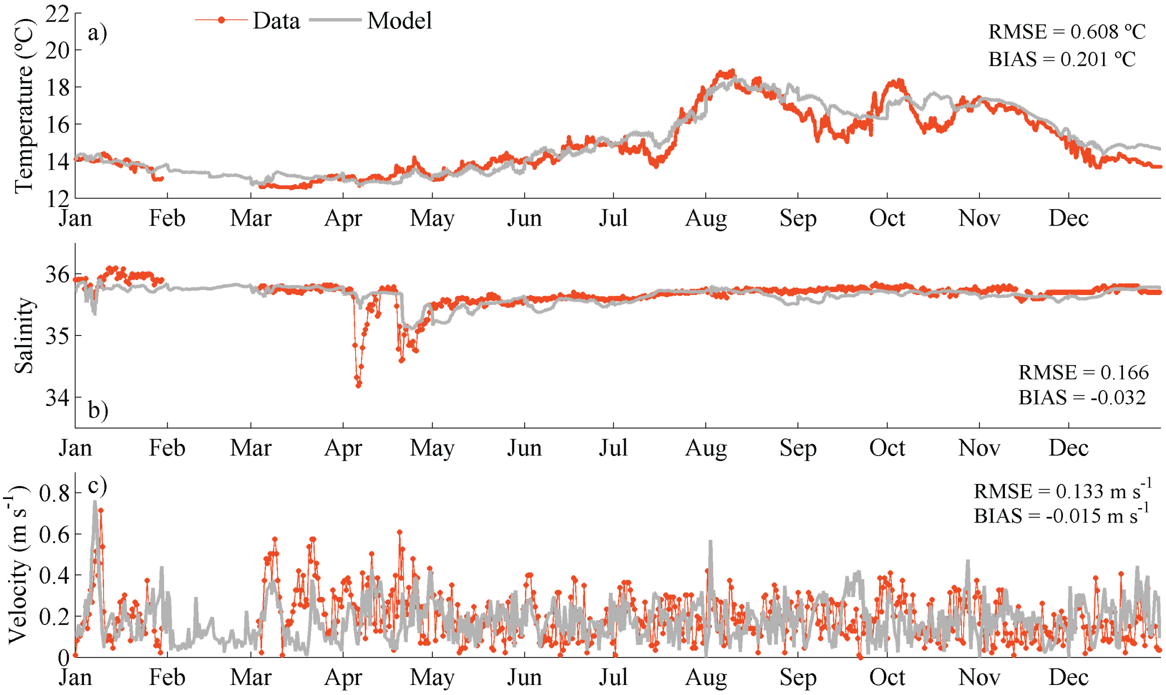

Figure 5.8: Observed and predicted water temperature (°C), salinity and velocity (m s^{-1}) for the Villano-Sisargas station (VS) represented in Figure 5.4 for 2013. Statistical results are also presented.

to September) is 0.444 (0.416) °C, for Cape Peñas (Villano-Sisargas) station. These differences may be attributed to the mixed layer that is thinner in summer than in winter months and, therefore, model vertical resolution should be high to accurately reproduce the summer water temperature (Mateus et al., 2012a).

Salinity time series (Figures 5.7b and 5.8b) show a $RMSE$ of 0.20 and 0.17 for Cape Peñas and Villano-Sisargas stations, respectively. In these cases, the highest errors occur during winter and are due to low time resolution of the flow imposed in model. Indeed, Cape Peñas buoy is very close to Nalon River mouth and, between February and May, high discharges were observed, with salinity reaching 34. Although model predictions showed the same trend, salinity minimum is not so low as observed in data, and therefore, higher $RMSE$ are found between February and May (0.19) than for rest of the year (0.08).

For the Villano-Sisargas the major difference between predicted and measured salinity was found for April and May, with a $RMSE$ of 0.14, while for the rest of the year the $RMSE$ is 0.09.

Relatively to velocity time series (Figures 5.7c and 5.8c), data and model predictions are represented every 12 hours, because velocity is a property with high variations and therefore visualization is not easy. $RMSE$ for the whole year, except gaps, is 0.098 m s^{-1} for Cape Peñas, being the model predictions higher than data (positive $BIAS$). Otherwise, for Villano-Sisargas the model predictions are generally lower than measurements, with a mean difference of -0.015 m s^{-1} and a $RMSE$ of 0.133 m s^{-1}.

To make more visible the comparison between measured data and model predictions, water temperature, salinity, velocity and Chl-a concentration are represented in Figures 5.9 and 5.10 during five days considering all stations (P, B, VS, S and R).

Results suggest a good agreement between data and model predictions, however, several differences are detected. The highest water temperature and salinity $RMSE$ are found for Bares station, with errors of 0.6°C and 0.2, respectively. Otherwise, water temperature lowest $RMSE$ was found for Raia buoy, with a value of 0.15°C. Silleiro and Bares stations present the best fit between data and predicted current velocity ($RMSE = 0.07$ m s^{-1}). The highest $RMSE$ between predicted and measured velocity is observed for the Cape Peñas, with an error higher than 0.12 m s^{-1}, and an average

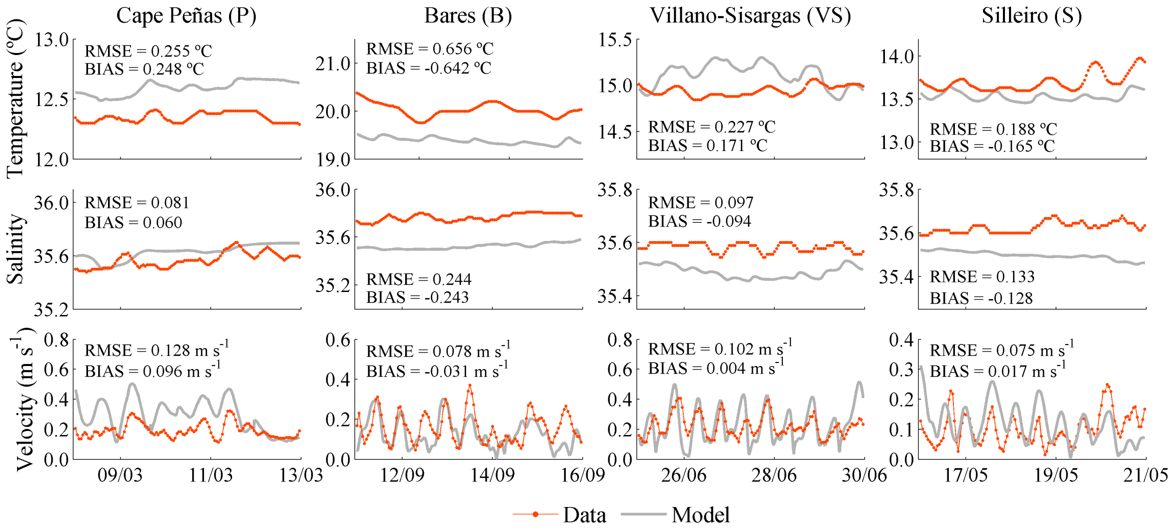

Figure 5.9: Observed and predicted water temperature (°C), salinity and velocity (m s^{-1}) for stations P, B, VS and S represented in Figure 5.4. Statistical results are also present.

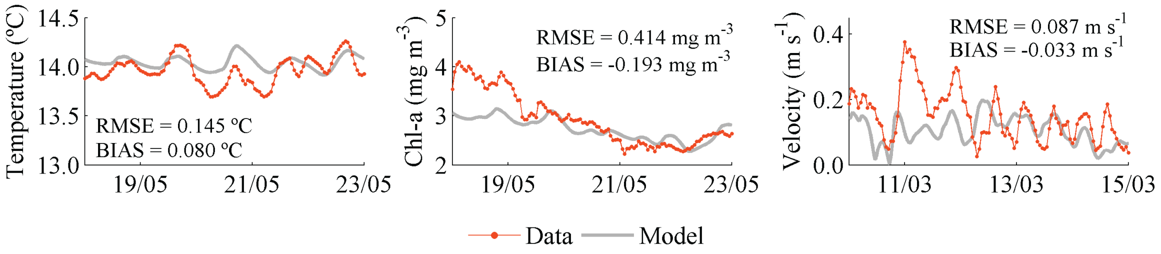

Figure 5.10: Observed and predicted water temperature (°C), Chl-a concentration (mg m^{-3}) and velocity (m s^{-1}) for Raia station (R in Figure 5.4). Statistical results are also present.

difference of 0.096 m s^{-1}. Chl-a concentration data is only available for R buoy and model predictions are usually lower than data ($BIAS = -0.193$ mg m^{-3}) with a $RMSE$ of 0.4 mg m^{-3}.

To validate model predictions of current velocity at 1000 m depth, trajectories of Argo # 1 during the drift phase (phase 2 to 3 in Figure 5.5) were simulated using Lagrangian model. 100 particles were released at the known Argo float position (1 in Figure 5.5) and the average final positions were registered. This procedure was performed for almost three months (between 05/02 and 20/05/2013) and results are represented in Figure 5.11.

The analysis of Figure 5.11, show that both predicted and observed trajectories are similar. The average distance between predicted and measured positions is approximately 6 km, however in some specific locations the distance can reach 15 km (Figure 5.11b). The highest differences were found for positions 6 and 22 (dots black

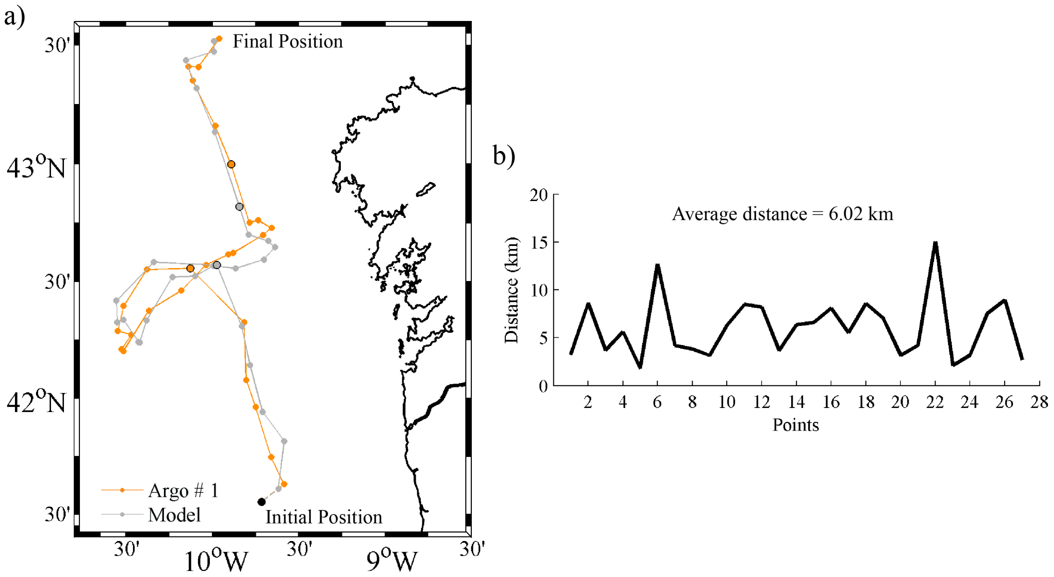

Figure 5.11: a) Observed and predicted trajectories of Argo # 1 during the drift phase, b) distance between Argo and model predicted positions (km).

delimited in Figure 5.11a), with values of 12 and 15 km, respectively. The differences observed can be attributed to the uncertainty of the initial and final positions of the drift phase (2 to 3 in Figure 5.5), that in simulations were approximated to the positions 1 and 5 from Figure 5.5, respectively. Model spatial resolution (3 km) can also contribute to the differences observed.

5.9.3.1 Vertical profiles validation

Model predictions were compared with Argo profiles, for the year of 2013, being results presented in Figures 5.12 to 5.16. In addition to the visual comparison, a simple statistical analysis ($RMSE$ and $BIAS$) was performed, interpolating the model output through the cubic interpolation method, *i.e.* using a third degree polynomial.

Argo # 1 float travelled through the study region between 2012 and 2013, entering in the domain by the south boundary at the end of May 2012 and leaving it through the north coast during September 2013. Once initial data from MyOcean is only available from December 2012, validation was performed for 2013.

In general, results of Figure 5.12 show that model overestimates water temperature values (with positive $BIAS$), nonetheless the upper layer thermodynamics and vertical stratification of thermohaline are well reproduced by the model. Also, the model is able to represent the temporal evolution of the seasonal thermocline. It often starts

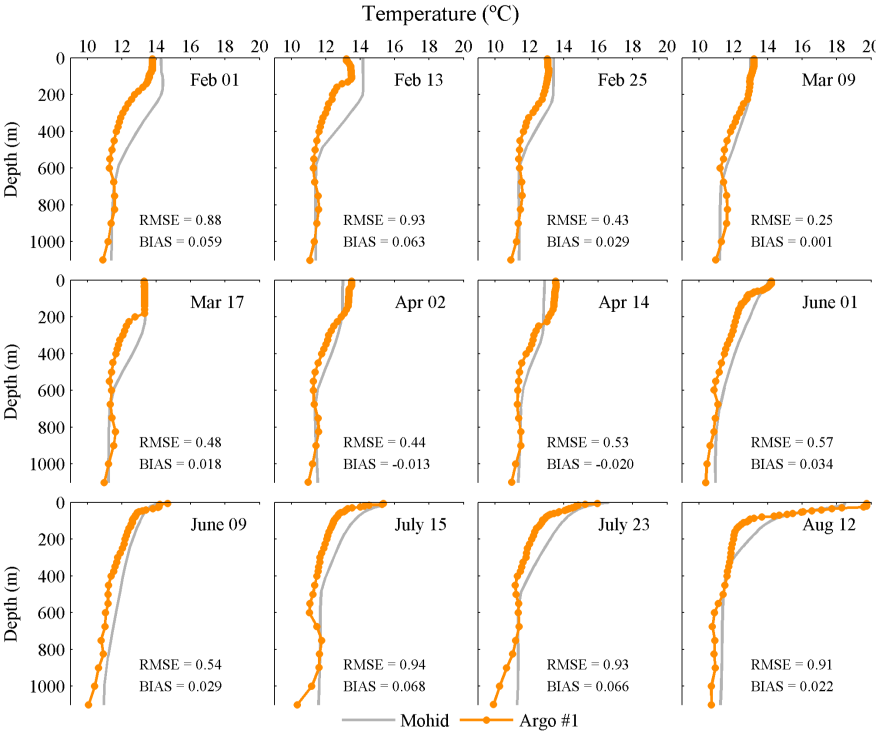

Figure 5.12: Predicted water temperature (°C) profiles compared with Argo (Argo # 1), for 2013. Statistical results ($RMSE$ and $BIAS$) are also presented in °C.

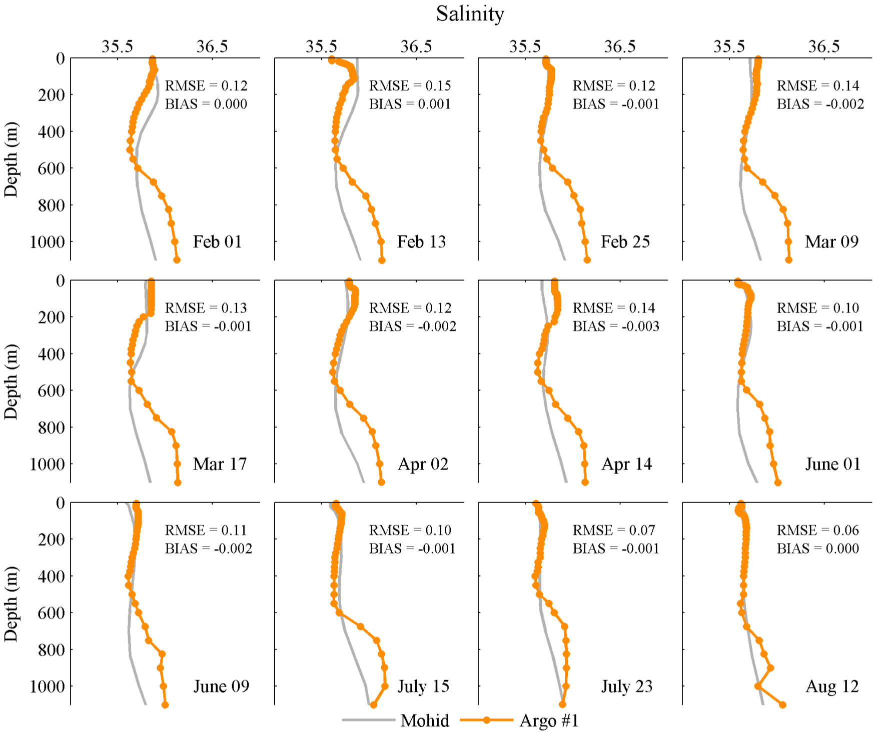

Figure 5.13: Predicted salinity profiles compared with Argo (Argo # 1), for 2013. Statistical results ($RMSE$ and $BIAS$) are also presented.

to develop in spring above the permanent thermocline as surface temperature rise and mixing by wind decreases (Figure 5.12 - April 2), reaching maximum development in summer (Figure 5.12 - August 12).

$RMSE$ between model predictions and measurements ranges from 0.25 °C on March 9 to 0.94 °C on July 15, revealing a good agreement between data and model predictions. These results are better than those achieved by Mateus et al. (2012a), that obtained a $RMSE$ of 1.25 °C in a point located at 42 °N and 11.5 °W.

Regarding salinity profiles (Figure 5.13), small differences were observed at surface, increasing for depths higher than 600 m. Nonetheless, the highest $RMSE$ is 0.14 which, relatively to mean salinity values, corresponds to an error of less than 0.5 %. $RMSE$ for salinity profiles are also lower than those achieved by Mateus et al. (2012a), revealing the importance of the model spatial resolution. Therefore, results suggest that model adequately reproduces the vertical structure of salinity, including the permanent pycnocline features.

Another Argo float was identified in the study region during 2013, entering through the west part of the domain during March and leaving it through the north coast in November (Figure 5.4, Argo # 2). Water temperature, salinity and oxygen concentration profiles are available for this float and then used to validate the model predictions at different locations. Results are presented in Figures 5.14, 5.15 and 5.16.

Water temperature and salinity profiles (Figures 5.14 and 5.15) suggest that model accurately reproduces the surface features, as well as the vertical stratification and permanent pycnocline. In this case, the highest $RMSE$ for water temperature and salinity were found in August (1.10°C) and May (0.19), respectively.

The distribution and variability of dissolved oxygen in the ocean is controlled by physical and biological factors and by the complex interactions among them. This includes the large scale and regional circulation, vertical mixing, air-sea exchange, oxygen release by primary production and oxygen consumption by respiration/mineralization. Therefore, in marine environments, is difficult to reproduce oxygen concentration as well as other biogeochemical variables. Nonetheless, model reproduces well oxygen distribution along water column (Figure 5.16). High levels of oxygen (> 8 mg l^{-1}), produced through photosynthesis, are observed at the surface layers for both data and model predictions. Oxygen concentration decrease with depth,

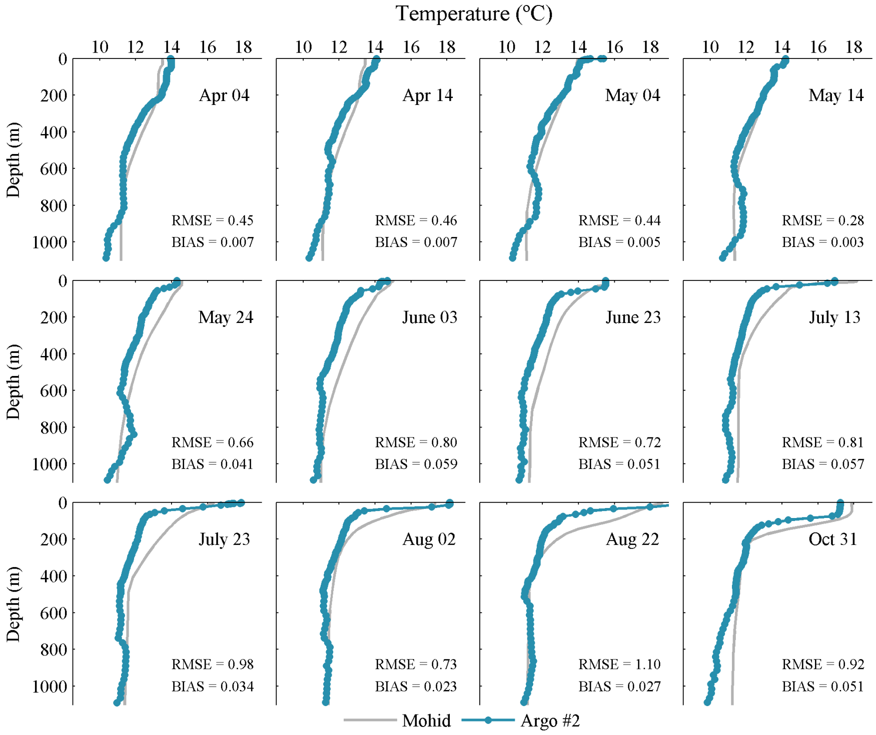

Figure 5.14: Predicted water temperature (°C) profiles compared with Argo (Argo # 2), for 2013. Statistical results ($RMSE$ and $BIAS$) are also presented in °C.

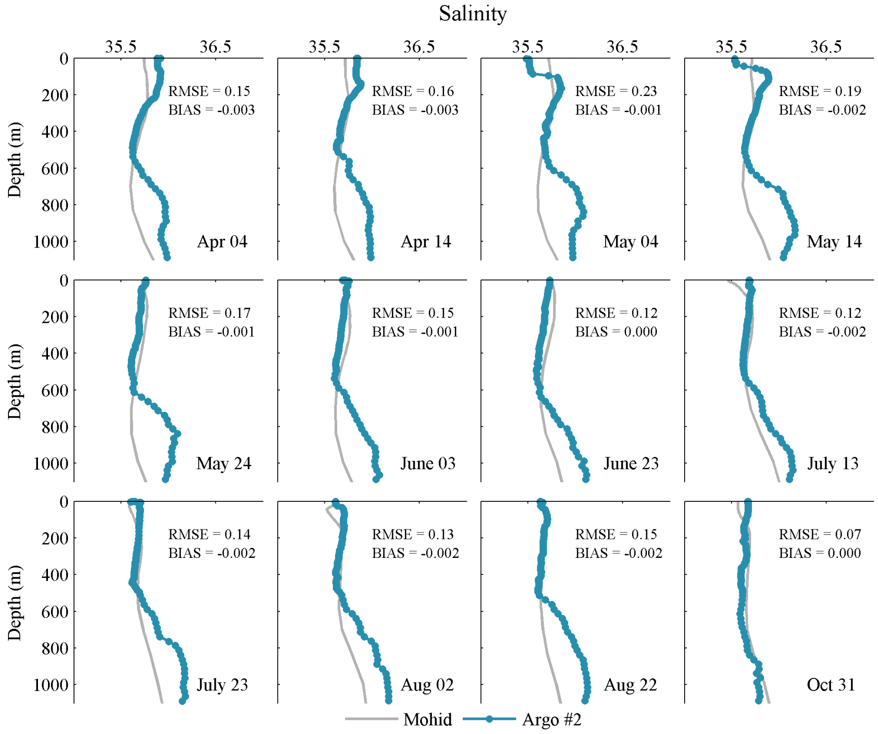

Figure 5.15: Predicted salinity profiles compared with Argo (Argo # 2), for 2013. Statistical results ($RMSE$ and $BIAS$) are also presented.

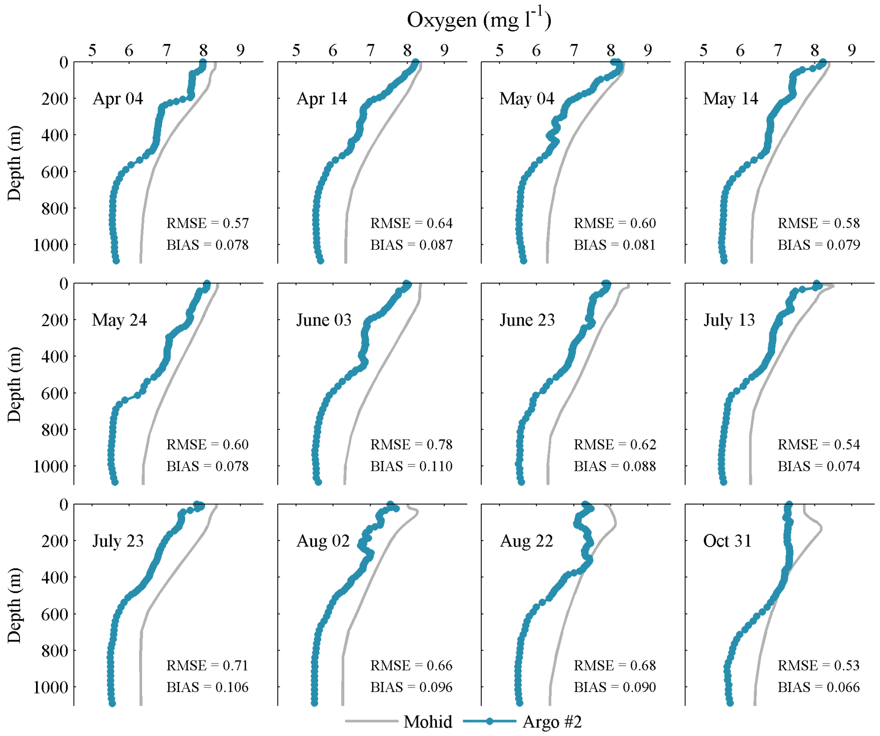

Figure 5.16: Predicted dissolved oxygen (mg l^{-1}) profiles compared with Argo (Argo # 2), for 2013. Statistical results ($RMSE$ and $BIAS$) are also present in mg l^{-1}.

reaching a minimum at approximately 1000 m, where the oxygen is consumed through respiration and photosynthesis does not occur due to absence of light. In deeper layers (not shown here), the oxygen concentration increases again reaching the values observed at the surface, due to the bottom currents that carry dense and oxygenated water. Results suggest that model systematically overestimates data, with $RMSE$ ranging from 0.53 mg l^{-1} on October 31 to 0.71 mg l^{-1} on July 23.

5.9.4 Spatial validation

A spatial comparison between predicted and remote sensing SST and Chl-a concentrations was also performed, by interpolating the satellite data grid (1 km) into the model grid (3 km). Difference between predictions and satellite data was computed as well as the regression equation parameters, $RMSE$, $BIAS$ and Pearson correlation. Results for SST are presented in Figures 5.17 and 5.18 and for Chl-a concentration in Figures 5.19 and 5.20. The images date was chosen as representative of winter (January 3, 2013) and summer seasons (June 2, 2013 for SST and July 11, 2014 for Chl-a concentration).

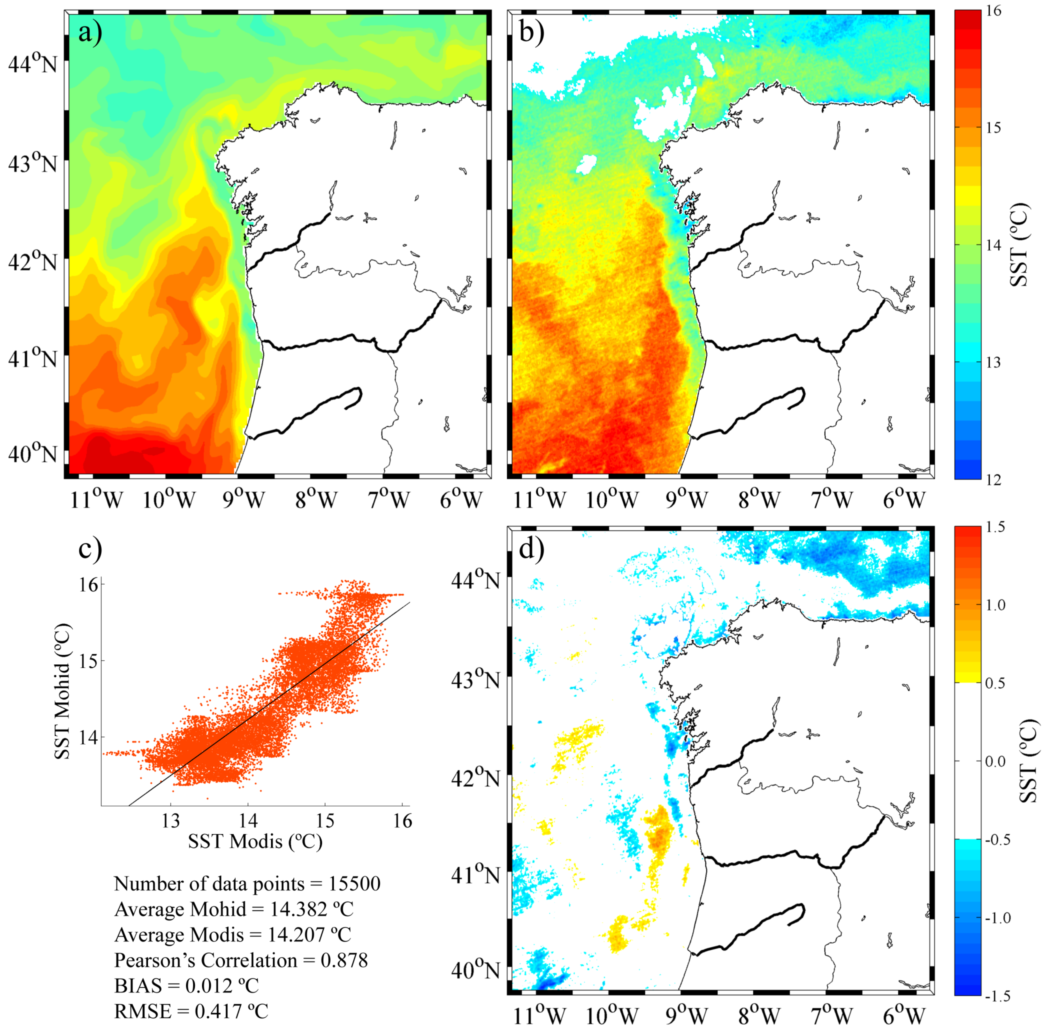

Figure 5.17: SST (°C) on January 3, 2013 obtained from a) model predictions and b) satellite data. c) Linear fit between predictions and satellite data ($y = 0.73x + 4.00$) and d) difference between measured and predicted SST (°C). Results from statistical analysis are also shown.

When comparing satellite imagery and predicted SST, some considerations must be taken into account. Satellite instruments that observe in the infra-red part of the spectrum measure skin SST, *i.e.* a layer of a few millimetres thick which characteristics are due to the exchange of heat and moisture to atmosphere as well as the emission of infra-red radiation. Otherwise, the predicted SST corresponds to the bulk temperature (average water temperature of surface layer). In this case, model surface layer has a thickness of 0.98 m and therefore, skin SST can be significantly different from the bulk SST, especially under weak winds and high incoming sunlight (Fairall et al., 1996; Wick et al., 1996), and differences between model predictions and satellite data are expected.

From Figures 5.17 and 5.18 is observed a good agreement between predicted and

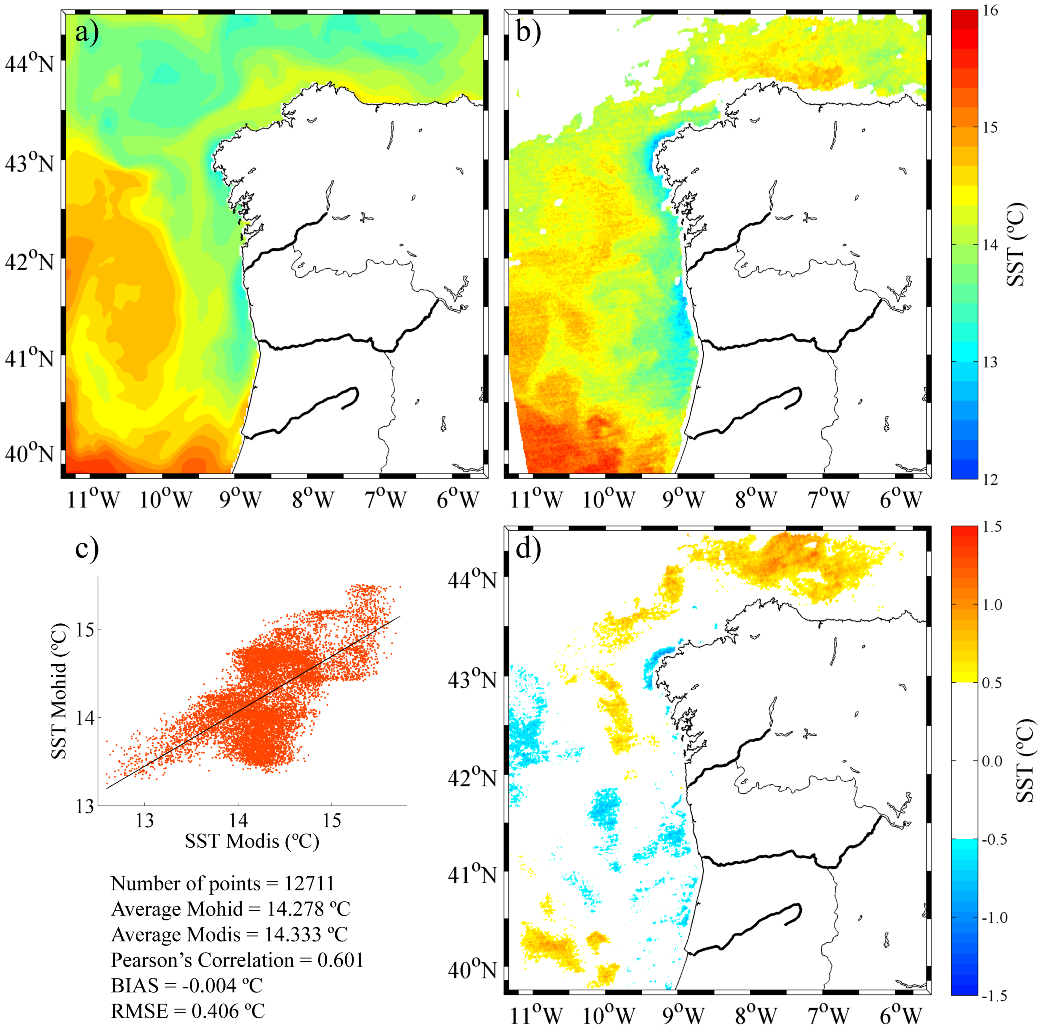

Figure 5.18: SST (°C) on June 2, 2013 from a) model predictions and b) satellite data. c) Linear fit between predictions and satellite data ($y = 0.62x + 5.40$) and d) difference between measured and predicted SST (°C). Results from statistical analysis are also shown.

satellite SST. For January 3, both simulated and observed SST patterns equally reflect the main features of the water temperature field, namely the meridional gradient of temperature, characterized by high temperatures at the south decreasing northward. Also, both model predictions and data show lower water temperatures (14 °C) near coast than offshore. Moreover, surface water temperatures (Figures 5.17a and b) reveal evidence of a filament of warmer water than surrounding coastal and oceanic waters turning east of Cape Finisterre, which is associated to the IPC that usually arrives to the IP north coast at the beginning of winter (Garcia-Soto et al., 2002; Peliz et al., 2005; deCastro et al., 2011) and is usually sharper during January.

Difference between satellite and predicted SST were computed for the whole study area, being the highest differences found at northern coastal segment, however never exceeding 1.5 °C (Figure 5.17d). Statistical parameters (Figure 5.17c) show a $BIAS$ of 0.012 °C between two winter maps, suggesting that model predictions tend to overestimate the satellite SST. Regarding the SST average for all domain, a difference between MOHID and MODIS of 0.17 °C was found. Also a $RMSE$ of 0.417 °C was found between predicted and satellite SST as well as a correlation coefficient of 0.878 (Figure 5.17c), revealing that predicted and satellite data are strongly correlated.

For June 2 (Figure 5.18a and b) predicted and measured SST also show a meridional gradient (warming southward). Moreover, the common wind induced upwelling phenomenon can be identified in both model predictions and satellite imagery, through the cold water mass ($13 - 14$ °C) along the western coast of IP.

As in winter maps (Figure 5.17), the highest differences were found at northern coastal segment, however never exceeding 1.5 °C (Figure 5.17d). In this case, from statistics (Figure 5.18c), model predictions are in general lower than satellite data, being $BIAS$ equal to -0.004 °C and $RMSE$ to 0.406 °C. Indeed, the average SST for all the domain is higher 0.055 °C for MODIS sensor than for MOHID. A correlation coefficient of 0.601 °C was found revealing a strong correlation between predicted and satellite data. These results are similar to those obtained by Mateus et al. (2012a) for 2011, revealing that model adequately reproduces SST patterns for the study region.

Regarding Chl-a concentration, on January 3, both satellite and predictions show a coastal fringe of high values, with the maximum found at western coastal segment (Figure 5.19). Generally, a good agreement between predicted and measured Chl-a concentration is found, however some differences were observed, with the highest near the coastal region (Figure 5.19d). Indeed, between Mondego and Douro Rivers, the predicted band of high Chl-a is larger than the observed. Otherwise, near Minho River, Rias Baixas and Cape Peñas, predicted Chl-a concentration is lower than observed. Actually, several works have reported that an overestimation of Chl-a concentration is often observed when using MODIS sensor in coastal waters (Werdell, 2009; Darecki and Stramski, 2004; Oliveira et al., 2007; Sá et al., 2008). In the outer shelf no significant differences were found between model predictions and satellite data (lower than 0.5 mg m^{-3}). A $BIAS$ of -0.047 mg m^{-3}, a $RMSE$ of 0.365 mg m^{-3} and a correlation coefficient of 0.812 (Figure 5.19c), reflect the model ability to reproduce Chl-a concentration in

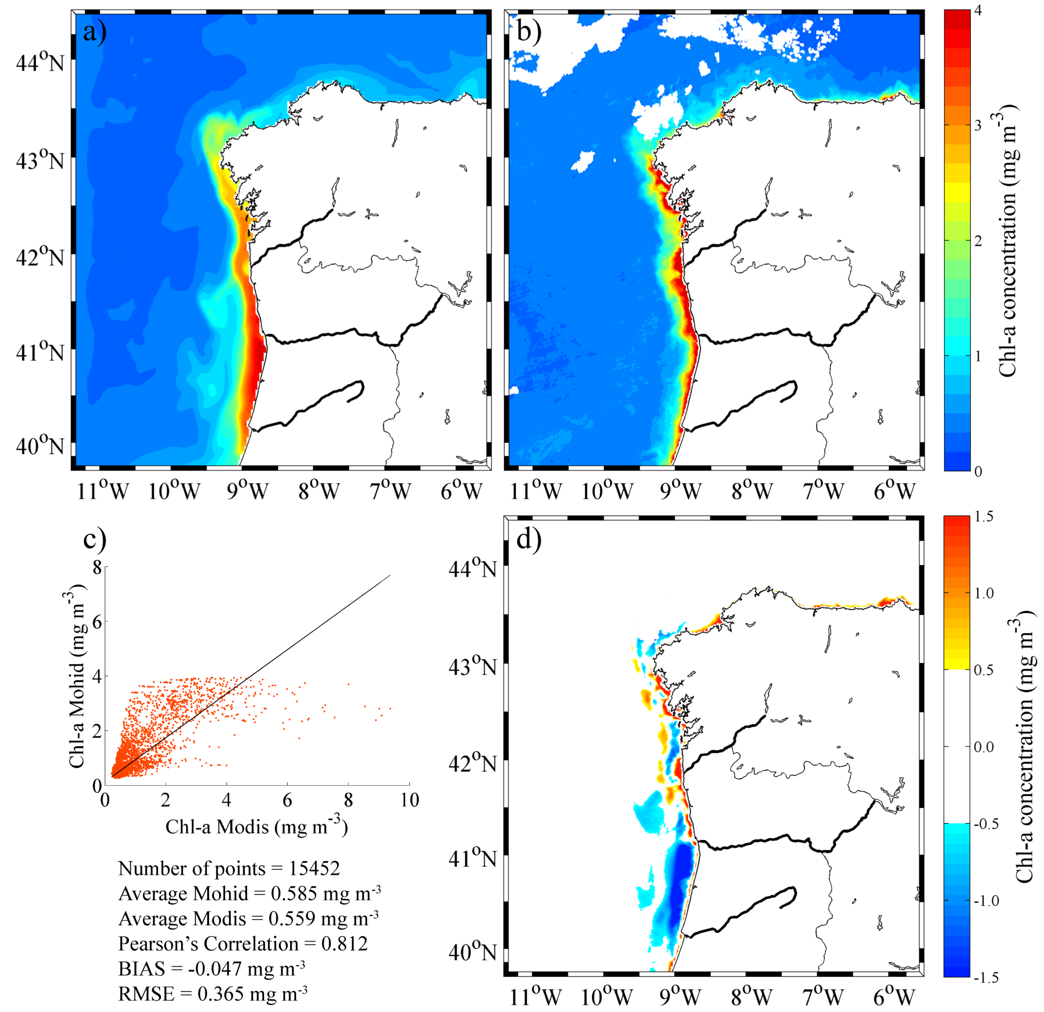

Figure 5.19: Chl-a concentration (mg m^{-3}) on January 3, 2013 from a) model predictions and b) satellite data. c) Linear fit between predictions and satellite data ($y = 0.81x + 0.13$) and d) difference between measured and predicted Chl-a concentration (mg m^{-3}). Results from statistical analysis are also shown.

winter along the northwestern coast of IP. In addition, the average Chl-a concentration for all domain is slightly higher (0.026 mg m^{-3}) for MOHID than for MODIS sensor, revealing a good agreement between predictions and observations.

For summer (Figure 5.20), differences between predicted and measured Chl-a concentrations are higher than for winter, however the main spatial patterns are well represented, mainly near coastal areas. Indeed, for both predicted and observed Chl-a concentrations, high values were identified upstream Mondego River and near Rias Baixas, as result of upwelling favourable winds, with the predictions underestimating satellite data. Near Minho River and Cape Finisterre, low Chl-a concentrations (lower

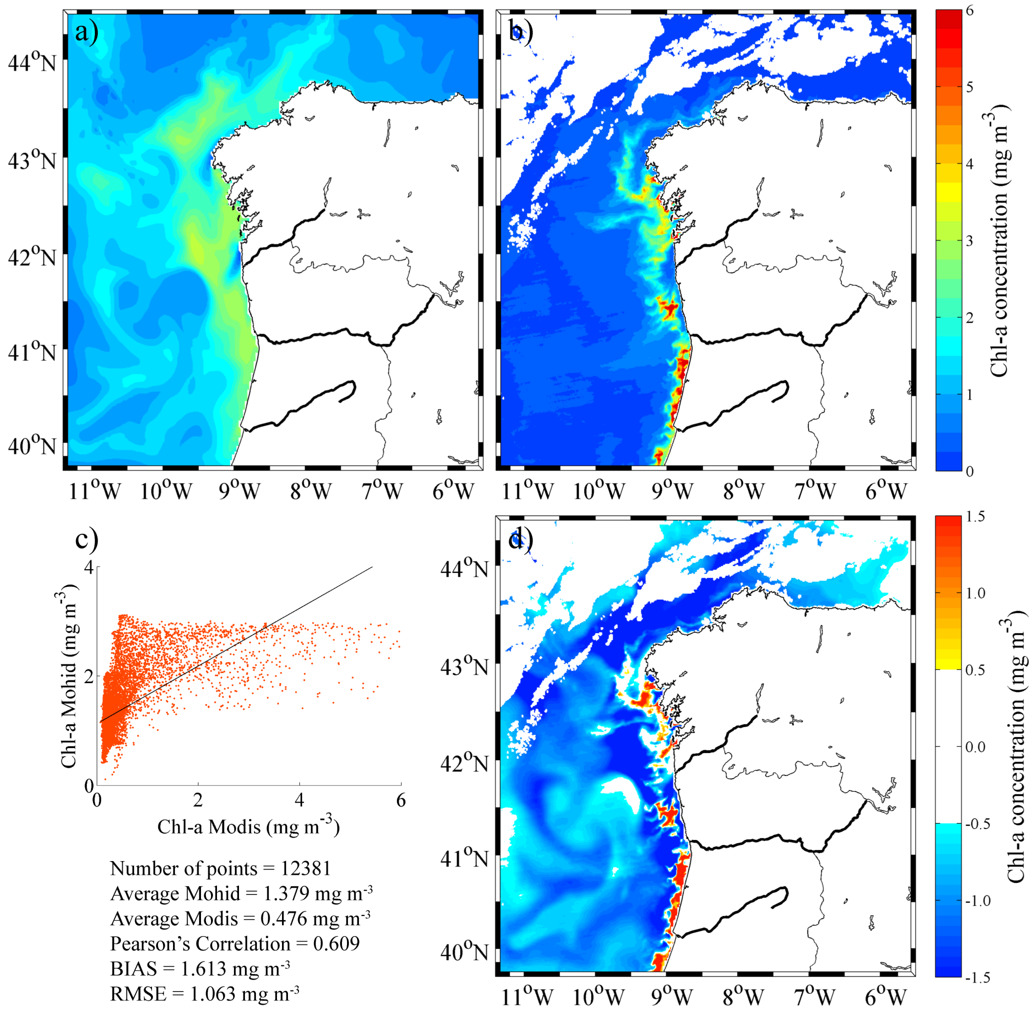

Figure 5.20: Chl-a concentration (mg m^{-3}) on July 11, 2014 from a) model predictions and b) satellite data. c) Linear fit between predictions and satellite data ($y = 0.53x + 1.13$) and d) difference between measured and predicted Chl-a concentration (mg m^{-3}). Results from statistical analysis are also shown.

than 1 mg m^{-3}) are observed for both satellite data and predictions.

Outer shelf waters are usually less productive than coastal waters, which can be observed in both predicted and satellite maps (Figure 5.20). However, at western coastal segment, the predicted Chl-a concentration is higher than the measured by the satellite (Figure 5.20). Statistical results show that the mean difference between predictions and satellite data is 1.6 mg m^{-3}, with a $RMSE$ of approximately 1.0 mg m^{-3} (Figure 5.20c). The correlation between predicted and measured Chl-a concentration is lower (0.60) than for winter, which may be due to differences observed in outer shelf waters, however predictions and observations still strong correlated. At northern coastal segment no significant differences were found, however model predictions reveal an overestimation of data.

5.10 Conclusions

The present chapter aimed to present the implementation and validation of the coupled circulation and biogeochemical model for the northwestern coast of IP, which was successfully achieved. Results indicate the following:

- A good agreement between predicted and synthesized SSE for the three stations analysed was attained, revealing that model accurately reproduces tidal components;
- Predicted water temperature, salinity, current velocity and Chl-a concentration were also validated near the coast, using data of five buoys. Results suggest a good agreement between predictions and observations. For water temperature, the highest errors were found during summer, while for salinity they occur during winter, due to the rivers impact in the coast. Observed Chl-a concentration show a good agreement with the predicted and therefore reveals model accuracy;
- Vertical profiles show a good agreement between data and predicted water temperature, salinity and oxygen, revealing the model's accuracy to reproduce the upper layer thermodynamics and vertical stratification, as well as the distribution of oxygen in water column;
- Deep current velocity was also validated through trajectories of Argo # 1 during the drift phase, at 1000 m depth. Results suggest that model accurately reproduce the float trajectory during the selected months, despite some uncertainties in determining float initial position. A mean difference of approximately 6 km was found between Argo and lagrangian tracers final positions;
- Remote sensing images also show that model reproduces the main features of SST and Chl-a concentration in the region under study, however some differences were found, mainly for Chl-a during summer. Indeed, biogeochemical properties are very difficult to reproduce, once they are controlled by the interactions between several physical, chemical and biological factors.

In summary, the accuracy of MOHID to reproduce physical and biogeochemical properties in the study region was satisfactorily demonstrated. The model is able to reproduce the main features of the water column as well as the surface patterns. However, model presented some limitations that should be taken into account for future applications, namely the overestimation of Chl-a concentration in the outer shelf of western coastal segment of IP. To overcome this issues, the implementation of a third domain with higher resolution should be tested, however the computational effort will increase significantly. Also, initial and boundary conditions with higher resolution may improve model predictions and surpass the issues pointed out in this chapter.

Notwithstanding, in next chapter this configuration will be used to study physical and biological features of the study area during two summer upwelling events.

Chapter 6

Phytoplankton generation under coastal upwelling: a modelling study

6.1 Introduction

At mid-latitudes, the phytoplankton development is strongly controlled by the circulation in the upper layers of the ocean waters (Fraga, 1981) and is both light and nutrients limited (Levy et al., 2005; Oliveira et al., 2009).

Coastal upwelling plays an important role in phytoplankton distribution over the world ocean, being substantially researched. Some of this research includes the use of physical-biological coupled models, which are valuable tools for the understanding of physical and biogeochemical processes in coastal upwelling regions at seasonal and event time scales. In recent years, a strong effort has been performed to implement biophysical models along the Iberian margin, from which resulted several studies: Marta-Almeida et al. (2012), Mateus et al. (2012a) and Reboreda et al. (2014, 2015). These studies revealed the numerical models relevance in reproducing the main circulation and biological features of the study region, highlighting the importance of operational systems in providing biological variables for research or coastal management. Focused in Galician coast (between Cape Finisterre and Cape Ortegal), Rocha et al. (2013) analysed the Chl-a concentration response to an extreme upwelling event of September 2007. Authors highlighted the importance of ocean circulation in the Chl-a distribution and an inverse relation with SST.

In this chapter, the physical-biological coupled model implemented and validated in the previous chapter is used aiming to establish the link between circulation, SST and phytoplankton generation during two summer upwelling events. Through the analysis of wind velocities and SST imagery a strong upwelling event was identified, between 8 and 18 of July 2014. A weaker event was found between 9 and 17 of August 2013 and used for comparison purposes, in order to infer about implications of upwelling intensity on Chl-a patterns.

6.2 Model and methods

In order to identify a strong upwelling event (with the N-S wind component higher than 5 m s^{-1}), two years (2013 and 2014) of WRF wind velocity data provided by MeteoGalicia and remote sensed SST imagery from MODIS sensor were analysed along the study area. Strong favourable upwelling winds were found from 8 to 18 July 2014 at western and intermediate coastal segments. The same databases were analysed to identify a weaker upwelling event to further infer about the influence of upwelling intensity on the circulation, SST and Chl-a patterns. Weaker upwelling favourable winds were found between 9 and 17 of August 2013.

Therefore, in order to assess the phytoplankton patterns in northwestern IP waters under these upwelling events, two simulations were performed, one for July 2014 and other for August 2013, keeping all the setups described in previous chapter and applying the circulation, biogeochemical and lagrangian models. Physical and biogeochemical variables were validated in previous chapter with satisfactory results. The Lagrangian model used herein was also previously validated (Chapter 5), through the analysis of Argo buoys trajectory during their drift phase, with satisfactory results.

The wind time evolution during both simulations periods was analysed at the stars represented in Figure 6.1, which locations are representative of the three coastal segments. Also, N-S wind component inside boxes C, E and F for July 2014 event will be analysed in the frame of results discussion, to understand the wind spatial variability.

After, 8 days average and standard deviation of predicted SST, Chl-a concentration

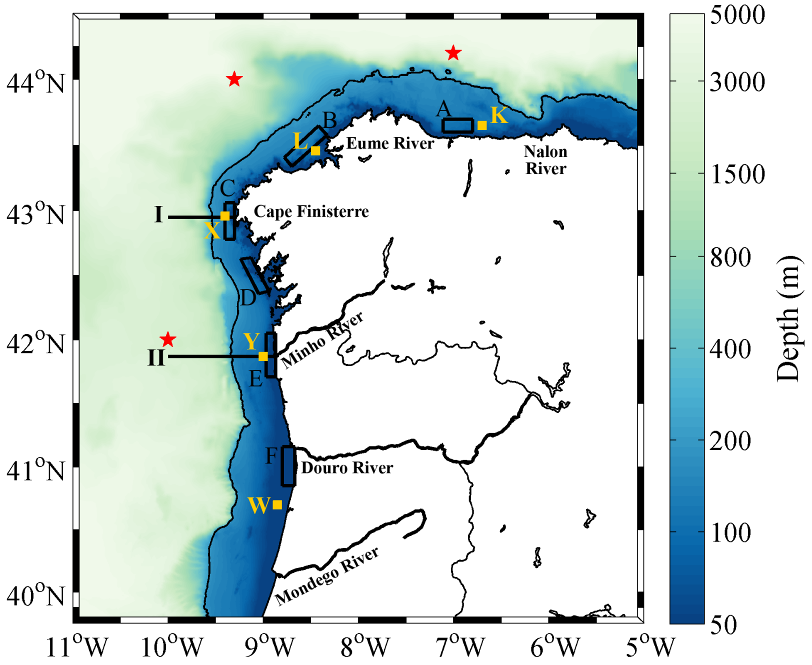

Figure 6.1: Bathymetry of the study area, with the black line representing the 200 m isobath. The boxes (A, B, C, D, E and F) identify the areas where particles were released. The stars marks the location of WRF wind at each coastal segment, squares the location of the time series analysed (X, Y and W) and I and II the zonal sections.

and mean current velocity were analysed for the periods identified (8 to 18 July, 2014 and 9 to 17 August, 2013), in order to study the response of the coastal ocean upper layer along all study region to upwelling favourable winds.

Daily average SST, Chl-a, nitrate and oxygen surface fields were computed and analysed during July 2014 event for days 8, 10, 14, 16 and 18. Based on these results, times series of these variables were also analysed at points X, Y and W (Figure 6.1), located at the western coastal segment, between 8 and 18 of July. Vertical variability of SST, Chl-a, oxygen and nutrients was analysed at three points at western coastal segment (X, Y and W), one at intermediate (L) and one at northern (K), for the period between 7 to 18 July, 2014 (Figure 6.1). Since all properties exhibit fluctuations at tidal frequencies, these were removed by using a 33 hours low-pass filter (Sousa et al., 2014b), for both, time series and vertical analysis.

Finally, was performed a comparison between both events previously identified (July 2014 and August 2013) through the analysis of SST, Chl-a and currents at two strategically located cross-sections (sections I and II of Figure 6.1). This analysis was performed for three different instants: onset of upwelling (August 9 and July 8), peak of N-S wind component (August 13 and July 10) and beginning of relaxation period (August 16 and July 16).

To provide insight on possible pathways of phytoplankton along the study area during both upwelling events, a particle tracking model was used coupled to the circulation model. Several particles were released inside the regions delimited by the boxes depicted in Figure 6.1, in order to simulate phytoplankton trajectories, since they are aquatic drifting organisms (Chen et al., 2015). Particles were released continuously at surface during the onset of each upwelling event (July 8/August 9) every half-hour, during two days. Particles location was analysed 48, 96 and 132 hours after release.

6.3 Results and discussion

6.3.1 Events characterization

In this section wind velocity for both upwelling events previously defined (July 2014 and August 2013) is analysed at the three stars represented in Figure 6.1. Spatio-temporal variability of SST and Chl-a concentration along the entire study area is also analysed in order to evaluate the response of coastal ocean upper layers to different wind intensity.

6.3.1.1 Wind evolution

From 8 to 18 July a complete cycle of intensification and relaxation of upwelling favourable winds (with a northerly component) occurred along western coastal segment of the IP (Figure 6.2a). This was considered a strong upwelling event once N-S wind component is higher than 5 m s^{-1} for a 8 day period (Figure 6.2, grey area). This value was considered according to Oliveira et al. (2009), that studied the Chl-a and SST patterns during an upwelling event off central Portugal (southern region of the study area, between 38 and 40°N) and to Rocha et al. (2013) that studied a strong upwelling event at Galician coast. Peak velocities (N-S wind component) were achieved on July 10, exceeding 13 m s^{-1}, starting to relax after July 16. At July 18, the N-S wind component reverses, reaching the maximum (8 m s^{-1}) at July 19. It is noteworthy the existence of strong upwelling favourable winds before this event, on July 3 (with a N-S component of approximately 12.5 m s^{-1}) and at the end of June (not shown here).

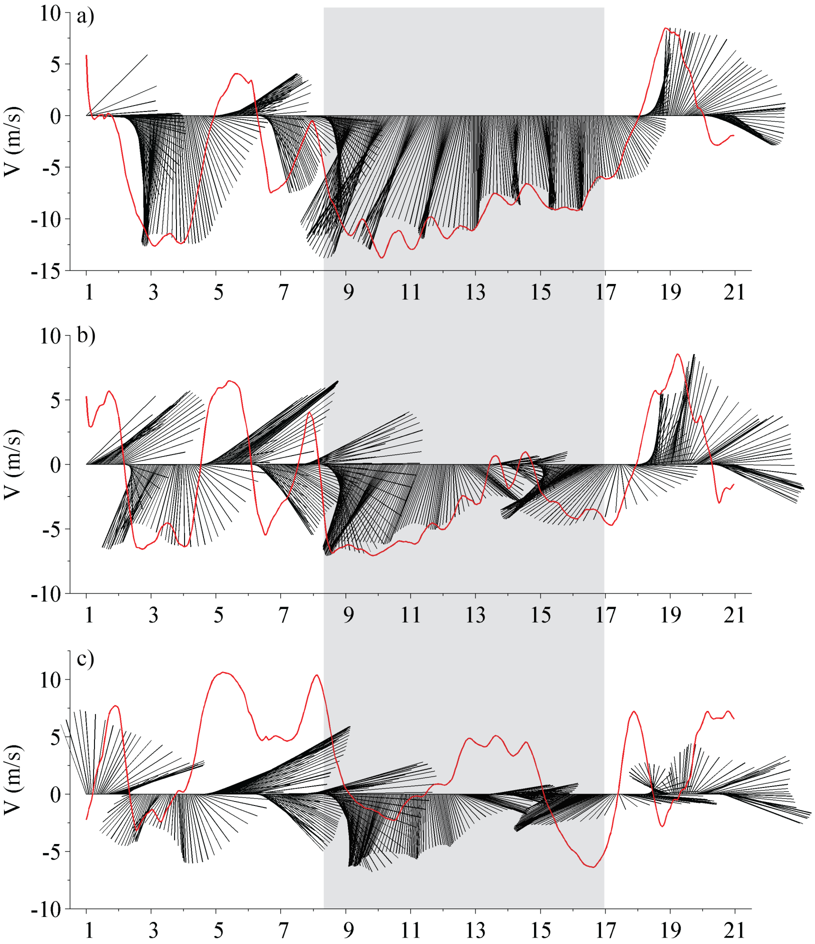

Figure 6.2: Wind regime for July 2014, from WRF model at a) western (42°N, 10.5°W), b) intermediate (44°N, 9.3°W) and c) northern (44°N, 7°W) coastal segments (red stars in Figure 6.1). Red lines represents the a) and b) N-S wind component and c) W-E wind component at each coastal segment. Grey area indicates the period when the N-S wind component was higher than 5 m s^{-1} (July 8 – 17) at the western coastal segment.

At intermediate coastal segment, wind patterns are very similar to those observed at western coast, however with lower intensity (Figure 6.2b). N-S wind component peak velocities also occurred at July 10, exceeding 7 m s^{-1}. On July 12, a decrease of approximately 4 m s^{-1} in the N-S wind component is observed.

At northern coastal segment, during this period, winds are weaker than at western and intermediate segments, and upwelling favourable winds (with a easterly component) occur from July 9 to 11 and between July 15 and 17 (Figure 6.2b). In this case peak velocities (W-E wind component) occurred at July 16, exceeding 5 m s^{-1}.

For August 2013, wind patterns are depicted in Figure 6.3 for the three coastal segments. At western coastal segment peak velocities (N-S wind component) were

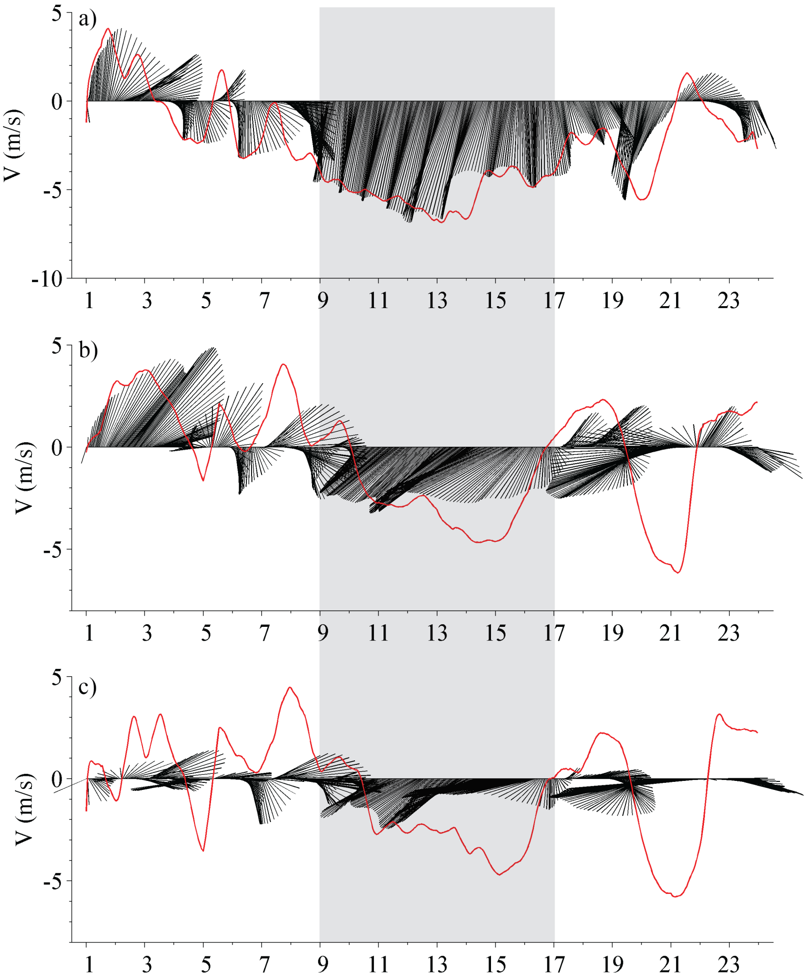

Figure 6.3: Wind regime for August 2013, from WRF model at a) western (42°N, 10.5°W), b) intermediate (44°N, 9.3°W) and c) northern (44°N, 7°W)coastal segments (red stars in Figure 6.1). Red lines represents the a) and b) N-S wind component and c) W-E wind component at each coastal segment. Grey area indicates the period where the average and standard deviation of Chl-a and SST where computed (August 9-17).

achieved on August 13, while at intermediate segment were found one day later, with values of 7 m s^{-1} (Figure 6.3a and b, respectively). At northern coastal segment favourable upwelling winds also occur, with the W-E component reaching 5 m s^{-1} on August 15 (Figure 6.3b).

Comparing the wind pattern that occurred for both events, two main differences are visible along western and intermediate coastal segments (Figure 6.3a and b): intensity of northerly winds is stronger in July 2014 event; wind pattern of the preceding period. For July 2014, the preceding days were characterized by short periods ($2 - 3$ days) of strong northerly winds, with N-S wind component reaching 10 m s^{-1}, alternated with even shorter periods (1 day) of southerly winds. Otherwise, for August 2013 event, preceding days were characterized by strong southerly alternated with weak northerly winds. For northern coastal segment, upwelling favourable winds (easterly winds) are more intense and persistent for August 2013 than for July 2014.

6.3.1.2 Spatio-temporal variability patterns

Predicted SST and Chl-a concentration time averaged (8 days) and the corresponding standard deviation were computed for the entire study region and depicted in Figures 6.4 and 6.5, for July 2014 and August 2013 events, respectively.

Generally, for July 2014 event mean SST field, for western coastal segment, shows a typical coastal upwelling pattern, with a band of cold surface water near the coast. This pattern is stronger in the northern region (between Douro and Cape Finisterre),

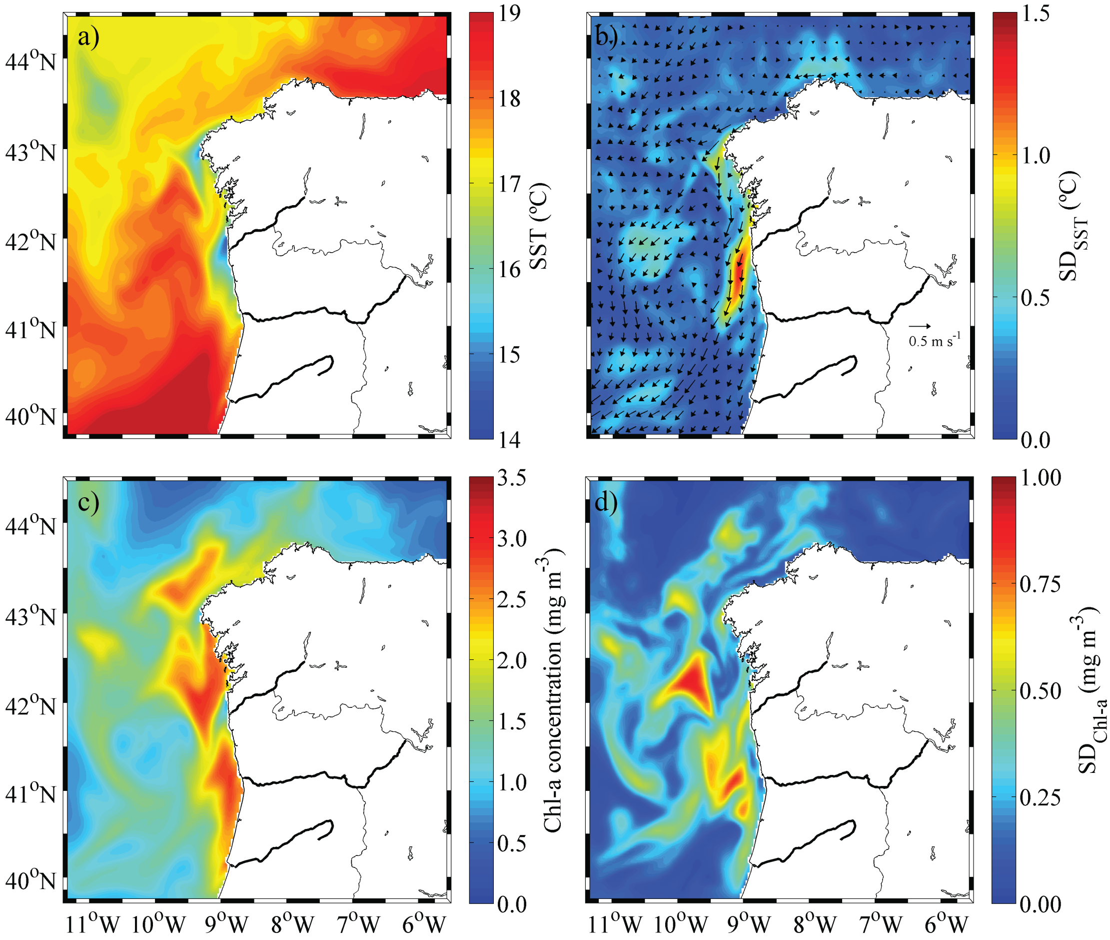

Figure 6.4: Average (left) and standard deviation (SD) (right) of SST (a and b) and Chl-a concentration (c and d), for the 8 days of intense northerly winds (July 8-16, 2014). Vectors on SD_{SST} standard deviation map are the 8 days average of the upper layer current velocity.

reaching water temperatures close to 14°C in front of Minho river mouth and 15.5°C in Cape Finisterre, while offshore waters temperature is approximately 19°C. This pattern is also clearly marked in the standard deviation field (Figure 6.4b), showing high values in these regions (1°C at Cape Finisterre and 1.5°C at Minho). This feature is common in other upwelling regions, such as the Benguela upwelling system (Hardman-Mountford et al., 2003; Demarcq et al., 2007), being these regions often designated upwelling cells. Therefore, from now on, the regions with the referred high standard deviation will be designated Cape Finisterre and Minho upwelling cells (CFUC and MUC), due to its proximity with Cape Finisterre and Minho River, respectively.

Surface Chl-a concentration field provides an informative view of the ecosystem response to surface enrichment resulting from coastal upwelling. A preliminary visual

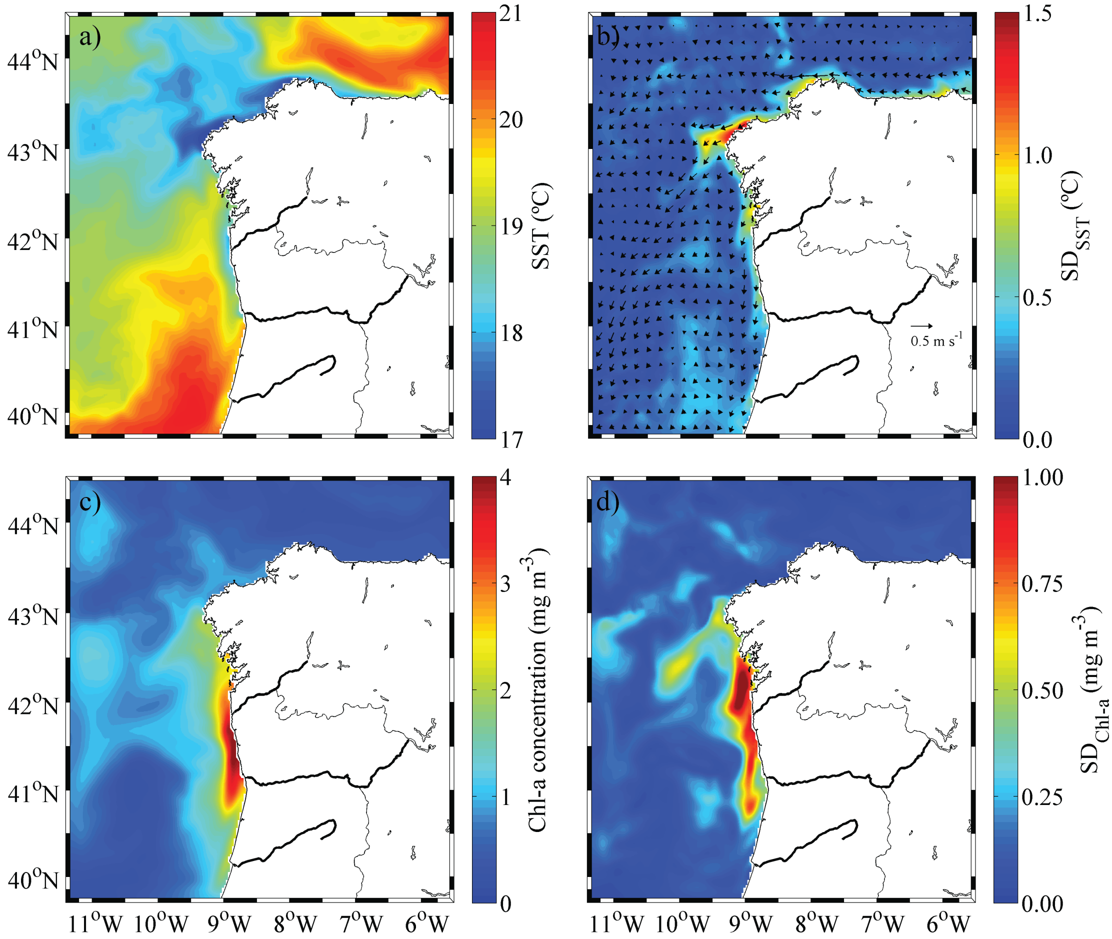

Figure 6.5: Average (left) and standard deviation (right) of SST (a and b) and Chl-a concentration (c and d), for the 8 days of intense northerly winds (August 9-16, 2013). Vectors on SST standard deviation map are the 8 days average of the upper layer current velocity.

analysis reveals an inverse relationship between SST and Chl-a concentration, with high concentrations near western (more than 3 mg m^{-3}) and intermediate (approximately 2.5 mg m^{-3}) coastal segments. A deeper analysis at the center of the CFUC and MUC shows very low values of Chl-a concentration, with mean values of approximately 0.5 mg m^{-3}, while surrounding waters present concentrations higher than 3 mg m^{-3}. This feature is also marked in the standard deviation field, with a deviation of 0.6 mg m^{-3} relative to mean values. Also, a strong standard deviation of approximately 1 mg m^{-3} was detected off Rias Baixas.

In a study that characterizes SST and Chl-a patterns during an upwelling event in a southward region (Oliveira et al., 2009), it was found that upwelling is less intense/persistent in southern regions, however mean Chl-a concentration is similar.

At western coastal segment, average surface current shows an important southwestward component, usually associated with upwelling events (Otero et al., 2008), which is more intense near CFUC and MUC, while at intermediate segment the current is weak and directed westward.

Along the northern coastal segment the mean SST shows a longitudinal gradient, characterized by water temperatures of 19°C at 6°W, decreasing to 18°C westward. Also, from the mean temperature field, no evidence of upwelled water in the northern coastal segment was found. Indeed, the W-E wind component at this coastal segment (Figure 6.2b) during this period is not intense (lower than 2.5 m s^{-1}), neither persistent (2 days). Chl-a concentrations are between 1 and 1.5 mg m^{-3}, however with a low standard deviation, meaning that these values are close to the region average. Here the surface current is weak and directed westward.

For August 2013 event, the average and standard deviation SST and Chl-a concentration were computed between 9 and 17 August and are represented in Figure 6.5. Comparing SST fields for both events (Figures 6.4 and 6.5), no significant differences are observed. The average SST between 9 and 17 August of 2013 also shows a typical coastal upwelling pattern at three coastal segments. At western coastal segment this signature is also stronger in CFUC and MUC, suggesting that northerly winds are stronger here. The standard deviation is high in all the coastal area under analysis (higher than 0.5°C), being strongest northward Cape Finisterre (1.5°C). Mean surface current is also directed westward, with the highest currents found at the Cape

Finisterre adjacent region, however, weaker when compared to July 2014 event.

The main differences between these two upwelling events are observed in Chl-a concentration patterns. Indeed, for August 2013 event, Chl-a distribution shows an inverse relation with SST for the 8 days of upwelling favourable winds. Chl-a levels are strongest between Douro and Minho Rivers (higher than 4 mg m^{-3}) and near Cape Finisterre (2 mg m^{-3}), the regions of intense upwelling conditions (Figure 6.5), conversely to the observed in July 2014 event, when a decay of Chl-a concentration was observed. Also Chl-a concentration standard deviation is higher off Rias Baixas, between Minho and Douro Rivers (higher than 1 mg m^{-3}) and in Cape Finisterre (higher than 0.5 mg m^{-3}). It is also noteworthy a southwestward displacement of the rich Chl-a surface water from Cape Finisterre region (Figure 6.5), during August 2013 event.

6.3.2 Surface time evolution: July 2014 event

As previously referred, daily average of SST, Chl-a, oxygen and nitrate concentrations are analysed at coastal ocean surface layer for July 2014 event during five days, between the onset (July 8) and cessation (July 18) of upwelling. Also, time series of these properties are analysed at points X, Y and W of Figure 6.1.

6.3.2.1 Spatial variability

Time evolution of daily averaged predictions of SST, Chl-a, oxygen and nitrate concentration, throughout July 2014 upwelling event, is presented in Figures 6.6 and 6.7, for the entire study region.

At the beginning of upwelling event (July 8 - Figure 6.6a), surface ocean at western coastal segment is characterized by high temperatures (19°C), with exception between Douro and Minho Rivers where a band of cold water (17°C) is detected. This pattern is generated by the northerlies (upwelling favourable) observed at July 3 (before the event, Figure 6.2), which induced the rise of cold water. The western coastal segment is also characterized by high oxygen levels (between 8.2 and 8.8 mg l^{-1}), with the highest values found in the coastal fringe coincident with the location of low temperature band (Figure 6.7a).

At intermediate coastal segment, SST is lower than at the western, presenting values of approximately 17°C and an average oxygen concentration of 8.2 mg l^{-1}.

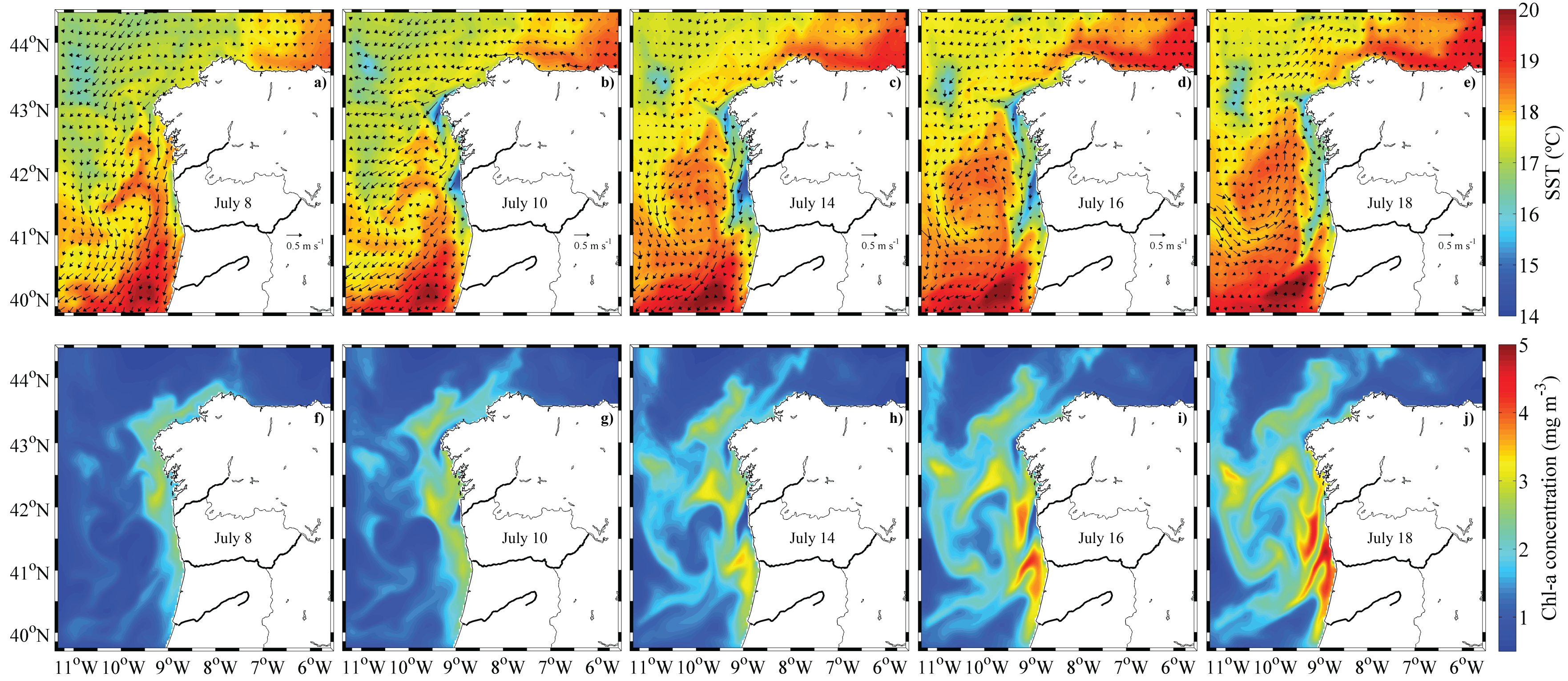

Figure 6.6: Daily averaged SST (°C), Chl-a concentrations (mg m^{-3}) for 8, 10, 14, 16 and 18 of July 2014. Vectors on SST maps are the daily average of the upper layer current velocity .

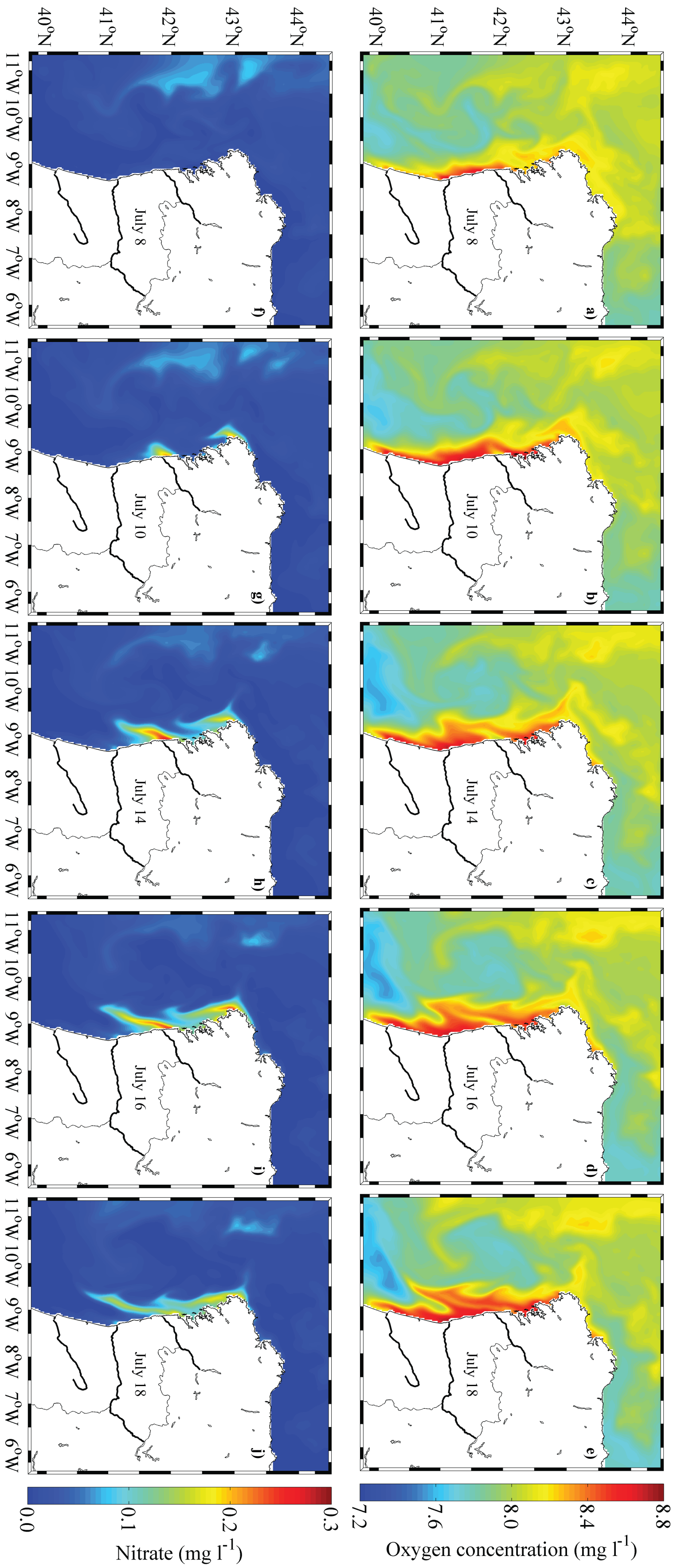

Figure 6.7: Daily averaged oxygen and nitrate concentrations (mg l^{-1}) for 8, 10, 14, 16 and 18 of July 2014.

Regarding the Chl-a distribution (Figure 6.6f), concentrations between 2 and 3 mg m^{-3} are observed near the coastal region at both western and intermediate segments, with current directed southward and southwestward, respectively.

Northern coastal segment is characterized by SST higher than 18°C at the longitude of 6°W, decreasing westward. This region is the least productive, with Chl-a concentrations lower than 1 mg m^{-3} and oxygen levels lower than 8 mg l^{-1}. The average nitrate concentration is low (less than 0.5 mg l^{-1}) in the whole study region (three coastal segments) for July 8 (Figure 6.7f).

As N-S wind component increases, near coast SST decreases and the equatorward flow is intensified (see Figures 6.6b, c and d), at western and intermediate coastal segments. The intensity of the coastal cooling is not homogeneous, but is reinforced in some locations where the vertical surface flux is stronger. Indeed, northerly winds lead to a decrease of more than 3°C in the adjacent region of Cape Finisterre and near Minho River, while south of Douro River only a decrease of approximately 1.5°C is observed. N-S wind component is stronger at northern regions (at boxes C and E of Figure 6.1) than at southern (box F of Figure 6.1) between days 8 and 11 (Figure 6.8), which is in accordance with Nelson and Hutchings (1983) statement that suggests that upwelling occurs preferentially where the continental shelf is narrowest and off salient capes.

During northerlies intensification period an increase of Chl-a and oxygen concentrations is observed at western and intermediate coastal segments, reaching values of 5 mg m^{-3} and 8.8 mg l^{-1}, respectively. However, near CFUC and MUC,

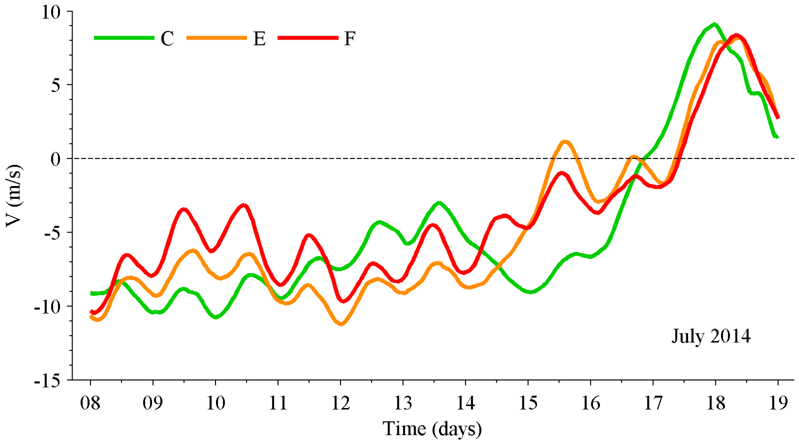

Figure 6.8: N-S wind component (m s^{-1}), at the boxes C, E and F represented in Figure 6.1.

where upwelling is stronger, an unexpected decrease of Chl-a and oxygen concentrations is observed along with an increase in nitrate concentration (Figure 6.7g, h and i). Upwelled waters have high nutrient concentrations as result of organic matter sinking from the sunlit layers into the deep ocean, where cells are decomposed by bacteria. This process enriches deep waters with nutrients that are transported to surface during upwelling events and are therefore available for photosynthesis. This nutrient rich upwelled waters become progressively richer in Chl-a when nutrients are consumed. However, in CFUC and MUC, the Chl-a concentration decreases and nutrients are not being consumed. This result can be explained by the low residence time of water masses in the euphotic layer, which is to short to allow significant multiplication of phytoplankton. Further offshore, where residence time at surface becomes higher, photosynthesis takes place (dissolved oxygen is produced) and therefore Chl-a (Figure 6.6g, h and i) and oxygen concentrations increase (Figure 6.7b, c and d). This situation is a common feature in Benguela upwelling system, where at least two of the existing upwelling cells in the region experiences a decay in Chl-a concentration due to strong surface flux (Hardman-Mountford et al., 2003; Demarcq et al., 2007).

At western coastal segment, six days after peak wind intensity, just before N-S wind component relaxation (lower than 5 m s^{-1}) (Figure 6.2a), Chl-a concentration is slightly higher (reaching 4 mg m^{-3} between Douro and Mondego Rivers) than during the days before and more confined to coast, as result of weakening of upwelling equatorward jet (Figure 6.6i). At July 18, two days after the relaxation phase and under calm wind conditions (close to 0 m s^{-1}), there is a general SST increase of approximately 1°C and the thermal gradient between coastal and offshore waters is smoother. At this time, surface Chl-a levels are further higher (between 4 and 5 mg m^{-3}) than during the preceding days and Chl-a and oxygen concentrations at CFUC and MUC increase (Figure 6.6j). Indeed, the available nutrients are being consumed by the existing phytoplankton (Figure 6.7j), and therefore nitrate concentration decrease to 0.1 mg l^{-1}.

The conditions at northern coastal segment are different than those observed at western and intermediate coasts. Indeed, a general increase of SST is observed over time, reaching values of 19°C on July 18. Here the current velocity is weak (less than 0.1 m s^{-1}) and directed westward, reaching a maximum of 0.2 m s^{-1} on July 16. The northern coastal segment is characterized by low Chl-a (less than 1 mg m^{-3}), nutrients (less than 0.5 mg l^{-1}) and oxygen concentrations (7.8 mg l^{-1}).

6.3.2.2 Temporal variability

In order to better understand the variability of Chl-a, SST and nutrients in the upwelling cells by comparison with other regions, time series of these variables (Figure 6.9) were analysed, between 8 and 18 July, in three regions: in CFUC and MUC (points X and Y of Figure 6.1, respectively) and in point W of Figure 6.1. Tidal frequencies of these properties were removed by using a 33 hours low-pass filter.

As previously referred, the SST decay during the intensification of northerly winds was more significant in MUC (point Y), where it decreases approximately 3.5°C (Figure 6.9). For CFUC (point X) the decrease is 1.5°C and at point W is only 1°C. The biological response to the rise of cold water from lower levels is different at upwelling cells and at point W. In CFUC and MUC, Chl-a concentration slightly increases (approximately 0.6 mg m^{-3}) from 8 to 9 July, decreasing then to very low values (1.7 and 0.6 mg m^{-3} at CFUC and MUC, respectively). At this time, nitrate concentration increases, as result of deep, nutrient-rich waters rise. In summary, in the upwelling cells wind stress promotes the offshore spreading of upwelled waters, yielding unfavourable conditions for phytoplankton growth, despite the high level of nutrient enrichment. This confirms the results found by Hardman-Mountford et al. (2003), which established that the major upwelling cells occur over narrow shelf areas

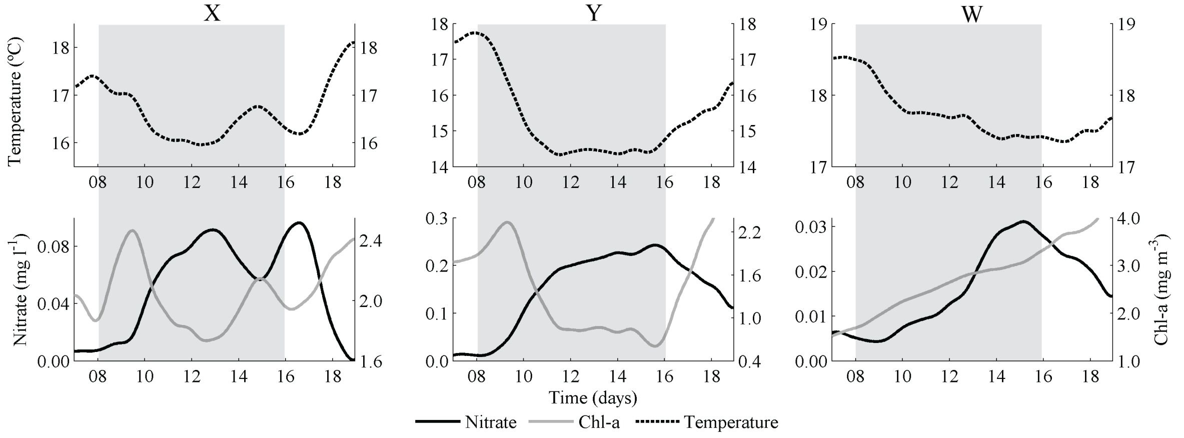

Figure 6.9: Time evolution of the water temperature (°C), Chl-a (mg m^{-3}) and nitrate (mg l^{-1}) concentrations for the squares X (left panel), Y (middle panel) and W (right panel).

leading to greater offshore losses. Conversely, at point W, the decrease of SST results in nitrate and Chl-a concentrations increase, reaching 0.03 mg l^{-1} and 3.5 mg m^{-3}, respectively. After the wind relaxation period (July 16), SST starts to rise and nitrate concentrations drop to very low values (0, 0.1 and 0.01 mg l^{-1} at X, Y and W points, respectively).

6.3.3 Vertical time evolution: July 2014 event

Temporal evolution of SST, Chl-a, oxygen and nitrate concentrations was also analysed between 7 and 19 July, along water column for X, Y, W, L and K points, being results depicted in Figures 6.10 to 6.14. Tidal frequencies of each property were also removed by using a 33 hours low-pass filter.

Regarding Figure 6.10, which is representative of CFUC (Point X) conditions, at July 8, the first 9 m of the water column (named mixed layer or epipelagic zone) are characterized by water temperature of 16.5°C, Chl-a concentration of 2.2 mg m^{-3} and very low nitrate concentrations (0.01 mg l^{-1}). Here the oxygen concentration is approximately 8.2 mg l^{-1} and a sub-superficial maximum (8.4 mg l^{-1}) is observed at 17 m depth (Figure 6.10e and f), which is associated to the presence of the well oxygenated ENACW in the thermocline (Castro et al., 2000). At the surface, the N-S component of the current velocity is directed southward with an intensity of 0.2 m s^{-1}, reaching a maximum of more than 0.3 m s^{-1} at July 10 (peak of N-S wind component). Along water column, vertical current velocity is approximately 0.006 cm s^{-1}. All the properties decrease with depth, except nitrate concentration that increases to values higher than 0.2 mg l^{-1}, as result of organic matter sink into deep waters. The mixed layer water temperature decreases over time, reaching a minimum of 14.5°C at July 12, when its depth is 8 m. Unexpectedly, surface Chl-a concentration decreases to 0.8 mg m^{-3} and nitrate concentrations increase to 0.2 mg l^{-1}. At July 15, an increase in surface water temperature (to 16°C) and Chl-a concentration (to 1.8 mg m^{-3}) is observed, which is related to N-S wind component relaxation that occurs in the preceding days (Figure 6.8). At the end of the event (July 17), N-S component of the current velocity at surface decreases to 0.1 m s^{-1} and a poleward flow develops in deep layers (-0.1 m s^{-1}). Surface waters downwelling is observed, with a vertical current velocity of -0.005 cm s^{-1} (Figure 6.10d) and therefore nutrients depletion occur at surface. An increase in

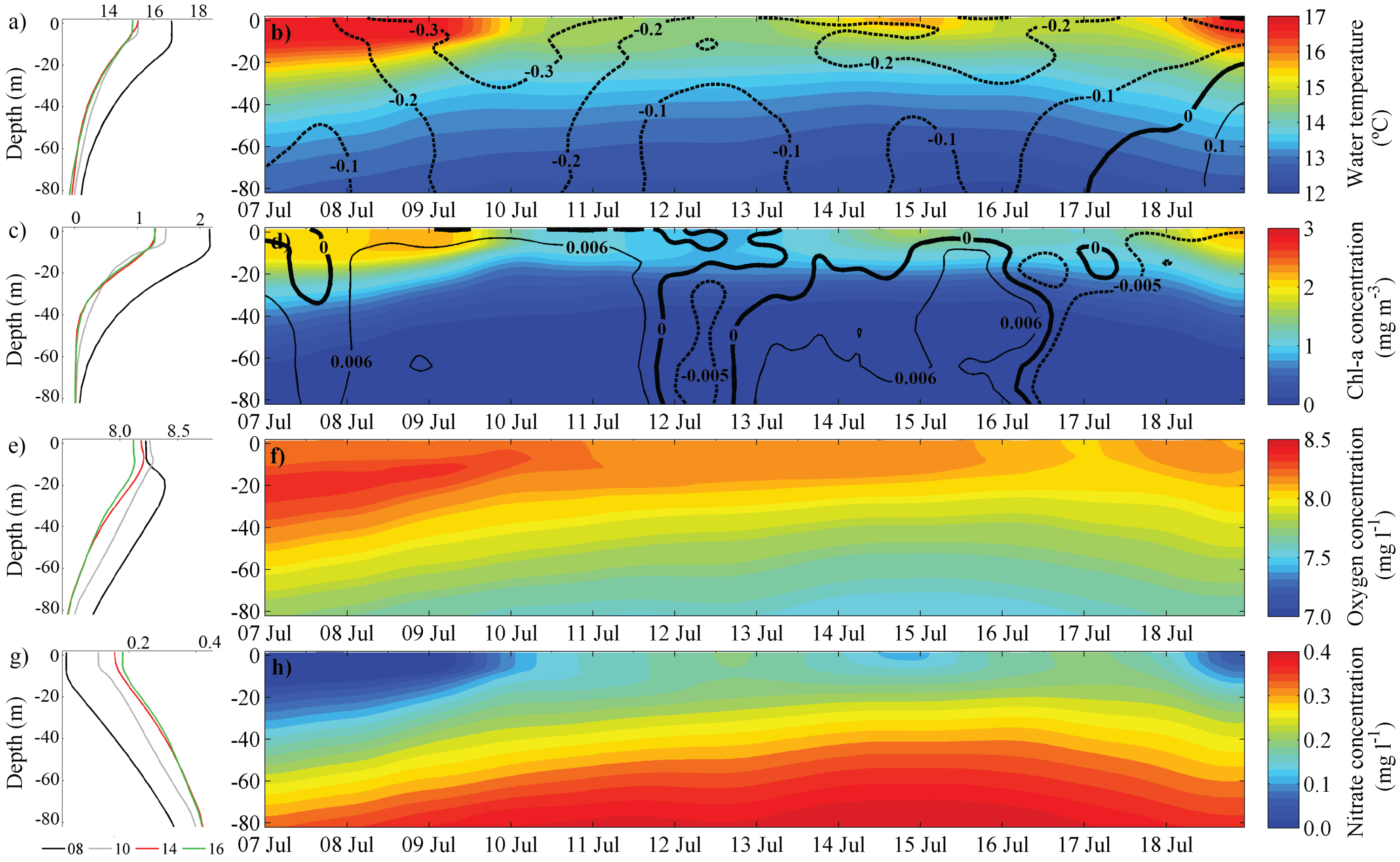

Figure 6.10: Time evolution of water temperature (°C) (a and b), Chl-a concentration (mg m^{-3}) (c and d), oxygen (e and f) and nitrate concentrations (mg l^{-1}) (g and h) along the water column, at point X. Contours in b represents the N-S component of current velocity (m s^{-1}) and in d the vertical current velocity (cm s^{-1}). Profiles are represented for days 8, 10, 14 and 16 of July.

surface water temperature (17°C), Chl-a (more than 2 mg m^{-3}) and oxygen (8.2 mg l^{-1}) concentrations are observed after July 18.

For MUC (point Y, Figure 6.11), at onset of the upwelling event (July 8), water temperature is approximately 18°C at the epipelagic zone, which has 18 m depth, where a sub-superficial maximum of Chl-a (1.8 mg m^{-3}) and oxygen (8.75 mg l^{-1}) concentrations occur (Figure 6.11e, f, g and h). These sub-superficial Chl-a and oxygen maxima are due to nitrate concentration increase at 18 m depth (Figure 6.11g and h). Here, the current velocity is directed southward along the water column, being stronger at the upper layers (0.2 m s^{-1}), due to wind stress. As deep water rises (0.005 cm s^{-1}), as response to northerly winds, water temperature decreases more than 2°C and the depth of the epipelagic zone gradually decreases, reaching 16 m on July 10. At this time nitrate concentration increases along water column, reaching 0.1 mg l^{-1} at surface. As consequence, in the epipelagic zone Chl-a and oxygen concentrations also increase to 2 mg m^{-3} and 8.5 mg l^{-1}, respectively. However, at thermocline, Chl-a and oxygen concentrations decrease to values lower than those found in previous instants, which is due to high concentrations in the upper levels that not allow the penetration of light at this depth.

Until July 14, water temperature, Chl-a, oxygen and nitrate vertical gradients decrease (Figure 6.11a, e and g). At the epipelagic zone water temperature reaches a minimum of 14.5°C and nitrate reaches a maximum of 0.2 mg l^{-1} on July 13 (Figure 6.11a, b, e and f). As in CFUC, Chl-a and oxygen concentrations gradually decrease, which can be explained by the residence time, which is insufficient for phytoplankton to complete nutrient uptake and carry out photosynthesis. At the end of the event (from July 17) water temperature increases and N-S component of current velocity attenuates on the upper layers (to -0.1 m s^{-1}), reversing in deeper layers and therefore resulting in an increase of ocean stratification, which is accompanied by the shallowing of the epipelagic zone. Chl-a and oxygen maxima are now observed, reaching concentrations of 3 mg m^{-3} and 8.5 mg l^{-1}, respectively.

Regarding the southern part of the study area (point W), the decrease of water temperature with the intensification of northerly winds is less accentuated (1°C) than for CFUC and MUC and therefore the Chl-a concentration patterns are different. At beginning of the upwelling event, N-S component of current velocity has a

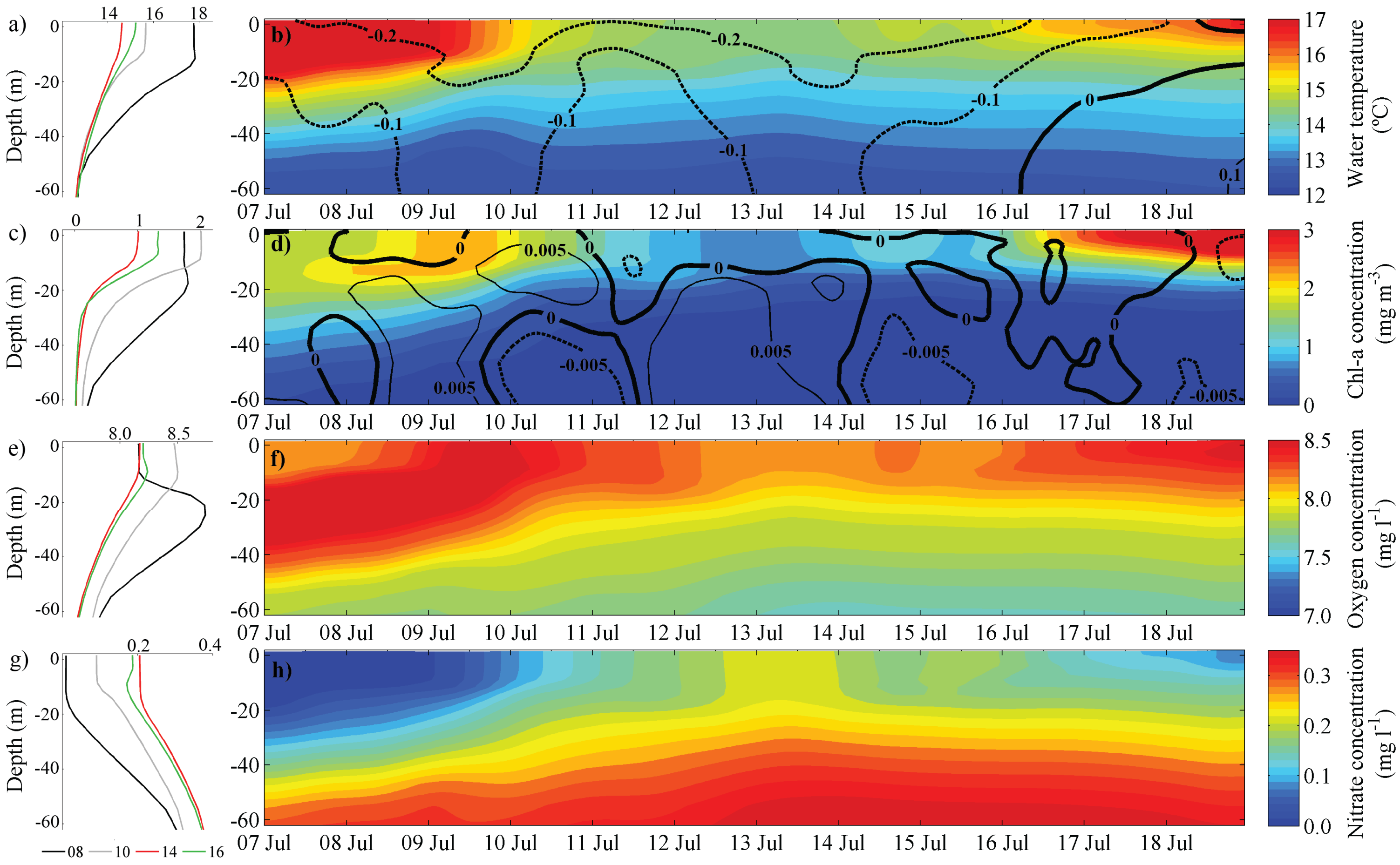

Figure 6.11: Time evolution of water temperature (°C) (a and b), Chl-a concentration (mg m^{-3}) (c and d), oxygen (e and f) and nitrate concentrations (mg l^{-1}) (g and h) along the water column, at point Y. Contours in b represents the N-S component of current velocity (m s^{-1}) and in d the vertical current velocity (cm s^{-1}). Profiles are represented for days 8, 10, 14 and 16 of July.

similar distribution to previous points analysed along time and water column, flowing southward with an intensity of 0.2 m s^{-1} in the upper and 0.1 m s^{-1} in deeper layers (Figure 6.12b). The epipelagic zone in this area is approximately 10 m deep and slightly decreases over time (Figure 6.12a). At July 8, oxygen concentration is approximately 8.1 mg l^{-1} in epipelagic zone and increases along water column, reaching a maximum of 8.8 mg l^{-1} at 19 m depth. Chl-a concentration is almost homogeneous along water column, with an average value of 1.7 mg m^{-3} (Figure 6.12c and d). Deep waters start to rise at July 10 with a vertical velocity of 0.001 cm s^{-1}, which is weaker than for CFUC and MUC. Conversely to upwelling cells, Chl-a concentration increases over time on the epipelagic zone, reaching values higher than 4 mg m^{-3} at the end of the upwelling event. Chl-a concentration becomes much lower at deep layers than at epipelagic zone, which can be explained by thermal stratification that helps phytoplankton to stay in the well-lit mixed layer zone and therefore supports primary production. Otherwise, once the surface layers are well mixed, light is not able to penetrate in deeper waters (thermocline) and a decrease of Chl-a concentration is observed. However, because mixed layer is difficult to mix deeply, it becomes depleted in nutrients (Figure 6.12h). In summary, results show a clear relation between thermal stratification and nutrient availability, highlighting the importance of ocean physical structure in primary production patterns.

Regarding point L, representative of intermediate coastal segment, the mixed layer on July 8, which has 10 m depth, is characterized by water temperature of approximately 17°C and Chl-a concentration of 1.7 mg m^{-3} (Figure 6.13a, b, c and d). At this time vertical current is approximately 0.005 cm s^{-1}, bringing the nutrients from deep layers to surface, where they are consumed by phytoplankton organisms and therefore producing oxygen. Also, a sub-superficial oxygen maximum (8.5 mg l^{-1}) is observed at beginning of the event, being transported towards surface over time (Figure 6.13f). An equatorward flow is observed, with an intensity of approximately 0.05 m s^{-1}. Over time, mixed layer depth decreases reaching a minimum of 2.5 m on July 14, and Chl-a concentration increases to 2 mg m^{-3}.

At northern coastal segment (point K), the epipelagic zone has a constant depth of approximately 20 m during all period analysed (Figure 6.14a and b), characterized by high water temperature (between 18 and 19°C). This high SST causes a stable water-

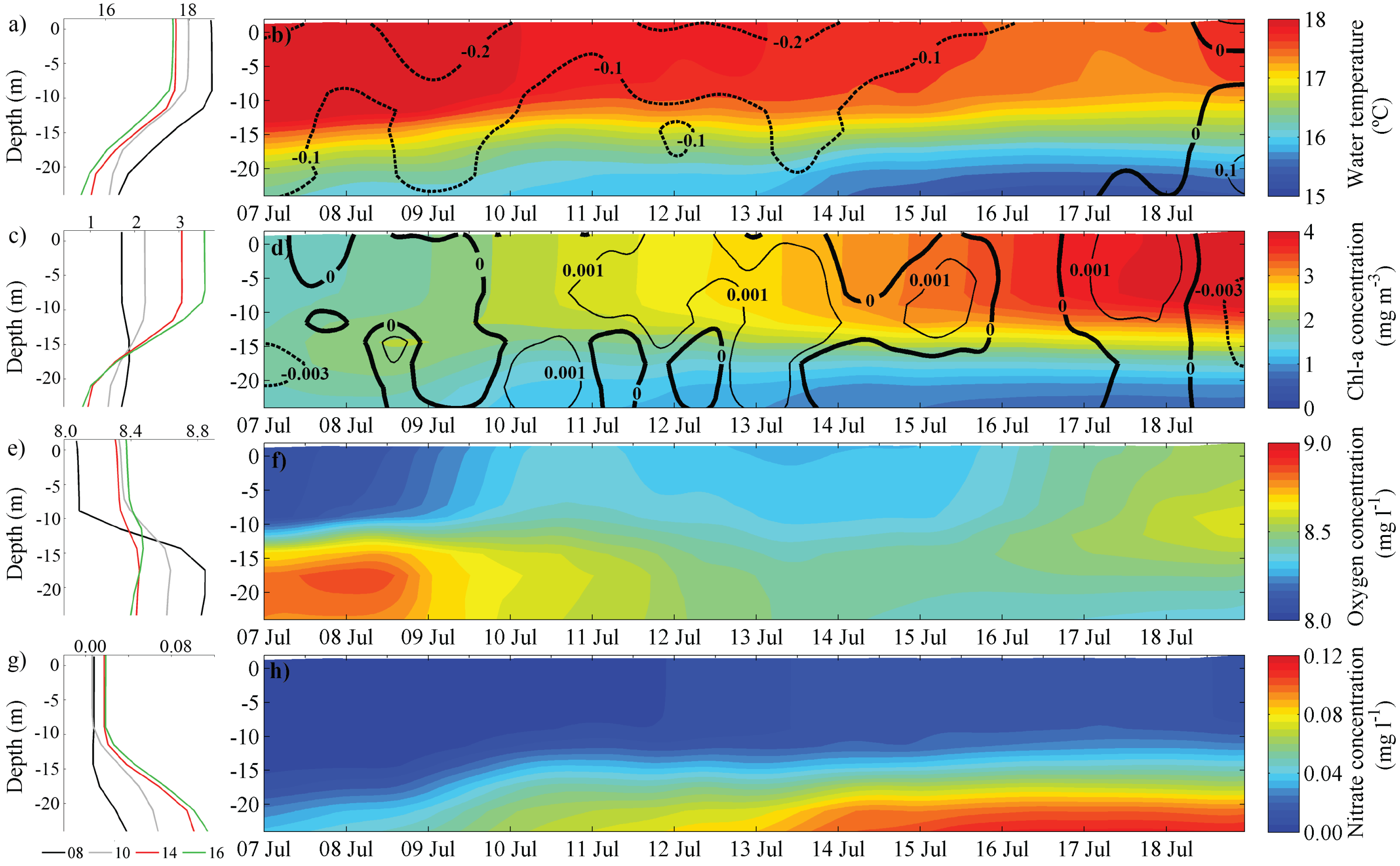

Figure 6.12: Time evolution of water temperature (°C) (a and b), Chl-a concentration (mg m^{-3}) (c and d), oxygen (e and f) and nitrate (g and h) concentrations (mg l^{-1}) along the water column, at point W of Figure 6.1. Contours in b represents the N-S component of current velocity (m s^{-1}) and in d the vertical current velocity (cm s^{-1}). Profiles are represented for days 8, 10, 14 and 16 of July.

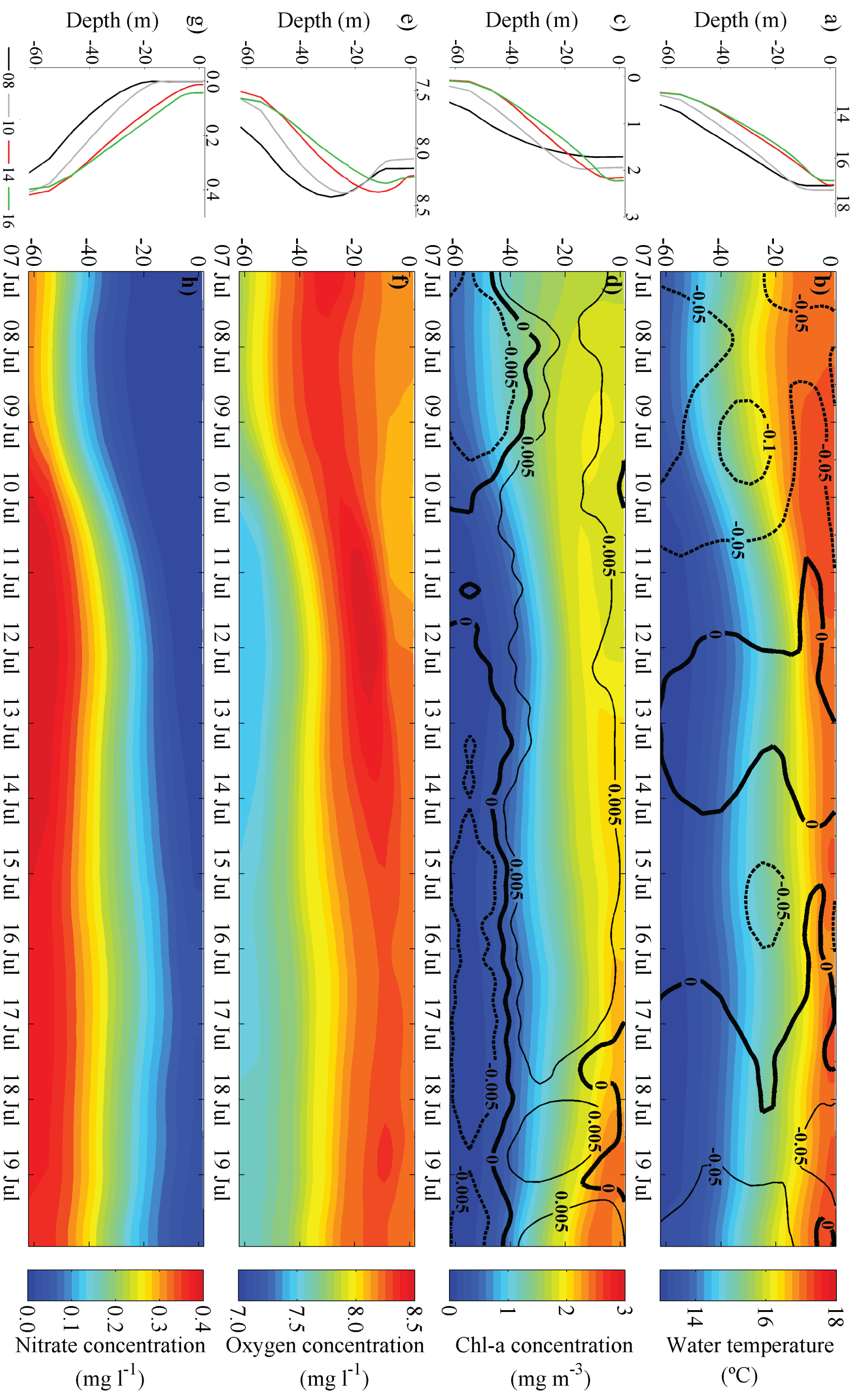

Figure 6.13: Time evolution of water temperature (°C) (a and b), Chl-a concentration (mg m^{-3}) (c and d), oxygen (e and f) and nitrate concentrations (mg l^{-1}) (g and h) along the water column, at point L. Contours in b represents the N-S component of current velocity (m s^{-1}) and in d the vertical current velocity (cm s^{-1}). Profiles are represented for days 8, 10, 14 and 16 of July.

column, resulting in stratification that might limit nutrient injection into the euphotic zone, as observed through Figure 6.14g and h, and therefore primary production observed herein is weaker than at western coastal segment. Indeed, in upper layers, Chl-a concentration is approximately 1.2 mg m^{-3} on July 8 decreasing to values lower than 1 mg m^{-3} on July 18. A positive vertical flow is observed (0.003 cm s^{-1}) on July 9, as result of easterly winds observed in the region (Figure 6.2c), however not strong enough to reduce the mixed layer depth and provide nutrients for photosynthesis. Nutrients that eventually reach surface are consumed by the existent phytoplankton (Figure 6.14d).

Here, the general surface circulation flows eastward, however in summer change to westward following the wind forcing (Lavín et al., 2006). Indeed, during the period of easterly winds (between July 8 and 12 and July 15 and 17) along shore current velocity is directed westward (0.1 m s^{-1}), while during westerly winds (between 12 and 15) current velocity is directed eastward (0.05 m s^{-1}) (Figure 6.14b).

Regarding oxygen distribution along water column, low concentrations are detected at surface (7.7 mg l^{-1}), while a maximum (8.5 mg l^{-1}) is observed in the thermocline during all the period under analysis. In fact, the study region has the particularity of being well oxygenated due to the presence of ENACW in the main thermocline (Castro et al., 2000; Reboreda et al., 2015). Therefore, once the water mass that upwells in the northern coastal segment is the BBCW, a variety of subpolar ENACW (Tréguer et al., 1979; Fraga et al., 1982; Botas et al., 1989), are expected high levels of oxygen in thermocline, that do not reach the surface due to the low vertical current observed during this event.

6.3.4 Comparison between July 2014 and August 2013 upwelling events

In order to better understand the origin of the decay of Chl-a levels in upwelling cells, July 2014 was compared with August 2013 event, in which this decay does not occur. As previously referred, the latter event is characterized by lighter winds than July 2014 and although the generation of two upwelling cells (CFUC and MUC) is also observed.

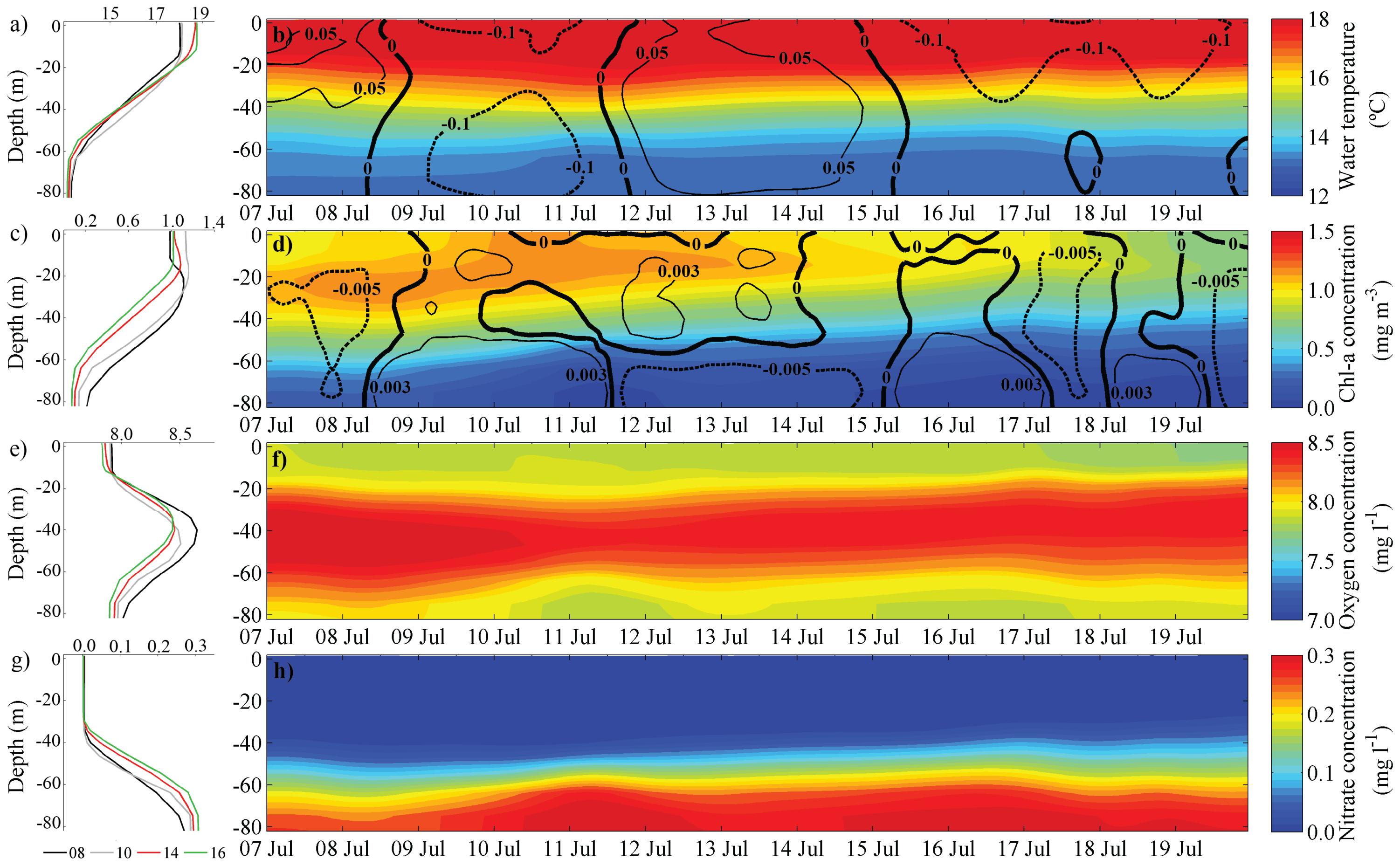

Figure 6.14: Time evolution of water temperature (°C) (a and b), Chl-a concentration (mg m^{-3}) (c and d), oxygen (e and f) and nitrate concentrations (mg l^{-1}) (g and h) along the water column, at point K. Contours in b represents the N-S component of current velocity (m s^{-1}) and in d the vertical current velocity (cm s^{-1}). Profiles are represented for days 8, 10, 14 and 16 of July.

6.3.4.1 Vertical structure of SST, Chl-a concentration and circulation patterns

Based on previous results, vertical structure of daily average SST and Chl-a concentration along with zonal and meridional current velocities were analysed in two sections (Figure 6.1): one located in front of Cape Finisterre (section I at 42°54′N) and other in front of Minho River (section II at 41°52′N), for both upwelling events. Results are presented in Figures 6.15 to 6.18, for three moments: onset of upwelling, peak of N-S wind component and at beginning of wind relaxation.

Regarding Cape Finisterre section (section I), during onset of upwelling, vertical temperature pattern is similar for both events (Figures 6.15a and 6.16a), with higher temperatures at surface layers. However, for July 2014, a slightly water temperature difference between coastal (17°C) and offshore (17.5°C) waters is noticeable, while for August 2013 the zonal water temperature is almost uniform (18.5°C in upper layer). This is related with wind pattern of preceding days that were characterized by short periods of strong northerly winds in 2014. Flow is directed westward at upper layers for both situations, with an intensity of 0.05 m s^{-1} and eastward in depth. Chl-a patterns are also similar, with higher concentrations near the coast than offshore, 1.5 mg m^{-3} for 2013 and more than 2 mg m^{-3} for 2014. N-S component of the current velocity suggests that the flow is equatorward, with higher values on the surface (-0.2 m s^{-1} near coast and -0.1 m s^{-1} offshore). At deep levels a poleward slope-trapped flow is found for both situations, however in 2014 event this flow almost reaches the surface (Figures 6.15b and 6.16b). Oliveira et al. (2009) found similar Chl-a concentration, water temperature and current patterns during the first days of an upwelling event off central Portugal.

During peak of N-S wind component, for July 2014, the zonal thermal gradient is clearly identifiable (Figure 6.16c), with a difference of approximately 2°C. It is also detected a surface core of Chl-a concentrations higher than 2 mg m^{-3} near 9.6°W, while near coast Chl-a concentration is low (less than 1 mg m^{-3}). This is related with strong southwestward flow (-0.2 m s^{-1}), that promotes offshore transport of coastal waters. For August 2013, this thermal gradient is also detected, however located slightly westward, with the productive (2 mg m^{-3}) water retained near the coastal area by weak poleward flow (0.05 m s^{-1}) visible in Figure 6.15. Indeed, poleward current

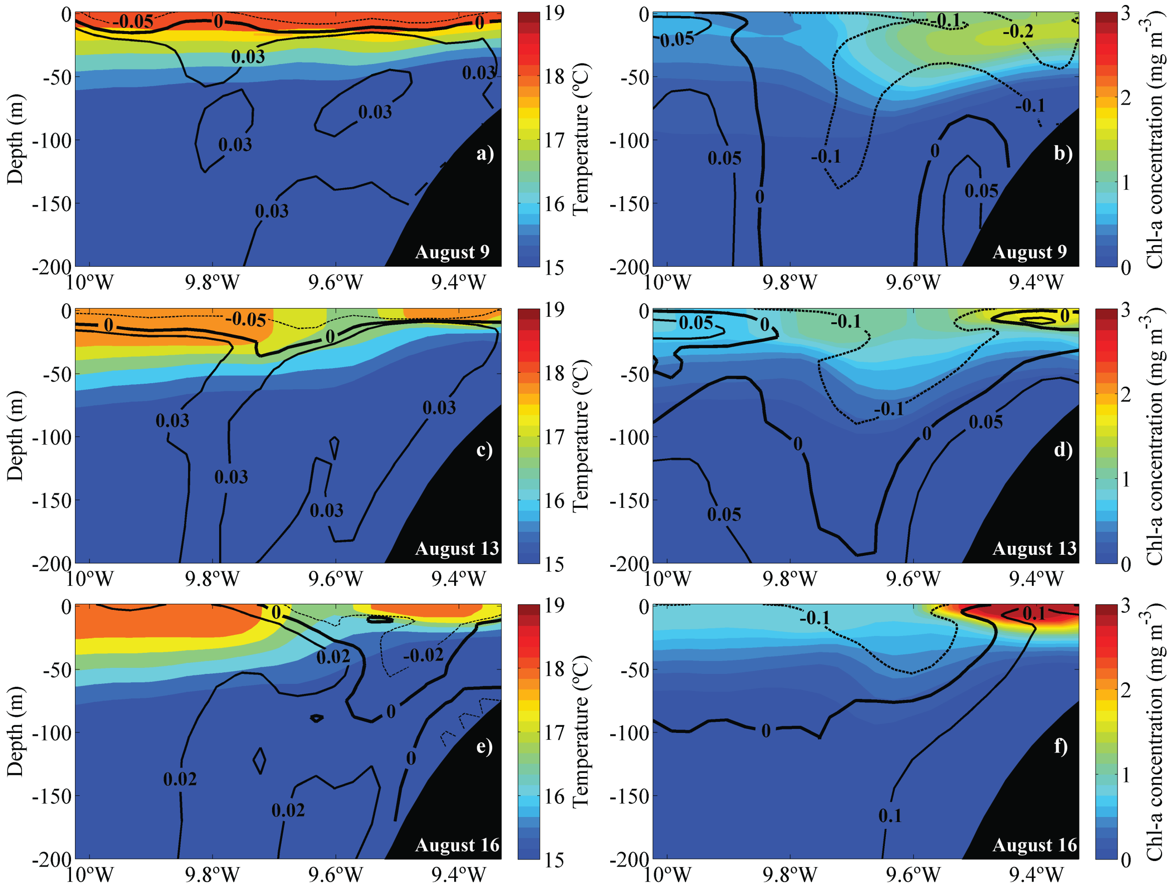

Figure 6.15: Daily average vertical temperature (a, c and e) and Chl-a concentration (b, d and f) along the zonal transect 42°54′N (setion I at Figure 6.1), for 2013 upwelling event and for three moments: onset of upwelling (August 9), peak of N-S wind component (August 13) and at beginning of the relaxation period (August 16). Contours in a, c and e represents the W-E component of current velocity and in b, d and f the N-S component.

would increase during the reinforcement of northerly winds (Pérez et al., 1995; Bode et al., 2002) and according to Arístegui et al. (2009), features such as poleward flows could help to promote retention over the shelf, spreading phytoplankton rich waters in alongshore direction.

Finally, at beginning of relaxation phase (Figures 6.15e, f and 6.16e, f), vertical water temperature patterns are similar to previous instant analysed and between both events. A weakening of near surface westward flow is observed and, for August 2013 case, near the coastal region, this flow extends up to 50 m depth, while for 2014 it is confined to surface layer. The core of high Chl-a concentration detected before is stronger now and slightly dispersed westward. Moreover, poleward (equatorward) flow is intensified (weakened) for August 2013 (July 2014) event. Indeed, when upwelling

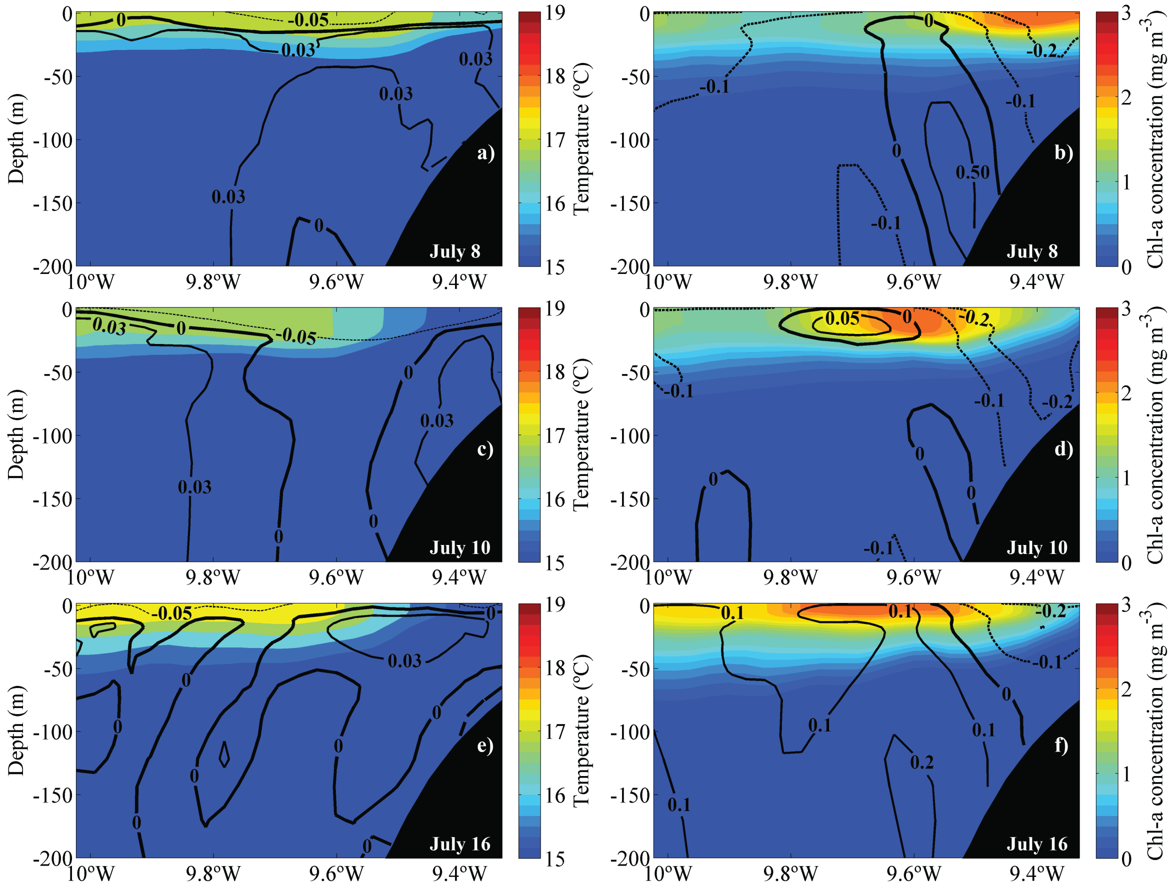

Figure 6.16: Daily average vertical temperature (a, c and e) and Chl-a concentration (b, d and f) along the zonal transect 42°54′N (section I at Figure 6.1), for 2014 upwelling event and for three moments: onset of upwelling (July 8), peak of N-S wind component (July 10) and at beginning of the relaxation period (July 16). Contours in a, c and e represents the W-E component of current velocity and in b, d and f the N-S component.

favourable wind relaxes, equartorward currents often weaken and then reverse to form poleward currents (Otero et al., 2008; Shulman et al., 2010).

In summary, main differences between the two analysed situations are detected after the establishment of upwelling and refers to N-S component of current velocity, and therefore in the efficiency trapping of phytoplankton, which is high (low) when N-S wind component is weak (strong). Results for the section near Minho River (section II) confirms these assumptions (Figures 6.17 and 6.18).

At section II, a zonal water temperature difference of approximately 1°C was found at the onset of both events (Figures 6.17a and 6.18a). This difference is enhanced with the intensification of northerly winds, reaching 2°C for 2013 event and 3°C in 2014, at peak of N-S wind component. W-E component of the current velocity in upper layers

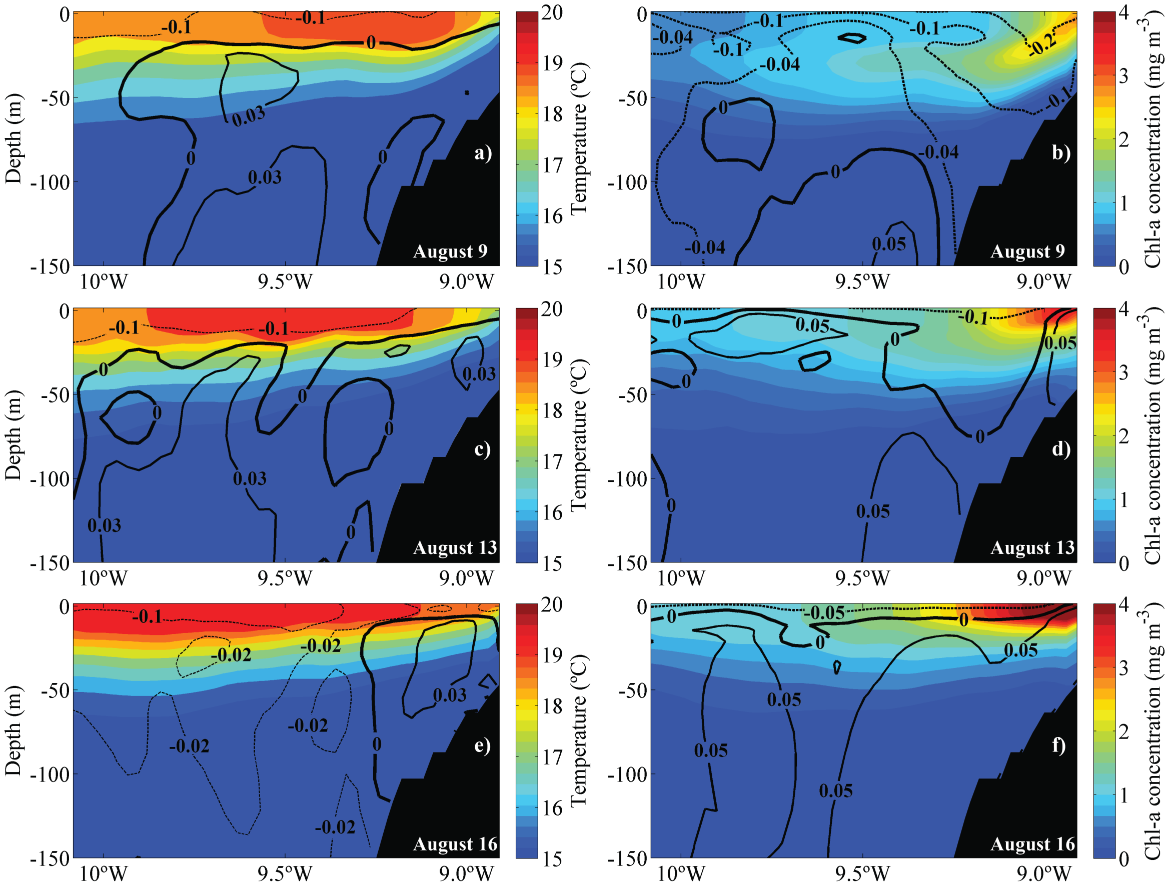

Figure 6.17: Daily average vertical temperature (a, c and e) and Chl-a concentration (b, d and f) along the zonal transect 41°52′N (section II at Figure 6.1), for 2013 upwelling event and for three moments: onset of upwelling (August 9), peak of N-S wind component (August 13) and at beginning of the relaxation period (August 16). Contours in a, c and e represents the W-E component of current velocity and in b, d and f the N-S component.

is directed westward for both cases, with higher current for July 2014 event (higher than -0.1 m s^{-1}).

For 2013, a core of high Chl-a concentration (2.5 mg m^{-3} at August 9 and more than 4 mg m^{-3} at August 16) is also found near the coast. A poleward flow, slightly weaker than in section I, is observed (0.05 m s^{-1}), promoting retention over the shelf.

For 2014 event, at the latitude of section II, wind relaxation phase occurs in July 14 (two days earlier than at section I), as depicted in Figure 6.8. Therefore, vertical water temperature, Chl-a concentration and current velocities are represented for this day instead July 16 (Figure 6.18). Here, a westward displacement of the high Chl-a concentration core (3 mg m^{-3}) is observed, being associated with the equatorward flow observed along water column, which is stronger on surface layer (-0.2 m s^{-1}) (Figures

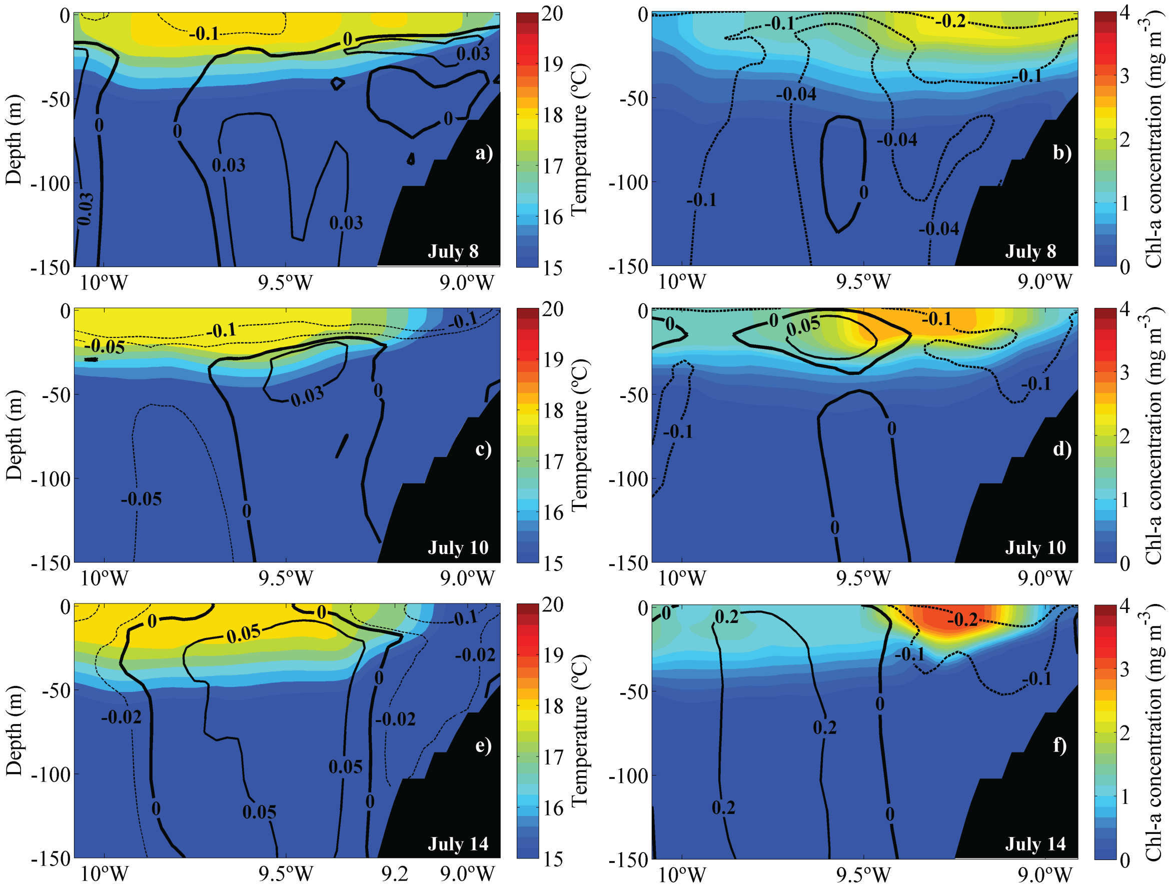

Figure 6.18: Daily average vertical temperature (a, c and e) and Chl-a concentration (b, d and f) along the zonal transect at 41°52′N (section II at Figure 6.1), for 2014 upwelling event and for three moments: onset of upwelling (July), peak of N-S wind component (July 10) and at beginning of the relaxation period (July 14). Contours in a, c and e represents the W-E component of current velocity and in b, d and f the N-S component.

6.18d and f).

Therefore, when strong upwelling events occur (July 2014) circulation patterns, namely the strong equatorward flow near coast, promote phytoplankton off shelf export (Figure 6.19a). Thus, photosynthesis occur in outer shelf waters and therefore Chl-a levels increase. Otherwise, for weak upwelling events (like August 2013) a poleward flow develops near coastal region promoting the retention of phytoplankton near surface layers. These conditions are outlined in Figure 6.19b.

6.3.4.2 Potential phytoplankton pathways

As previously referred a particle tracking model was used to analyse water parcel trajectories for both events. Particles were continuously released at surface during

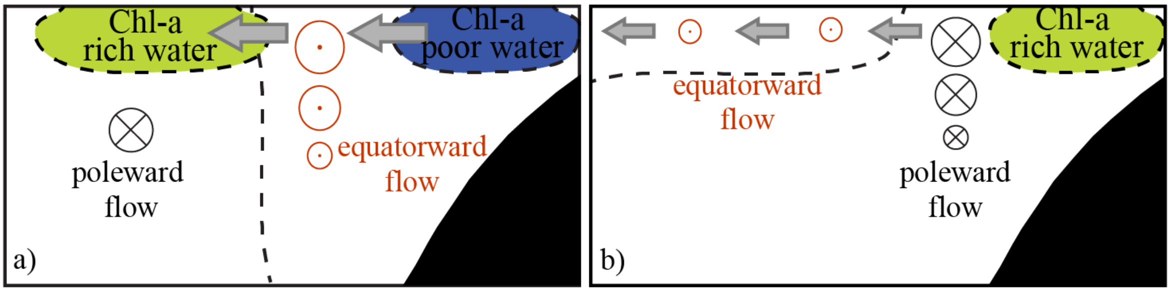

Figure 6.19: Schematic cross-sections of the upwelling cells for a) a strong upwelling event and b) a weak upwelling event.

upwelling onset and their location was analysed 48, 96 and 132 hours after release, with results presented in Figure 6.20.

In general, results suggest that particles released at boxes B (located at intermediate coastal segment), C and D (located at northern part of western coastal segment) tend to be advected southwestward over time, for both upwelling events (Figure 6.20), due to the contribution of wind intensity and direction, which is northeasterly. However, it seems that for July 2014 event this advection occurs faster. Indeed, 48 hours after release (Figure 6.20a and d), 91% of the particles released at box C crossed the 200 m isobath (limit of continental shelf (Patti et al., 2008)), whereas for 2013 event only 78% of the particles crossed this isobath. 96 hours after release, all particles have already passed the 200 m isobath, for both cases, however for 2014 event, particles are more dispersed than in 2013. The difference between both events is higher for particles released at box D. For the 2014 event, the percentage of particles that have crossed the 200 m isobath, 48 hours after release, is 36.5%, while for 2013 event is only 9% (Figure 6.20a and d). 96 hours after (Figure 6.20b and e) the percentage increases to 95% (84%) for 2014 (2013) event.

Regarding particles with origin at box B, 48 hours after release, all particles remain near the coast for both events, however, 96 hours after, 13%(22%) of the particles, for 2013 (2014) event, were advected to western coastal segment and have crossed the 200 m isobath (Figure 6.20b(e)).

132 hours later, particles with origin at boxes B, C and D remained between 10 and 11°W, however due to stronger current velocities observed during July 2014, particles are spread from 40°N to 42.5°N, while for August 2013, the majority of particles are accumulated off Douro River (in the outer shelf) (Figure 6.20c and f).

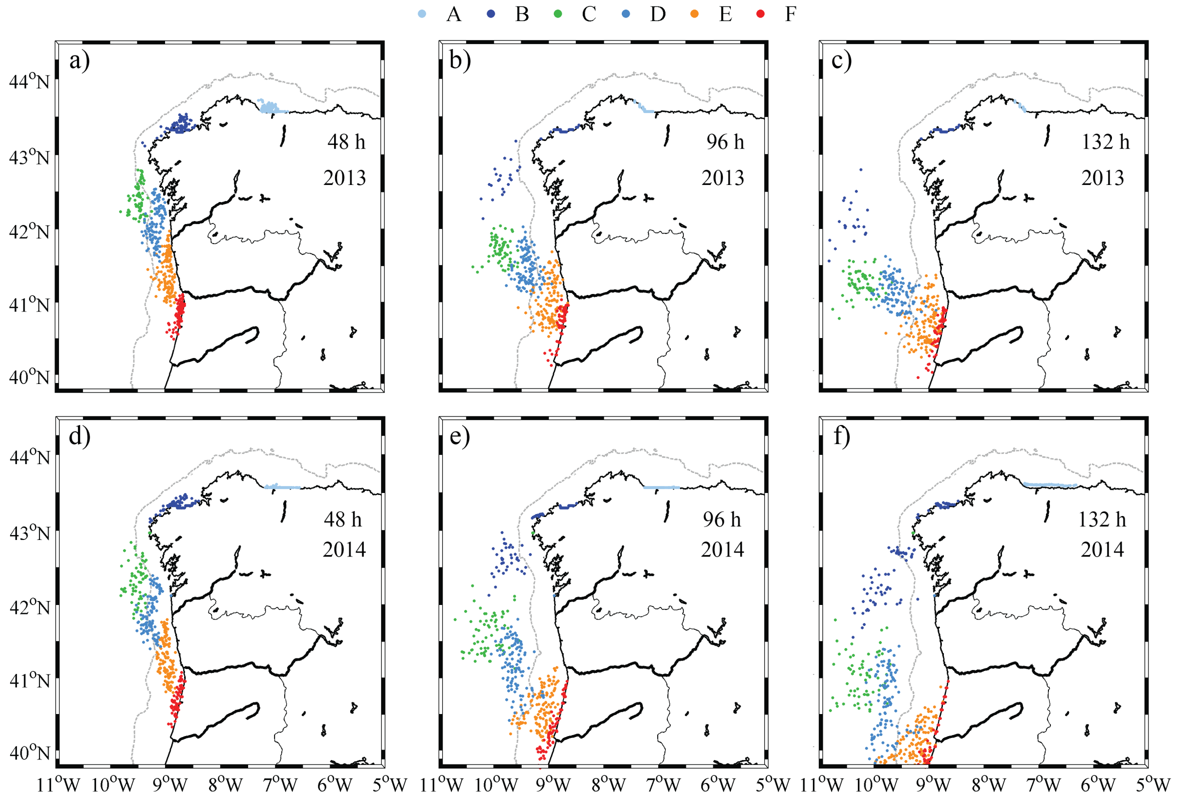

Figure 6.20: Position of particles released during the onset of upwelling events (July 8, 2014/August 9, 2013) at sites represented in Figure 6.1, 48 hours (a and d), 96 hours (b and e) and 132 hours (c and f) after the onset of upwelling.

Concerning particles with origin at northern coastal segment (box A) it is noteworthy that they are retained near coast, for both events. This happens due to coastline orientation and current velocity that, despite being directed westward, is not strong enough (0.1 m s^{-1}) to transport near coast water parcels from northern coastal segment to western segment (Figure 6.20).

Finally, particles released at southern part of western coastal segment (boxes E and F) seem to accumulate in inner shelf, however with some differences between both upwelling events. Indeed, 132 hours after release, an accumulation of particles from boxes E and F are found from 40.5°W to the southern part of study region, while for 2013 event the accumulation area extends from the Minho until the Mondego River (6.20c and f).

The trajectories obtained with the particle tracking model confirmed earlier suggestions: that for July 2014 event phytoplankton generated near Cape Finisterre and Minho River does not have enough time for multiplication, due to the strong surface currents observed. For August 2013 event, water parcels are advected slower than for 2014, and photosynthesis takes place near the coast, generating high levels of Chl-a concentration. For both events, an accumulation of Chl-a rich water is observed in the southern part of western coastal segment, which could be explained by the wider (between $60 - 65$ km near the Mondego River) continental shelf that favours the trapping of nutrients and phytoplankton near coast (Arístegui et al., 2009).

6.4 Conclusions

The numerical model MOHID was used to describe the spatial and temporal evolution of physical-biological features during two summer upwelling events off northwestern coast of IP. Main conclusions of this study are the following:

- From average fields of SST, two upwelling cells (CFUC and MUC) were found during both upwelling events analysed;
- For the strongest event, a decay of Chl-a concentration was observed over time in the upwelling cells, which may be attributed to the short residence time of water parcels on coastal ocean surface, due to a strong southwestward jet observed at these regions, which promotes offshore transport of pigment-rich water;
- During weak upwelling events an inverse relation between SST and Chl-a concentration was found, *i.e.*, Chl-a concentration is maximum in the upwelling cells. In this case, lighter upwelling favourable winds induce weaker surface currents;
- Results of in depth analysis carried out in cross-sections representative of upwelling cells, suggested that when strong northerly winds occur, a strong equatorward flow develops near coast promoting off-shelf export of phytoplankton, and therefore high levels of Chl-a concentration are advected to the outer shelf region. Conversely, during weak upwelling events, circulation in upwelling cells promote retention of nutrients and phytoplankton near coastal region. A poleward flow develops near coast and offshore transport is weak and therefore high levels of Chl-a are found here;

- The set of particles released at onset of upwelling events confirmed previously conclusions. A general southwestward displacement of particles released at intermediate and northern part of western coastal segments are observed, however this transport is faster for strong upwelling conditions. Also, particles released at southern part of western coastal segment tend to accumulate in the inner shelf for both cases, once wider shelves tend to favour the trapping of nutrients and phytoplankton.

Chapter 7

Final conclusions

This chapter provides a summary of the thesis main results, which main objective was to understand the physical factors that influence primary production along the northwestern coast of IP. With this propose two approaches were used: remote sensing imagery analysis and numerical modelling. Due to the coastline direction, three coastal segments were considered: western (from 40 °N to 43 °N, north-south direction), intermediate (between Cape Finisterre and Cape Ortegal, northeast-southwest direction) and northern (between 8 °W and 5 °W, west-east direction) coastal segments.

The study began with a ten years (1998-2007) general characterization of the study area through remote sensed data in terms of Chl-a concentration, SST, wind-derived UI, Ekman transport and *in situ* river discharges. All these variables were analysed simultaneously to interpret the main spatio-temporal processes that occur in this highly dynamic region and explore the enrichment mechanisms that occur in euphotic layer, highlighting differences between each coastal segment.

A seasonal analysis was performed and results revealed high seasonal variability and different annual cycles in each coastal segment. Indeed, for western coastal segment the strongest Chl-a levels occur during spring (AMJ) and summer (JAS), which are related to the frequent upwelling events that allow the displacement of cold and nutrient rich waters to surface layers. Actually, during this period Ekman transport is strong and directed westward and a water lens of cold water is observed in the region. During winter (JFM) and autumn (OND) high primary production levels are also detected. These conditions may be related to the cumulative effect of winter upwelling events and river runoff (Mondego, Douro and Minho), favouring the entrance of nutrients onto the coast, as well as the mixing/stratification season cycle, which transport nutrients to surface in winter. However, river plumes may also induce surface stratification which may be a restrictive factor to phytoplankton growth, by limiting light availability. At intermediate coastal segment, conditions are similar to those described for western coastal segment, however production levels are slightly lower. In fact, in spring and summer months the Ekman transport is upwelling favourable but less intense comparing to that observed at western coastal segment. Likewise, the river that influences the region (Eume) has a very low flow and therefore primary production generated from the input of nutrients from land is also low. Moreover, from maxima Chl-a levels and timing of these maxima, it can be concluded that, in western and intermediate coastal segments, the mechanism that most influences phytoplankton growth is upwelling, once maxima values occur during upwelling season (August and September). Northern coastal segment is the least productive, and showed an opposite pattern, with the highest Chl-a concentrations occurring during autumn (OND) and winter (JFM). However, in the surroundings of Nalon River mouth high Chl-a levels exists most of the year. JFM peaks are associated with the transitional period from winter mixing to summer stratification periods that favour phytoplankton blooms. For remaining seasons, Chl-a high levels are attributed to the presence of Nalon River that is an important source of nutrients in the region, once during this period the Ekman transport is strong and directed southward (upwelling unfavourable at northern coastal segment).

An empirical orthogonal function (EOF) analysis was applied to the weakly images of Chl-a concentration over the whole study area, using the SVD method. This kind of analysis provides a compact description of temporal and spatial variability of long time series. Results suggest that dynamics of the first mode that contains 21.54% of the data total variance, is only related with dynamics of nearshore region of western and intermediate coastal segments, once positive coefficients were found. Positive deviation from the mean values were found for JAS for all years. Otherwise, coefficients computed for northern coastal segment are close to zero. Second EOF mode explains 8% of total Chl-a variance and its spatial variability allows to identify two regions: one northward Minho River (42 °N), including intermediate and northern coastal segments, with strong negative coefficients and other comprising the Portuguese coast (southward Minho River). This indicates a dynamical response of different phases in these two regions, which are associated with the vertical mixing cycle.

The influence of upwelling events and river runoff on Chl-a patterns along IP northwestern coast was also analysed considering the interannual variability of SST, Chl-a concentration, UI and river discharges as well as correlation coefficients between these variables, for summer (JAS) and winter (JFM/FMA). Results suggest that at western and intermediate coastal segments, 2005, 2006 and 2007 were the most productive years during summer season, which is associated with cold waters, strong upwelling favourable UI and low discharges. Indeed, strong positive (negative) correlations were found between Chl-a concentration and UI (SST) during JAS for three locations at western coastal segment: 0.40 (-0.52) near Mondego, 0.35 (-0.26) near Minho and 0.33 (-0.36) near Douro Rivers and for the location at intermediate coastal segment: 0.43 (-0.30) near Eume River mouth. The least productive years were 2003 and 2004 for western and 1999 and 2004 for intermediate coastal segments. During winter, in general, primary production is weaker, however some particular situations should be highlighted. For instance, 1998 and 2001 showed high Chl-a concentration at western coastal segment. The absence of upwelling favourable conditions together with localized low SST and considerable discharges suggests that this high levels of Chl-a is mainly attributed to nutrients input from land. Indeed, correlation analysis corroborate this assumption. A correlation coefficient of 0.29, 0.51 and 0.43 was found between Chl-a concentration and discharges of the Mondego, Minho and Douro Rivers, respectively.

At northern coastal segment during the summer season low Chl-a concentrations were generally observed, however 2007 revealed high values in September, which are associated to strong upwelling UI observed here. Correlation coefficients of 0.22 (-0.28) were found between Chl-a concentration and UI (SST). During winter, high levels of phytoplankton were mainly detected during March, being 2005 and 2006 the most productive years. Indeed, at northern coastal segment, these years were characterized by extreme mixed layer deepening, resulting in a nutrient increase and consequently high levels of Chl-a occur. Discharges from Nalon River are also important during JFM and a correlation with Chl-a concentration of 0.25 was found.

The study of forcing mechanisms of phytoplankton formation and growth is of extreme importance in such a highly dynamic region. Moreover, several analysis of ocean temperature all around the world reveal a global warming trend in the ocean and an acceleration of coastal upwelling circulation, inducing changes on phytoplankton development and therefore in the whole marine ecosystem. Accordingly, the influence of meteorological conditions on upwelling and phytoplankton (Chl-a concentration) is highly relevant. In this context, the link among atmospheric conditions, identified through CWTs, upwelling and Chl-a conditions was established for the entire study area, through a probability analysis. Generally, results suggest that for western coastal segment north component CWTs (N, NE and NW) induced most of the times upwelling and phytoplankton generation. It is noteworthy that during winter, when SW weather type occur (recurrent, considering a frequency between 9 and 12%), upwelling was never observed; however, Chl-a concentrations had high conditional probabilities (between 10 and 20%). Therefore, in this case, Chl-a existing in ocean surface was related with rivers outflow that transports nutrients to the coast. At intermediate coastal segment, upwelling occurred essentially under NE, E and S CWTs during spring and summer. A probability of 100% was found as well as an offshore surface transport almost perpendicular to coast, favouring upwelling and generating high rates of phytoplankton at surface. Finally, at northern coastal segment and for both seasons, south CWT (S) induced significant upwelling generation with the highest probability for Chl-a to exceed its mean value. Indeed, due to coastline orientation (parallel to equator) S type can generate upwelling favourable conditions transporting nutrient-rich water from lower depths to the surface and thus generating high primary production. Probabilities of upwelling occurrence under NE and E CWTs were also high (30–100%) for both seasons, being the probability of Chl-a to exceed its mean value under these conditions about 10% (except for NE during October to March). The definition of these relations constitutes a novel result and is of major importance considering that nowadays synoptic situations can be settled and forecasted in advance. Consequently, the connections established in this study between weather types and marine variables allow to identify the most productive regions according to weather conditions and therefore optimize resources and improve fisheries and aquaculture activities, both offshore and at the coast.

Numerical models are powerful tools to perform ocean high resolution (spatial and temporal) studies, allowing the study of specific events as well as to design future scenarios. Physical-biological coupled models have been recently explored by the scientific community and had showed strong potential to understanding the ocean biogeochemical processes. Accordingly, a coupled circulation and biogeochemical model was implemented in the study region, with the objective to study the ocean biological response to physical factors. The model used was MOHID and a downscalling approach with two nested domains was applied. Model results were evaluated against several databases of *in situ* and remote sensed data of physical and biological variables available for the study area, during years 2013 and 2014. Variables such as water temperature, salinity and current velocity were compared along the whole 2013 year for five buoys located along Galician coast. Results reveal the model accuracy in reproducing the seasonal evolution of water temperature and salinity, showing a maximum $RMSE$ of 0.6°C for water temperature and 0.21 for salinity, during the period analysed. Predicted current velocity also showed good agreement with measurements ($RMSE$ at most 0.13 m s^{-1}). *In situ* SSE at three locations near coast was also compared with model predictions, with the higher error achieved for the Aveiro station ($RMSE$ of 0.13 m).

Model accuracy in reproducing the main vertical features of the ocean was also evaluated through comparison with Argo buoys data, which are programmed to operate in regions where bathymetry is deeper or equal to 2000 m depth. Variables such as water temperature, salinity and oxygen were compared with model predictions, revealing models accuracy to reproduce the upper layer thermodynamics and vertical stratification, as well as the distribution of oxygen along the water column. Finally, a set of remote sensed images was used to validate the spatial distribution of SST and Chl-a concentrations. Despite some differences, mainly in summer Chl-a distribution, good agreement was observed. Indeed, ocean biological features are strongly dependent from the interactions between physical, chemical and biological factors and therefore are very difficult to reproduce.

Once validated, the numerical model was used to explore phytoplankton patterns during two upwelling events: a strong that occurred during July 2014, and a weak during August 2013. For both events two upwelling cells (regions where the upwelling of cold water is strong) were identified along the western coastal segment: one near

Cape Finisterre and other near Minho River. For the weakest event (2013) the Chl-a concentration shows inverse relation with SST, with maxima values occurring in Minho and Cape Finisterre upwelling cells. Otherwise, for the strongest event (2014), a decay of Chl-a concentration in upwelling cells was observed. Intense and persistent winds induce appreciable offshore movement of water masses and create excessive turbulence yielding an environment unsuitable for phytoplankton growth. Bakun (2006) proposed that biological success is only possible in a marine environment if the balance between enrichment, concentration and retention is preserved. Here retention process, which represents the ability of surface currents to keep phytoplankton in coastal areas, are not preserved for the case of 2014 event. Indeed, for this event a strong equatorward flow develops near coast promoting advection offshore, where residence time is higher and phytoplankton grows. Otherwise, for 2013 event a poleward flow is detected near coastal region promoting high Chl-a waters retention. Due to wide continental shelf at the southern part of western coastal segment an accumulation of pigment rich waters is observed, for both events.

Overall, the outcome of this thesis show different conditions at each coastal segment, leading to an unbalanced phytoplankton distribution along the study area. Seasonal wind induced coastal upwelling, freshwater input and vertical mixing cycle were considered the main responsible for high biological diversity of the region, with important implications on phytoplankton growth. Both remote sensing imagery and numeric modelling revealed to be valuable methodologies to study physical and biological features in the region under study. Therefore, results of this thesis, as well as the methodologies developed, may be replicated in other upwelling systems, to improve understanding of main factors influencing phytoplankton generation and growth.

All the aims established for this thesis were achieved and new insights in the comprehension of primary production along the northwestern coast of IP were proposed. Some limitations were identified, mainly in the modelling task. The major problems concern the biogeochemical variables, namely the temporal resolution of the initial conditions and the lack of *in situ* data with appropriate temporal resolution for all rivers discharging in the region. It remains for future the implementation of a more complex ecologic model developed for MOHID, the Life modulus. Future research should also focus in the study of the continental runoff influence on the phytoplankton blooms, mainly in winter, through the numerical application developed. Also the dynamics of upwelling cells should be further explored, in order to understand if the decay of Chl-a concentration is a recurrent phenomenon and/or a problem for the fisheries in the region.

References

Allain G., Petitgas P. and Lazure P. (2001). The influence of mesoscale ocean processes on anchovy Engraulis encrasicolus recruitment in the Bay of Biscay estimated with a threedimensional hydrodynamic mode. *Fisheries Oceanography*, 10, 151–163.

Allen C.M. (1982). Numerical simulation of contaminant dispersion in estuary flows. In *Proceddings of the Royal Society of London A*. Vol. 381, 179–194.

Alvarez I., deCastro M., Gomez-Gesteira M. and Prego R. (2005). Inter- and intra-annual analysis of the salinity and temperature evolution in the Galician Rías Baixas-ocean boundary (northwest Spain). *Journal of Geophysical Research: Oceans*, 110, C04008.

Alvarez I., deCastro M., Prego R. and Gomez-Gesteira M. (2003). Hydrographic characterization of a winter-upwelling event in the Ria of Pontevedra (NW Spain). *Estuarine, Coastal and Shelf Science*, 56, 869–876.

Alvarez I., Gomez-Gesteira M., deCastro M. and Carvalho D. (2014). Comparison of different wind products and buoy wind data with seasonality and interannual climate variability in the southern Bay of Biscay (2000-2009). *Deep-Sea Research Part II: Topical Studies in Oceanography*, 106, 38–48.

Alvarez I., Gomez-Gesteira M., deCastro M. and Dias J.M. (2008a). Spatiotemporal evolution of upwelling regime along the western coast of the Iberian Peninsula. *Journal of Geophysical Research: Oceans*, 113, C07020.

Alvarez I., Gomez-Gesteira M., deCastro M., Lorenzo M.N., Crespo A.J.C. and Dias J.M. (2011). Comparative analysis of upwelling influence between the western and northern coast of the Iberian Peninsula. *Continental Shelf Research*, 31, 388–399.

Alvarez I., Gomez-Gesteira M., deCastro M. and Novoa E.M. (2008b). Ekman transport along the Galician Coast (NW, Spain) calculated from QuikSCAT winds. *Journal of Marine Systems*, 72, 101–105.

Alvarez I., Lorenzo M.N. and deCastro M. (2012). Analysis of chlorophyll a concentration along the Galician coast: seasonal variability and trends. *ICES Journal of Marine Science*.

Alvarez-Salgado X.A., Figueiras F.G., Perez F.F., Groom S., Nogueira E., Borges A., Chou L., Castro C.G., Rios G.M.A.F., Miller A.E.J., Frankignoulle M., Savidge G. and Wollast R. (2003). The Portugal coastal counter current off NW Spain: new insights on its biogeochemical variability. *Progress in Oceanography*, 56, 281–321.

Alvarez-Salgado X.A., Rosón G., Perez F.F. and Pazos Y. (1993). Hydrographic variability off Rías Baixas (NW Spain) during the upwelling season. *Journal of Geophysical Research: Oceans*, 98, 14447–14455.

Alvarez-Salgado X.A., Rosón G., Pérez F.F. and Pazos Y. (1996). Nitrogen cycling in an estuarine upwelling system, the Ria de Arousa (NW Spain) I Short-time-scale patterns of hydrodynamic and biogeochemical circulation. *Marine Ecology Progress Series*, 135, 259–273.

Ambar I. and Fiúza A.F.G. (1994). Some features of the Portugal Current System: a poleward slope undercurrent, an upwelling-related summer southward flow and an autumn-winter poleward coastal surface current. In *Proceedings of the International Conference on Air-Sea Interaction and on Meteorology and Oceanography of the Coastal Zone*. American Meteorological Society, 286–287.

Anderson T.W. (1963). Asymptotic theory for principal component analysis. *The Annals of Mathematical Statistics*, 34, 122–148.

Antoine D., Morel A., Gordon H.R., Banzon V.F. and Evans R.H. (2005). Bridging ocean color observations of the 1980s and 2000s in search of long-term trends. *Journal of Geophysical Research: Oceans*, 110, C06009.

Arakwa A. and Lamb V. (1977). Computational design of the basic dynamical processes of the UCLA general circulation model. *Methods in Computational Physics*, 17, 174–267.

Aravena G., Broitman B. and Stenseth N.C. (2014). Twelve years of change in coastal upwelling along the central-northern coast of Chile: spatially heterogeneous responses to climatic variability. *PLoS ONE*, 9(2).

Arrigo K.R., Worthen D., Schnell A. and Lizotte M.P. (1998). Primary production in southern ocean waters. *Journal of Geophysical Research: Oceans*, 103(C8), 15587–15600.

Arístegui J., Barton E.D., Álvarez Salgado X.A., Santos A.M.P., Figueiras F.G., Kifani S., Hernández-León S., Mason E., Machú E. and Demarcq H. (2009). Sub-regional ecosystem variability in the Canary Current upwelling. *Progress in Oceanography*, 83, 33–48.

Arístegui J., Álvarez Salgado X.A., Barton E.D., Figueiras F.G., Hernández-León S., Roy C. and Santos A.M.P. (2006). Oceanography and fisheries of the Canary Current/Iberian region of the eastern North Atlantic. In *The Global Coastal Ocean. Interdisciplinary Regional Studies and Synthesis, The Sea: Ideas and Observations on Progress in the Study of the Seas* (Robinson A. and Brink K.H., eds.), Vol. 14, Harvard University Press, 877–931.

Bailey S.W. and Werdell P.J. (2006). A multi-sensor approach for the on-orbit validation of ocean color satellite data products. *Remote Sensing of Environment*, 102, 12–23.

Bakun A. (1990). Global climate change and intensification of coastal ocean upwelling. *Science*, 247, 198–201.

Bakun A. (2006). Front and edies as key structures in the habitat of marine fish larvae: opportunity, adaptative and response and competitve advantage. *Scientia Marina*, 70S2, 105–122.

Bakun A., Field D., Redondo-Rodriguez A. and Weeks S. (2010). Greenhouse gas, upwelling-favorable winds, and the future of coastal ocean upwelling ecosystems. *Global Change Biology*, 16, 1213–28.

Barton E.D., Field D.B. and Roy C. (2013). Canary current upwelling: More or less? *Progress in Oceanography*, 116, 167–178.

Blanton J.O., Tenore K.R., Castillejo F., Schwing L.P.A.F.B. and Lavín A. (1987). The relationship of upwelling to mussel production in the rias of the western coast of Spain. *Journal of Marine Research: Oceans*, 45, 497–511.

Bode A., Alvarez-Ossorio M.T., Cabanas J.M., Miranda A. and Varela M. (2009). Recent trends in plankton and upwelling intensity off Galicia (NW Spain). *Progress in Oceanography*, 83, 342–350.

Bode A., Casas B. and Varela M. (1994). Size-fractionated primary productivity and biomass in the Galician shelf (NW Spain): Netplankton versus nanoplankton dominance. *Scientia Marina*, 58, 131–141.

Bode A., Varela M., Casas B. and Gonzalez N. (2002). Intrusions of eastern North Atlantic central waters and phytoplanktonin north and northwestern Iberian shelf during spring. *Journal of Marine Systems*, 36, 197–218.

Borges M.F., Santos A.M.P., Crato N., Mendes H. and Mota B. (2003). Sardine regime shifts off Portugal: a time series analysis of catches and wind conditions. *Scientia Marina*, 67, 235–244.

Botas J.A., Fernandez E., Bode A. and Anadon R. (1989). Water masses off the Central Cantabrian coast. *Scientia Marina*, 53, 755–761.

Botas J.A., Fernandez E., Bode A. and Anadon R. (1990). A persistent upwelling off central Cantabrian Coast (Bay of Biscay). *Estuarine, Coastal and Shelf Science*, 30(2), 185–199.

Brickley P.J. and Thomas A.C. (2004). Satellite-measured seasonal and inter-annual chlorophyll variability in the Northeast Pacific and Coastal Gulf of Alaska. *Deep Sea Research Part II: Topical Studies in Oceanography*, 51, 229–245.

Brock T.D. (1981). Calculating solar radiation for ecological studies. *Ecological Modelling*, 14, 1–19.

Burchard H. (2002). *Applied Turbulence Modelling in Marine Waters, Lecture Notes in Earth Sciences*, Vol. 100. Springer, NY, 215 pp.

Cabrillo R.S., González-Pola C., Ruiz-Villareal M. and Montero A.L. (2011). Mixed layer depth (MLD) variability in the southern Bay of Biscay. Deepening of winter MLDs concurrent with generalized upper water warming trends? *Ocean Dynamics*, 61, 1215–1235.

Canuto V.M., Howard A., Cheng Y. and Dubovikov M.S. (2001). Ocean turbulence. Part I: One-point closure model - momentum and heat vertical diffusivities. *Journal of Physical Oceanography*, 31(6), 1413–1426.

Cardeira S., Rita F., Relvas P. and Cravo A. (2013). Chlorophyll a and chemical signatures during an upwelling event off south Portuguese coast (SW Iberia). *Continental Shelf Research*, 52, 133–149.

Carder K.L., Chen F.R., Lee Z.P., Hawes S.K. and Kamykowski D. (1999). Semianalytic moderate-resolution imaging spectrometer algorithms for chlorophyll a and absorption with bio-optical domains based on nitrate-depletion temperatures. *Journal of Geophysical Research: Oceans*, 104, 5403–5421.

Carrera P. and Porteiro C. (2003). Stock dynamics of the Iberian sardine (Sardina pilchardus, W.) and its implication on the fishery off Galicia (NW Spain). *Scientia Marina*, 67, 245–258.

Carvalho D., Rocha A., Gómez-Gesteira M. and Santos C.S. (2014a). Comparison of reanalyzed, analyzed, satellite-retrieved and NWP modelled winds with buoy data along the Iberian Peninsula coast. *Remote Sensing of Environment*, 152, 480–492.

Carvalho D., Rocha A., Gómez-Gesteira M. and Santos C.S. (2014b). Offshore wind energy resource simulation forced by different reanalyses: Comparison with observed data in the Iberian Peninsula. *Applied Energy*, 134, 57–64.

Casas B., Varela M., Canle M., Gonzalez N. and Bode A. (1997). Seasonal variations of nutrients, Seston and phytoplankton, and upwelling intensity off La Coruña (NW Spain). *Estuarine, Coastal and Shelf Science*, 44, 767–778.

Castro C.G., Perez F.F., Alvarez-Salgado X.A. and Fraga F. (2000). Coupling between the thermohaline, chemical and biological fields during two contrasting upwelling events off NW Iberian Peninsula. *Continental Shelf Research*, 20, 189–210.

Chen P., Pan D. and Mao Z. (2015). Application of a laser fluorometer for discriminating phytoplankton species. *Optics & Laser Technology*, 67, 50–56.

Chippada S., Dawson C. and Wheeler M. (1998). A godunov-type finite volume method for the system of shallow water equations. *Computer Methods in Applied Mechanics and Engineering*, 151, 105–130.

Coelho H., Neves R., Leitão M. and Santos A. (2002). A model for ocean circulation on the Iberian coast. *Journal of Marine Systems*, 32, 153–179.

Cortesi N., Gonzalez-Hidalgo J., Trigo R. and Ramos A. (2014). Weather types and spatial variability of precipitation in the Iberian Peninsula. *International Journal of Climatology*, 34, 2661–2677.

Cravo A., Cardeira P.R.S., Rita F., Madureira M. and Sanchez R. (2010). An upwelling filament off southwest Iberia: effect on the chlorophyll a and nutrient export. *Continental Shelf Research*, 30, 1601–1613.

Darecki M. and Stramski D. (2004). An evaluation of MODIS and SeaWiFS bio-optical algorithms in the Baltic Sea. *Remote Sensing of Environment*, 89(3), 326–350.

deCastro M., Dale A.W., Gomez-Gesteira M., Prego R. and Alvarez I. (2006). Hydrographic and atmospheric analysis of an autumnal upwelling event in the Ria of Vigo (NW Iberian Peninsula). *Estuarine, Coastal and Shelf Science*, 68, 529–537.

deCastro M., Gómez-Gesteira M., Alvarez I. and Gesteira J.L.G. (2009). Present warming within the context of cooling-warming cycles observed since 1854 in the Bay of Biscay. *Continental Shelf Research*, 29, 1053–1059.

deCastro M., Gomez-Gesteira M., Alvarez I. and Crespo A.J.C. (2011). Atmospheric modes influence on Iberian Poleward Current variability. *Continental Shelf Research*, 31, 425–432.

Demarcq H. (2009). Trends in primary production, sea surface temperature and wind in upwelling systems (1998-2007). *Progress in Oceanography*, 83, 376–385.

Demarcq H., Barlow R. and Hutchings L. (2007). Application of a chlorophyll index derived from satellite data to investigate the variability of phytoplankton in the Benguela ecosystem. *African Journal of Marine Science*, 29(2), 271–282.

Denman K.L. and Gargett A.E. (1995). Biological/physical interactions in the upper oceans: The role of vertical and small scale transport processes. *Annual Review of Fluid Mechanics*, 27, 225–255.

dePablo F., Tomás C., Soriano L.R. and Diego L. (2009). Winter circulation weather types and hospital admissions for cardiovascular, respiratory and digestive diseases in Salamanca, Spain. *International Journal of Climatology*, 29(11), 1692–1703.

Dickson R.R. and Hughes D.G. (1981). Satellite evidences of mesoscale eddy activity over the Bay Biscay abyssal plain. *Oceanologica Acta*, 4, 43–46.

DiLorenzo E., Schneider N., Cobb K.M., Franks P.J.S., Chhak K., Miller A.J., McWilliams J.C., Bograd S.J., Arango H., Curchitser E., Powell T.M. and Rivière P. (2008). North Pacific Gyre Oscillation links ocean climate and ecosystem change. *Geophysical Research Letters*, 35, 1944–8007.

Donnelly C., Arheimer B., Capell R., Dahne J. and Strömqvist J. (2013). Regional overview of nutrient load in Europe – challenges when using a large-scale model approach, E-HYPE. Understanding fresh-water quality problems in a changing world. In *Proceedings of IAHS-IAPSO-IASPEI Assembly, Gothenburg, Sweden.* Vol. 361, 49–58.

dos Santos A., Santos A.M.P., Conway D.V.P., Bartilotti C., Lourenço P. and Queiroga H. (2008). Diel vertical migration of decapod larvae in the Portuguese coastal upwellling ecosystem: implications for offshore transport. *Marine Ecology*, 359, 171–183.

Duarte A.A.L.S., Pinho J.L., Pardal M.A., Neto J.M., Vieira J.P. and Santos F.S. (2002). Hydrodynamic modelling for Mondego estuary water quality management. *Imprensa da Universidade de Coimbra*, 12pp.

Echevin V., Aumont O., Ledesma J. and Flores G. (2008). The seasonal cycle of surface chlorophyll in the peruvian upwelling system: A modelling study. *Progress in Oceanography*, 79(2-4), 167–176.

Edwards C.A., Batchelder H.P. and Powell T.M. (2000). Modeling microzooplankton and macrozooplankton dynamics within a coastal upwelling system. *Journal of Plankton Research*, 22, 1619–1648.

EPA (1985). *Rates, constants and kinetics formulations in surface water quality modelling.* United States Environmental Protection Agency, Report EPA/600/3-85/040, 2nd ed., 454 pp.

Esteban P., Jones P.D., Martin-Vide J. and Mases M. (2005). Atmospheric circulation patterns related to heavy snowfall days in Andorra, Pyrenees. *International Journal of Climatology*, 25(3), 319–329.

Fairall C.W., Bradley E.F., Godfrey J.S., Wick G.A. and Edson J.B. (1996). Cool-skin and warm-layer effects on sea surface temperature. *Journal of Geophysical Research: Oceans*, 101, 1295–1308.

Fasham M.J.R., Ducklow H.W. and McKelvie S.M. (1990). A nitrogen-based model of plankton dynamics in the oceanic mixed layer. *Journal of Marine Research*, 48(3), 591–639.

Fasham M.J.R., Sarmiento J.L., Slater R.D., Ducklow H.W. and Williams R. (1993). Ecosystem behavior at Bermuda Station and Ocean Weather Station India: A general circulation model and observational analysis. *Global Biogeochemical Cycles*, 7, 379–416.

Fennel K., Hetland R., Feng Y. and DiMarco S. (2011). A coupled physical-biological model of the Northern Gulf of Mexico shelf: model description, validation and analysis of phytoplankton variability . *Biogeosciences*, 8, 1881–1899.

Figueiras F.G., Labarta U. and Reiriz M.J.F. (2002). Coastal upwelling, primary production and mussel growth in the Rías Baixas of Galicia. *Hydrobiologia*, 484, 121–131.

Fiúza A.F.G. (1983). Upwelling patterns off Portugal. In *Coastal Upwelling: Its Sediment Record, Part A: Responses of the Sedimentary Regime to Present Coastal Upwelling* (Suess E. and Thiede J., eds.), Springer US, 85–98.

Fiúza A.F.G. (1984). *Hidrologia e dinâmica das águas costeiras de Portugal.* PhD Thesis, Universidade de Lisboa, 294 pp.

Fiúza A.F.G., Hamann M., Ambar I., del Rio G.D., Gonzales N. and Cabanas J.M. (1998). Water masses and their circulation off western Iberian during May 1993. *Deep-Sea Research I: Oceanographic Research Papers*, 45, 1127–1160.

Fiúza A.F.G., Macedo M.E. and Guerreiro M.R. (1982). Climatological space and time variation of the Portugal coastal upwelling. *Oceanologica Acta*, 5(1), 31–40.

Flather R.A. (1976). A tidal model of the northwest European continental shelf. *Mémoires de la Société Royale des Sciences de Liège*, 6, 141–164.

Fofonoff P. and Millard R. (1983). Algorithms for computation of fundamental properties of seawater. *Unesco technical papers in marine science*, 44, 58 pp.

Fraga F. (1981). Upwelling off Galician Coast, Northwest Spain. In *Coastal Upwelling* (Richardson F., ed.), American Geophysical Union, Washington, DC, 176–182.

Fraga F., Mourino C. and Manriquez M. (1982). Las massas de agua en las costas de Galicia: junio-octubre. *Resultados Expediciones Cientificas*, 10, 51–77.

Franz B.A., Bailey S.W., Werdell P.J. and McClain C.R. (2007). Sensor-independent approach to the vicarious calibration of satellite ocean color radiometry. *Applied Optics*, 46(22), 5068–5082.

Frouin R., Ambar I. and Boyd T.J. (1990). Observations of a poleward surface current off the coast of Portugal and Spain during winter. *Journal of Geophysical Research: Oceans*, 95, 679–691.

Gao S., Wang H., Liu G. and Li H. (2013). Spatio-temporal variability of chlorophyll a and its responses to sea surface temperature, winds and height anomaly in the western South of China Sea. *Acta Oceanologica Sinica*, 32, 48–58.

Garcia C.A.E. and Garcia V.M.T. (2008). Variability of chlorophyll-a from ocean color images in the La Plata continental shelf region. *Continental Shelf Research*, 28, 1568–1578.

Garcia-Reys M. and Largier J. (2010). Observations of increased wind-driven coastal upwelling off central California. *Journal of Geophysical Research: Oceans*, 115, C04011.

Garcia-Soto C., Pingree R.D. and Valdes L. (2002). Navidad development in the southern Bay of Biscay: Climate change and swoddy structure from remote sensing and in situ measurements. *Journal of Geophysical Research: Oceans*, 107, 3118.

Gómez-Gesteira M., Gimeno L., deCastro M., Lorenzo M.N., I, Nieto R., Taboada J.J., Crespo A.J.C., Ramos A.M., Iglesias I., Gómez-Gesteira J.L., Santo F.E., Barriopedro D. and Trigo I.F. (2011). The state of the climate in NW Iberia. *Climate Research*, 48, 109–144.

Gomez-Gesteira M., deCastro M., Alvarez I. and Gomez-Gesteira J.L. (2008). Coastal sea surface temperature warming trend along the continental part of the Atlantic Arc (1985-2005). *Journal of Geophysical Research: Oceans*, 113, C04010.

Gomez-Gesteira M., Moreira C., Alvarez I. and deCastro M. (2006). Ekman transport along the Galician coast (northwest Spain) calculated from forecasted winds. *Journal of Geophysical Research: Oceans*, 111, C10005.

González-Quirós R., Cabal J., Alvarez-Marqués F. and Isla A. (2003). Ichthyoplankton distribution and plankton production related to the shelf break front at the Avilés Canyon. *ICES Journal of Marine Science*, 60(2), 198–210.

Gordon H.R. and Morel A.Y. (1983). *Remote assessment of ocean color for interpretation of satellite visible imagery*, Vol. 4 of *Lecture notes on coastal and estuarine studies*. American Geophysical Union, 114 pp.

Gotelli N. (1995). *A Primer of Ecology*. Sinauer Associates Inc., 206 pp.

Gregg W.W. and Casey N.W. (2004). Global and regional evaluation of the SeaWiFS chlorophyll data set. *Remote Sensing of Environment*, 93, 463–479.

Gregg W.W., Casey N.W. and McClain C.R. (2005). Recent trends in global ocean chlorophyll. *Geophysical Research Letters*, 32, L03606.

Gregg W.W. and Conkright M.E. (2002). Decadal changes in global ocean chlorophyll. *Geophysical Research Letters*, 29(15), 1730.

Gregg W.W., Conkright M.E., Ginoux P., O'Reilly J.E. and Casey N.W. (2003). Ocean primary production and climate: global decadal changes. *Geophysical Research Letters*, 30(15), 1809.

Gruber N., Frenzel H., Doney S.C., Marchesiello P., McWilliams J.C., Moisan J.R., Oram J., Plattner G.K. and Stolzenbach K.D. (2006). Eddy-resolving simulation of plankton ecosystem dynamics in the California Current System. *Deep-Sea Research Part I: Oceanographic Research Papers*, 53(9), 1483–1516.

Hardman-Mountford N.J., Richardson A.J., Agenbag J.J., Hagen E., Nykjaer L., Shillington F.A. and Villacastin C. (2003). Ocean climate of the South East Atlantic observed from satellite data and wind models. *Progress in Oceanography*, 59(2-3), 181–221.

Haynes R., Barton E.D. and Pilling I. (1993). Development, persistence and variability of upwelling filaments off Atlantic coast of the Iberian Peninsula. *Journal of Geophysical Research: Oceans*, 98, 22681–22692.

Hernández-Carrasco I., Rossi V., Hernández-García E., Garçon V. and López C. (2014). The reduction of plankton biomass induced by mesoscale stirring: A modeling study in the Benguela upwelling. *Deep Sea Research Part I: Oceanographic Research Papers*, 83, 65–80.

Herrera J.L., Varela R.A. and Roson G. (2008). Spatial variability of the barotropic M2 constituent tidal current over the Rías Baixas Galician shelf (NW Spain). *Journal of Marine Systems*, 72(1-4), 189–199.

Hickey B.M. and Banas N.S. (2003). Oceanography of the US Pacific Northwest Coastal Ocean and estuaries with application to coastal ecology. *Estuaries*, 26, 1010–1031.

Ho C.R., Zheng Q.N. and Kuo N.J. (2004). SeaWiFs observations of upwelling south of Madagascar: long-term variability and interaction with East Madagascar Current. *Deep Sea Research Part II: Topical Studies in Oceanography*, 51, 59–67.

Hu C.M., Carder K.L. and Muller-Karger F.E. (2001). How precise are SeaWiFS ocean color estimates? Implications of digitization-noise errors. *Remote Sensing of Environment*, 76, 239–249.

Huthnance J.M., Aken H.M.V., White M., Barton E.D., Cann B.L., Coelho E.F., Fanjul E.A., Miller P. and Vitorino J. (2002). Ocean margin exchange - water flux estimates. *Journal of Marine Systems*, 32, 107–137.

Jones P.D., Hulme M. and Briffa K. (1993). A comparison of Lamb circulation types with an objective classification scheme. *International Journal of Climatology*, 13(6), 656–663.

Kaplan E.L. and Meier P. (1958). Nonparametric-estimation from incomplete observations. *Journal of the American Statistical Association*, 53(282), 457–481.

Koutsikopoulos C. and Cann B.L. (1996). Physical processes and hydrological structures related to the Bay of Biscay anchovy. *Scientia Marina*, 60, 9–19.

Krauss W. (1986). The North Atlantic current. *Journal of Geophysical Research: Oceans*, 91, 5061–5074.

Krezel A., Szymanek L., Kozlowski L. and Szymelfenig M. (2005). Influence of coastal upwelling on chlorophyll a concentration in the surface water along the Polish coast of the Baltic Sea. *Oceanologia*, 47, 433–452.

Lachkar Z. and Gruber N. (2011). What controls biological productivity in coastal upwelling systems? Insights from a comparative modeling study. *Biogeosciences Discussions*, 8, 5617–5652.

Lamb H.H. (1972). British Isles weather types and a register of the daily sequence of circulation patterns, 1861-1971. *Geophysical Memoires*, 85, 88 pp.

Large W. and Pond S. (1981). Open Ocean momentum flux measurements in moderate to strong winds. *Journal of Physical Oceanography*, 11, 324–3361.

Lavín A., Moreno-Ventas X., de Zarate V.O., Abaunza P. and Cabanas J.M. (2007). Environmental variability in the North Atlantic and Iberian waters and its influence on horse mackerel (Trachurus trachurus) and albacore (Thunnus alalunga) dynamics. *ICES Journal of Marine Science*, 64, 425–438.

Lavín A., Valdes L., Sanchez F., Abaunza P., Forest J., Boucher P., Lazure P. and Jegou A.M. (2006). The Bay of Biscay: the encountering of the ocean and the shelf. In *The Global Coastal Ocean. Interdisciplinary Regional Studies and Synthesis, The Sea: Ideas and Observations on Progress in the Study of the Seas* (Robinson A. and Brink K.H., eds.), Vol. 14, Harvard University Press, 933–1001.

Leendertse J.J. (1967). Aspects of a computational model for long-period water-wave propagation. *Rand Corporation for the United States Air force Project Rand*, 179 pp.

Lemos R.T. and Pires H.O. (2004). The upwelling regime off west Portuguese coast, 1941-2000. *International Journal of Climatology*, 24(4), 511–524.

Levitus S., Antonov J.I., Boyer T.P. and Stephens C. (2000). Warming of the world ocean. *Science*, 287, 2225–2229.

Levy M., Lehahn Y., Andre J.M., Memery L., Loisel H. and Heifetz E. (2005). Production regimes in the northeast Atlantic: A study based on Sea-viewing Wide Field-of-view Sensor (SeaWiFS) chlorophyll and ocean general circulation model mixed layer depth. *Journal of Geophysical Research: Oceans*, 110(C7), C07S10.

Li Y. and He R. (2014). Spatial and temporal variability of SST and ocean color in the Gulf of Maine based on cloud-free SST and chlorophyll reconstructions. *Remote Sensing of Environment*, 144, 98–108.

Lihan T., Mustapha M.A., Rahim S.A. and Iida K. (2011). Influence of river plume on variability of Chlorophyll-a concentration using satellite images. *Journal of Applied Sciences*, 11, 484–493.

Liu M., Liu X., MA A., Li T. and Du Z. (2014). Spatio-temporal stability and abnormality of chlorophyll-a in the Northern South China Sea during 2002-2012 from MODIS images using wavelet analysis. *Continental Shelf Research*, 75, 15–27.

Longhurst A. (1998). *The ecological geography of the sea.* Academic Press, Elsevier, 2nd ed., 560 pp.

Lopes C., Azevedo A. and Dias J.M. (2013). Flooding assessment under sea level rise scenarios: Ria de Aveiro case study. *Journal of Coastal Research*, SI65, 766–771.

Lorenzo M.N., Ramos A.M., Taboada J.J. and Gimeno L. (2011). Changes in present and future circulation types frequency in Northwest Iberian Peninsula. *PLoS ONE*, 6(1).

Lorenzo M.N., Taboada J.J. and Gimeno L. (2008). Links between circulation weather types and teleconnection patterns and their influence on precipitation patterns in Galicia (NW Spain). *International Journal of Climatology*, 28(11), 1493–1505.

Lunven M., Guillaud J.F., Youenou A., Crassous M.P., Berric R., Gall E.L., Kerouel R., Labry C. and Aminot A. (2005). Nutrient and phytoplankton distribution in the Loire River plume (Bay of Biscay, France) resolved by a new Fine Scale Sampler. *Estuarine Coastal and Shelf Science*, 65, 94–108.

Lyard F., Lefevre F., Letellier T. and Francis O. (2006). Modelling the global ocean tides: modern insights from FES2004. *Ocean Dynamics*, 56(5-6), 394–415.

Macias D., Guerreiro C.T., Prieto L., Peliz A. and Ruiz J. (2014). A high-resolution hydrodynamic-biogeochemical coupled model of the Gulf of Cadiz - Alboran Sea region. *Mediterranean Marine Science*, 739–752.

Marques V., Chaves C., Morais A., Cardador F. and Stratoudakis Y. (2005). Distribution and abundance of snipefish (Macroramphosus spp.) off Portugal (1998–2003). *Scientia Marina*, 69(4), 563–576.

Marta-Almeida M. and Dubert J. (2006). The structure of tides in the Western Iberian region. *Continental Shelf Research*, 26(3), 385–400.

Marta-Almeida M., Reboreda R., Rocha C., Dubert J., Nolasco R., Cordeiro N., Luna T., Rocha A., e Silva J.D.L., Queiroga H., Peliz A. and Ruiz-Villarreal M. (2012). Towards Operational Modeling and Forecasting of the Iberian Shelves Ecosystem. *PLoS ONE*, 7(5).

Martins C.S., Hamann M. and Fiuza A.F.G. (2002). Surface circulation in the Eastern North Atlantic from drifters and altimetry. *Journal of Geophysical Research: Oceans*, 107(C12), 1–10.

Martins F., Leitão P., Silva P. and Neves R. (2001). 3D modelling in the Sado estuary using a new generic vertical discretization approach. *Oceanologica Acta*, 24(1), 1–12.

Martins F., Reis M.P., Neves R., Cravo A.P., Brito A. and Venâncio A. (2004). Molluscan shellfish bacterial contamination in Ria Formosa coastal lagoon: A modelling approach. *Journal of Coastal Research*, SI39, 1551–1555.

Martinsen E. and Engedahl H. (1987). Implementation and testing of a lateral boundary scheme as an open boundary condition in a barotropic ocean model. *Coastal Engineering*, 11, 603–627.

Mateus M., Riflet G., Chambel P., Fernandes L., Juliano M., Campuzano F., de Pablo H. and Neves R. (2012a). An operational model for the West Iberian coast: products and services. *Ocean Science*, 8, 713–732.

Mateus M., Vaz N. and Neves R. (2012b). A process-oriented model of pelagic biogeochemistry for marine systems. Part II: Application to a mesotidal estuary. *Journal of Marine Systems*, 94, S90–S101.

McClain C.R., Chao S.Y., Atkinson L.P., Blanton J.O. and Decastillejo F. (1986). Wind-driven upwelling in the vicinity of Cape Finisterre, Spain. *Journal of Geophysical Research: Oceans*, 91, 8470–8486.

McGregor G.R., Walters S. and Wordley J. (1999). Daily hospital respiratory admissions and winter air mass types, Birmingham, UK. *International Journal of Biometeorology*, 43, 21–30.

McGregor H.V., Dima M., Fisher H.W. and Mulitza S. (2007). Rapid 20th-century increase in coastal upwelling off northwest África. *Science*, 315, 637–639.

Mellor G.L. and Yamada T. (1982). Development of a turbulence closure model for geophysical fluid problems. *Review of Geophysics and Space Physics*, 20, 851–875.

Mendes R., Sousa M.C., deCastro M., Goméz-Gesteira M. and Dias J.M. (2016). New insights into the Western Iberian Buoyant Plume: Interaction between the Douro and Minho River plumes under winter conditions. *Progress in Oceanography*, 141, 30–43.

Mendes R., Vaz N., Fernández-Nóvoa D., da Silva J.C.B., deCastro M., Gomez-Gesteira M. and Dias J.M. (2014). Observation of a turbid plume using MODIS imagery: The case of Douro estuary (Portugal). *Remote Sensing of Environment*, 154, 127–138.

Miles T.N. and He R. (2010). Temporal and spatial variability of Chl-a and SST on the South Atlantic Bight: Revisiting with cloud free reconstructions of MODIS satellite imagery. *Continental Shelf Research*, 30, 1951–1962.

Miranda P.M.A., Alves J.M.R. and Serra N. (2012). Climate change and upwelling: response of Iberian upwelling to atmospheric forcing in a regional climate scenario. *Climate Dynamics*, 40(11), 2813–2824.

Montes I., Dewitte B., Gutknecht E., Paulmier A., Dadou I., Oschlies A. and Garçon V. (2014). High-resolution modeling of the Eastern Tropical Pacific oxygen minimum zone: sensivity to the tropical oceanic circulation. *Journal of Geophysical Research: Oceans*, 119, 5515–5532.

Moore J.K., Done S.C., Gloverb D.M. and Fungc I.Y. (2002). Iron cycling and nutrient-limitation patterns in surface waters of the World Ocean. *Deep-Sea Research Part II: Topical Studies in Oceanography*, 49, 463–507.

Murta A.G., Abaunza P., Cardador F. and Sanchez F. (2008). Ontogenic migrations of horse mackerel along the Iberian coast. *Fisheries Research*, 89, 186–195.

Nababan B., Muller-Karger F.E., Hu C. and Biggs D.C. (2011). Chlorophyll variability in the Northeastern Gulf of Mexico. *International Journal of Remote Sensing*, 32, 8373–8391.

Narayan N., Paul A., Mulitza S. and Schulz M. (2010). Trends in coastal upwelling intensity during the late 20th century. *Ocean Science*, 6, 815–823.

Narimousa S. and Maxworthy T. (1989). Application of a laboratory model to the interpretation of satellite and field observations of coastal upwelling. *Dynamics of Atmospheres and Oceans*, 13(1-2), 1–46.

Navarro G. and Ruiz J. (2006). Spatial and temporal variability of phytoplankton in the Gulf of Cadiz through remote sensing images. *Deep Sea Research Part II: Topical Studies in Oceanography*, 53, 1241–1260.

Nelson G. and Hutchings L. (1983). The Benguela upwelling area. *Progress in Oceanography*, 12, 333–356.

Nolasco R., Pires A.C., Cordeiro N.G.F., Cann B.L. and Dubert J. (2013). A high-resolution modeling study of the Western Iberian Margin mean and seasonal upper ocean circulation. *Ocean Dynamics*, 63(9-10), 1041–1062.

North G.R., Bell T.L., Cahalan R.F. and Moeng F.J. (1982). Sampling errors in the estimation of Empirical Orthogonal Functions. *Monthly Weather Review*, 110, 699–706.

Oliveira P.B., Moita T., Catarino R. and da Silva A.J. (2007). Wintertime SST and Chla off NW Iberian shelf from satellite and insitu data. In *Joint 2007 EUMETSAT Meteorological Satellite Conference and the 15th Satellite Meteorology & Oceanography Conference*. American Meteorological Society, 8 pp.

Oliveira P.B., Nolasco R., Dubert J., Moita T. and Peliz A. (2009). Surface temperature, chlorophyll and advection patterns during a summer upwelling event off central Portugal. *Continental Shelf Research*, 29, 759–774.

Otero J., Alvarez-Salgado X.A., Gonzalez A.F., Gilcoto M. and Guerra A. (2009). High-frequency coastal upwelling events influence Octopus vulgaris larval dynamics on the NW Iberian shelf. *Marine Ecology-Progress Series*, 386, 123–132.

Otero P., M Ruiz-Villareal A.P. and Cabanas J.M. (2010). Climatology and reconstrution of runoff time series in northwest Iberia: influence in the shelf buoyancy budget off Ria de Vigo. *Scientia Marina*, 74(2), 247–266.

Otero P., Ruiz-Villareal M. and Peliz A. (2008). Variability of River plumes off Northwest Iberia in response to wind events. *Journal of Marine Systems*, 72, 238–255.

Parada M. and Canton M. (1998). Sea surface temperature variability in Alboran sea from satellite data. *International Journal of Remote Sensing*, 19, 2439–2450.

Paredes D., Trigo R.M., Garcia-Herrera R. and Trigo I.F. (2006). Understanding precipitation changes in Iberia in early spring: Weather typing and storm-tracking approaches. *Journal of Hydrometeorology*, 7, 101–113.

Patti B., Guisande C., Riveiro I., Thejll P., Cuttitta A., Bonanno A., Basilone G., Buscaino G. and Mazzola S. (2010). Effect of atmospheric CO_2 and solar activity on wind regime and water column stability in the major global upwelling areas. *Estuarine, Coastal and Shelf Science*, 88, 45–52.

Patti B., Guisande C., Vergara A.R., Riveiro I., Maneiro I., Bonanno A.B.A., Buscaino G., Cuttitta G., Basilone G. and Mazzola S. (2008). Factores responsible for the differences in satellite based chlorophyll a concentration between the major global upwelling areas. *Estuarine, Coastal and Shelf Science*, 76, 775–786.

Pauly D. and Christensen V. (1995). Primary production required to sustain global fisheries. *Nature*, 374, 255–257.

Pelegri J.L., Cana L. and Gonzalez-Davila M. (2005). Coupling between the open ocean and the coastal upwelling region off northwest Africa: water recirculation and offshore pumping of organic matter. *Journal of Marine Systems*, 54, 3–37.

Peliz A., Buutov D. and Teles-Machado A. (2013). The Alboran Sea mesoscale in a long term high resolution simulation: statistical analysis. *Ocean Modelling*, 72, 32–52.

Peliz A., Dubert J. and Haidvogel D.A. (2003). Subinertial response of a density driven eastern boundary poleward current to wind forcing. *Journal of Physical Oceanography*, 33, 1633–1650.

Peliz A., Dubert J., Santos A., Oliveira P. and Cann B.L. (2005). Winter upper ocean circulation in the Western Iberian Basin - Fronts, Eddies and Poleward Flows: an overview. *Deep Sea Research I*, 52, 621–646.

Peliz A. and Fiúza A.F.G. (1999). Temporal and spatial variability of CZCS-derived phytoplankton pigment concentrations off western Iberian Peninsula. *International Journal of Remote Sensing*, 20(7), 1363–1403.

Peliz A., Rosa T.L., Santos A.M.P. and Pissarra J.L. (2002). Fronts, jets, and counter-flows in the Western Iberian upwelling system. *Journal of Marine Systems*, 35, 61–77.

Perez F.F., Castro C.N., Rios A.F. and Fraga F. (2005). Chemical properties of the deep winter mixed layer in the Northeast Atlantic ($40 - 47\,^{\circ}$N). *Journal of Marine Systems*, 54, 115–125.

Picado A., Lopes C., Mendes R., Vaz N. and Dias J.M. (2013). Storm surge impact in the hydrodynamics of a tidal lagoon: the case of Ria de Aveiro. *Journal of Coastal Research*, SI65, 796–801.

Pina P. (2001). *An integrated approach to study the Tagus estuary water quality.* MSc Thesis, Instituto Superior Técnico, Universidade de Lisboa, Portugal, 70 pp.

Pingree R. and Cann B.L. (1990). Structure, strength and seasonality of the slope currents in the Bay of Biscay region. *Journal of the Marine Biology Association of U.K.*, 70, 857–885.

Pingree R.D. and Cann B.L. (1989). Celtic and armorican slope and shelf residual currents. *Progress in Oceanography*, 23, 303–338.

Pollard R. and Pu S. (1985). Structure and circulation of the upper Atlantic Ocean northeast of Azores. *Progress in Oceanography*, 14, 443–462.

Portela L.I. (1996). *Modelação matemática de processos hidrodinâmicos e de qualidade da água no estuário do Tejo.* PhD Thesis, Instituto Superior Técnico, Lisboa, 240 pp.

Powell T.M., Lewis C.V.W., Curchitser E.N., Haidvogel D.B., Hermann A.J. and Dobbins E.L. (2006). Results from a three-dimensional, nested biological-physical model of the California Current System and comparisons with statistics from satellite imagery. *Journal of Geophysical Research: Oceans*, 111, C07018.

Prego R. and Bao R. (1997). Upwelling influence on the Galician coastal: silicate in shelf water and under lying surface sediments. *Continental Shelf Research*, 17, 307–318.

Prego R., Guzman-Zuniga D., Varela M., deCastro M. and Gomez-Gesteira M. (2007). Consequences of winter upwelling events on biogeochemical and phytoplankton patterns in a western Galician ria (NW Iberian Peninsula). *Estuarine, Coastal and Shelf Science*, 73, 409–422.

Prego R., Álvarez Vázquez M.A., Uña-Álvarez E. and Doval M.D. (2015). Fluvial contributions of nutrients and dissolved organic matter to the Ria of Ares-Betanzos. *Panorámica Interdisciplinar sobre el agua, Educación Editora*, 89–93.

Prego R. and Varela M. (1998). Hydrography of the Artabro Gulf in summer: western coastal limit of the Cantabrian seawater and wind-induced upwelling at Prior Cape. *Oceanologica Acta*, 21, 145–155.

Prego R. and Vergara J. (1998). Nutrient fluxes to the Bay of Biscay from Cantabrian rivers (Spain). *Oceanologica Acta*, 21, 271–278.

Pérez F.F., Rios A.F., King B.A. and Pollard R.T. (1995). Decadal changes of the θ-S relationship of the eastern North Atlantic Central Water. *Deep Sea Research Part I: Oceanographic Research Papers*, 42, 1849–1864.

Queiroga H., Cruz T., dos Santosc A., Dubert J., González-Gordilloe J.I., Paulaf J., Peliz A. and Santos A.M.P. (2007). Oceanographic and behavioural processes affecting invertebrate larval dispersal and supply in the western Iberia upwelling ecosystem. *Progress in Oceanography*, 74, 174–191.

Ré P., Silva R.C., Cunha E., Farinha A., Menezes I. and Moita T. (1990). Sardine spawning off Portugal. *Boletim do Instituto Nacional de Investigaco das Pescas, Portugal*, 15, 31–44.

Ramos A.M., Lorenzo M.N. and Gimeno L. (2010). Compatibility between modes of low-frequency variability and circulation types: A case study of the northwest Iberian Peninsula. *Journal of Geophysical Research-Atmospheres*, 115, D02113.

Ramos A.M., Pires A.C., Sousa P.M. and Trigo R.M. (2013). The use of circulation weather types to predict upwelling activity along the western Iberian Peninsula coast. *Continental Shelf Research*, 69, 38–51.

Ramos A.M., Ramos R., Sousa P., Trigo R., Janeira M. and Prior V. (2011). Cloud to ground lightning activity over Portugal and its association with circulation weather types. *Atmospheric Research*, 101, 84–101.

Reboreda R., Castro C.G., Álvarez Salgado X.A., Nolasco R., Cordeiro N.G.F., Queiroga H. and Dubert J. (2014). Modeling the seasonal and interannual variability (2001-2010) of chlorophyl-a in the Iberian margin. *Journal of Sea Research*, 93, 133–149.

Reboreda R., Castro C.G., Álvarez Salgado X.A., Nolasco R., Cordeiro N.G.F., Queiroga H. and Dubert J. (2015). Oxygen in the Iberian margin: A modeling study. *Progress in Oceanography*, 131, 1–20.

Relvas P., Barton D., Dubert J., Oliveira P.B., Peliz A., da Silva J.C.B. and Santos A.M.P. (2007). Physical oceanography of the western Iberia ecosystem: latest views and challenges. *Progress in Oceanography*, 74, 149–173.

Relvas P., Luís J. and Santos A.M.P. (2009). Importance of the mesoscale in the decadal changes observed in the northern Canary upwelling system. *Geophysical Research Letters*, 36.

Ribeiro A.C., Peliz A. and Santos A.M.P. (2005). A study of the response of chlorophyll-a biomass to a winter upwelling event off Western Iberia using SeaWiFS and in situ data. *Journal of Marine Systems*, 53, 87–107.

Richardson A.J. (2008). In hot water: zooplankton and climate change. *ICES Journal of Marine Science*, 65, 279–295.

Richardson A.J. and Schoeman D.S. (2004). Climate impact on plankton ecosystems in the Northeast Atlantic. *Science*, 305, 1609–1612.

Rios A.F., Perez F.F. and Fraga F. (1992). Water masses in upper and middle North Atlantic Ocean east of Azores. *Deep Sea Research I*, 39, 645–658.

Rocha C., Cordeiro N., Nolasco R. and Dubert J. (2013). Numerical modelling of the phytoplankton patterns in an upwelling event off the NW Iberian Margin. *Journal of Coastal Research*, SI65, 117–122.

Roe P.L. (1985). Some contributions to the modeling of discontinuous flows. *Proceedings of the Fifteenth Summer Seminar on Applied Mathematics*, 22, 163–193.

Ruiz-Villareal M., Bolding K., Burchard H. and Demirov E. (2005). Coupling of the GOTM turbulence module to some three-dimensional ocean models. In *Results of the CARTUM Project* (Baumert H.Z., Simpson J.H. and Sundermann J., eds.), Cambridge, 225–237.

Sá C., Silva J.D., Oliveira P.B. and Brotas V. (2008). Comparison of Meris (Algal-1 and Algal-2) and Modis (Oc3M) chlorophyll products and validation with Hplc in situ data collected off the western Iberian Peninsula. *European Space Agency, (Special Publication) Esa Sp*, 4 pp.

Saha S., Moorthi S., Pan H.L., Wu X.R., Wang J.D., Nadiga S., Tripp P., Kistler R., Woollen J., Behringer D., Liu H.X., Stokes D., Grumbine R., Gayno G., Wang J., Hou Y.T., Chuang H.Y., Juang H.M.H., Sela J., Iredell M., Treadon R., Kleist D., Delst P.V., Keyser D., Derber J., Ek M., Meng J., Wei H.L., Yang R.Q., Lord S., den Dool H.V., Kumar A., Wang W.Q., Long C., Chelliah M., Xue Y., Huang B.Y., Schemm J.K., Ebisuzaki W., Lin R., Chen P.P.X.M.Y., Zhou S.T., Higgins W., Zou C.Z., Liu Q.H., Chen Y., Han Y., Cucurull L., Reynolds R.W., Rutledge G. and Goldberg M. (2010). The NCEP climate forecast system reanalysis. *Bulletin of the American Meteorological Society*, 91, 1015–1057.

Santos A.M.P., Borges M.F. and Groom S. (2001). Sardine and horse mackerel recruitment and upwelling off Portugal. *Journal of Marine Sciences*, 58(3), 589–596.

Santos A.M.P., Kazmin A. and Peliz A. (2005). Decadal changes in the Canary upwelling system as revealed by satellite observations: their impact on productivity. *Journal of Marine Research*, 63, 359–379.

Santos A.M.P., Peliz A., Dubert J., Oliveira P.B., Angelico M.M. and Re P. (2004).

Impact of a winter upwelling event on the distribution and transport of sardine (Sardina pilchardus) eggs and larvae off western Iberia: a retention mechanism. *Continental Shelf Research*, 24, 149–165.

Saraiva S., Pina P., Martins F., Santos M., Braunschweig F. and Neves R. (2007). Modelling the influence of nutrient loads on Portuguese estuaries. *Hydrobiologia*, 587, 5–18.

Scarla J.W. and Frank A.S. (1994). Interannual scales of variation of pigment concentrations from coastal zone color scanner data in the Benguela Upwelling system and the Subtropical Convergence zone south of Africa. *Journal of Geophysical Research: Oceans*, 99(C4), 7385–7399.

Seo H., Brink K.H., Dorman C.E., Koracin D. and Edwards C.A. (2012). What determines the spatial pattern in summer upwelling trends on the U.S. West Coast? *Journal of Geophysical Research: Oceans*, 117, C08012.

Shulman I., Anderson S., Rowley C., DeRada S., Doyle J. and Ramp S. (2010). Comparisons of upwelling and relaxation events in the Monterey Bay area. *Journal of Geophysical Research: Oceans*, 115, C005483.

Siedlecki S.A., Banas N.S., Davis K.A., Giddings S., Hickey B.M., MacCready P., Connolly T. and Geier S. (2015). Seasonal and interannual oxygen variability on the Washington and Oregon continental shelves. *Journal of Geophysical Research: Oceans*, 120, 608–633.

Sánchez F., Rodríguez-Cabello C. and Olaso I. (2005). The role of Elasmobranchs in the Cantabrian Sea Shelf ecosystem and impact of the fisheries on them. *Journal of Northwest Atlantic Fishery Science*, 35, 467–480.

Somavilla R., González-Pola C., Rodriguez C., Josey S.A. and Sánchez R.F. (2009). Large changes in the hidrographic structure of the Bay Biscay after the extreme mixing of winter 2005. *Journal of Geophysical Research: Oceans*, 114, C01001.

Sousa M.C., Vaz N., Alvarez I., Gomez-Gesteira M. and Dias J.M. (2014a). Influence of the Minho River plume on the Rías Baixas (NW of the Iberian Peninsula). *Journal of Marine Systems*, 139, 248–260.

Sousa M.C., Vaz N., Alvarez I., Gomez-Gesteira M. and Dias J.M. (2014b). Modeling the Minho River plume intrusion into the Rías Baixas (NW Iberian Peninsula). *Continental Shelf Research*, 85, 30–41.

Sverdrup H. (1953). On conditions for the vernal blooming of phytoplankton. *Journal Cons. Int. Explor. Mer.*, 18(1), 287–295.

Swinbank W.C. (1963). Long-wave radiation from clear skies. *Quarterly Journal of the Royal Meteorological Society*, 89(381), 339–348.

Tenore K.R., Alonso-Noval M., Alvarez-Ossorio M., Atkinson L.P., Cabanas J.M., Cal R.M., Campos H.J., Castillejo F., Chesney E.J., Gonzalez N., Hanson R.B., McClain C.R., Miranda A., Roman M.R., Sanchez J., Santiago G., Valdes L., Varela M. and Yoder J. (1995). Fisheries and oceanography off Galicia, NW Spain: mesoscale spatial and temporal changes in physical processes and resultant patterns of biological productivity. *Journal of Geophysical Research*, 100, 10943–10966.

Torres R. and Barton E. (2006). Onset and development of the Iberian poleward flow along the Galician coast. *Continental Shelf Research*, 26, 1134–1153.

Torres R., Barton E.D., Miller P. and Fanjul E. (2003). Spatial patterns of wind and sea surface temperature in the Galician upwelling region. *Journal of Geophysical Research: Oceans*, 108, 3130–3143.

Tréguer P., Corre P.L. and Grall J.R. (1979). The seasonal variations of nutrients in the upper waters of the Bay Biscay region and their relation to phytoplankton growth. *Deep Sea Research*, 26A, 1121–1152.

Trigo R.M. and DaCamara C.C. (2000). Circulation weather types and their influence on the precipitation regime in Portugal. *International Journal of Climatology*, 20(13), 1559–1581.

Uiboupin R., Laanemets J., Sipelgas L., Raag L., Lips I. and Buhhalko N. (2012). Monitoring the effect of upwelling on the chlorophyll a distribution in the Gulf of Finland (Baltic Sea) using remote sensing and in situ data. *Oceanologia*, 54, 395–419.

Valiela I. (1995). *Marine Ecological Processes, Chapter 2 - Factors affecting primary production.* Springer, 2nd ed., 686 pp.

van Aken H.M. (2002). Surface currents in the Bay of Biscay as observed with drifters between 1995 and 1999. *Deep Sea Research Part I: Oceanographic Research Papers*, 49(6), 1071–1086.

Varela M., Alvarez-Ossorio M.T., Bode A., Prego R., Bernardez P. and Garcia-Soto C. (2010). The effects of a winter upwelling on biogeochemical and planktonic components in an area close to the Galician Upwelling Core: The Sound of Corcubion (NW Spain). *Journal of Sea Research*, 64, 260–272.

Varela M., Prego R. and Pazos Y. (2008). Spatial and temporal variability of phytoplankton biomass, primary production and community structure in the Pontevedra Ria (NW Iberian Peninsula): oceanographic periods and possible response to environmental changes. *Marine Biology*, 154, 483–499.

Varela M., Prego R., Y Pazos Y. and Morono A. (2005). Influence of upwelling and river runoff interaction on phytoplankton assemblages in a Middle Galician Ria and comparison with northern and southern rias (NW Iberian Peninsula). *Estuarine, Coastal and Shelf Science*, 64, 721–737.

Vaz N. (2007). *Study of heat and salt transport processes in the Espinheiro Channel (Ria de Aveiro)*. PhD Thesis, Departamento de Física, Universidade de Aveiro, Portugal, 151 pp.

Vaz N. and Dias J.M. (2014). Residual currents and transport pathways in the Tagus estuary, Portugal: the role of freshwater discharge and wind. *Journal of Coastal Research*, SI70, 610–615.

Vaz N., Dias J.M., Leitão P. and Martins I. (2005). Horizontal patterns of water temperature and salinity in an estuarine tidal channel: Ria de Aveiro. *Ocean Dynamics*, 55, 416–429.

Vaz N., Mateus M., Plecha S., Sousa M.C., Leitão P.C., Neves R. and Dias J.M. (2015). Modeling SST and chlorophyll patterns in a coupled estuary-coastal system of Portugal: The Tagus case study. *Journal of Marine Systems*, 147, 123–137.

Venegas R.M., Strub P.T., Beier E., Letelier R., Thomas A.C., Cowles T., James C., Soto-Mardones L. and Cabrera C. (2008). Satellite-derived variability in chlorophyll, wind stress, sea surface height, and temperature in the northern California Current System. *Journal of Geophysical Research: Oceans*, 113, C03015.

Villamor B., Gonzalez-Pola C., Lavín A., Valdés L., de Lanzós A.L., Franco C., Cabanas J.M., Bernal M., Hernandez C., Carrera P., Porteiro C. and Alvarez E. (2004). Distribution and survival of larvae of mackerel (Scomber scombrus) in the North and Northwest of the Iberian Peninsula, in relation to environmental conditions during spring 2000. *ICES CM*, J:07.

Waite J.N. and Mueter F.J. (2013). Spatial and temporal variability of chlorophyll-a concentrations in the coastal Gulf of Alaska, 1998–2011, using cloud-free reconstructions of SeaWiFS and MODIS-Aqua data. *Progress in Oceanography*, 116, 179–192.

Wallace J.M. and Hobbs P.V. (2006). *Atmospheric Science. An Introductory Survey.* Academic Press, UK, 2nd ed., 504 pp.

Wang Y., Jiang H., Jin J., Zhang X., Lu X. and Wang Y. (2015). Spatial-temporal variations of chlorophyll-a in the adjacent sea area of the Yangtze River Estuary influenced by Yangtze River discharge. *International Environmental Research Public Health*, 12(5), 5420–5438.

Ware D.M. and Thomson R.E. (2005). Bottom-up ecosystem trophic dynamics determine fish production in the Northeast Pacific. *Science*, 308, 1280–1285.

Werdell J. (2009). Global bio-optical algorithms for ocean color satellite applications: inherent optical properties algorithm workshop at ocean optics XIX; Barga, Italy, 3–4 October 2008. *Eos Trans. AGU*, 90(1), 4–4.

Wick G.A., Emery W.J., Kantha L.H. and Schluessel P. (1996). The behavior of the bulk-skin sea surface temperature difference under varying wind speed and heat flux. *Journal of Physical Oceanography*, 26, 1969–1988.

Williams G., Sapoznik M., Ocampo-Reinaldo M., Solis M., Narvarte M., Gonzalez R., Esteves J.L. and Gagliardini D. (2010). Comparison of AVHRR and SeaWiFS imagery with fishing activity and insitu data in San Matias Gulf, Argentina. *International Journal of Remote Sensing*, 31, 4531–4542.

Wooster W.S., Bakun A. and McClain D.R. (1976). The seasonal upwelling cycle along the eastern boundary of the North Atlantic. *Journal of Marine Research*, 34, 131–141.

Xu Y., Chant R., Gong D.L., Castelao R., Glenn S. and Schofield O. (2011). Seasonal variability of chlorophyll a in the Mid-Atlantic Bight. *Continental Shelf Research*, 31, 1640–1650.

Yoder J.A., O'Reilly J.E., Barnard A.H., Moore T.S. and Ruhsam C.M. (2001). Variability in coastal zone color scanner (CZCS) chlorophyll imagery of ocean margin waters off US East Coast. *Continental Shelf Research*, 21, 1197–1218.

Yoder J.A., Schollaert S.E. and O'Reilly J.E. (2002). Climatological phytoplankton chlorophyll and sea surface temperature patterns in continental shelf and slope waters off the northeast US coast. *Association for the Sciences of Limnology and Oceanography*, 47, 672–682.